The Development of an Automated, Fluorescent, Quantitative Three-Dimensional *In Vitro* Organotypic Invasion Assay

Ketan Vinodbhai Patel

This thesis is submitted for the degree of

Doctor of Philosophy

Centre for Tumour Biology, Barts Cancer Institute

Barts and The London School of Medicine & Dentistry

Queen Mary University of London

September 2017

Declaration of Originality

I, Ketan Vinodbhai Patel, confirm that the research included within this thesis is my own work or that where it has been carried out in collaboration with, or supported by others, that this is duly acknowledged and my contribution indicated. Previously published material has also been acknowledged in the correct manner.

I attest that I have exercised reasonable care to ensure that the work is original, and does not to the best of my knowledge break any UK law, infringe any third party's copyright or other Intellectual Property Right, or contain any confidential material.

I accept the College has the right to use plagiarism detection software to check the electronic version of this thesis.

I confirm that this thesis has not been previously submitted for the award of a degree by this or any other university.

This study was sponsored and supported by the Biotechnology and Biological Sciences Research Council (BBSRC) and AstraZeneca.

Signature: 

Date: 29.09.2017

Acknowledgments

The work presented in this thesis would not have been possible without the contribution and support from others. I would like to extend my gratitude to those who have assisted me throughout this journey.

Firstly, a very special mention to my supervisor, John Marshall. Thank you for not only for giving me the opportunity to work on such a fascinating project within your group, but also for your unwavering enthusiasm, guidance and support. Thank you for supervising me through this PhD with continued patience and opportunities. Not many PhDs involve drinking whisky until 2am, whilst sat in a roof top swimming pool in Singapore after a week-long conference. It has been a pleasure to work with you during the past four years.

This project would not have been possible without the contributions and support of my sponsors BBSRC and AstraZeneca. Thank you to Simon Barry and Cath Eberlein of AstraZeneca, for all of your advice and the insightful discussions throughout my project. I am incredibly appreciative to members of the High-Content Biology group at AstraZeneca led by Beverley Isherwood. Thank you for all of your advice and guidance, but also making me feel welcome and part of the team from the very beginning. Additionally, thank you to Cerith Pierce, for his persistent willingness to help me during my visits to AstraZeneca. I further extend my gratitude to Sam Peel, thank you for your constant assistance and positive approach during the last four years, but also for all of your help in the lab at Alderley Park and Cambridge and for getting me out of my room to join for beers with everyone.

To the past and present β6 group members; I would like to thank you all for welcoming me in to the group from day one. I've enjoyed the many laughs we've had during our group meetings and the β6 group retreat. I am truly grateful for all of your professional guidance over the past four years.

I am thankful to those at the BCI who have helped me during my project. Thank you; Yasmine and Ed C for your knowledge and help with lentiviral particles; Bakhouche, King of the West(ern blots); Joseph Brook, for that amazing mathematical brain of yours; Beta, Claire and Zareen for your kind words of advice with writing; Debbie for running the lab; Linda for helping me with the microscopes and George for his histopathology help and most importantly his delicious shortbread.

Thank you Claire, Caroline, Zareen, Banu and Ami for always being available to help and support me in the lab but also for the great laughs and fun times we all shared. I further extend my gratification to Claire and Caroline for all the support during writing.

For those who have not had 'the PhD experience'; it can be laborious days, late nights and long weekends and then you realise the experiment didn't work! However, I am grateful to have shared such challenging and frustrating times with the tumour biology lab members who kept spirits high and provided more than a few laughs along the way.

Special thanks to ar' kid - Prabhu, for never failing to make me laugh with your humorous antics. Thank you Yasmine, for being there to support and help me, but more importantly for all the countless little things that you did to cheer me up, from kindly bringing me treats, always making me laugh and going for spontaneous cake and pint breaks with me. Bakhouche, thank you for the stimulating debates on world politics, the education system, Brexit and countless other topics, but most importantly for your help, support and laughter during writing. Thanks to the brewing squad who provided many enjoyable evenings, in particular to Fulford and Ed W, for always being up for a laugh, supportive and good friends throughout.

Thanks to my friends outside of the lab, Adam, Arthur, James, Nacho and Rushen for all of your advice and support during the last years.

It's not very common to call your dad's best friend 'uncle', however I do. Not only out of respect, but because to me he is family. Sunil, you have been a constant presence in my life and I cannot thank you enough for all of the advice and support you have given me over the years.

I consider myself privileged to have a very caring and involved family. Firstly, to my uncles Vinod and Kishor and my aunties Gita and Mina. I cannot thank you enough for all of the encouragement and guidance you have continually given me and more importantly all of the delicious food that I have been lavished with over the last four years. I give my deepest gratification to my grandparents Ram Dada and Sita Baa, you are the pillars of hard work and strength for me and installed the importance of education into my life. To my late-grandmother Rukhi Baa, your care, encouragement and love will always be with me. To my siblings Anant, Rushina, Rashmi, Amish and Janak, thank you for the boundless support, not just during this PhD but also throughout my life. Adding to that, Janak, you have been supportive and helpful at every moment. Thank you so much for getting me out of the lab to enjoy pizza and

movie nights and providing me with a place to stay in the most crucial of times. I am truly grateful to all of you.

I am incredibly thankful to my brother Kumul, who has never stopped showing care and reassurance. Thank you for your endless support and most importantly all of the continued laughs we've had.

None of this would have been remotely possible without the two most important people in my life. There are not enough words to describe how grateful I am for everything that you have done for me. I am eternally grateful for the continuous care, guidance, love and support you have infinitely given me during this PhD but also throughout everything I have chosen to pursue. Thank you for believing in me and guiding me through life.

Mum and dad, you are my ultimate role models and this is for you.

I do not know what I may appear to the world; but to myself I seem to have been only like a boy playing on the seashore and diverting myself in now and then finding a smoother pebble or a prettier shell than ordinary, whilst the great ocean of truth lay undiscovered before me.

Isaac newton (1643 – 1727)

Abstract

Tumour metastasis is a complex multi-step biological process, which involves dispersion of cancer cells to various organ sites within the body. The tumour-stroma interface plays an important role within cancer progression and is a major area of focus within cancer research. It is imperative that we are able to understand what mechanisms the tumour cells use in order to achieve maximum invasive potential. Fibroblasts are one of the major host cell types that are usurped by the tumour cells to promote invasion. Thus, we must understand the molecular mechanisms by which fibroblasts are transformed by the tumours into tumour-promoting fibroblasts, thus enabling cancer progression.

Over 10 years ago our laboratory developed a quantitative image analysis methodology for analysing tumour and stromal fibroblast-interactions using 1ml collagen type I based three-dimensional (3D) organotypic gels. The assay is expensive, slow and can take 3-4 weeks before results are available.

In this study I have developed two smaller versions of this assay that enable drug/gene screening in 3D, that are quicker to analyse and affordable; mini-organotypics (100µl) and micro-organotypics (50µl). Using fluorescently labelled tumour (red) and fibroblast (green) populations, it is possible to view the invasive process live and *in situ*, using confocal microscopy. Analysis of fluorescent organotypic gels after 72 hours, showed that the fibroblasts are the principal invading cell type that commence invasion and are followed by the tumour cells.

For a proof-of-principle study I transfected human dermal fibroblasts with a customised SMARTpool siRNA library targeting proteases. Data collection was automated, thus allowing results within three days instead of three weeks. Relative to siRNA control treated fibroblasts, 16 out of 60 targeted proteases significantly reduced fibroblast and tumour cell invasion. Moreover, re-analysis of five lead proteases using individual siRNA for each gene identified that fibroblast MMP-17 and TMPRSS-13 is required by dermal fibroblasts to support invasion of cancer cells within this 3D assay.

I believe this novel 24-well 3D fluorescent mini-organotypic invasion assay will allow drug/gene screens to be conducted affordably on multiple different tumour-stroma cell combinations. Moreover, the 96-well 3D fluorescent micro-organotypic invasion assay is almost ready for use in high-throughput screening and thus will be of great value in both academia and industry.

Table of Contents

List of Figures

List of Tables

Abbreviations

.csv	comma separated values
.lsm	laser scanning microscope
.tiff	tagged image file format
2D	two-dimensional
3D	three-dimensional
ADAM	a disintegrin and metalloproteinase
ANOVA	analysis of variance
APS	ammonium persulphate
BM	basement membrane
BSA	bovine serum albumin
CAF	cancer associated fibroblast
CAPN	calcium dependent cysteine proteases
CASP	cysteine-aspartic proteases
CAT	collective amoeboid transition
CLSM	confocal laser scanning microscopy
CRISPR	clustered regularly interspaced short palindromic repeat
CS	chondroitin sulphate
CSPG	chondroitin sulphate proteoglycan
CVH	chronic vascular hyperpermeability
DCR	Dicer
DED	de-epidermised dermis
DHH	desert hedgehog
DMEM	Dulbecco's modified Eagle's medium
DMSO	dimethyl sulphoxide

DNA	deoxyribonucleic acid
DS	dermatan sulphate
dsRNA	double stranded RNA
E-cadherin	epithelial cadherin
ECL	enhanced chemiluminescence
ECM	extracellular matrix
EDTA	ethylenediaminetetraacetic acid
EGF	epidermal growth factor
EGFP	enhanced green fluorescent protein
EGFR	epidermal growth factor receptor
EHS	Engelbreth-Holm-Swarm
EMT	epithelial to mesenchymal transition
FBS	foetal bovine serum
FDA	Food and Drug Administration
FGF	fibroblast growth factor
FSC	forward scatter
FSF	foreskin fibroblast
GAG	glycosaminoglycan
GCU	green calibrated units
GPI	glycosyl-phosphatidyl inositol
H&E	haematoxylin and eosin
HA	hyaluronic acid
HDF	human dermal fibroblast
HEK293T	human embryonic kidney 293T
HER2	human epidermal growth factor receptor 2
HIV	human immunodeficiency virus

HPRT-1	hypoxanthine phosphoribosyltransferase-1
HRP	horseradish peroxidase
HS	heparan sulphate
HSC-70	heat shock chaperone-70
HSPG	heparan sulphate proteoglycan
HTS	high-throughput screening
IGF	insulin-like growth factor
IHH	Indian hedgehog
KD	knockdown
kDa	kilo Dalton
KGM	keratinocyte growth medium
KS	keratan sulphate
LED	light-emitting diode
LOF	loss of function
LWD	long working distance
MAT	mesenchymal amoeboid transition
MatLab®	Matrix Laboratory
MET	mesenchymal to epithelial transition
MIT	Massachusetts Institute of Technology
MMP	matrix metalloproteinase
MRC5	Medical Research Council cell stain 5
mRNA	messenger RNA
MT-MMP	membrane type matrix metalloproteinase
NP40	nonidet-P40
NSCLC	non-small cell lung carcinoma
NT	non-targeting siRNA control

OSC	organotypic skin culture
OSCC	oral squamous cell carcinoma
PAA	polyacrylic acid
PBS	phosphate-buffered saline
PCL	polycaprolactone
PDAC	pancreatic ductal adenocarcinoma
PEDF	pigment epithelium derived factor
PEG	polyethylene glycol
PET	polyethylene terephthalate
PG	proteoglycans
PGA	polyglycolic acid
PHA	polyhydroxyalkanoate
PLA	polylactic acid
PPF	polypropylene fumarate
PSC	pancreatic stellate cell
PVA	polyvinyl alcohol
qPCR	quantitative polymerase chain reaction
RCU	red calibrated units
RFP	red fluorescent protein
RISC	RNA-induced silencing complex
RNAi	ribonucleic acid interference
RPM	revolutions per minute
RPMI	Roswell Park Memorial Institute
SAR	structure-activity relationship
SCC	side scatter
sCMOS	scientific complementary metal-oxide semiconductor

SDS-PAGE	sodium dodecyl sulphate poly acrylamide gel electrophoresis
SERPIN	serine proteinase inhibitors
SHH	sonic hedgehog
siRNA	small interfering RNA
TBS-T	tri-buffered saline supplemented with Tween-20
TEMED	tetramethylethylenediamine
TGF-β	transforming growth factor-beta
TIMP	tissue inhibitors of metalloproteinase
TMPRSS	transmembrane serine proteases
TR-FRET	time resolved-fluorescence resonance energy transfer
TTSP	type 2 transmembrane serine proteases
VEGF	vascular endothelial growth factor
VPF	vascular permeability factor
WHO	World Health Organisation
α-mem	alpha-minimum essential medium

CHAPTER I: INTRODUCTION

1.0 Introduction

1.1 Approximately 38,630 new cancer cases worldwide each day

Data from the GLOBOCAN project, led by the World Health Organisation (WHO), estimated that in 2012 there were approximately 14.1 million new cancer cases of which 8.2 million deaths occurred worldwide (Torre et al., 2015). The causes of cancer are complex, diverse and only partially understood.

Tumour invasion and metastasis are the prime cause of death within cancer patients. The biological processes involved in metastasis are a series of very complex molecular mechanisms that consist of cells absconding from a primary tumour through loss of cohesion with their neighbouring cells, followed by local invasion into the surrounding matrix and ultimately formation of tumours at secondary sites. Secondary tumour sites develop as migrating cancer cells intravastate the lymphatic and vascular system, thus circulating and extravasting into a niche environment within the body that can support tumour growth (Hart, 1982; Hart and Fidler, 1980b).

1.2 Origins of cancer metastasis

In 1889 British surgeon, Stephen Paget, examined post mortem data from 735 women, all of whom died from breast cancer and noted that the distribution of tumour metastases was non-random. Interestingly, he described that tumour cells (the ‘seed’) grew preferentially within the surrounding vicinity of select organs (the ‘soil’) (Paget, 1889). This idea was challenged in 1928 by American pathologist, James Ewing, who proposed the idea that circulatory patterns between a primary tumour and specific secondary organs were sufficient in accounting for organ-specific metastasis (Ewing, 1928).

1.2.1 Defining metastasis

Metastasis, is regarded as an inefficient process due to the inability of most circulating tumour cells to grow at distant sites (Luzzi et al., 1998; Weiss, 1990). Metastasis is commonly defined as the ability of cancer cells to disperse from one tumour site to organs and tissues beyond where they originated and form new tumours (Chambers et al., 2002; Jiang et al., 2015) (**Figure 1.1**).

The process is a series of complex steps, driven by an accumulation of DNA mutations, that include; (1) the initial loss or disruption of the cell-cell adhesion molecules, such as epithelial (E)-cadherin (important for cell polarity and epithelial organisation (van Roy and Berx, 2008)). Thus, reduced adhesion may enhance the potential for metastasis through loss of contact and promotes uncontrolled proliferation (Cavallaro and Christofori, 2004). Tumour cells acquire an invasive and migratory phenotype, thus enabling penetration into surrounding tissue (Wells et al., 2013). This instigates; (2) invasion of tumour cells, degradation of basement membrane (BM) and extracellular matrix (ECM) and a transition from *in situ* to invasive carcinoma (Liotta et al., 1980). Tumour cells then migrate and intravastate the lymphatic or vascular system (Clark and Vignjevic, 2015); (3) tumour cells circulate and survive within the circulatory system until they arrest in microvascular beds (Fidler, 2003); (4) next, the tumour cells form adhesions to the endothelial cells, causing them to retract or die and thus begin to penetrate into the surrounding stromal microenvironment, known as extravasation (Liotta and Rao, 1986); (5) tumour cells acclimatise and thrive within the stroma, displaying increased levels of proliferation and angiogenesis leading to the development of a secondary foci and ultimately formation of micro-or macrometatasis (Fidler, 2003).

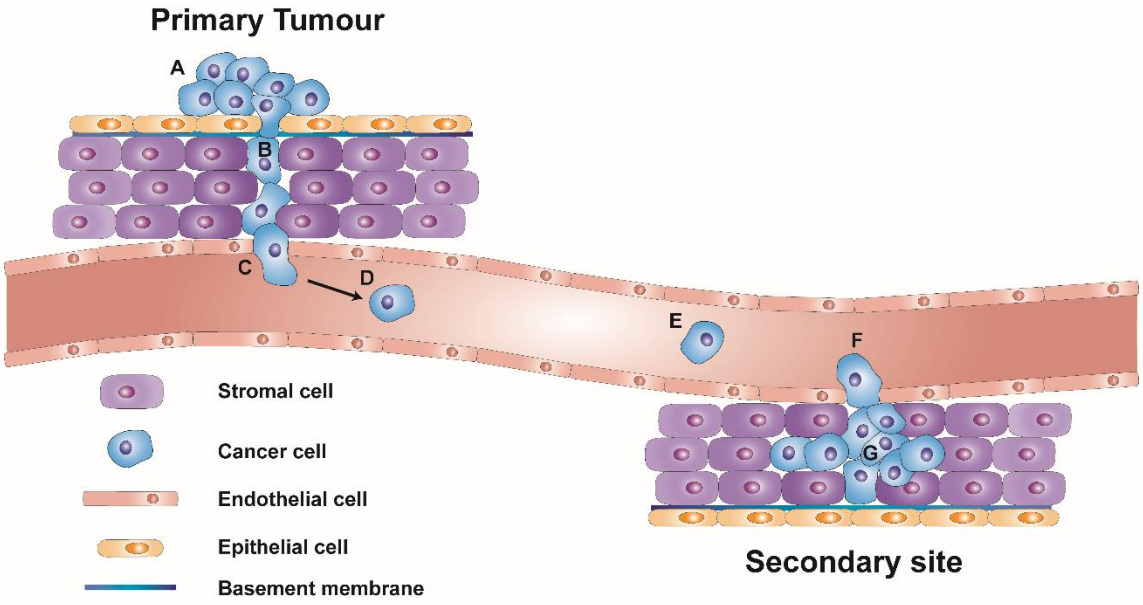

Figure 1.1: Steps in metastasis

During metastasis, cancer cells form an overt secondary tumour site through a series of complex processes. **A)** Cancer cells begin to loose cohesive properties with neighbouring cells and detach from the primary tumour site. **B)** Cancer cells invade through the basement membrane and migrate into the vasculature rich-stroma. This process is known as intravastation. **C)** Cancer cells cause endothelial retraction, thus breaching the vasculature system. **D)** Cells then begin migrating through the circulatory system, **E)** before arresting at microvascular beds. **F)** Cancer cells cause retraction of endothelial cells and extravastate into the surrounding microenvironment before **G)** forming secondary tumour sites, where cancer cells not only survive, but thrive and proliferate. (Image adapted from (Schroeder et al., 2011)).

1.2.2 Models of metastasis

The debate whether cancer metastasis is an early or late event in tumour progression is still ongoing and remains elusive (Friberg and Nystrom, 2015). Two distinct systematic progression models exist. The linear progression model is based on Leslie Fould's description of a stepwise progressive tumour development, by means of a permanent or irreversible qualitative change in one or more the tumours characteristics (Foulds, 1954).

On the contrary, the parallel progression model suggests a stepwise tumour development via morphological abnormalities and accumulation of genetic alterations that cause the cancer cells within a primary tumour to pass through multiple rounds of mutation and selection, before disseminating to form secondary sites (Cairns, 1975; Klein, 2009).

In line with linear progression, Olivier and colleagues reported an increase in mutation frequency for the tumour suppressor TP53, during advanced stages of breast cancer when compared to smaller earlier stage tumours (Olivier et al., 2006). On the other hand, the parallel progression model claims that tumour cell dissemination occurs early due to genetic alterations, thus leading to early separation and independent development of tumour cells (van Zijl et al., 2011).

Paget's 'seed and soil' theory describing an organ-specific pattern of metastasis has been reported by others. For example, the brain, bone, liver and lungs are the most assaulted organs for breast cancer metastasis (Chambers et al., 2002). Bone and lungs being the most common site of occurrence for metastasis (Langley and Fidler, 2011) and early tumour cell dissemination and formation of micrometastasis in these sites were reported for HER2 mutant breast cancer cells (Husemann et al., 2008). In addition, Hiratsuka and colleagues suggested that some primary tumours may transmit pro-metastatic signals to the lung, thus priming the metastatic soil for the arrival of the tumour cells (Hiratsuka et al., 2002).

1.2.3 Mechanisms of cancer cell invasion

Cancer cells can invade and migrate through tissues by moving collectively as epithelial sheets, detached clusters or as single cells via mesenchymal or amoeboid

cell migration; these invasion and migration modalities are themselves associated with cellular behaviours such as adhesion (Friedl and Wolf, 2003).

Collective cell migration is characterised by groups of cells which retain cellular adhesions and display a high correlation in directional movement between neighbouring cells and feature three distinct hallmarks; (1) cell-cell junctions remain intact during movement, resulting in cohorts of migrating cells (Friedl et al., 2004); (2) multicellular polarity and organisation of the actin-cytoskeleton generate traction forces that are required for collective cell movement (Hegerfeldt et al., 2002); and (3) collective cell migration requires rearrangement of the BM and remodelling of the ECM (Wolf et al., 2007). Collective cell migration includes movement of cells either as narrow linear strands which can occur by two-dimensional (2D) sheet migration or the formation of broad layered multicellular strands through three-dimensional (3D) tissues (Friedl et al., 2004; van Zijl et al., 2011). Collective cell migration was reported to occur during embryogenesis (Davidson and Keller, 1999) and branching morphogenesis (Simian et al., 2001).

Collective cell migration is typically known as the slowest form of migration and has been reported in wound closure during skin (Poujade et al., 2007) or corneal epithelium repair (Zelenka and Arpitha, 2008) after injury. Additionally, collective cell migration has been reported in breast cancer (Giampieri et al., 2009) and fibroblast-led collective invasion of oral squamous cell carcinoma (OSCC) (Gaggioli et al., 2007).

Single cell migration is characterised by the lack of cell-cell interactions with neighbouring cells. Tumour cells can apparently interconvert between various migratory strategies in response to a changing microenvironment. Thus, suggesting that suppression of single cell migration may require inhibition of mesenchymal or amoeboid-like migration (Valastyan and Weinberg, 2011). *In vitro* studies have reported that individually migrating cancer cells display increased contractility under control of the Rho-pathway and favours an amoeboid-like migration pattern (Sahai and Marshall, 2003), whereas lower contractility (or increased adhesion) favour more mesenchymal-like properties (Wolf et al., 2003).

Mesenchymal (or fibroblast-like) cell migration employs a five step cycle, including; (1) pseudopod protrusions at the leading edge; (2) formation of focal contacts; (3) focalised proteolysis; (4) actomyosin contraction; and (5) detachment of the trailing

edge (Friedl and Wolf, 2003). Cells that go through mesenchymal migration possess a fibroblast-like spindle shape that have been reported to be dependent on α6β4 and α2β1 integrin mediated adhesions. Mesenchymal migration takes place on cells from within the connective tissue of tumours, such as fibrosarcomas (Wolf et al., 2003) and gliomas (Paulus et al., 1996).

Amoeboid cell invasion hallmarks include, loss of polarity and loose attachment to the ECM, thus making it the fastest type of invasion (Condeelis and Segall, 2003). Cancer cells may acquire these characteristics through inhibition of integrin β1, leading to collective-to-amoeboid transition (CAT), where tumour masses invading surrounding tissues collectively dissociate into single migrating cells using amoeboid-like movement (Friedl, 2004). The transition from mesenchymal to amoeboid-like cells (MAT) was reported to be dependent on Rac and Rho/ROCK signalling and is independent of protease activities (Friedl and Wolf, 2003). Valastyan and colleagues reported that the microRNA, miR-31, inhibits breast cancer mesenchymal migration through concurrently supressed integrin α5 and amoeboid migration through RhoA suppression (Valastyan et al., 2009).

Furthermore, single-cell invasion pathways maybe incompatible without the loss of epithelial tissue organisation molecules, specifically E-cadherin (Jensen et al., 2015). Thus, tumour cells can undergo a cell-programmed transition, known as epithelial-mesenchymal transition (EMT) in order to become invasive. EMT is a normal process during development whereby epithelial cells obtain mesenchymal, fibroblast-like properties and are often identified by downregulation of E-cadherin and upregulation of vimentin (Larue and Bellacosa, 2005) as well as loss of apical-basal polarity (Thiery, 2002).

EMT contributes not only to tissue repair and embryonic development but also organ fibrosis and can promote cancer progression through loss of cell-cell adhesion molecules, such as E-cadherin (Thiery et al., 2009). Brabletz and colleagues reported that EMT occurs at the invasive front in colon carcinoma and produces single migratory cells that lose E-cadherin (Brabletz et al., 2001). In addition, transforming growth factor-beta (TGF-β) has been reported to promote EMT via blocking expression of E-cadherin, thus leading to increased expressions of mesenchymal proteins (vimentin and fibronectin) (Miyazono, 2009). The reversal of EMT is referred to as epithelial to mesenchymal transition (MET) and can be characterised by

epithelial reorganisation and also described as individual to collective transition (Thiery et al., 2009). During MET, mesenchymal cells regain their epithelial cell-cell junctions, thus, able to colonise at secondary tumour sites (Kalluri and Weinberg, 2009).

Circulating tumour cells (CTCs) (or tumour microemboli) are suggested to be a precursor to metastatic cancer and were first proposed in 1869 by Australian pathologist, Thomas Ashworth (Ashworth, 1869). CTCs must detach from tumours, probably through loss of cell-cell adhesions and intravastate in small groups of collectively-migrating tumour cells (Clark and Vignjevic, 2015). Studies have reported that clusters of CTCs are present in the circulatory system and blood of patients with invasive cancers, such as, breast (Cristofanilli et al., 2004), colon (Choy and McCulloch, 1993), lung (Hou et al., 2012), prostate (Makarovskiy et al., 1997) and renal cancer (Kats-Ugurlu et al., 2009). Identifying CTCs in the peripheral blood has become a valuable diagnostic tool and a predictor of clinical outcomes in patients with solid tumours (Pantel et al., 2008).

Intervention, but ideally prevention of metastasis pathways would provide a promising clinical therapy for cancer patients with or at risk of metastatic disease. Thus, development of a preclinical model to validate potential anti-metastatic therapies is in high demand.

1.3 Two-dimensional vs three-dimensional cultures

Currently the *in vitro* screening of synthetic and natural product compound libraries for anticancer agents focuses on cytotoxicity data using established cancer cell lines. The majority of these cell based assays are performed on 2D substrates (i.e. tissue culture plastic). Cell-based assays are an important pillar of the drug discovery process, providing a fast, repeatable and cost effective tool, thus avoiding large scale and cost intensive animal testing.

2D cell based assays have proven to be a reliable tool for drug discovery, especially within cancer research, for example, identifying small molecules for colorectal cancer treatment (Bialkowska and Yang, 2012) or when developing and validating functional cell-based assays (Sadikot et al., 2013). However, their limitations prohibit translational studies to be performed. In particular, the lack in capability of 2D cultures to accurately mimic the complexity and heterogeneity of tumours as observed *in vivo*. Consequently this leads to the loss of numerous signalling pathways being expressed, changes in cellular processes and changes in cell shape when grown on a 2D substrate (Lee et al., 2007).

Cellular behaviour, such as proliferation, differentiation, metabolism, motility, gene and protein expression and response to stimuli are all strongly influenced by the surrounding microenvironment. Evidently, it has been reported that these factors can be impeded and in some cases not present whatsoever within 2D environments (Chen et al., 1997; Itano et al., 2003; McBeath et al., 2004; Singhvi et al., 1994). It has been suggested that in 2D cultures, cell attachment onto planar surfaces occurs on one side of the cell, thus becoming flatter (von der Mark et al., 1977), and losing their differentiated phenotype (Petersen et al., 1992). Conversely, in 3D cultures, cell attachment occurs around the entire surface of the cell, thus regaining their physiological form and function (Baker and Chen, 2012). In general, cell attachment and spreading on 2D substrates occurs within a few minutes or hours, however in 3D this process can take several hours and even days (Khetan et al., 2013). **Table 1.1** summarises the advantages and disadvantages of both culturing methods.

Several studies have reported the use of 3D culture models over the commonly used 2D monolayer culture format (Ghajar and Bissell, 2010; Lee et al., 2007; Pampaloni et al., 2007; Rizki et al., 2008; Santiago-Walker et al., 2009) specifying their evident

advantages in providing a more physiological milieu and being able to recapitulate the architecture of living tissue.

3D cultures can be specifically synthesised using various substrates and scaffolds, thus providing environmental conditions that closely mimic those observed *in vivo* (Edmondson et al., 2014). The addition of the third dimension is a crucial feature, not only having an influence on the spatial organisation of the cells, but also inducing physical constraints. These spatial and physical constraints have a direct impact on the interactions between cells and their environment thus influencing various processes, such as differentiation (Weaver et al., 1997), proliferation (Bhadriraju and Chen, 2002) and cell-cell and cell-matrix signalling pathways, all which may not be observed in 2D (Baker and Chen, 2012; Hubbell, 1995; Kim et al., 2004).

Table 1.1: Summary of the advantages and disadvantages of 2D & 3D culture methods

Culture method	Advantages	Disadvantages
2D	Cost effective	Cells only form monolayers
	Ease of use	Reduced cell-cell and biomechanical interactions
	Fast results	Reduced signalling
3D	More accurate representation of *in vivo* environment and cell morphology & signalling	Complex culture system Lack vasculature and normal transport of small molecules
	Cells can grow in multiple layers	Increased expense
	Cell-cell and cell-ECM signalling present	Require sophisticated imaging platforms

1.3.1 Two-dimensional *in vitro* models

Historically cell migration experiments were performed via *in vitro* scratch assays, as described (Liang et al., 2007), whereby a wound is inflicted on a confluent monolayer of cells and the ability of the wound to close is assessed by capturing images at various time points using a phase contrast microscope. The simplicity and low cost of the assay allows us to study movement of cell populations, thus producing quantitative migration value. However the scratch assay does not permit the study of chemotactic (chemical) or haptotactic (substrate) agents; for this, a commonly used migration assay system, based on that developed by Boyden (Boyden, 1962) to study neutrophil migration, is employed. Often documented as the Boyden Chamber Assay, in this method, a cell suspension is placed in an upper chamber of a sterile plastic insert, allowing cells to migrate through a cell-permeable membrane towards a chemotactic or haptotactic agent placed below the membrane.

However, while this assay measures migration, it still does not accurately depict the migration of cells within an *in vivo* environment, where invasive and metastatic cells must pass through cross-linked fibrillar-based matrices including the BM and underlying stroma in order to disseminate. BMs are thin (20-300nm (Laurie et al., 1982)) sheets of continuous of ECM that separate epithelial tissues from adjacent stroma (Vracko, 1974). The BM is composed of large structural proteins, such as

laminin-5 (laminin-332), heparin sulphate and collagen type IV. These proteins form an organised scaffold to provide structural support to epithelial tissue but also offer functional input to modulate cellular and thus tissue function (Laurie et al., 1982; LeBleu et al., 2007; Timpl et al., 1979). BMs act as a physical barrier to the passage of cells and macromolecules unless it becomes more permeable, as occurs during tissue development, wound repair and at inflammatory sites (Liotta, 1984).

For many years it has been know that BM can be degraded by specific enzymes secreted from invasive cells such as cancer cells, thus allowing them to cross the BM towards lymphatic or vascular systems (Nicolson, 1982). As I will show later, it may be that many tumour cells can invade due to the invasive behaviour of host cells native to the stroma.

The Boyden Chamber Assay has been modified to assess the ability of cells to invade across a reconstituted BM. In these assays the upper membrane of the sterile insert is usually coated with a gel-matrix, such as Matrigel® derived from the secretions of Engelbreth-Holm-Swarm sarcoma (EHS) (Orkin et al., 1977).

Matrigel® is meant to represent the physical barrier of the BM and also the glycoprotein component. Whilst Matrigel® does include laminin within its composition, it is laminin-1 not laminin-5. Moreover, the Matrigel® does not form a cross-linked fibrillar matrix like a BM, but does have numerous growth factors and proteases embedded within it, unlike a BM (Kleinman and Martin, 2005). Despite the fact that it imperfectly replicates a natural BM, Matrigel® has been used to assess invasion through a physical matrix barrier (Moutasim et al., 2011; Nystrom et al., 2005; Tolboom and Huizinga, 2007). Thus cells must now destroy the gel in order to invade through towards the chemoattractant below within the lower chamber (Albini and Benelli, 2007).

Today commercially available plastic inserts, for multi-well plates contain a porous permeable membrane permitting cellular invasion. Transwell® inserts possess varying pore sizes (ranging 3.0-8.0µm) which can be blocked with gel in order to mimic the *in vivo* invasion process *in vitro*. Migration of invasive cells is determined by counting the cells that have navigated through the gel and the 10µm thick permeable membrane (as described (Marshall, 2011)). Additionally, Kenny and colleagues developed a 8.0µm pore sized Transwells® model to understand the adhesion and

invasion of ovarian cancer cells to the omentum, using primary human mesothelial cells and primary human omental fibroblasts (Kenny et al., 2007).

The assays described have many advantages, such as the ease of repetition and low cost, but a major disadvantage is that they do not take into consideration the complex process of invasion and the dynamic interactions with other host cells which occurs within the ECM. Therefore using a 3D *in vitro* organotypic method to inspect and quantify invasion considered a superior representation of the *in vivo* microenvironment.

1.4 3D cell culture techniques

It is recognised that flat and hard plastics or glass substrates commonly used for cell culture are not representative of the ECM environment found in multicellular organisms. In fact, tissue specific architecture, homeostasis, mechanical and biochemical cues and cell-cell communications are lost under such simplified conditions (Bissell et al., 2003; Cukierman et al., 2001; Cukierman et al., 2002; Nelson and Bissell, 2006). Cells cultured in a 3D organisation have been reported to exhibit biochemical and morphological features similar to their corresponding tissues *in vivo*, such as formation of actin-rich podosomes and invadopodia on migrating and invading cells (Artym et al., 2006; Gligorijevic et al., 2012).

3D culturing methods have been used widely and proved to not only aid the drug discovery process but also increase the understanding of mechanical, chemical and physical behaviours of cells *in vivo*. These complex systems are employed by tissue engineers, stem cell scientists, cell biologists and cancer researchers (Cairns et al., 2016; Fong et al., 2014; Wang et al., 2014). Establishing 3D culture systems requires the development of precise protocols, new cell lines, well suited 3D imaging platforms and sophisticated quantitative analysis techniques.

Approaches to 3D culture can be broadly categorised as scaffold-based and scaffold-free platforms; with innovative new materials and a greater understanding of the *in vivo* microenvironment, scientists can now incorporate these discoveries into designing novel experimental systems. 3D cultures are not just limited to cancer invasion studies, they have been reported in the development and engineering of cardiac tissue (Zimmermann et al., 2006) and used to establish an *in vitro* tool for monitoring the process of hippocampal neurogenesis (Usui et al., 2017). Overall, one of the most fundamental aspects of *in vitro* 3D models is the need to mimic the *in vivo* microenvironment as accurately as possible, thus allowing a prediction of cellular and tissue response to various stimuli.

There is no panacea or individual technology that fulfils the needs of all 3D cell culture requirements. All tissues are different and therefore users have an array of materials and fabrication techniques to develop the most appropriate model for their cell-based assays needs. Several types of 3D culture methods have been developed and can be grouped into different formats; (1) cells embedded within a natural or synthetically produced matrix; (2) cells cultured in sterile plastic inserts; and (3) cells cultured as

multicellular aggregates without the use of matrix based substrates. These different formats are summarised in **Table 1.2** and are further discussed.

Table 1.2: Summary of the different 3D cell culture systems

3D culture system	Advantages	Disadvantages	Matrix material needed	References
Spheroids	Easy and quick to produce Cost effective HTS compatible Easy to image Easy to track nanoparticles	Limited spheroid size Lack of matrix interaction Potential unrealistic particle uptake	Cells native ECM	(Kramer et al., 2013; Kunz-Schughart et al., 2004; Lee et al., 2016; Vinci et al., 2012; Zanoni et al., 2016)
Scaffold (Gels, sponges, fibres, inserts)	Customisable Physical, mechanical and biochemical environment achieved Ready to use Variety of size formats (6, 12, 24, 96-well)	Batch variation Additional processing steps Difficult to image/harvest Expensive materials Change in scaffold material (degradation)	Natural polymers* (Cultrex®, Matrigel®, Geltrex®) Synthetic polymers (PEG gels) Solid scaffolds/inserts (Transwells®/Alvetex®, AlgiMatrix™)	(Caicedo-Carvajal et al., 2011; Hofmann et al., 2008; Loessner et al., 2010; Tolboom and Huizinga, 2007; Zhang et al., 2005)
Organ-on-a-chip	Minimal variations Precise control of environment Real time analysis Very sophisticated model	Skill intensive Very expensive materials Difficult to reproduce exact conditions	Micro fluid chip	(Bhise et al., 2014; Huh et al., 2011; Hwang et al., 2008; Sung et al., 2009)

3D culture system	Advantages	Disadvantages	Matrix material needed	References
Organotypic cultures	Built from relevant cells to mimic the real tissue organisation Reproducibility	Skill intensive Expensive Require many growth factors Time consuming Low throughput	Natural* or synthetic+ polymers Scaffold inserts	(Froeling et al., 2009; Fusenig et al., 1983; Mackenzie, 2004; Mueller et al., 2014; Nystrom et al., 2005; Vorsmann et al., 2013; Worst et al., 1982)
Explant cultures	Native matrix Realistic cell-cell interactions Study histotypic relationship between various cell types within an organ/tissue	Limited supply of sample Short experiment time Large genetic variations Low throughput Difficult to image	None	(Brandenburger et al., 2012; Jain et al., 2009; Meng et al., 2007)

***Natural polymers: Collagen, fibrin, elastin, gelatin, fibronectin, vitronectin, hyaluronic acid (HA), alginate, glycosaminoglycan, chitosan, keratin**
+Synthetic polymers: polyglycolic acid (PGA), polylactic acid (PLA), polycaprolactone (PCL), polyethylene glycol (PEG), polyvinyl alcohol (PVA), polyhydroxyalkanoate(PHA), polypropylene fumarate (PPF), polyacrylic acid (PAA) synthetic peptides, synthetic DNA and the co-polymers of any of these. High-throughput screening (HTS) (Table modified from (Leong and Ng, 2014)).

1.4.1 Scaffold based 3D culture methods

Scaffold-based 3D cultures are generated by using either of two techniques; (1) seeding cells on to an acellular 3D matrix (e.g. Alvetex® polystyrene scaffold (Reinnervate Ltd, UK, acquired by ReproCELL, Japan) or AlgiMatrix™ alginate sponge (ThermoFisher Scientific)); (2) dispersion of cells in a liquid matrix material.

Commonly used scaffold matrix materials includes biologically derived constituents that provide a support for the growth of cells and mimic the ECM environment, such as Matrigel® from Corning. Matrigel® (product of EHS mouse sarcoma cells) provides additional ECM proteins (laminin type I, enactin and collagen type IV) and an abundance of growth factors, such as epidermal growth factor (EGF), fibroblast growth factor (FGF), insulin-like growth factor (IGF) and TGF-β (Corning, 2016).

Other commercially available matrices include; (1) Cultrex® (Trevigen, USA) a BM extract, also obtained from purified EHS tumours; (2) Geltrex® (ThermoFisher Scientific) a reduced growth factor EHS gel product; and (3) synthetically formed hydrogels (polyethylene glycol (PEG)) mixed with naturally occurring ECM components (e.g. collagen, heparin, hyaluronan). The BM mimetic matrices can be integrated with sterile plastic inserts with cell-permeable supports such as Transwells® (Corning) and ThinCerts™ (Greiner Bio-one).

Hydrogels and ECM mimetic matrices are comprised of networks of cross-linked polymer chains or complex protein molecules, that when combined in the optimum formula produce a complex nanoscale architecture resembling the native ECM tissue environment. Hydrogels serve as highly effective matrices for 3D cell culture due to their significant hydrophilic structure, which allows them to retain large amounts water, thus making them similar to natural tissue (Ahmed, 2015). Furthermore, hydrogels can be used as stand-alone 3D matrices or combined with other technologies, such as, a coating reagent for various solid scaffolds (Alvetex® or AlgiMatrix™) (Andersen et al., 2015), encapsulating cells plated on to permeable supports (Transwell® or ThinCert™) (Torisawa et al., 2011), or within microfluidic devices (Sung et al., 2009).

The ECM components of Matrigel® have been reported to activate numerous signalling pathways in cancer cells controlling motility (Carpenter et al., 2009) and angiogenesis (Languino et al., 1989; Zhou et al., 2004). However such natural hydrogels do present the disadvantage of batch-to-batch variation in composition due to their isolation from animal-derived sources.

To circumvent some of the issues related to animal-derived biomaterials, matrices have been developed that are animal-free. One such example is the use of hyaluronic acid (HA) as a biologically derived matrix (David et al., 2008; Pan et al., 2015), which can be modified by the addition of ECM components, such as collagen (Suh and Lee, 2002) for improving cell proliferation and attachment (Lam et al., 2014a).

Hydrogels comprised entirely of synthetic polymers and non-natural molecules are PEG hydrogels and have been used to form bioerodible hydrogel film coatings at wound sites in animals (Sawhney et al., 1994). PEG gels provide structural support for a variety of cell types however they are biologically inert. Moreover they have been shown to maintain viability of encapsulated cells whilst allowing for ECM deposition as the hydrogel degrades (Bryant and Anseth, 2002).

1.4.2 Scaffold-free 3D culture methods

Scaffold free cultures have existed since the 1970's, when Robert Sutherland successfully cultured spheroids using spinner flasks (Sutherland et al., 1970) and shortly after cultured multicellular spheroids using Chinese hamster v79 lung cells resembling the nodules observed in several animal and human carcinomas (Sutherland and Durand, 1984; Sutherland et al., 1971). Scaffold-free models primarily consist of multicellular aggregates, often referred to as spheroids.

Cellular spheroids are relatively simple to culture and an easy way to make 3D models that can be generated from different of cell types, such as the formation of single celled cancer spheroids using non-small cell lung carcinoma (NSCLC) A549 (Zanoni et al., 2016) or Colo-699 lung cancer cells (Amann et al., 2014), and furthermore formation of neuro-spheroids using pluripotent stem cells for Alzheimer's disease (Lee et al., 2016).

Tumour spheroids have become a very commonly used and versatile scaffold-free method, due to their availability and ability to mimic the heterogeneous population of cells with areas of proliferation and quiescent centre's (Ware et al., 2016) (Mehta et al., 2012).

Multicellular spheroids can be generated using a variety of techniques; (1) forced-aggregation suspension technique obtains a homogenous population of uniform sized spheroids (Yamada and Cukierman, 2007) (Baraniak and McDevitt, 2012); (2) the hanging droplet technique, whereby cells are cultured in an aliquot of suspended media and incubated under the correct physiological conditions until 3D spheroids are formed (Ware et al., 2016) (Foty, 2011); (3) agitation-based approaches include gyratory rotation techniques and stirred suspension culture systems to regulate spheroid formation through cell-cell collisions. (Breslin and O'Driscoll, 2013; Serra et al., 2012).

Multicellular spheroids can be custom made, using a range of cell lines and varying in final spheroid size (150-500µm in diameter). Spheroids, much like tumours, usually contain a heterogeneous population of cells that are proliferative at the periphery and less or non-proliferative within core. A situation that resembles tumour edges adjacent to capillaries *in vivo*. Also similar to some tumours, the inner-most cells gradually become quiescent and eventually die by apoptosis or necrosis, thus forming a necrotic core (Ryan et al., 2016). These changes occur in both spheroids and tumours, due in part to the limited inward and outward diffusion of nutrients and oxygen, resulting in hypoxia, accumulation of waste products and changes in pH (Acker et al., 1987; Carlsson and Acker, 1988; Vinci et al., 2012).

1.4.3 Limitations of 3D cell culture models

Several categories of 3D culture methods have been developed and are summarised in **Table 1.3**. Cells cultured within a 3D mimetic architecture have been shown to exhibit similar biochemical and morphological features corresponding to tissues *in vivo*. For example, the ability of breast cancer cells to form invadopodia (membrane protrusions specialised in degrading ECM) via upregulation of EGF (Yamaguchi et al., 2005) and the formation of functional acini as observed *in vivo* when mammary

epithelial cells were cultured on 3D collagen type I: laminin-1 gels (Gudjonsson et al., 2002).

Development of new materials and technologies has been driven by scientists to incorporate experimental systems that better represent the *in vivo* physiological microenvironment into their research. Establishing 3D cultures as a mainstream approach holds great promise for drug discovery, however requires the development of precise protocols, new cell lines, well suited 3D imaging platforms and sophisticated quantitative analysis techniques.

3D cultures possess specific limitations and disadvantages, for instance, most of the existing models only represent the biochemical characteristics of *in vivo* tissue during static conditions (Mathes et al., 2010). Additionally, using scaffold-based systems introduces reproducibility issues due to batch variation from commercially purchased matrices. Importantly use of animal-derived products potentially increases the risk of transmitting infections or disease (Raghunath et al., 2007).

Furthermore, 3D spheroid cultures may bring additional drawbacks with increased drug resistance possibly due to geno- and phenotypical changes induced by spheroids (Karlsson et al., 2012). Moreover, not all systems are imaging-friendly due to their opacity or contain auto-fluorescent component, thus generating high background fluorescence.

Another major limitation is cost; the simple fact that 3D culture systems are expensive is one of the main reasons why it has not yet been fully integrated and utilised within industry and drug discovery platforms. Maturity of sophisticated technology platforms, expensive consumables (plates, reagents etc.) and data storage facilities all add to the cost element. Apart from these reasons 3D cell culture models can be very complex, technically challenging and may require specialised consumables, equipment or detection techniques. These limitation are however, being overcome with improved 3D assays and emerging technology platforms.

Numerous 3D models within academia have been developed to focus on specific applications. Examples include, development of 3D prostaspheres to model growth, invasion and drug response using 29 different prostate cancer cell lines (Harma et al., 2010). Additionally, Loessner and colleagues reported that ovarian cancer cells (OV-MZ-6 and SKOV-3) formed and sustained 3D spheroids when cultured on PEG-

based hydrogels and showed mRNA expression of the cell surface receptors α3/α5/β1 integrins and the protease matrix metalloproteinase-9 (MMP-9) were increased in cells within the 3D spheroids compared to 2D monolayer cultures (Loessner et al., 2010). Furthermore, the development of a human lung 'small airway-on-a-chip' was reported to identify new therapeutics for chronic respiratory diseases (Benam et al., 2016).

By contrast the pharmaceutical industry are in search of a standardised 3D cell culture model which fits their stringent assay requirements. Such assays are required to be; (1) cost efficient; (2) reliable; (3) reproducible; (4) built into a standardised automated work flow; and (5) informatics integrated. Therefore the pharmaceutical industry aim to identify potential therapeutic targets by combining biological relevance with automated, versatile, scalable and quantitative high-throughput screening (HTS).

Table 1.3: 3D cell culture systems

	3D culture method	Scaffold material	Advantages	Disadvantages	Cost	HTS compatible	Vendor/s
Scaffold free	Spheroids Cells grown in suspension 150-500µm diameter	Cells native ECM	Easy to produce. No additional materials needed.	Limited spheroid size. High cost Lack of matrix interactions. Potentially unrealistic.	££	Yes	InSphero AG FluoFarma
	Spheroids Hanging droplets	-	No scaffold needed. Low attachment plates.	Cell proliferation is low, due to poor signalling from cell adhesion molecules. Uncontrolled spheroid size.	££	Yes	Organogenix (Previously known as SciVax Life Sciences)
	Nano culture Spheroids Artificial fibre/sponge	Cells native ECM Agarose	Mimics structural tissue. Tailor made plates for customer. Uniform spheroid size.	Scaffold materials has stability/reproducibility problems. Cumbersome pre-coating procedure. Mesh inhibits imaging	£££	No	Organogenix

	3D culture method	Scaffold material	Advantages	Disadvantages	Cost	HTS compatible	Vendor/s
Scaffold based	Alvetex® Porous polystyrene scaffold 200µm thick	Polystyrene Scaffold can be coated with ECM proteins	Inert. Non degradable. Cell-cell interaction. Cells are retrievable.	Requires 10^7 cells/insert. Not able to study invasive patterns. HTS not possible. Expensive	£	No	ReproCell/ Reinnervate
	Transwell® Inserts 0.4-8.0µm pore sizes	Polycarbonate PET (polyethylene terephthalate)	Inert. Can be coated with ECM proteins. Live imaging. Variety of applications.	Expensive. Frequent media renewal. Difficult to retrieve cells. Stringent set up process.	££	Yes	Corning
	Natural hydrogels	Matrigel® Cultrex® Geltrex®	Physiologically relevant. pH and temperature sensitive. Can be injected.	Batch variation. Animal-derived. Degradable.	£	-	Corning
	Synthetic hydrogels	PEG gels	Animal-free. No batch variation. Adjustable mechanical properties.	Difficult to sterilise. Contains toxic substances. Bio-inert.	£	-	Sigma Aldrich

1.5 Organotypic culture models

The term ‘organotypic’ describes tissue, removed from an *in vivo* host organ, placed and cultured *in vitro* in the hope that it continues to function physiologically and develop as it would within the original organ. The removed tissue is immediately placed into an *in vitro* substrate, supplemented with the necessary growth medium and maintained under physiological conditions.

During the last 47 years organotypic cultures have immensely advanced and been widely reported for their use within the dermatology, neuroscience and oncology research fields. The first detailed description of an *in vitro* brain tissue culture was published using an organotypic cerebellum model in the early 1970’s (Hauw et al., 1972; Wolf, 1970). Followed by the breakthrough made by Gähwiler, who cultured organotypic rat brain slices using the roller tube technique to model functional synaptic connections, neuronal differentiation and the effects of slowly acting neurotoxins on synaptic transmission (Gahwiler, 1981a, b, 1988).

1.5.1 Organotypic skin cultures

Organotypic skin culture (OSC) models have been utilised for the *in vitro* growth of complex biological tissues to replicate normal and diseased function and physiology (Bernerd and Asselineau, 2008; Carlson et al., 2008; Coleman et al., 2014b; Froeling et al., 2010; Igarashi et al., 2003; Mackenzie, 2004; Mackenzie and Fusenig, 1983; Mueller et al., 2014; Nystrom et al., 2005; Schneider et al., 2008; Vorsmann et al., 2013). Commonly used models are probably those of skin, consisting of keratinocytes grown on top of a collagen rich matrix populated with embedded dermal fibroblasts that are then fed from below using specialised growth medium (creating an important air-liquid interface) and exposed to humidified air. This tissue-air model has the ability to reproduce the 3D stratified organisation of normal skin *in vivo*.

Before the practice of using animal derived collagen lattices, split-thickness human allografts, derived from cadaveric donors, were commonly used to temporarily cover and treat wounds from thermal burns (Macmillan, 1962).

During the early 1970's German oncologist, Norbert Fusenig, started what lead to a series of influential discoveries that have moulded the way OSCs are executed in the laboratory today. In 1971, Fusenig successfully isolated epidermal cells from mouse skin and continued to culture them on collagen lattices (Fusenig, 1971). A few years later, he and his group grafted intact cultures of epidermal cells, grown on collagen gels, back onto the mouse recipient, thus investigating the function of epidermal skin grafts (Worst et al., 1974).

This led to further investigations; from using dermal equivalents (native collagen type 1 extracted from rat tail tendons) for organotypic co-cultures, whereby mammalian cells were isolated, and cultured *in vitro* and either re-implanted or used to study geno- and phenotypic characteristics from human skin carcinomas (Boukamp et al., 1982; Fusenig et al., 1983). To the development of epidermis dissociated cells originally from neonate mouse skin (Mackenzie and Fusenig, 1983; Worst et al., 1982) and furthermore, to the cultivation of skin grafts, grown on collagen lattices, embedded with fibroblasts exhibiting vascularisation and wound healing characteristics (Bell et al., 1981).

Similarly In 1979 a group at the Massachusetts Institute of Technology (MIT) used OSC's to study skin cell function and would healing. They observed that fibroblast cells were capable of interacting with collagen fibrils to produce a denser arrangement, thus having a direct impact on the rate and extent of lattice contraction (Bell et al., 1979).

These breakthroughs have since increased the usage of this particular style of 3D model to; (1) successfully culture acceptable artificial skin in the treatment of extensive burn injuries (Burke et al., 1981; Tompkins and Burke, 1990); (2) perform mechanistic studies of skin physiology for pharmacotoxicologic keratinocytes studies (Stark et al., 1999); (3) improve experimental designs to assess cutaneous skin photo-reaction, photo-damage and photo-protection for use within the cosmetic industry (Bernerd and Asselineau, 2008; Dreher et al., 2002); and (4) construct large organotypic cultures of oral mucosa and skin as potential tissue grafts to repair oral wounds (Igarashi et al., 2003).

1.5.2 Organotypic culture models in cancer

An organotypic cancer model must have the capability to emulate, as closely as possible, the physiological tumour-stromal microenvironment as seen *in vivo*. Engineered organotypic models are expected to recapitulate the natural features of tumour progression, which include cell invasion through basement membranes, oncogenic signalling and mimicking of the spatial organisation as well as the elaborate architecture of the ECM.

Achieving all of these parameters for all of the various types and stages of cancer is a near impossible task. Consequently, many groups have designed unique tailor-made organotypic cancer models addressing a specific investigative question. For example, to investigate the behaviour of melanocytes and of human melanoma cells, Eves and colleagues, used reconstructed de-epidermised human dermis (DED) composite in order to determine if pigmentary and invasiveness are influenced by interaction with co-cultured keratinocytes and fibroblasts (Eves et al., 2000). Additionally, Caswell and colleagues used a scaffold-based model (8.0μm pore size Transwell® inserts) to report the interaction between the cytodomain of the β1 integrin and Rab25 (a GTPase linked to tumour aggressiveness and metastasis) that strongly promotes an invasive mode of cell migration through a 3D fibronectin-containing ECM (Caswell et al., 2007).

1.5.3 Large organotypic gel cultures

In 1979 Bell and colleagues showed that skin fibroblasts seeded into collagen lattices severely contracted and also noted that contraction was cell and protein concentration dependent (Bell et al., 1979). In addition, suspensions of epidermal cells that were applied to the contracted lattices rapidly covered the entire surface and produced a differentiated phenotype (Bell, 1979). Demonstrating that collagen and isolated fibroblasts support an *in vitro* skin-like model. Our laboratory regularly and continuously uses the organotypic skin culture model developed by Fusenig and colleagues (Fusenig et al., 1983). In their study, Nystrom and colleagues, developed a method to quantify squamous cell carcinoma (SCC) invasion using an organotypic gel culture model (Nystrom et al., 2005). Human fibroblasts were embedded within a collagen gel and aliquoted into a 24-well plate (1ml per well) before being placed in

an incubator for 18 hours to polymerise. The next day keratinocytes were added on top of the polymerised fibroblast-containing gel. The following day, gels were removed from the 24-well plate and placed on to the individually collagen coated nylon squares which were rested on steel grids, housed in a 6-well plate. Sufficient media were added to reach the under surface of the gel allowing the cells to grow at an air-liquid interface. The gels were then fixed in formalin at specific time points and processed to paraffin for histological staining (**Figure 1.2**). Furthermore, Nystrom and colleagues grew organotypic gels *in* vitro for seven days before grafting the gel under the skin of nude mice. An invasion index was calculated from cytokeratin stained sections based on a the product of average depth of invasion, number cell colonies invaded and the total area of cells invaded below the overlying 'epithelium' providing a quantitative tumour invasion value (described in detail (Nystrom et al., 2005)).

Fusenig's model has since been widely used as 3D physiomimetic model to assess skin keratinocyte and fibroblast form and function (Parenteau et al., 1992), as well as being used to study the variation within growth rates and patterns of different OSCC cell lines, thus providing an *in vitro* model to assess tumour cell behaviour (Mackenzie, 2004).

In addition, Marsh and colleagues used the organotypic skin culture method to identify that the integrin αvβ6 is expressed at significantly higher levels in aggressive morphoeic basal cell carcinomas (Marsh et al., 2008). Similarly, adaptions of this model have been utilised within our department to study the role and mechanisms of cell-cell interactions (E-cadherin, β-catenin and Ezrin) in modulation of pancreatic cancer progression. In this adaption of the model, Froeling and colleagues, firstly isolated normal and cancer-associated pancreatic stellate cells (PSCs) and co-cultured with pancreatic cancer cells (capan-1 and PaCa-3) (Froeling et al., 2010; Froeling et al., 2009).

Additionally, retinoic acid treated organotypic gels were reported to induce quiescence and reduce motility of PSCs, thus resulting in reduced levels of pancreatic cancer cell proliferation (Froeling et al., 2011). Furthermore, the use of organotypic gels revealed that the nuclear translocation of fibroblast growth factor receptors within pancreatic stellate cells mediates invasion of cancer cells (Coleman et al., 2014a). Moreover, Kadaba et al, demonstrated that tumour-stroma interactions within the

pancreas altered cell cycle, motility, proliferation and signalling in addition to changing the stiffness of the surrounding ECM in 3D organotypic gels (Kadaba et al., 2013).

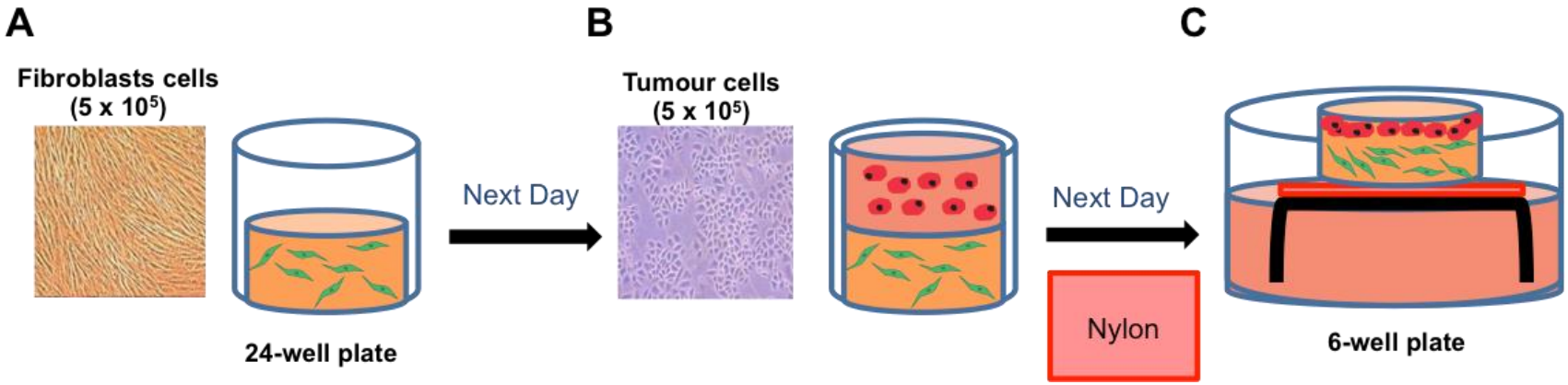

Figure 1.2: Development of organotypic gels

A) Gels composed of collagen type I (5.25 volumes) and Matrigel® (1.75 volumes), DMEM 10x, (1 volume), standard DMEM (1 volume) and of FBS (1 volume). 5 x 10^5 fibroblasts cells (green) are embedded within the gel. 1ml of gel solution aliquoted into a 24-well plate and incubated at 37°C for 18h (Day 0). **B)** The next day 5 x 10^5 tumour cells (red) are placed on top of the gel and placed in the incubator (start of day 1). Meanwhile the same day, a fibroblast-free collagen gel is made to coat sterile nylon sheets. **C)** The following day, the gels are lifted out of the 24-well plate using a sterile spatula and placed on top of a collagen coated nylon square and elevated on a metal grid (2.5cm^2 squares of stainless steel mesh with edges bent down to form 4-5mm legs). The steel grids are placed in a 6-well dish and a sufficient volume of serum-containing medium is placed underneath the grid. The medium coats the under surface of the nylon square creating an air-liquid interface.

1.5.4 Limitations of large organotypic gel cultures

As previously discussed, the practice of organotypic gel culture methods within cancer research provides a reliable and reproducible model, which has been used to quantify the growth and invasiveness of numerous cancer cell lines using standard pathology. It is highly adaptable and enables the user to incorporate different cell lines or matrices enabling a broad range of questions to be answered and allows for implantation *in vivo*. Thus creating a unique and customisable 3D modelling technique. However there are several drawbacks of this particular 3D *in vitro* model; (1) large numbers of cells are required for each experiment (5×10^5) fibroblast and tumour cells for one gel); (2) large volumes culture media and expensive reagents (collagen and Matrigel®) are required to sustain and construct the gels; (3) the assay lasts 2-3 weeks followed by several days of histological processing before samples are available for analysis; (4) due to the low-throughput assay format drug or gene screening cannot be supported without incurring heavy expenditure; and (5) the final data are generated from tissue sections of the organotypic gels, thus only producing 2D data after going to great lengths to create an elaborate 3D microenvironment. For these reasons it is necessary to create a cheaper and faster model.

1.5.5 Miniaturising organotypic gel cultures

With consideration to the limitations witnessed in the large organotypic gel cultures, our laboratory has miniaturised and optimised this assay to recapitulate the tumour-stroma interface as observed in the conventional model. With the use of sterile plastic Transwell® inserts, similarly used for inverse cell invasion studies (Caswell et al., 2008; Caswell et al., 2007), our laboratory employ inserts of 0.4µm pore size to guarantee cells do not traverse the permeable membrane. By coating the membrane with a collagen: Matrigel® rich gel, we have generated a physiologically biomimetic system that attempts to recapitulate the *in vivo* tumour-stroma microenvironment. The Transwell® inserts, possess a 6.5mm diameter polycarbonate translucent membrane with an approximate growth area of $0.33cm^2$. Each Transwell® rests inside a 24-well plate and is approximately elevated 5mm above the bottom of the well, thus creating the air-liquid interface (**Figure 1.3**). A detailed description of the protocol is described in **Section 2.3.1**.

The 3D mini-organotypic invasion assay has several major advantages over the conventional large organotypic model, namely; (1) requiring only 1/10th of the volume of gel (100µl per well); (2) the gel is plated directly into the Transwell® insert and remains inside for the duration of the assay; (3) each gel requires only a total of 10^5 cells, in a 2:1 ratio of fibroblast to tumour cells (ratio was determined by a previous PhD student, data not shown); (4) increased speed and ease of experimental configuration; (5) requires less media and reagents, therefore reducing costs; and (6) miniaturisation enables flexibility and diversity in experimental design, permitting drug and gene screening of small molecules.

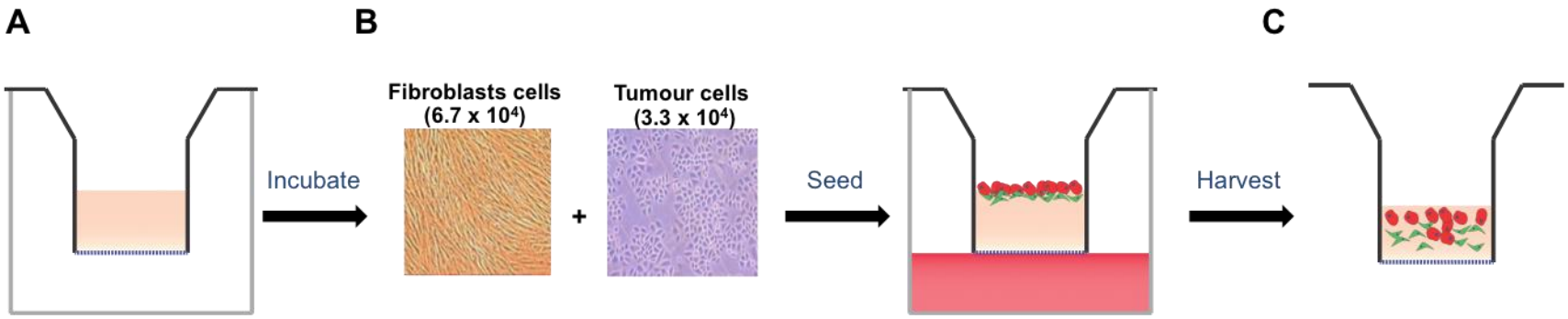

Figure 1.3: Development of mini-organotypic gels

A) 100µl of collagen: Matrigel® mix plated into a 6.5mm diameter, 0.4µm pore size Transwell® permeable support housed in a 24-well plate. Gel is incubated at 37°C for 45-60 minutes until set. **B)** 200µl suspension containing a known number of fibroblasts and tumour cells in a 2:1 ratio respectively is placed on top of the gel. 600µl of serum-containing media is added in the outer well. **C)** After 10-14 days gels are then fixed in formalin overnight and processed to paraffin. Histological sections can be cut and stained for quantitative 2D analysis.

1.5.6 Limitations of 3D mini-organotypics

Whilst no model has been yet developed to perfectly recapitulate the tumour microenvironment. This novel 3D mini-organotypic invasion assay allows us, at least in part, to mimic the stromal microenvironment, thus permitting the early stages of metastasis and cancer progression to be monitored. This intricate yet robust model allows the user to customise the organotypic gel composition to produce the desired tissue microenvironment. Additionally any cell type can be embedded within or on top of the gel and observations regarding, invasion and cell morphology can be measured on the histological stained sections of the fixed gels. Furthermore, with the use of Transwell® permeable supports, users now benefit from 10 mini-organotypic gels for the same volume required to make one large organotypic gel.

However, the limitations of the miniaturised model is the cost of the inserts (£170/case) and the lengthy fixation and histological processing required at the end of the assay. Additionally, staining, imaging and analysis, is slow, similar to the large organotypic gel system. Therefore performing functional screening or validation tests would require pro-longed periods of time before any analysis and conclusions can be examined. Furthermore, the same Transwell® cannot be monitored repeatedly over a set period of time and the user has to rely on technical repeats follow a process over time.

Therefore, it would seem imperative to design and develop a 3D mini-organotypic invasion assay that could permit functional screening as well as providing a means for faster delivery of results.

1.6 Tumour-stromal microenvironment

The composition of the tumour-stromal microenvironment is a complex mixture of connective tissue and extracellular space, filled with cellular (immune, endothelial, fibroblast, dendritic, macrophage, T and B cells) and non-cellular (ECM) components which facilitate homeostasis of normal tissue (Li et al., 2007a). The supporting role of the microenvironment towards metastasis was originally asserted by Paget's 'seed and soil' hypothesis (Paget, 1989). Paget's theory has led to the premise that survival of cancer cells within the tumour-stroma microenvironment depends, not only on their ability to adhere and attach, but also to infiltrate, receive sustenance and thrive within the ECM.

1.6.1 The Extracellular Matrix (ECM)

Once thought of as an inert scaffold, the ECM, is a multi-component, proteinaceous network, containing reservoirs of growth factors and intricate structural architectures, which is essential for supporting tissue organisation and cellular survival (Hynes, 2009).

The non-cellular component of connective tissue is formed of two main classes of macromolecules; (1) large linear polysaccharide chains, named glycosaminoglycans (GAGs) (e.g. HA, chondroitin sulphate (CS), dermatan sulphate (DS), heparan sulphate (HS) and keratin sulphate (KS)) which are covalently attached to a protein in the form of proteoglycans (PGs) (e.g. aggrecan, brevican, decorin, keratocan, lumican, neurocan, perlecan, syndecans and versican); and (2) fibrillar proteins (e.g., collagen, elastin, fibronectin and laminins) (Alberts et al., 2002). GAGs provide mechanical support to the ECM and maintain gel integrity by drawing in copious amounts of water due to their negative charge and hydrophilic properties. Whereas, the fibrous proteins (produced and secreted mostly but not exclusively by fibroblast cells) provide structural support to the 3D architecture of the connective tissue.

The ECM provides multi-functional biochemical and biomechanical cues that can; (1) function as an adhesive substrate to track and direct migrating cells; (2) provide a scaffold upon which tissues are organised yet also provides integrity and elasticity to developing organs; and (3) facilitate crosstalk between growth factors and their

cellular receptors in order to control spatial distribution of ECM molecules (Frantz et al., 2010; Pickup et al., 2014).

A non-component, but an important mediator receptor protein between the ECM and the cells are the adhesion molecules called integrins. Integrins are a fundamental family of heterodimeric cell membrane adhesion receptors that mediate cell-to-cell or cell-to-matrix interactions and facilitate cell adhesion, invasion, migration and survival (Barczyk et al., 2010; Hynes, 1992). Since their original discovery in 1987 (Hynes, 1987) integrin recognition has become widely expressed and to date there 24 different functional integrins formed in humans (Hynes, 2002) composed of 18α and 8β paired subunits. Each heterodimer has a different pattern of ligand specificity, for example, αvβ3 binds to fibronectin, vitronectin and more weakly to collagen and laminin, whereas α5β1 selectively binds predominantly to fibronectin (van der Flier and Sonnenberg, 2001). Integrin α6β4 is a laminin binding integrin that is an essential component of hemi-desmosomes anchoring keratinocytes to the BM (Geuijen and Sonnenberg, 2002; Wilhelmsen et al., 2006).

Additionally, integrins are able to transduce signals bi-directionally sending intracellular signals following ligand binding (known as outside-in signalling) or when talins or kindlins bind to cytoplasmic β tails resulting in integrin activation (known as inside-out signalling) (Bledzka et al., 2012; Harburger et al., 2009). Integrins in cancer have been reported to facilitate various functions, examples include, αvβ3 and αvβ5 Integrins were reported to inhibit tumour angiogenesis in animal models (Kumar et al., 2001) and have been reported to play key roles in vascular development (Hynes et al., 1999). Additionally, loss of α6 and/or β4 in basal cells coincides with loss of BM proteins in oral carcinomas (Downer et al., 1993). Furthermore, in 2001 our laboratory retrovirally infected a population of αv-negative oral SCC (H357) with β6 cDNA, creating the high αvβ6 expressing cell line (VB6) (Thomas et al., 2001a). Thomas and colleagues reported that expression of αvβ6 promoted invasion of the SCC cells through up-regulation of MMP-9 (Thomas et al., 2001c). More recently Moore and colleagues reported that simultaneous targeting of αvβ6 in combination with trastuzumab may potentially be effective against human epidermal growth factor receptor 2 (HER2) positive breast cancer (Moore et al., 2014).

1.6.1.1 Components of the ECM

Collagen is the most abundant fibrous protein in the body and is an essential structural element of all connective tissue. The majority of interstitial collagen is secreted by fibroblast cells that reside within the ECM or are recruited by neighbouring tissues. Collagen fibres are intricately interwoven with carbohydrate molecules called proteoglycans, producing resistant, strong fibril bundles within the tissue stroma that provide tensile strength, regulate cell adhesion, support migration and tissue development (Gelse et al., 2003; Ricard-Blum, 2011). To date 28 types of the collagen superfamily have been identified in vertebrates (Gordon and Hahn, 2010), of which, fibrillar collagens (type I, II and V) are most abundant in humans (approximately 90% of all collagens). Forming densely packed long (200-300nm) thin (15-50nm) fibrils and are prevalent in bone, cartilage, connective tissue, ligaments, skin and tendons (Gelse et al., 2003; Miller, 1985). Despite the large structural diversity amongst the different collagen types, all members of collagen have a common triple helix composed of three distinct α-polypeptide chains. Each chain containing an amino acid sequence of poly-L-proline (aka polyproline type II helix) (Shoulders and Raines, 2009) which itself contains a glycine residue in every third position of the chain resulting in multiple triplet sequences of a $(Gly\text{-}X\text{-}Y)_n$ repeat, where X and Y are often proline and 4-hyrdoxyproline respectively (Adzhubei et al., 2013).

Some collagens have restricted expression and functions, for example, type IV collagen, with its more flexible triple helix, can assemble into an intricate meshwork and expression is restricted to the basement membrane forming a sheet-like structure (Laurie et al., 1982). Similarly to type II, type IX collagen was reported in the formation articular cartilage in adults and type V associated with corneal formation (Ricard-Blum, 2011). It is common in many cancers including breast, pancreatic and skin to observe high levels of collagen type I deposition *in vivo*, thus forming a fibrotic (aka desmoplastic) stroma (Barsky et al., 1982; Ibbetson et al., 2013; Imamura et al., 1995). Breast cancers are often first detected as a collagen-dense shadow on X-rays and their growth and metastasis is shown to correlate with progression in collagen density (Levental et al., 2009; Provenzano et al., 2008). Thus collagens are major controllers of cellular behaviour.

Elastin, an associate of collagen and another major ECM protein, serves an important role, by providing elasticity to tissues that undergo repeated bending, stretching and recoil (Frantz et al., 2010). Elastin stretch capability is highly important and has been reported to be limited by its associations with collagen fibres (Wise and Weiss, 2009). Elastin provides crucial resilience to many tissues including, arteries, lung, tendons and skin. These resilient fibres are comprised of two components, the elastin protein and microfibrils (such as fibrillin). Elastin is rapidly assembled during cross-linking and polymerisation of its soluble precursor, tropoelastin, thus forming elastic fibres (Mecham, 2008; Wagenseil and Mecham, 2007).

Fibronectin mediates not only organisation of the ECM but also cellular adhesion, growth and migration (Pankov and Yamada, 2002). Fibronectin, is a large glycoprotein found in all vertebrates that binds to cell surface receptors (such as integrins) during ECM development. HT1080 cells were reported to attach through the integrin α5β1 when plated on a fibronectin-coated substrate (Friedland et al., 2009). Fibronectin contains multiple splice variants, which are classified into type I (12 domains), type II (two domains) and type III (15-17 domains) (Pankov and Yamada, 2002). Additionally, fibronectins importance has also been linked to cell migration during development and has been implicated in cardiovascular diseases (Astrof et al., 2007).

Laminin, a large multi-domain glycoprotein was discovered in 1979 as a product of EHS cells (Timpl et al., 1979). Together with collagen type IV, nidogen and perlecan, laminins are a major component of the ECM. Laminins are extracellular proteins of which, 16 known isoforms are produced from combinations of α, β and γ chains (as reviewed by (Aumailley et al., 2005; Tzu and Marinkovich, 2008)). Laminins have been reported to have a range of important roles, examples include; (1) laminin-5 (or -α3β3γ2) play a significant role in BM assembly and providing structural support to the ECM (Nishiyama et al., 2000); (2) laminin-211 (previously known as laminin-2 or laminin-α2β2γ1) was found predominantly in skeletal muscle tissues and serves as an anchor between glycoprotein complexes that lie at the surface of muscle cells and the surrounding ECM (Helbling-Leclerc et al., 1995); and (3) implications in the role of cell migration and motility. Zhang and Kramer demonstrated that for maximal cell motility, human foreskin keratinocytes secrete laminin-332 (laminin-5 or -α3β3γ2) when plated on to collagen type I or fibronectin coated substrate (Zhang and Kramer, 1996). Thus, it is not surprising that laminins have also been implicated with the

tumour invasion process. For example, high levels of laminin-γ2 chains were expressed at the leading invasive edges of human cervical (Noel et al., 2005), colon (Pyke et al., 1995) and lung cancers (Maatta et al., 1999).

Tenascins, another large ECM glycoprotein family member, are comprised of tenascin-C, -R, -W and –X all of which contribute to structure and physiology of connective tissue. Three of the four (-C, -X and –R) have been characterised in mammals (Chiquet-Ehrismann, 1995; Erickson, 1993). The first and best described member of the tenascin family (tenascin-C) was discovered in 1983 (Bourdon et al., 1983) and is hexameric protein highly expressed in connective tissues which surround inflamed tissues, tumours or wounds, where it may regulate cell growth and migration via intracellular signalling (Chiquet-Ehrismann and Tucker, 2004; Orend and Chiquet-Ehrismann, 2006). Tenascin-C has been reported to be involved in tumour invasion (De Wever et al., 2004), migration (Herold-Mende et al., 2002) and stimulate tumour angiogenesis (Ishiwata et al., 2005; Tanaka et al., 2004). Whereas, Tenascin-R is expressed and plays an important role within the central nervous system (as reviewed by (Anlar and Gunel-Ozcan, 2012)). Tenascin-X, the largest of the tenascin family members, is the only member to exert crucial architectural functions and is located in loose connective tissue during both development and adulthood (Valcourt et al., 2015). Tenascin-W, the last member of the tenascin family to be discovered was first described in zebrafish (Weber et al., 1998) and similar to –C, is highly expressed within connective tissue (Martina et al., 2010) but also been linked as an efficient biomarker for human breast (Degen et al., 2007) and colorectal cancer (Degen et al., 2008).

The ECM components discussed above are all involved with the matrix scaffold, either as a structural constituent (collagen, elastin) or as a molecular adhesive between the matrix and cells (integrins). PGs however, are also essential to the ECM of connective tissues, their major biological function is derived from the GAG component of the molecule, which is to provide hydration and swelling pressure to fill extracellular tissue and enable it to withstand compressional forces (Yanagishita, 1993). PGs (such as aggrecan, brevican, decorin, keratocan, lumican, neurocan, perlecan, syndecans and versican) are glycosylated proteins which have highly anionically charged GAGs attached to them. GAGs are large (4-8000 kDa), linear sulphated (except HA which is non-sulphated), polysaccharide chains, with an alternating repeating disaccharide unit, comprised of an acetylated amino sugar

group with uronic acid (CS, DS, HS and KS) (Gandhi and Mancera, 2008; Perrimon and Bernfield, 2001). The simplest non-sulphated GAG, HA, abundant in the ECM and cell surfaces has been implicated during important functional roles, including embryonic development (Camenisch et al., 2002), wound healing (West et al., 1997) and deposition of HA in tumour tissue was associated with malignant progression of colorectal cancers (Ropponen et al., 1998). The resulting PG/GAG complexes form a variety of combinations, the most common being perlecan and aggrecan. Perlecan or heparan sulphate proteoglycan (HSPG), which has been linked to angiogenesis and blood coagulation (Sarrazin et al., 2011). Aggrecan or chondroitin sulphate proteoglycan (CSPG) is essential for providing hydration to articular cartilage via its link to HA and resistant, smooth surfaces via its link to collagen type II (Kiani et al., 2002).

1.6.2 Changes in the ECM during cancer

The ECM, under normal physiological conditions provides a multi-functional service to maintain and organise the cellular dynamics, intercellular signalling and structural integrity of the connective tissue (Alberts et al., 2002). However, the ECM can and does change, gradually becoming disorganised and deregulated over time as a result of miscues. Dysregulation of matrix composition and structure can contribute to pathological conditions such as organ fibrosis and cancer (Lu et al., 2011) and pathological destruction of cartilage ECM in osteoarthritis (Dean et al., 1989). A main contributor of altered ECM are stromal cells; during normal wound healing, resting fibroblasts differentiate and secrete structural proteins (collagens) to form granulation tissues mediated through TGF-β stimulation (McAnulty, 2007). However, during altered conditions, copious amounts of TGF-β are released from platelets leading to increased trans-differentiation of normal fibroblasts to contractile myofibroblasts which in turn can lead to excess collagen deposition resulting in fibrosis and increased cancer risk (Bissell and Hines, 2011). In addition, ECM remodelling may promote intravastation of cancerous cells residing within the tumour-stroma microenvironment (Condeelis and Segall, 2003).

The structural architecture of the tumour-associated ECM is fundamentally different to that of normal ECM. For example, tumour cells may undergo morphological changes via regulation of Rho GTPases and RhoA and RhoC have been observed in

human cancers associated with invasiveness (Croft et al., 2004). Therefore initiating the Rho-associated kinase (ROCK) pathway to mediate actin-myosin contractility of collagen fibres was reported change the orientation of tumour cells and facilitate invasion (Han et al., 2016; Provenzano et al., 2006). Furthermore changes in ECM stiffness, induced by increased collagen cross-linking and disposition can contribute to cancer progression and stiffer matrix of cancerous tissue when compared to normal tissue (Paszek et al., 2005).

It appears that successful metastasis requires a local niche to support tumour cell growth but also an environment whereby cancerous cells can disseminate, thus allowing them to colonise, proliferate and survive (Chambers et al., 2002; Hart, 1982; Hart and Fidler, 1980a, b; Luzzi et al., 1998). Therefore targeting the ECM and its enzymes could be a promising potential therapeutic target.

1.7 Fibroblast biology

Fibroblasts are elongated, spindle-shaped cells that are ubiquitously distributed within all human tissue. Fibroblasts are a very resilient cell type and can survive stress-like conditions that would be lethal to other cells (Kalluri, 2016). One of the main roles of fibroblast cells is to maintain and organise the structural architecture and biological integrity of connective tissue by synthesising and depositing ECM components (collagens, fibronectins, laminins tenascins and PGs) (Kalluri, 2016).

For example, fibroblasts have been reported to secrete various type of collagen (type I, III & IV) (Li et al., 2007b), which are dragged along the fibrillar matrix of the connective tissue and re-modelled by fibroblast movement, thus forming elongated fibres. The fibres are subjected to a constant pulling in a magnitude of directions, therefore leading to contraction and re-organisation of the tissue. In addition, fibroblasts have been reported in regulating degradation of the ECM through production and secretion of enzymes known as MMPs (Baum and Duffy, 2011; Lu et al., 2011; Rhee, 2009).

1.7.1 Fibroblasts in wound healing

Fibroblasts that reside within the ECM are usually quiescent but play an important role in the restoration of injured tissue, for example during wound healing. In brief, this process is defined by three processes; (1) the inflammatory phase upon the inflicted wound; damage to the capillaries activates circulating platelets and triggers formation of blood clots consisting of fibrin (Li et al., 2007b). Consequently, the platelets release chemotactic and cytokine factors, such as TGF-β and platelet-derived growth factor (PDGF) which recruit inflammatory cells, including macrophages and neutrophils that in turn result in the migration of fibroblasts and endothelial cells to the wound site (Darby et al., 2014); (2) formulation of granulation tissue involves the migration of keratinocytes over the injured dermis, followed by angiogenesis, which is critical for delivery of nutrients to the wound (Darby et al., 2014). Importantly, it's at this stage differentiation of the recruited fibroblasts into an activated 'myofibroblast' phenotype occurs. The most defining physical features that distinguish fibroblasts to myofibroblasts is the development of actin stress fibres into organised microfilaments, allowing the cells to adopt a contractile phenotype

(Gabbiani et al., 1971). An additional feature that has been predominantly used as a marker of fibroblast differentiation is the expression of alpha-smooth muscle actin (α-SMA, also known as ACTA2) (Hinz et al., 2012). Myofibroblasts secrete ECM proteins (such as fibronectin and collagen type I and III) to form granulation tissue (the scab, rich in collagen type III) and provide a scaffold for collagen type I fibrils which mediate wound contraction (Li et al., 2007b); (3) resolution of the ECM; extracellular degradation is regulated through myofibroblast secretions of MMPs and tissue inhibitors of metalloproteinases (TIMPs), myofibroblasts cells are removed via apoptosis and the non-differentiated fibroblasts may exhibit a more quiescent, non-contractile phenotype (Li et al., 2007b; McAnulty, 2007). Interestingly, *in vitro* cultured fibroblasts are being used commercially as augmentations for tissue repair for a variety of conditions, such as acute and chronic wound injuries (Griffiths et al., 2004) and healing of extensive burns (Waymack et al., 2000).

1.7.2 Cancer associated fibroblasts (CAFs)

In 1986 Harold Dvorak published an article entitled, “Tumours: wounds that do not heal” (Dvorak, 1986). The article discussed the many similarities between wound healing and solid tumours, such as, the excess production of proteins (fibronectin and fibrinogen) and the fibrin-fibronectin clot that serves as a provisional stroma to surround ECM components (Dvorak, 1986). The novelty of Dvorak’s article was based upon two relevant findings; firstly, the discovery of vascular permeability factor (VPF, later renamed vascular endothelial growth factor (VEGF)) as a tumour product (Senger et al., 1986) and secondly the recognition that chronic vascular hyperpermeability (CVH) induced by VPF accounts for the fibrin deposition in solid tumours in early stages of wound healing (Dvorak et al., 1979). 36 years later Dvorak defended and evaluated the principal relationship between tumours and wound healing in light of subsequent research, stating that tumours strongly require stroma and depend on their host for survival (Dvorak, 2015). These seminal discoveries from the late 1970s have led to a greater understanding of the similarities between wound healing and tumour-microenvironment during tumour progression.

Similar to the myofibroblasts present during wound healing, fibroblasts in the presence of cancer cells have also been reported to adopt an ‘activated’ phenotype,

displaying traits similar to those of myofibroblasts, such as formation of elongated collagen fibres and expression of α-SMA (Hanley et al., 2016).

CAFs are present within the tumour-microenvironment and play an important role in promoting tumour growth, angiogenesis and invasion (Gaggioli et al., 2007; Pietras et al., 2008). CAFs have also been reported to alter expression of certain growth factors, such as, IGF I and II (Yee et al., 1991), PDGF (Ponten et al., 1994) and TGF-β (Frazier and Grotendorst, 1997) in breast cancer. In addition, introduction of CAFs isolated from head and neck SCC appeared to promote invasion of SCC cells into 3D organotypic gels (Gaggioli et al., 2007). Furthermore, Orimo and colleagues showed that CAFs extracted from human breast carcinoma promote growth of admixed breast carcinoma cells more than with normal mammary fibroblast (Orimo et al., 2005). Both examples suggest that CAFs may possess a more activated phenotype than normal fibroblasts, thus proposing they have increased ability to remodel ECM over normal fibroblasts.

CAFs are a critical component of the tumour-stroma microenvironment, and an important area of research within cancer (Kalluri, 2016; Kalluri and Zeisberg, 2006; Shiga et al., 2015). CAFs are highly recognised as a valid therapeutic target and academia and industry are actively looking for new CAF-selective drugs. However, the underlying molecular mechanisms of how CAFs regulate tumour progression are not fully understood.

1.8 Drug Discovery

Historically, new drugs were discovered through the identification of an active compound, however, there are examples in history where drugs have been identified through serendipitous events. From Alexander Fleming's accidental discovery of penicillin (Fleming, 1929) to Pfizer's' mid 90's blockbuster, Sildenafil, which was primarily targeted for treating patients with pulmonary arterial hypertension, but now is the most common treatment for erectile dysfunction in the world (Boolell et al., 1996).

1.8.1 The drug discovery process

Normal drug discovery is a series of complex processes through which potential new therapeutic targets and drugs can be identified. The identification process follows a general pattern for antibody, drug and gene discovery.

Specifically, the drug discovery pipeline consists of several stages, which include; (1) target identification – which involves early stage research and development of the disease pathway and initial genomic and proteomic data of the target; (2) discovery – starts with chemical synthesis of compounds specific to the target, followed by assay development to optimise the screening process concluded by performing HTS of compound libraries to identify hits; (3) lead validation – begins with analysing the effect of the identified hits and trying to improve their structure-activity relationship (SAR) to try and increase their potency before re-screening to validate the hits; (4) pre-clinical study – efficacy and potential risks are evaluated before human trials can begin, therefore *in vitro* and then *in vivo* experiments are performed to provide efficacy and toxicity data from lead compound candidates; (5) clinical trials – involve human participants and are normally split into four phases. The primary purpose of phase I trials is to evaluate drug safety, metabolism and side effect (cohort of 20-80 patients). Phase II trials sees the drug or treatment administered into a larger cohort of patients (between 100-300) and further determines drug effectiveness and safety in conjuncture with a placebo. Phase III trials further evaluate the efficacy, dosage and safety in a much larger population of patients (between 1000-3000). This phase also compares efficacy of existing treatments as well as different dosages and interactions with other combination therapies; finally (5) approval and launch – takes place if a

selected drug candidate is effective in clinical trials. The compound is submitted to regulating bodies for approval by the Food and Drug Administration (FDA). The drug is marketed and then released to the public however still monitored for side effects (also known as phase IV trials). The process to fully develop a drug from concept to shelf costs approximately £2 billion and take around 12-15 years (Hughes et al., 2011; Orloff et al., 2009; Strovel et al., 2004).

1.8.2 High-throughput screening (HTS) in drug discovery

Today, large pharmaceutical companies perform HTS of compound libraries (usually containing up to 1 million compounds which include various natural products, extra- and intracellular targets and even whole genome) as an initial step in the drug discovery and lead validation process. HTS is an approach to drug discovery that incorporates a broad range of robust automated technologies and advanced instruments, comprised of; (1) robotic arms programmed to efficiently and precisely, transport barcoded multi-welled plates from storage/incubator carousels to integrated liquid dispensing units and plate centrifuges/readers; (2) high-content image capturing machines such as microscopes and spectrophotometers; and (3) non-contact, tipless compound transfer machines which use acoustic energy, capable of transferring solutions ranging in volume from 25nl to 50µl (Echo, Labcyte, USA).

Fluorescence imaging microscopy within biomedical research has become an integral part of all cell biology studies. Many research institutes use advanced high powered fluoresce imaging technologies for a wide variety of biological studies. Examples include the use of laser scanning confocal microscopy to visualise detailed 3D adult Drosophila anatomy (McGurk et al., 2007). In addition, spinning disk confocal microscopy has been used to capture live imaging of neutrophil migration in zebrafish (Lam et al., 2014b). Furthermore, two-photon microscopy can image through thick sample specimens producing high quality 3D images and was used to detect breast cancer cell bone colonisation from frozen bone samples (Allocca et al., 2016).

These are just a few of the examples supplied through high-end companies, namely; Carl Zeiss, Leica, Nikon and Olympus. All of the mentioned technologies provide high quality of specimen imaging, however image capture via these techniques if often slow and normally samples have to be manually exchanged.

The pharmaceutical industry have adopted the use of high-content automated image capturing microscopes. These systems include the IN Cell Analyser 6000 (GE Healthcare Life Sciences, USA), Operetta (Perkin Elmer, USA), Cell Voyager 7000 (CV7000) (Yokogawa, Japan) and the Cell Discoverer 7 (Carl Zeiss, Germany) (Li et al., 2016). These high-spec machines use laser-based or light-emitting diode (LED) technology (Cell Discoverer 7) for live cell imaging and scientific complementary metal-oxide semiconductor (sCMOS) cameras for high-resolution imaging capture. The microscope systems are often large cabinet-like units that are sterile and environmentally controlled. The units contain built in microscopes with automated stage and objective turrets, thus no user intervention is required. Additionally, each system contains barcode readers and plate docking stations, thus enabling integration within a HTS platforms. Furthermore, one of the most important aspects; the speed of image acquisition in 2D and 3D for these systems is much faster compared with the conventional fluorescence laser scanning microscopes mentioned previously.

However, these high-end, full-spec systems are costly (approximately ranging from £500K – £1M) and also require elaborate data management systems to allow tracking of entire HTS campaigns as well as perform high-content data analysis (Buchser et al., 2004).

Additionally, advances in multi-welled plate technology has been reported to increase high-throughput capacity from screening 10,000 compounds a month using 96-well plates (200µl max working volume/well), to 10,000 a day using 384-well plates (100µl max working volume/well) and now ultra-HTS using 1,536-well plates (10µl max working volume/well) whereby 100,000 compounds a day can be screened (Klumpp et al., 2006; Mayr and Fuerst, 2008).

Some groups have also attempted the use of 3,456-well plates (Aurora Microplates, USA) (2.5µl max working volume/well), for example, Brandish and colleagues screened for inhibitors against D-amino acid oxidase, screening approximately 170,000 compounds a day (Brandish et al., 2006). However, such small working volumes and surface area will inevitably lead to technical limitations, therefore currently HTS laboratories within academia and industry favour the 384- and 1,536-well plate formats assays as they stay within the ‘magic triangle of HTS’ ; time, cost and quality of process (Mayr and Fuerst, 2008).

HTS can and does identify compounds which go through clinical trials and regulations to become FDA approved drugs. For example, Gefitinib an AstraZeneca drug (trade name Iressa) (Wakeling et al., 2002), is an oral epidermal growth factor receptor (EGFR) tyrosine kinase inhibitor for EGFR mutation-positive NSCLC, which was processed by HTS in 1993 before being FDA approved in 2003 (Macarron et al., 2011).

However, several postulations regarding the drug discovery industry have pointed to HTS as the sole benefactor of blame, such as HTS; (1) contributes to the decline of creativity within drug discovery; (2) data is of poor quality; (3) is expensive and time consuming; (4) fails to find leads for targets (Macarron et al., 2011). Nevertheless, many companies still do and will continue to use HTS technologies to perform primary and hit validation high-content screening, thus, driving engineers, scientists and technology companies to innovate and design faster and smarter automation platforms that can reduce and refine process flow and assay timelines (Hughes et al., 2011).

Aims of this study

As previously described in **Section 1.3**, 3D culture systems provide an *in vitro* model allowing the study of biological responses in an *in vivo* physiomimetic microenvironment. Data have reported that 3D culture systems not only allow cells to differ morphologically from 2D cultured cells, but also the 3rd dimension is a crucial feature adding to the spatial organisation in which cellular cues and responses are similar to those *in vivo* (Chen and Yoon, 2017; Gudjonsson et al., 2002; Harma et al., 2010; Haycock, 2011; Huh et al., 2011; Kimlin et al., 2013; Kramer et al., 2013; Lee et al., 2008a; McBeath et al., 2004; Nyga et al., 2011; Ryan et al., 2016; Thoma et al., 2013).

3D organotypic cultures adapted from the original Fusenig model (Fusenig et al., 1983) have been widely utilised not only in our laboratory (Froeling et al., 2010; Nystrom et al., 2005; Thomas et al., 2006) but also globally (Bernerd and Asselineau, 2008; Igarashi et al., 2003; Mueller et al., 2014; Schneider et al., 2008; Vorsmann et al., 2013). Moreover, data from our laboratory has demonstrated the importance and value of such 3D organotypic models in promoting migration and invasion of cancer cells (Moore et al., 2014; Nystrom et al., 2005). However the organotypic gel invasion assay is a slow experiment and it is not possible to examine the cells within the gel over time. Fibroblasts are implicated in tumour progression but they are often ignored in the analysis of organotypic gels largely because they are hard to see. Thus while the organotypic gel is an excellent tool, it still has several limitations. In this study I will attempt to resolve some of these limitations.

This study will aim to:

1) Develop a novel fluorescent 24-well mini-organotypic Transwell® invasion assay that can be examined automatically over time in 3D via confocal laser scanning microscopy. Data collection *in situ* will eliminate the need for histology before obtaining initial data.

2) Establish that the new assay will work with and support a variety of tumour and fibroblast cell combinations from different tissues.

3) Use the new assay to screen a library of small interfering RNA (siRNA) targeting proteases to determine if any affect the invasion of tumour cells. Moreover, I shall target the fibroblasts, not the tumour cells, since less is known about the molecular mechanisms of fibroblast invasion and this will examine further whether targeting fibroblasts can supress cancer growth and invasion.

4) Miniaturise the 24-well assay to suit a 96-well format enabling higher-throughput of samples for siRNA and drug screening.

CHAPTER II: MATERIALS AND METHODS

2.0 Materials and Methods

2.1 Cell culture

2.1.1 Routine cell culture and conditions

All cells were cultured as adherent monolayers in sterile tissue culture flasks of various sizes (Corning, 25cm^2 (430639), 75cm^2 (430641U) and 175cm^2 (431080)) in a humidified atmosphere of 37°C and 8% CO_2. Cells were routinely examined for the presence of *mycoplasma* using the polymerase chain reaction (PCR) method (detailed in **Section 2.7**). Cancer and fibroblast cells were grown using different growth media (detailed below).

2.1.1.1 Passaging cells

When cells reached 70-80% confluency, medium was carefully removed and cells were washed with sterile phosphate buffered saline (PBS) before adding trypsin (0.5%) – Ethylenediaminetetraacetic acid (EDTA) (0.2% w/v) (Sigma Aldrich, 59418C) for 2-5 minutes (dependant on cell type) at 37°C. Once detached from the surface of the culture flask, trypsin was inactivated by addition of medium containing 10% foetal bovine serum (FBS) (Gibco, 10500-604), the cell suspension was then centrifuged at 1200 revolutions per minute (rpm) for three minutes (ALC International, PK121). Cell pellets were re-suspended in the appropriate medium, if cell counting was required, 10µl of cell suspension were pipetted into a FastRead counting haemocytometer (Immune Systems, BVS100) and cells were manually counted under a phase-contrast light microscope (Olympus, IMT-2, Japan). Cells would then be prepared for experimental purposes or placed back into the desired culture flasks at various dilutions (1:3 to 1:20) dependant on their growth rates and needs.

2.1.1.2 Cryopreservation of cells

For cell preservation, cell pellets were re-suspended in 90% FBS and 10% dimethyl sulphoxide (DMSO) (Fisher Scientific, D/4120/PB08). A total volume of 1ml cell suspension (containing approximately 10^6 cancer cells or 2 x 10^6 fibroblast cells) was transferred to Corning 1.5ml cryovial (Corning, 430489). Cryovials were placed in a Mr Frosty™ freezing vessel (ThermoFisher Scientific, 5100-0001) at -80°C for 24

hours before being transferred to liquid nitrogen (-196°C) long-term cryogenic storage.

2.1.1.3 Thawing cryopreserved cells

Frozen cryovials were transferred directly to a 37°C water bath until thawed (approximately 90 seconds). Once thawed, the contents of the cryovials were transferred to a 15ml Falcon™ tube (Corning, CLS430791) containing pre-warmed culture medium, centrifuged (1200rpm for three minutes) and the pellet was re-suspended in fresh medium and immediately plated into the appropriate tissue culture flasks.

2.1.2 Human fibroblasts

Three types of fibroblasts were used in this study (**Table 2.1**); neonatal human foreskin fibroblasts (FSF), adult derived human dermal fibroblasts (HDF) and Medical Research Council cell strain 5, a human foetal isolated lung fibroblasts (MRC5). HDF, FSF and MRC5 were cultured in Dulbecco's Modified Eagle's Medium (DMEM) (Sigma Aldrich, D6429), supplemented with 10% FBS.

Table 2.1: Details of human primary fibroblasts used

Cell Strain	Donor detail	Tissue type	Provider
FSF – skin strain 1	Male, 28 days	Foreskin	Dr Su Marsh (Blizard Institute, QMUL)
HDF – skin strain 2	Adult, unknown	Dermal	
MRC5 – lung strain	Male, 14 week gestation	Lung	Dr Zareen Khan (Barts Cancer Institute, QMUL)

2.1.3 Human cancer cells

Three cancer cell lines were used in this study (**Table 2.2**). Oral squamous cell carcinoma (OSCC) VB6 (derivation described in (Thomas et al., 2001b)) cells were cultured in keratinocyte growth medium (KGM) comprised of α-Minimum Essential Medium (α-MEM) (Invitrogen, 22571-020), supplemented by 10% FBS, 18mM adenine (Sigma Aldrich, A2786-2SG), 1% L-glutamine (Sigma Aldrich, G7513), 0.5µg/ml hydrocortisone (Sigma Aldrich, H4001), 10µg/ml insulin (Sigma Aldrich, I1882), 10ng/ml epidermal growth factor (EGF) (Sigma Aldrich, E9644) and 10^{-10}M cholera toxin (Calbiochem, 227035). MD Anderson (MDA)-MB-468 cells are a breast adenocarcinoma line, isolated from the right mammary gland of breast cancer patients. MDA-MD-468 cells were cultured in DMEM supplemented with 10% FBS (Cailleau et al., 1978). National Cancer Institute (NCI)-H1299 cells are a human non-small cell lung carcinoma (NSCLC) line derived from a lymph node metastasis of a lung cancer patient. H1299 cells were cultured in Roswell Park Memorial Institute (RPMI-1640) (Sigma Aldrich, R8758) medium supplemented with 10% FBS (Phelps et al., 1996).

Table 2.2: Details of human cancer cells used

Cell line	Donor detail	Cell details	Reference
VB6 (OSCC)	-	Differentiated, retroviral infection to overexpress β6 integrin	(Thomas et al., 2001b)
MDA-MB-468 Breast adenocarcinoma	Female, 51 years	Pleural effusion metastasis, PTEN, RBI1, SMAD4, TP53 mutations	(Cailleau et al., 1978; Mu et al., 2002)
H1299 Lung carcinoma	Male, 43 years	Non-small cell, lung cancer, lymph node metastasis, NRAS mutation	(Phelps et al., 1996)

2.2 Western blotting

2.2.1 Cell lysis

Fibroblast cells were grown to 80% confluency prior to two washes with sterile ice cold PBS. Cells were lysed for 15 minutes on ice in lysis buffer (Nonidet-P40 (NP40), Invitrogen, FNN0021) containing 1:100 dilution of protease inhibitor cocktail 1 stock (Calbiochem, 539131) and 1:100 phosphatase inhibitor (Calbiochem, 524625)) (200µl/well in a 6-well plate). Cell lysates were collected and transferred into 1.5ml microcentrifuge tubes on ice and vortexed every five minutes for three cycles. After centrifugation (13,000rpm for 10 minutes at 4°C), supernatants were carefully removed and transferred to pre-labelled, chilled, 1.5ml microcentrifuge tubes for immediate protein concentration determination. Protein concentration was quantified in a 96-well plate (Corning, #3599) using Bio-Rad DC Protein Assay reagents according to manufacturer's instructions (Bio-Rad Laboratories, Reagent A – 500-0113, Reagent B – 500-0114, Reagent S – 500-0115), alongside a series of pre-prepared known bovine serum albumin standards (BSA) (0.0-5.0mg/ml). The absorbance of each lysate samples were measured at 550nm using a microplate reader (Tecan, Infinite F50, Switzerland). Once sample concentration was determined, lysates were subsequently diluted in an appropriate volume of 2x Laemmli sample buffer (Sigma Aldrich, S3401) to the desired final protein concentration. Samples were stored at -20°C if not immediately used.

2.2.2 Sodium dodecyl sulphate polyacrylamide gel electrophoresis (SDS-PAGE)

Samples were thawed then briefly centrifuged to collect any residual contents from tube walls before heating to 95°C for five minutes to denature proteins. Gel cassettes (ThermoFisher Scientific, NC2010) were inserted into SDS-PAGE tank (ThermoFisher Scientific, EI0001) with 10x tris-glycine SDS-PAGE buffer (Severn Biotech, 20-6300-100) diluted in distilled water. Protein samples and Amersham ECL Rainbow Protein Ladder (10µl) (GE Healthcare Life Sciences, RPN800E) were loaded into gel cassettes containing freshly made 12% polyacrylamide gels (**Table 2.3**) and run at 120 volts (V) for 95 minutes.

2.2.3 Western blotting

Proteins were transferred on to Hybond nitrocellulose membranes (GE Healthcare Life Sciences, 10600002), using an Invitrogen wet transfer chamber inside the SDS-PAGE tank. Proteins from the gel were transferred at 35V for 95 minutes. The nitrocellulose membrane was removed and incubated in 20ml of Ponceau S (0.1% (w/v) in 5% acetic acid) (Sigma Aldrich, P7170) for 10 minutes to confirm efficient protein transfer. Nitrocellulose membranes were subsequently washed four times in PBS to remove the Ponceau S, before non-specific protein binding was blocked by incubation for 45 minutes, in 5% w/v non-fat milk (Sigma Aldrich, 70166), 0.1% Tween-20 (Sigma Aldrich, P9416) and tris-buffered saline (TBS) (Severn Biotech, 20-7301-10) (TBS-T) at room temperature. Membranes were rinsed in TBS-T four times before being placed inside a 50ml Falcon™ tube (Corning, 430290) and incubated with a specific dilution of primary antibody (**Table 2.4**) in TBS-T containing 5% BSA (5ml final volume) and left rotating overnight at 4°C.

The next day membranes were washed thoroughly for one hour with TBS-T, replenishing the washing solution every five minutes, before being incubated with species-specific secondary horseradish-peroxidase (HRP) conjugated antibody for 40 minutes at room temperature, followed by an additional one hour wash step with TBT-T. Specific proteins were detected using an Enhanced Chemiluminescence detection reagent kit (ECL) (GE Healthcare Life Sciences, RPN2106) and visualised using the ChemiDoc Imager 600 (GE Healthcare Life Sciences).

2.2.4 Densitometry analysis

Densitometric analysis of protein bands was performed using Image J Software (National Institutes of Health, USA). Protein band densities were normalised to the loading control housekeeping protein, Heat-shock chaperone-70 (HSC-70, Santa Cruz Biotech, SC-7298).

Table 2.3: Formulation of 12% polyacrylamide gels

Resolving gel		Stacking gel	
dH_2O	5.3ml	dH_2O	2.7ml
30% Polyacrylamide solution (ThermoFisher Scientific, NC2010)	6.4ml	30% Polyacrylamide solution (ThermoFisher Scientific, NC2010)	670ml
Tris-HCL (1.5M, pH 8.8)	3.75ml	Tris-HCL (1M, pH 6.8)	0.5ml
10% SDS (Fisher Scientific, BP1311-1)	0.15ml	10% SDS (Fisher Scientific, BP1311-1)	0.05ml
10% Ammonium persulphate (APS) (Sigma Aldrich A3678)	0.075ml	10% Ammonium persulphate (APS) (Sigma Aldrich A3678)	0.05ml
TEMED (National Diagnostics, EC503)	0.0075ml	TEMED (National Diagnostics, EC503)	0.005ml

APS - ammonium persulphate; dH_2O - distilled water; SDS - sodium dodecyl sulphate; TEMED - tetramethylethylenediamine

Table 2.4: List of primary and secondary antibodies used for western blotting

Target	Type	Host/Isotype	Clone	Supplier	Concentration
MMP-17	Primary	Rabbit/IgG	-	ThermoFisher Scientific (PA5-28219)	1:1000
TMPRSS-13	Primary	Rabbit/IgG	-	ThermoFisher Scientific (PA5-30935)	1:1000
HSC-70	Primary	Mouse/IgM	B-6	Santa Cruz Biotech (SC-7298)	1:5000
Anti-Mouse HRP	Secondary	Mouse/IgG	-	Dako (P0260)	1:2000
Anti-Rabbit HRP	Secondary	Donkey	-	GE Healthcare Life Sciences (NA9340)	1:2500

2.3 Organotypic cultures

Organotypic cultures are so-called as they are *in vitro* attempts to recreate and recapitulate part of a normal 3D tissue. Norbert Fusenig originally developed the organotypic model by culturing a solid squamous cell carcinoma *in vitro* and then plating these cells onto collagen gels prepared in silicon chambers. Once cell attachment was achieved, the collagen gels were lifted to an air-liquid interface, thus nourishment of gels occurred from below whilst the surface of the gel was exposed to air (Boukamp et al., 1982). The addition of cancers cells and stromal fibroblasts enables the study of invasion using the organotypic gel model.

2.3.1 Preparation of mini-organotypic cultures – 24-well assay

The mini-organotypic assays are miniaturised versions of the organotypic gels, which have previously been published by our laboratory (Nystrom et al., 2005). This miniaturised version recreates the organotypic gel in a hanging basket-like sterile Transwell® insert.

0.4µm-pore size, optically clear polyethylene terephthalate (PET) Transwells® (Corning, #3470) were coated using a 300µl solution of ice cold collagen type I – rat tail (Corning, #354236) diluted 1:100 with cold sterile PBS and placed inside a sterile plastic 24-well plate (Corning, #3524). In the meantime a collagen: Matrigel® mixture was prepared in cold sterile 15ml Falcon™ tubes. To produce 1ml of organotypic gel mixture, the following volumes were used, all reagents were kept on ice; 525µl collagen type I, 175µl Matrigel® (Corning, #354234), 100µl 10x DMEM (Sigma, D2429), 100µl cell culture media, 100µl sterile FBS and neutralised using 1M sterile sodium hydroxide (NaOH) solution (80µl/ml). When mixed together correctly, the gel should produce a straw like colour until addition of the NaOH, which rapidly transforms the solution to a bright pink colour.

All reagents must be kept on wet ice at all times during assembly of the gels. The Falcon™ tube containing the bright pink gel mixture was buried within the wet ice. Next the excess collagen: PBS solution was carefully removed from the Transwell®, before 100µl of collagen: Matrigel® organotypic gel mixture was added (dropwise) and placed in an incubator at 37°C for 1.5 hours, thus allowing the proteins to cross link and polymerise. Fibroblasts and tumour cells were counted and plated on top of the mini-organotypic gels in a 200µl cell suspension, either alone (10^5 in total) or in a 2:1 co-culture ratio of fibroblast (6.7×10^4) and tumour cells (3.3×10^4). Next, 600µl of cell culture medium was added underneath each Transwell®. The following day the

medium below each Transwell® was replaced with 350µl of fresh medium and the medium above the gel was carefully removed (not disturbing the top surface of the gel) and replaced with 200µl serum-free medium (only for cultures containing MDA-MD-468 and H1299 cells, VB6 were left exposed). To maintain a chemotactic gradient this process of changing medium was carried out every two days, until samples were fixed or analysed by microscopy and then fixed.

2.3.2 Fixation, harvesting and processing

Transwells® were fixed in 10% v/v neutral buffered formalin (Cellstor, BAF-0010-25A) for 24 hours and the following day transferred to 70% v/v ethanol for at least three hours. Gels were removed from the Transwell® by use of scalpel to cut the membrane before being placed into a histology embedding cassette. The fixed gel was processed to paraffin wax and 4µm thick sections were cut and stained with haematoxylin and eosin (H&E) by Mr George Elia (Histopathology Department, Barts Cancer Institute).

2.4 Transient labelling of cells with fluorescent dyes

CellTracker™ Red (C34552) and CellTracker™ and Green (C7025) (50µg aliquots, ThermoFisher Scientific) were dissolved in anhydrous DMSO to produce 5mM and 10mM stock concentrations respectively. CellTracker™ Red and Green were diluted 1:1000 in serum-free α-MEM or DMEM producing 5µM and 10µM final concentrations respectively. Cell culture media were removed from the desired flasks and the cells were washed once with sterile PBS. The serum-free medium containing the fluorescent dyes were added to the appropriate flasks and incubated at 37°C for 45 minutes. Subsequently, the serum-free medium containing the fluorescent dye was removed, cells were then washed with sterile PBS before serum-containing media were added to each flask and incubated at 37°C for a further 40 minutes.

2.4.1 Use of IncuCyte™ ZOOM® to determine optimal exposure time

To determine the time required for each fluorescent dye to internalise to a maximum, cells labelled with CellTracker™ within their flasks were immediately placed inside an IncuCyte™ ZOOM® imaging system (Essen BioScience). The IncuCyte™ ZOOM® consists of a microscope gantry that resides within a cell incubator and can obtain

real time live cell imaging. Images were captured at various time points and fluorescence intensity was measured over time.

2.5 Live image acquisition, rendering and quantification of mini-organotypic gels

The mini-organotypic gels contain fluorescently labelled cancer (red) and fibroblast (green) cells. The Transwells® used have an optically clear membrane, thus enabling imaging through the insert. Obtaining live, *in situ* images of cancer and fibroblast cell invasion, at various time points was performed using a Confocal Laser Scanning Microscope (CLSM) 710 (Carl Zeiss GmbH, Germany). This was the most suitable imaging platform available at the time. However in January 2017 Barts Cancer Institute purchased a Nikon Eclipse Ti-E spinning disk confocal microscope (Nikon Instruments, Europe BV). Going forward, this system would be better suited to image 3D gels, specifically, for the speed of acquisition, but also for ease of use of the software.

2.5.1 Live image acquisition

In initial studies, Transwells® were removed with tweezers from the plastic 24-well plate and placed onto a 35mm-diameter glass coverslip-bottomed dish (MatTek, USA, P35G-1.0-14-C). This was positioned inside a heated 35mm dish-holder on an automated *x-y* scanning stage. The confocal was equipped with a heated chamber set to 37°C, supplied with 5% CO_2 and a humidifier to simulate the same conditions present in an incubator. *In situ* optical overlapping sections in the *z*-axis were obtained using a 568nm excitation line and 602nm emission for the CellTracker™ Red dye and 488nm excitation line and 517nm emission for the CellTracker™ Green dye.

Series of *x-y-z* images of 700µm square (in the *x-y* plane) were collected along the *z*-axis at 4µm intervals with a 1µm overlap to approximately 1400µm depths throughout the gel using a 20x air objective. Scanning through one gel of approximately 1400µm thickness, in two colour channels, took 20-23 minutes. During the image acquisition, the sample needed to be removed from the 24-well plastic plate and was not in contact with any cell culture medium. While this method allowed for imaging, it was slow and cumbersome. After three months of optimising the gel system, I tested several glass bottomed 24-well plates so that imaging could take place within the plate. I chose the black polystyrene 24-well sterile SensoPlate™, fitted with a 0.17mm

thick glass bottom coverslip (Greiner Bio-one, 662892), I also purchased a scanning stage designed for multi-welled plates (Carl Zeiss, 0496-315) and a long working distance 20x air objective (Carl Zeiss, Objective LD Plan-Neofluar 20x/0.4 Corr M27).

Programming the microscope's automated positioning system, ensured that each Transwell® was imaged in the same position every time. These changes to the image acquisition process made collection of the *z*-stack images increasingly swifter. Additionally the samples remained inside a sterile environment and were always in contact with cell culture media. Before imaging, Transwells® were removed from the 24-well plastic host plate and transferred into the Greiner 24-well glass bottomed plate by use of sterile tweezers under a lamina flow hood.

2.5.2 Image rendering using Imaris

The raw laser scanning microscope (.lsm) *z*-stack data files obtained from the CLSM 710 were imported to the image analysis software Imaris (Bitplane AG, Switzerland). The base software enables rendering and removal of background noise of the image; providing smooth surfaces, higher resolution and sharper 3D images. A wide range of additional add-ons can be purchased allowing for multi-purpose and in-depth quantification and analysis.

2.5.3 Image quantification using Imaris XT

After purchasing Imaris XTensions (XT), an add-on, that calculates and quantifies cell movements; depth of invasion from the base of the Transwell® (defined as point '0') to the centre of each cell within a 700µm x 700µm x 1400µm volume were measured. Comma-separated value (.csv) files were generated for a wide range of parameters in both channels (including, area, intensity, position, sphericity, and volume) thus allowing high content data analysis to be performed.

2.6 Small interfering RNA (siRNA) transfection

The optimised 24-well fluorescent mini-organotypic assay has become more affordable and justified as a 3D invasion assay for many reasons, in particular, due to reductions in the required volumes of costly reagents (collagen and Matrigel®). The use of Transwells® has permitted the assay to be easily repeated using a variety of experimental conditions, thus increasing the ease of attaining triplicate results and varying plate conditions. As a direct result of these improvements it has now become achievable and affordable to perform siRNA transfections. Described below are the procedures used to transfect HDF cells with a customised pooled library of siRNA (**Table 2.5**) and the deconvoluted individual validation screen from specifically chosen hit targets (**Table 2.7**).

2.6.1 SMARTpool siRNA screen

A custom library of 60 SMARTpool siGENOME siRNA (Dharmacon, GE Healthcare) was purchased. The 60 siRNA's (0.5nmol) used for the primary gene screen are listed in **Table 2.5**. 25µl of 1x siRNA buffer (300mM KCl, 30mM HEPES-pH 7.5 (4-(2-hydroxyethyl)-1-piperazineethanesulfonic acid), 1.0mM $MgCl_2$) was added to each siRNA when needed, producing a 20µM stock solution and stored at -20°C until use. Due to the amount of time required to manually perform this screen, the 60 SMARTpool siRNAs were analysed in 15 groups (**Table 2.6**). Meaning, four siRNAs were tested, in triplicate, at one time, alongside a non-targeting (NT) siRNA control and a non-siRNA treated control, shown in **Figure 2.1**.

This proof-of-principle screen targeted genes in fibroblasts. HDF cells were seeded into 6-well plates (1.5×10^5 cells per well) in serum-containing DMEM. Subsequently, 24 hours later the 70% confluent HDF cells were transfected with the SMARTpool siRNA. Briefly, in a labelled microcentrifuge tube, the target siRNA were added with the transfection reagent (INTERFERin®, Polyplus, 409-10) to serum-free DMEM, producing a 20nM final concentration according to the manufacturer's instructions.

The microcentrifuge tubes were vortexed and incubated at room temperature for 10 minutes. The vehicles and siGENOME NT siRNA controls (Dharmacon, GE Healthcare, D-001206-14-05) were prepared similarly. During incubation of the siRNA and INTERFERin® complexes, cells were washed once with sterile PBS. The transfection reagent mixture (1.224ml) was added to triplicate wells at 400µl volumes per well, dropwise and mixed gently by rocking the 6-well plate back and forth before being incubated. 72 hours post transfection, media were removed from the 6-well

plates and gently washed once with sterile PBS (not disturbing the cell layer). CellTracker™ Green was administered to the siRNA transfected HDF cells (as described in **Section 2.4**). During the incubation time, mini-organotypic gels were prepared. Fluorescently labelled green HDFs were trypsinised, counted and plated in co-culture with fluorescently labelled red VB6 cell on top of mini-organotypic gels and imaged via confocal microscopy.

2.6.2 Deconvoluted siRNA

The SMARTpool siRNA system mixes four different siRNAs to the same gene target. A standard practice when screening pooled siRNA is to conduct a deconvolution screen, where each of the individual siRNA sequences of the top scoring hits are screened independently, thus, providing a technical validation of the reagents (Chia et al., 2010; Falkenberg et al., 2014; Simpson et al., 2008). The primary SMARTpool siRNA screen yielded 16 gene hits that induced significant ($p<0.05$) changes versus a NT siRNA control (**Figure 4.7**). Five of the 16 SMARTpool hits were selected for a validation screen; these were tested using the four individual constituent siRNAs of each SMARTpool (**Table 2.7**). Transfection of HDF cells were carried out as described in **Section 2.6.1**.

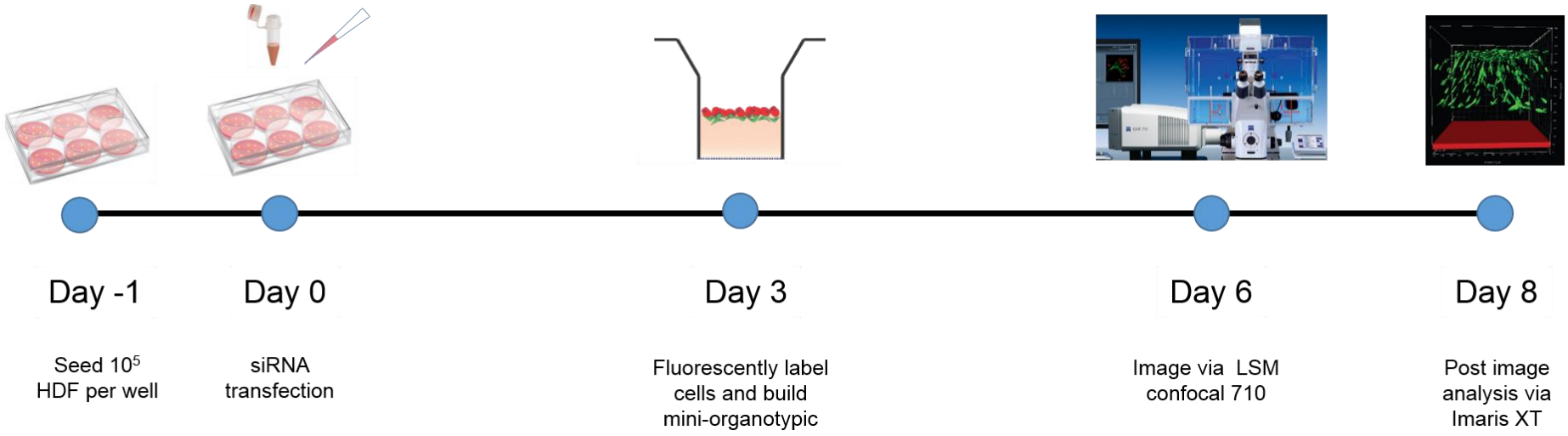

Figure 2.1: Timeline of siRNA transfection protocol

The figure displays the timeline and processes undertaken to perform one of the 15 groups of the 60 siRNA experiments.

Table 2.5: List of SMARTpool siRNAs used for primary screen

siRNA targets	Aliases	Function
CAPN-1,2,3,5,6,7,9,10,11,13	Calpain Calcium-activated neutral proteases	Apoptosis Proliferation Migration Adhesion Autophagy
CAPNS-1	Calpain sub unit 1 Calpain-4	As Above
CASP-1^,2,3*,4^,5^,6*,7*,8*,9*, 10,14	Cysteine-aspartic proteases Cysteine-dependant asparate-directed proteases	*Apoptosis Necrosis ^Inflammation
MMP-1,2,3,7,8,9,10,11,12,13,14,15,16,17,19,20,21,24,25,26,27,28	Matrix metalloproteases Zinc-dependant endopeptidases	ECM degradation metastasis Angiogenesis Wound healing Cell migration
SERPIN-A1,A3	Serine protease inhibitor Serpin peptidase inhibitor, clade A(alpha 1 antiproteinase, antitrypsin) member 1 & 3	Deficiency results in:- - Liver disease - COPD - Alzheimer's
SERPIN-B2,B12	Serpin peptidase inhibitor, clade B (ovalbumin) member 2,12 Plasminogen activator inhibitor-2	Deficiency results in :- - Inflammatory disease
SERPIN-D1	Heparin cofactor II Serpin peptidase inhibitor, clade D member 1	Thrombin inhibitor Dysfibrinogenemia (fibrin clot formation)
SERPIN-E1	Serpin peptidase inhibitor, clade E (nexin, plasminogen activator inhibit type 1) Endothelial plasminogen activator inhibitor	Deficiency results in:- - Thrombosis - Fibrosis - Cancer
SERPIN-F1	Serpin peptidase inhibitor, clade F (alpha 2 antiplasmin) Pigment epithelium-derived factor (PEDF)	Antiangiogenic Antitumourigenic
SHH	Sonic Hedgehog	Vertebrate organogenesis Proliferation of adult stem cells
TMPRSS-11A	Transmembrane protease, serine 11A	Overexpression: - - Inhibits cell growth - G1 cell cycle arrest Diseases: - - Oesophageal cancer - Avian influenza
TMPRSS-2,3,4,5,6,9,13	Transmembrane protease, serine 2,3,4,5,6,9,13	Deficiency results in: - - Tumourigenesis - Infection - Prostate cancer - Ovarian cancer - Deafness

Table 2.6: Identity of siRNAs tested in experimental subgroups

siRNA experiments	siRNA	Appendix Figure
1	CAPN-5, MMP-15, CASP-4, CASP-8	7.1
2	SERPIN-E1, MMP-3, CAPN-10, CASP-1	7.2
3	CASP-9, MMP-7, MMP-19, SHH	7.3
4	CAPN-11, CASP-10, MMP-1, MMP-2	7.4
5	CASP-14, CAPN-13, MMP-8, TMPRSS-11A	7.5
6	CASP-6, MMP-10, SERPIN-A1, TMPRSS-13	7.6
7	MMP-24, CASP-2, TMPRSS-3, MMP-21	7.7
8	MMP-20, TMRPSS-2, CAPN-3, CASP-3	7.8
9	MMP-12, CAPN-2, SERPIN-A3, MMP-11	7.9
10	MMP-17, MMP-13, MMP-25, CAPN-1	7.10
11	SERPIN-B12, TMPRSS-4, CAPN-6, CASP-5	7.11
12	MMP-14, MMP-26, SERPIN-B2, TMPRSS-5	7.12
13	CAPN-7, MMP-9, CAPNS-1, MMP-27	7.13
14	SERPIN-D1, TMPRSS-6, CAPN-9. CASP-7	7.14
15	MMP-16, MMP-28, SERPIN-F1, TMPRSS-9	7.15

Table 2.7: List of individual siRNA's used for deconvoluted validation

siRNA target	Product code	Individual code	Target sequence
CAPN-10	11132	D-005800-01	CCGUCAUGGCAGUGAUGAA
		D-005800-02	GGGCCUUCACAGUGACCAU
		D-005800-03	GCUGCGUGCCACAUCGCUA
		D-005800-04	CCAUUCACAGCCAGGAGAU
CASP-8	841	D-003466-01	GGACAAAGUUUACCAAAUG
		D-003466-02	CAACGACUAUGAAGAAUUC
		D-003466-07	GCAAGAACCCAUCAAGGAU
		D-003466-25	GAAGAUAAUCAACGACUAU
MMP-17	4326	D-005958-01	GGUACUGGGUCUUCAAGGA
		D-005958-04	UAACGUAGAGGAAGGAUAC
		D-005958-05	GUUCAAGGACAAUAACGUA
		D-005958-19	UGGCUAAGCAGGUUCGGUU
SERPIN-F1	5176	D-010153-01	GGAGGAUCCUUUCUUCAAA
		D-010153-02	GCUGAAGCUGAGUUAUGAA
		D-010153-03	GCACAGGGGCGCUGGUGGA
		D-010153-04	GCACGAGCCCCACGACCAA
TMPRSS-13	84000	D-005973-01	GGACAAGUCUCUGCUUAAA
		D-005973-02	AAACAAACCUGGUGUGUAC
		D-005973-03	GAAUGCAUCUCCAGCAAGA
		D-005973-04	GCCAACAGCUUCUCAAUCU

2.7 Polymerase chain reaction (PCR) primer design

All primers were manually designed using the National Centre for Biotechnology Information (NCBI) primer design tool (https://www.ncbi.nlm.nih.gov/tools/primer-blast/) and specificity was validated using the online Basic Local Alignment Search Tool (BLAST) (https://blast.ncbi.nlm.nih.gov/Blast.cgi). When designing primers, criteria included that primer should span exon-exon junctions to avoid transcription of genomic DNA and that the primer pair should be separated by at least one intron on the corresponding genomic DNA. In addition, guanine-cytosine content in each primer was approximately 50% to regulate primer melting temperature and PCR product size was measured between 90-150 base pairs to ensure an efficient reaction. All primers (Sigma Aldrich) used are detailed in **Table 2.8**.

Table 2.8: Primer details

Primers	Primer Sequence
Calpain-10:	
CAPN-10 – Forward (F)	GGTCTCAGAACCGAGTGAGGT
CAPN-10 – Reverse (R)	CCACGAAGTATGACTGTCACC
Caspase-8:	
CASP-8 – F	TCATGGACCACAGTAACATGGA
CASP-8 – R	AGTGAACTGAGATGTCAGCTCAT
Matrix metalloproteinase-17:	
MMP-17 – F	TGGCAGCTGTACGGTGT
MMP-17 – R	CCGCCAGAAGTACTTGCCTT
Serpin peptidase inhibitor clade F:	
SERPIN-F1 – F	TTCAAGGGGCAGTGGGTAACAAA
SERPIN-F1 – R	TACTCATGCTTCCGGTCAAGG
Transmembrane protease serine 13:	
TMPRSS-13 – F	ATCTCCTGCCAGGTCAGCAC
TMPRSS-13 – R	AACTGGAAGAGGATGATGAGCGA

2.8 RNA extraction & cDNA synthesis

To extract RNA from the HDF cells at the end of each transfection period, cells were first trypsinised, centrifuged, washed with PBS and lysed at 4°C using lysis buffer (RLT buffer) provided with the RNeasy Mini kit (Qiagen, 74104). Total RNA was then extracted according to the manufacturer's protocol and quantified using a NanoDrop 1000 spectrophotometer (ThermoFisher Scientific), resulting HDF RNA was stored at -80°C. Total RNA (0.5-1.0µg) was reverse transcribed according to the manufacturer's protocol in a 20µl reaction volume using QuantiTech Reverse Transcription kit containing random primers (Qiagen, 205311). The resulting cDNA was then diluted 1:40 in RNAase-free water (Sigma, W4502) and stored at -20°C, ready for qPCR.

2.9 Quantitative real-time polymerase chain reaction (qPCR)

qPCR was performed in a 96-well plate format (Applied Biosystems, 4346906). The qPCR was completed in triplicate wells using 20µl total reaction volumes with SYBR Green (Qiagen, 204145), 0.5µM primers and executed using the StepOne Plus system (Applied Biosystems, 4376598). The cycling conditions were; one cycle for 10 minutes at 95°C, 40 cycles for 15 seconds at 95°C, one minute cycle at 60°C, 30 seconds at 72°C and one cycle for 15 seconds at 95°C.

An additional melt curve analysis step was included which ran for one minute at 60°C and 15 seconds at 95°C. At the end of each PCR run, a cycle threshold (Ct) value was generated, which is the number of cycles that were required for the fluorescence signal to cross the threshold/exceed background levels. These values were used for data analysis. Hypoxanthine phosphoribosyltransferase-1 (HPRT-1) housekeeping gene was required to act as an internal control to ensure that the quality and quantity of the cDNA was similar to each of the samples. The $2^{-\Delta Ct}$ equation was used to determine the housekeeping gene produced similar Ct values between vehicle and siRNA treated samples. Data were analysed by normalising the siRNA induced and vehicle induced fibroblasts against the housekeeping gene Ct. Fold changes between only 0.5-1.5 in the siRNA treated samples relative to vehicle were considered appropriate. Fold change = 2^{-}[(siRNA Ct – housekeeping Ct)-(vehicle Ct – housekeeping Ct)]. Summarised by the equation $2^{-\Delta\Delta Ct}$, as described (Livak and Schmittgen, 2001).

2.10 96-well micro-organotypic invasion assays

One of the aims of this project was to develop and optimise a novel 3D organotypic based invasion model which could be integrated into a laboratory automation platform, permitting higher-throughput of samples and would allow industry to perform HTS.

Miniaturisation would obviously have the financial advantages of reducing assay volumes, allowing higher throughput, faster data acquisition time and most importantly, permit automated robotic screening of drugs and genes. However the optimisation presents its own challenges, trials and developments, such as, discovering a suitable plate type, optimising cell numbers and reagent volumes, sourcing an appropriate imaging platform and finally, analysing large amounts of data to deduce valuable conclusions.

2.10.1 Procurement the correct plate type

Corning produce HTS 96-Transwell® insert permeable support plates, covering a series of various pore sizes, ranging from 0.4-8.0µm (Corning, 0.4µm - #3391, 1.0µm - #3392, 3.0µm - #3386, 5.0µm - #3388, 8.0µm - #3384). The product includes; a Transwell® unit (1 integral insert with 96-wells), a reservoir plate and a receiver plate. The 96-well Transwell® insert possess large apical and basolateral access ports for ease of medium exchange. Additionally the receiver plate has oval, rather than circular, shaped wells which are better suited for the addition of reagents or cell culture medium via liquid handling systems. For invasion studies pore sizes of <1.0µm were of interest to our laboratory.

A single free sample plate of Corning #3391 (0.4µm pore size) was requested for optimisation. However the porous membrane material is synthetic polycarbonate, an opaque material, as seen in **Figure 2.2A**, which not suitable for imaging platforms. Furthermore a case of plates (five plates per case) costs £1245.99. During a secondment at AstraZeneca in 2014, I contacted Corning requesting a unique prototype 96-Transwell® insert containing 0.4µm pore size and a PET membrane (transparent material). I received 10 free sample plates to use for development and optimisation of the micro-organotypic invasion assay (**Figure 2.2B**). These membranes are optically clear and suitable for 3D imaging. These plates are now commercially available (Corning, #7369, **Figure 2.2C**), at a cost of £884.61 per case (five plates).

Due to the high cost of the plastic consumables and absence of automated liquid handling systems I also investigated alternative assay formats that would fit the following criteria; (1) affordability to perform screening (e.g. RNAi or compound screens); (2) can be performed manually but also integrated into an automated work flow process using laboratory automation; (3) remain consistent in mimicking the 3D microenvironment as observed with the large and mini-organotypic invasion assay; (4) produce high content phenotypic data for multi parameter analysis; (5) undemanding experimental procedure and reproducibility.

In 2008 Christopher Marshall's group described a 96-well invasion assay whereby, cells of interest were suspended in collagen type I and dispensed into 96-well ViewPlates (Perkin-Elmer) coated with BSA. Plates were then centrifuged and incubated before addition of FBS. After 24 hours of incubation, cells were fixed in formaldehyde and stained with Hoechst before confocal z-slices were collected via an INCELL3000 imager (GE Healthcare). Nuclear staining was quantified to produce an invasion index (Sanz-Moreno et al., 2008).

On the foundation of this assay I have developed a multicellular, live, 3D organotypic invasion assay that recapitulates the microenvironment and does not require the use of Transwell® Inserts. However I also investigated the use of the 96-well Transwell® insert with 0.4µm PET optically clear membranes.

2.10.2 96-well Transwell® insert

Organotypic gel was prepared as described in **Section 2.3.1**. However the collagen: PBS pre-coating step was not performed, due to the difficulties when removing this solution. This step can be performed with great care and precision, nonetheless, without use of liquid handling systems to remove the solution, it is not advised. Even using a manual multichannel pipette risks piercing the membrane.

The plate was placed into a small polystyrene box containing ice. This was to ensure the plastic and the overall plate temperature was as low as possible. Consequently 50µl of organotypic gel mixture was pipetted into each well. The plate was then placed in a pre-chilled (4°C) centrifuge and spun for 45 seconds at 1500rpm, forcing any residual gel attached to the inside wall to the bottom of each well. The plate was swiftly removed from the centrifuge and immediately incubated at 37°C for one hour. During the incubation step cells were labelled with CellTracker™ Red and Green as described in **Section 2.4**. Fibroblast and tumour cells were then counted and plated

on top of the polymerised organotypic gels in a 50µl cell suspension in serum-free medium, either alone (5×10^3), or in a 2:1 co-culture ratio of fibroblast (3.3×10^3) and tumour cells (1.6×10^3). Next, 150µl of serum containing media were added to the 96-well receiver plate. The following day the media below each Transwell® was replaced with 150µl of fresh media. The process of changing medium was carried out every two days, thus maintaining a chemotactic gradient.

A

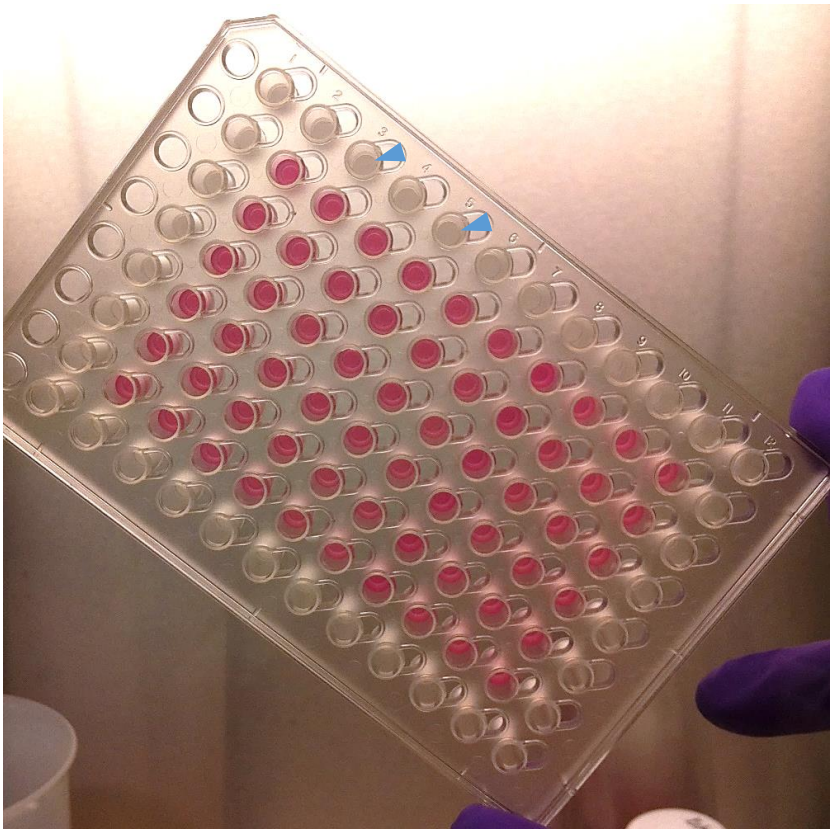

B

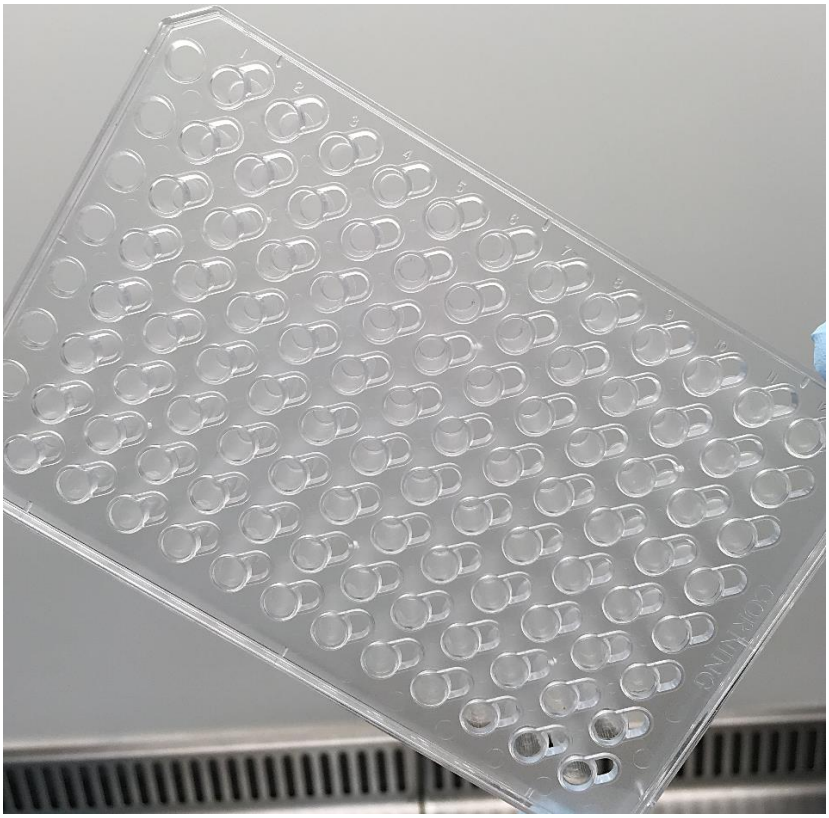

C

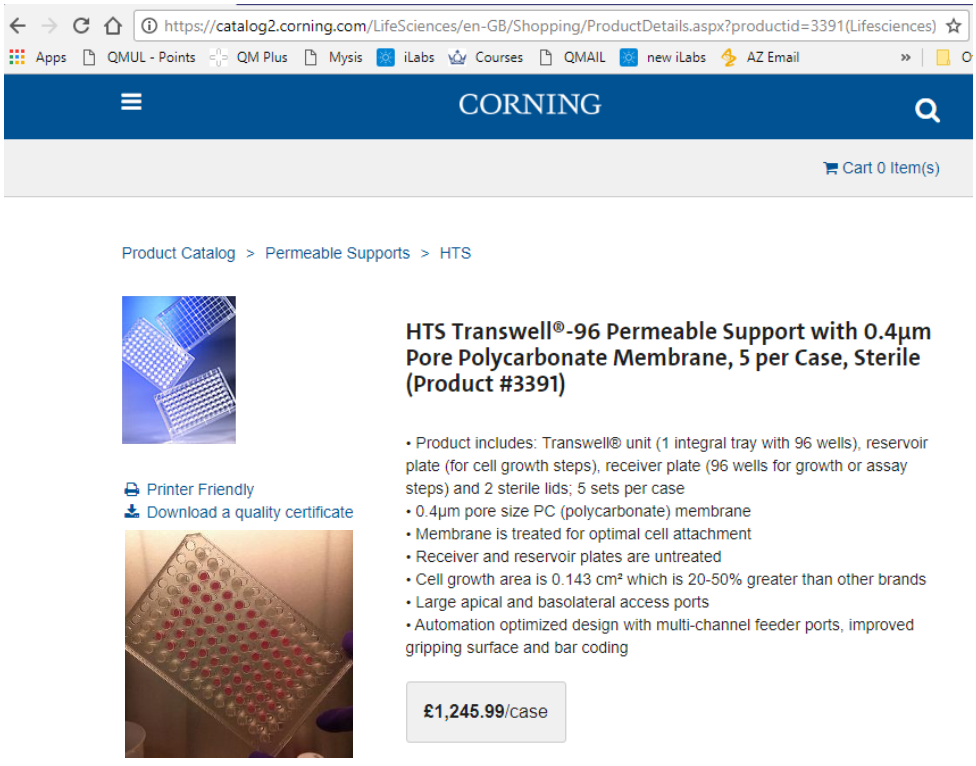
https://catalog2.corning.com/LifeSciences/en-GB/Shopping/ProductDetails.aspx?productid=3391(Lifesciences)
Apps
QMUL - Points
QM Plus
Mysis
iLabs
Courses
QMAIL
new iLabs
AZ Email
CORNING
Cart 0 Item(s)
Product Catalog > Permeable Supports > HTS
HTS Transwell®-96 Permeable Support with 0.4µm Pore Polycarbonate Membrane, 5 per Case, Sterile (Product #3391)
• Product includes: Transwell® unit (1 integral tray with 96 wells), reservoir plate (for cell growth steps), receiver plate (96 wells for growth or assay steps) and 2 sterile lids; 5 sets per case
• 0.4µm pore size PC (polycarbonate) membrane
• Membrane is treated for optimal cell attachment
• Receiver and reservoir plates are untreated
• Cell growth area is 0.143 cm² which is 20-50% greater than other brands
• Large apical and basolateral access ports
• Automation optimized design with multi-channel feeder ports, improved gripping surface and bar coding
Printer Friendly
Download a quality certificate
£1,245.99/case

D

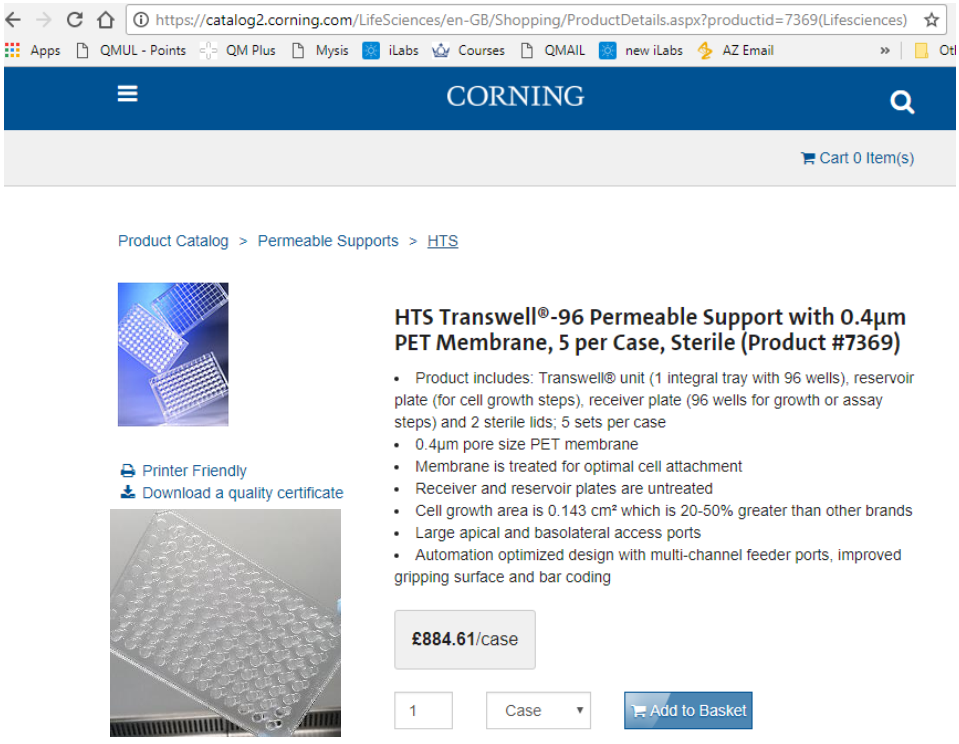
https://catalog2.corning.com/LifeSciences/en-GB/Shopping/ProductDetails.aspx?productid=7369(Lifesciences)
Apps
QMUL - Points
QM Plus
Mysis
iLabs
Courses
QMAIL
new iLabs
AZ Email
CORNING
Cart 0 Item(s)
Product Catalog > Permeable Supports > HTS
HTS Transwell®-96 Permeable Support with 0.4µm PET Membrane, 5 per Case, Sterile (Product #7369)
• Product includes: Transwell® unit (1 integral tray with 96 wells), reservoir plate (for cell growth steps), receiver plate (96 wells for growth or assay steps) and 2 sterile lids; 5 sets per case
• 0.4µm pore size PET membrane
• Membrane is treated for optimal cell attachment
• Receiver and reservoir plates are untreated
• Cell growth area is 0.143 cm² which is 20-50% greater than other brands
• Large apical and basolateral access ports
• Automation optimized design with multi-channel feeder ports, improved gripping surface and bar coding
Printer Friendly
Download a quality certificate
£884.61/case
1
Case
Add to Basket

E

Figure 2.2: 96-Transwell® insert plates produced by Corning

A) Shows the 0.4µm pore size, 96-well Transwell® insert plate with a polycarbonate membrane (Corning #3391). The inner 60 wells contain 40µl of organotypic gel which were manually pipetted into each well. The outer wells are empty and the opaque porous membrane can be recognised. The insert possess large access ports for addition of reagents of media exchange via liquid handling robotics (identified by blue arrows). **B)** Displays the 0.4µm pore size, 96-well Transwell® insert plate with a PET membrane (Corning #7369). The transparent membrane can be seen. **C**-**D)** Screen shot from Corning online website displaying unit price of 1 case of plates (C - #3391 polycarbonate membrane, D - #7369 PET membrane). **E)** 96-well oval shaped receiver plate.

2.10.3 96-well reverse organotypic invasion assay

Following a similar method as described by Sanz-Moreno and colleagues, I devised a method whereby fluorescently labelled cells were embedded within the collagen: Matrigel® mixture and then forced to the bottom of the plate by centrifugal force.

A sterile black 96-well glass bottom microplate (Greiner Bio-One, 655892) was placed on ice to ensure the surface of the plate was kept cold. Organotypic gel was prepared as described previously in **Section 2.3.1**, with the exception of omitting the 10% cell culture media. The mixture was divided into the appropriate aliquots for each corresponding condition (i.e. fibroblast cells alone, cancer cells alone and fibroblast: cancer cells co-culture). Fluorescently labelled fibroblast and cancer cells were counted, re-suspended in growth medium and added to each condition aliquot in place of the absent 10% cell culture volume. Cell numbers per well were, 7.5×10^3 cells if plated alone, or if plated as a 2:1 co-culture, 5.0×10^3 fibroblasts and 2.5×10^3 cancer cells. The organotypic gel was gently mixed, avoiding development of bubbles to produce a homogenous cell suspension. 50ul of the organotypic gel containing cells was added to each well.

The plate was then placed in a pre-chilled (4°C) centrifuge and spun for three minutes at 1500rpm, forcing the cells to the bottom of the gel. The plate was removed from the centrifuge and immediately incubated at 37°C for one hour. After polymerisation of the gel, the plate was viewed under a light microscope and cells were observed at the bottom of each well. Subsequently 100µl of serum-containing media were added on top of the gel, thus creating a chemotactic gradient to drive invasion upwards. Media were exchanged manually every second day. 10µl of sterile polystyrene microsphere blue fluorescent beads (10µm diameter) (ThermoFisher Scientific, F8829) were added to each well before imaging via confocal microscopy to determine the top surface of the gel.

During these initial experiments, fibroblast and cancer cells did not appear to invade upwards through the organotypic gel. When viewed under a light microscope 48 hours after plating, cells remained at the bottom of the plate, adhered and spread on to the glass substrate. After further investigation, the assay plate was changed to a sterile, black 96-well ultra-clear (µClear®) non-binding microplate (Greiner Bio-One, 655906). The non-binding surface from Greiner are achieved through stable chemical modification. The surface substrate forms a hydrostatic layer preventing binding to

the microplate, thus, cells can no longer adhere, forcing them to settle in the organotypic gel.

2.11 Generation of stably transduced fluorescent cell lines using lentiviral particles

2.11.1 Lentiviral particle production

Use of CellTracker™ dyes permits any cells to be used in organotypic gels, however once inside the cell, the cell permeant dyes are modified into cell-impermeant reaction products. Thus although the dye does not leak out of the cells, each proliferation cycle halves the fluorescence intensity per cell. Also I noted that by 72 hours, the distribution of the dye was not uniformly distributed within individual cells.

To establish cells with a more stable and uniform fluorescence I employed a lentivirus expression systems. The lentivirus transduction system is based on the human immunodeficiency virus (HIV) and utilises a packing, vehicle and vector plasmid (Dull et al., 1998). The plasmids are combined and simultaneously transfected into virus-producing cells (human embryonic kidney 293T (HEK293T)), that in turn generate and release an abundance of viral particles into the cell culture medium. The medium is then collected and used to infect the desired cell lines.

2.11.1.1 Production of lentiviral particles encoding: histone H2B-GFP

HEK293T cells were plated into a 6-well plate (10^5 cells/well) and grown to 80% confluency. Prior to viral transfection cell culture medium was replaced with fresh DMEM supplemented with 10% FBS. Packaging plasmids pMD2.G (1.75µg, Addgene, #12259) and pCMVR8.74 (3.25µg, Addgene, #22036) with pLV-H2B-GFP vector (5.0ug, Addgene, #11680) was added with 30µl FuGENE HD (Promega, E2311) transfection reagent. The lentiviral construct was added to Opti-MEM (ThermoFisher Scientific, 31985070) and incubated at room temperature for 20 minutes. The resulting complex was carefully added dropwise to the HEK293T cells and incubated at 37°C in a 5% CO_2 incubator. After 48 hours, the resulting viral containing cell culture medium was collected, centrifuged at 2000rpm for five minutes to remove cellular debris, divided into 1ml aliquots and stored at -80°C until required.

2.11.1.2 Lentiviral particle production: histone H2B-RFP

The same procedure as described above using the vector pLV-H2B-RFP (5.0ug, Addgene, #26001) was used.

2.11.1.3 Lentiviral particle production: enhanced green fluorescent protein (EGFP)

The same procedure as described in **Section 2.11.1.1** using the vector PL-SIN-PGK-EiP EGFP (5.0ug, Addgene, #21312) was used.

Both packaging plasmids and the EGFP vector were kindly donated by Yasmine Tanner & Dr Ed Carter (Grose group, Department of Tumour Biology, Barts Cancer Institute). The H2B-GFP and -RFP vectors were kindly donated by Dr Pedro Monteiro (Godinho group, Department of Molecular Oncology, Barts Cancer Institute).

2.12 Fluorescence activated cell sorting (FACS)

VB6 cells infected with H2B-RFP and HDF cells infected with H2B-GFP were trypsinised and collected into 15ml Falcon™ tubes before centrifugation at 1200rpm for three minutes. Medium containing trypsin was carefully removed not disturbing the cell pellet and replaced with 10ml of sterile serum-free DMEM. Prior to cell sorting using BD FACSAria™ II (BD Bioscience, USA) 1ml of the cell suspension was placed into a 5ml round bottom polystyrene test tube (Corning, #352235). Cells were gated based on forward scatter (FSC) and side scatter (SCC) to exclude debris and a second gate was set to exclude doublets on a dot plot of pulse area (FSC-A) versus height (FSC-H). H2B-RFP was detected using a yellow laser at 610nm bandpass filter and H2B-GFP was detected using a blue laser at 525nm bandpass filter.

2.13 Statistical analysis

All quantitative statistics were performed using Prism 5 (Graphpad, USA) software, unless otherwise stated. Descriptive statistics are presented as a mean or median ± standard deviation (s.d). Comparisons between two samples used Students t-tests whereas comparison of more than two samples used one-way analysis of variance (ANOVA).

CHAPTER III: RESULTS PART I

DEVELOPMENT OF A FLUORESCENT MINI-ORGANOTYPIC INVASION ASSAY

3.0 Development of a fluorescent mini-organotypic invasion assay

3.1 Background

A vast amount of evidence suggests that cellular cues, functions, homeostasis, invasion, migration, phenotype, shape, structural complexity and protein and gene expression may all be modified within 3D spatial architecture (Baker and Chen, 2012; Brock et al., 2003; Chen et al., 2013; Chen et al., 1997; Hess et al., 2010; Lee et al., 2007; Moutasim et al., 2011; Nyga et al., 2011; Petersen et al., 1992; Thomas et al., 2001c; von der Mark et al., 1977). Thus, it would seem imperative that we design assays that allow analysis of cell biology within relevant 3D environments. In this chapter I will describe the optimisation steps that were undertaken in order to achieve an elegant, robust, yet reproducible and quantifiable 3D mini-organotypic invasion assay that could be analysed *in situ* by measuring cell fluorescence. The steps included; (1) fluorescently-labelling cells to be used in the assay; (2) identifying and optimising a suitable imaging platform; (3) optimising the length of the assay time; (4) accumulating multi-parameter 3D phenotypic data from the mini-organotypic gels; (5) image processing and data analysis of the 3D images.

3.2 Optimising CellTracker™ labelling using IncuCyte™ ZOOM®

To develop the fluorescent mini-organotypic invasion assay, I chose the VB6 OSCC cell line that had been previously studied in mini-organotypic gels (Nystrom et al., 2005) and used HDF's as tissue-matched fibroblasts. I sought to develop an assay that could be executed by most modern cell and molecular biology research laboratories using their own cells. Thus initially, rather than using genetically-labelled fluorescent cells I chose to use membrane permeable fluorescent dyes.

To determine how long VB6 and HDF cells had to be exposed to the dyes to achieve maximal fluorescence, the cells were labelled *in vitro* with fluorescent CellTracker™ Red and Green dyes, respectively (detailed in **Section 2.4**). Briefly, DMSO was added to CellTracker™ Red and Green dyes (50µg aliquots), producing a stock concentration of 5mM and 10mM respectively. CellTracker™ Red and Green were diluted 1:1000 in serum-free medium producing 5µM and 10µM solutions respectively. Subsequently, VB6 and HDF culture media were replaced with CellTracker™-treated serum-free medium. The flasks containing CellTracker™-treated cells were placed into an IncuCyte™ ZOOM® system, where the microscope obtained 2D fluorescent images every four minutes over a period of 44 minutes. At the end of the experiment the images were analysed using the IncuCyte™ ZOOM® Analyser 2015A and were data plotted as a function of average object intensity against time (**Figure 3.1** and **Figure 3.2**). This experiment was conducted during a secondment at AstraZeneca (Alderley Park, UK).

Figure 3.1A and **Figure 3.2A** display overlapping phase contrast and fluorescence images of VB6 and HDF cells treated with CellTracker™ Red and Green respectively. **Figure 3.1B** and **Figure 3.2B** display the average object intensity over a 44 minute period. VB6 cells appear to internalise around eight minutes and fluorescence intensity continues to increase steadily during the 44 minute period. However, HDF cell internalisation is initially slower and then rapidly increases almost three-fold between 16-20 minutes. Both cell types appear vibrantly labelled and healthy after 44 minutes.

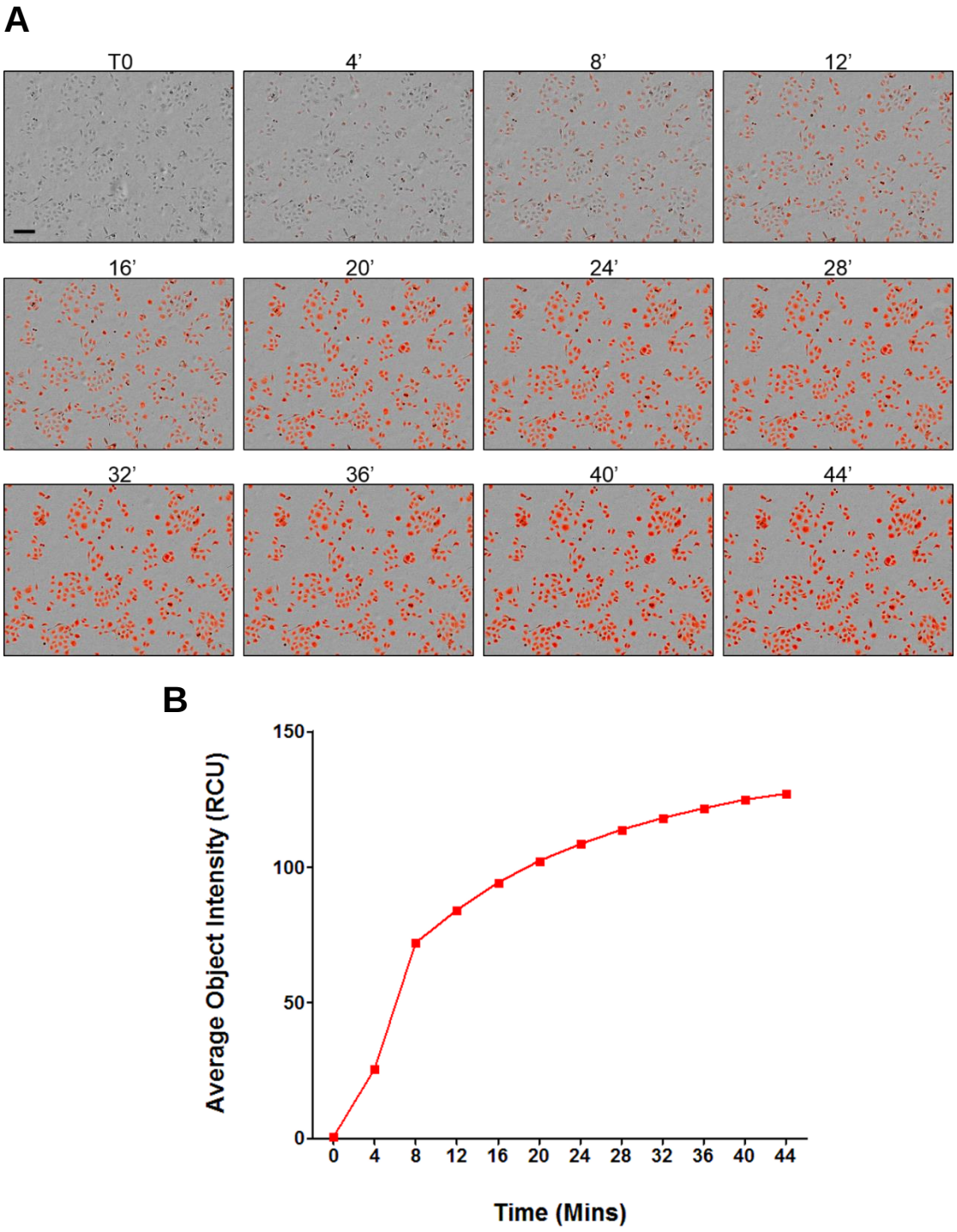

Figure 3.1: Fluorescence internalisation and average object intensity data from IncuCyte™ ZOOM® – VB6 cancer cells

The figure displays CellTracker™ Red internalisation within VB6 cancer cells. **A)** Displays overlapping phase contrast and red fluorescence time lapse images of VB6 cells exposed to the red dye over a period of 44 minutes. **B)** Displays the average object intensity over time (red calibrated units (RCU)). Scale bar 100µm, 4x objective. One set of representative images and data from three independent experiments.

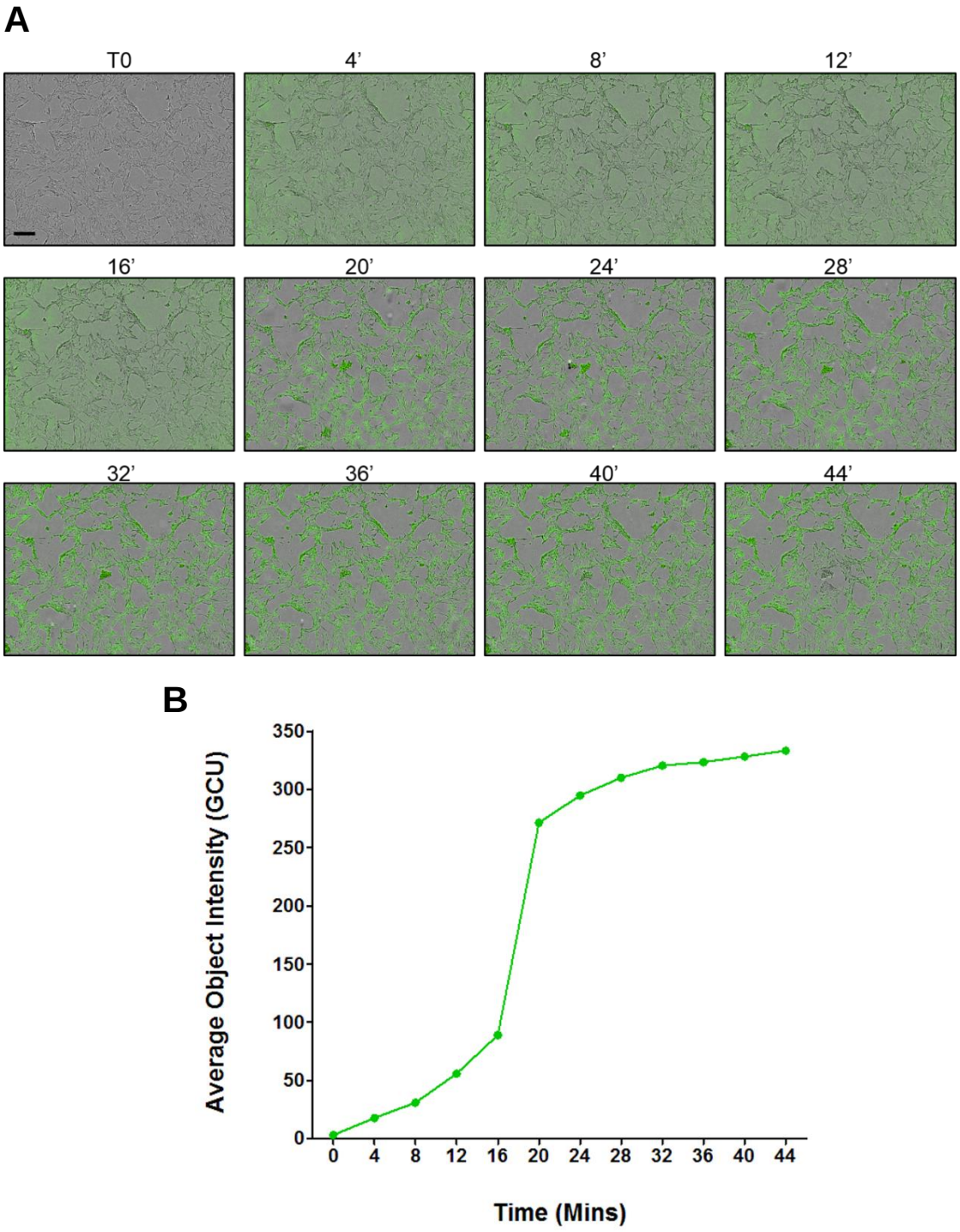

Figure 3.2: Fluorescence internalisation and average object intensity data from IncuCyte™ ZOOM® – HDF cells

The figure displays CellTracker™ Green internalisation within HDF cells. **A)** Displays overlapping phase contrast and green fluorescence time lapse images of HDF cells exposed to the green dye over a period of 44 minutes. **B)** Displays the average object intensity over time (green calibrated units (GCU)). Scale bar 100µm, 4x objective. One set of representative images and data from three independent experiments.

3.2.1 Fluorescently labelled VB6 & HDF cells

VB6 and HDF cells were labelled with fluorescent CellTracker™ Red and Green dyes respectively and observed by confocal microscopy to confirm fluorescence internalisation (**Figure 3.3**). **Figure 3.3A** shows rounded red (VB6) and green (HDF) cells after 15 minutes incubation with fluorescent dyes at 37°C (T0). **Figure 3.3B** shows VB6 and HDF cells 24 hours after exposure to fluorescent dyes (T24). Both cell types have adhered and spread out on to the glass substrate and exhibit whole cell fluorescent at a high intensity. After a period of four days the fluorescence intensity had vastly reduced as result of cell proliferation.

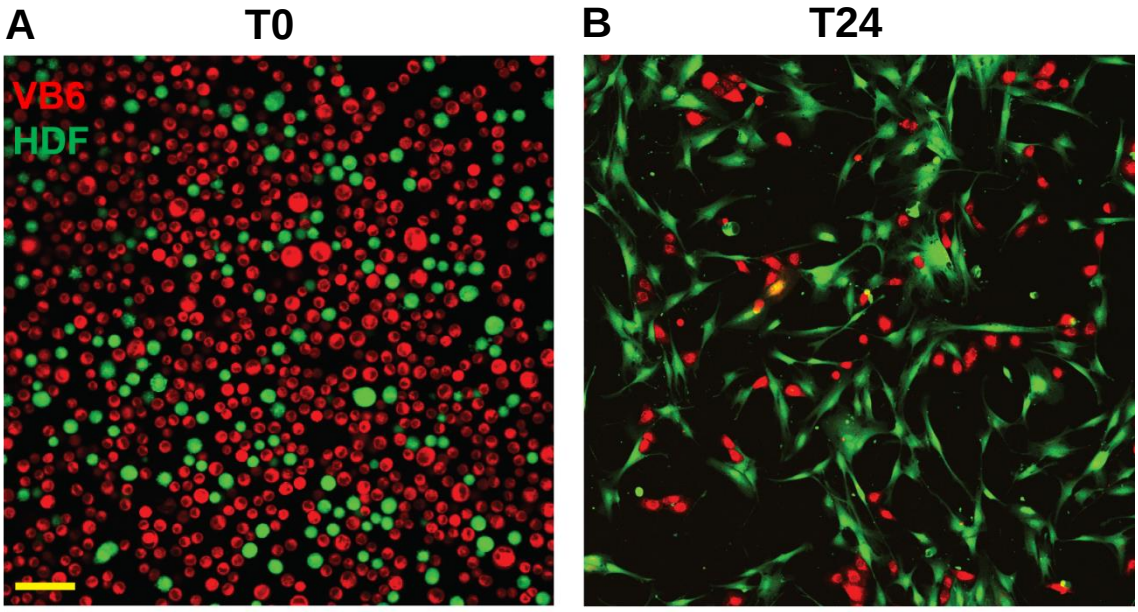

Figure 3.3: Fluorescently labelled VB6 & HDF cells

VB6 and HDF cells were labelled with CellTracker™ Red (5µM) and CellTracker™ Green (10µM), respectively, for 45 minutes at 37°C. After labelling, cells were washed with PBS then mixed in a 2:1 ratio of tumour to fibroblasts (10^5 cell/ml) and co-cultured into a MatTek 35mm-diameter glass coverslip-bottomed petri dish. The MatTek dish was imaged at two time points using a CLSM 710 microscope. **A)** Time point 0 (T0) shows high intensity internalisation of fluorescent dyes into both cell types imaged 15 minutes post labelling. **B)** T24 shows appearance of cells 24 hours after plating. Both cell types exhibit whole cell fluorescence and have adhered and spread out on to the glass substrate. Scale bar 50µm, 10x objective. One set of representative images from one experiment.

3.3 Confocal laser scanning microscopy of mini-organotypic gels: preliminary studies

To obtain high resolution images from these experiments I chose confocal laser scanning microscopy. The term 'Confocal' is described as having one focus point, directed at a small spot on the specimen, thus giving greater resolution. In confocal microscopy this is achieved by the introduction of an adjustable pinhole that functions as a versatile iris placed between the specimen and the detector. The function of the pinhole is to reject out of focus light and select information from a single focal plane, producing a sharply focussed optical slice through the specimen.

However if the pinhole size is significantly reduced, so too are the number of photons arriving at the detector from the specimen (Denis Semwogerere, 2005). This is achieved by excluding as much external light away from the specimen as possible thus improving contrast and reducing haze. Obtaining true confocality and high optical resolution for samples using CLSM, the following must be considered; (1) the numerical aperture of the optical system; (2) the wavelength of light used to detect the image; (3) selecting the optimum diameter for the pinhole.

In situ *z*-stacks were acquired using the Zeiss CLSM 710 system. The mini-organotypic gels that were created in optically-clear Transwells® were removed from their 24-well source plate and placed onto a MatTek glass coverslip-bottomed 35mm-diameter dish. The dish was transferred to the microscopes heated (37°C), gassed (5% CO_2) and humidity-controlled chamber. A series of *x*-*y*-*z* images of 700µm square (in *x*-*y* plane) were collected along the *z*-axis at 4µm intervals with a 1µm overlap to approximately 1400µm depths throughout the mini-organotypic gel. This required the use of a Zeiss long working distance 20x objective (LWD 20x). Fluorescence images were generated using 568nm excitation line and 602nm emission for detection of CellTracker™ Red and 488nm excitation line and 517nm emission for detection of CellTracker™ Green.

3.3.1 Fluorescently labelled VB6 cancer cells in mini-organotypic gels imaged at 24, 48 & 72 hour time points

To investigate whether VB6 cells invade through mini-organotypic gels, the cells were labelled with CellTracker™ Red (5μM) and plated alone on top of mini-organotypic gels (10^5 cells total). 24 hours post plating, KGM medium underneath each Transwell® was exchanged and excess medium from the surface of the gel was carefully removed leaving the gels exposed for the remainder of the assay.

3D *z*-stack images were obtained over a period of 72 hours via CLSM **(Figure 3.4**). The solid red square (700μm x 700μm in the *x-y* plane) seen in the images represents the PET membrane at the bottom of the Transwell®, which auto-fluoresces red. VB6 cancer cells appear attached and evenly spread on the surface of the gel forming layers. Over the course of 72 hours, the cells do not appear to invade through the gel, the gel appeared to maintain integrity and composition, however the gel does appear to shrink vertically over time. This is possibly due to evaporation within the incubator as the top of the gel was exposed (not protected by a serum-free medium layer).

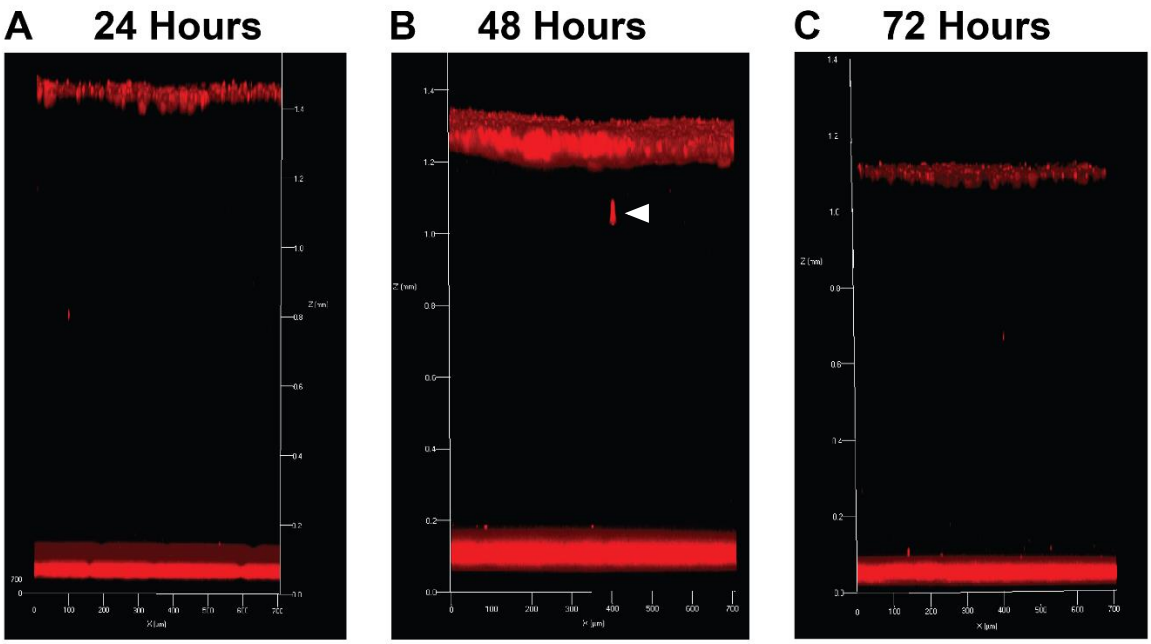

Figure 3.4: Fluorescently labelled VB6 cancer cells in mini-organotypic gels imaged at 24, 48 & 72 hour time points

The above images display VB6 cancer cells labelled with CellTracker™ Red (5µM) and plated on top of mini-organotypic gels. The same Transwell® was imaged every 24 hours for a total period of 72 hours. Live 3D *z*-stack images were achieved via confocal microscopy. **A)** 24 hours post plating; VB6 cells adhere and spread on to the surface of the mini-organotypic gel. Gel thickness approximately 1400µm. **B)** 48 hours post plating; VB6 cell layer appears to be denser, no definitive signs of invasion, however a cluster of cells or single cell appears to have progressed away from the main keratinocyte layer (indicated by white arrow). To confirm whether this is in fact a cell or an artefact within the gel, image analysis and image rendering was performed. Gel thickness contracts to approximately 1200µm. **C)** 72 hours post plating; VB6 cells show no evident signs of invasion through mini-organotypic gels. Level of fluorescence intensity appears to be reduced compared with that of the 24 and 48 hour time point. Gel thickness further contracts to approximately 1100µm. One representative image for each time point from triplicate gels belonging to one of three independent experiments.

3.3.2 Fluorescently labelled HDF cells in mini-organotypic gels imaged at 24, 48 & 72 hour time points

To examine the behaviour of HDF cells in mini-organotypic gels, HDF cells were labelled with CellTracker™ Green (10μM) and plated alone on top of mini-organotypic gels (10^5 cells total). 24 hours post plating, fibroblast growth medium underneath each Transwell® was exchanged with fresh serum-containing media and excess medium from the surface of the gel was carefully removed and replaced by serum-free medium. 3D *z*-stack images were obtained over a period of 72 hours (**Figure 3.5**). Interestingly, after 24 hours (**Figure 3.5A**), HDF cells appear to become polarised, change their morphology and orientation (compared with the 2D observations seen in **Figure 3.3B**). Additionally, at the 24 hour time point the mini-organotypic gel has contracted considerably compared to that of **Figure 3.4A** (reduced from a height of approximately 1400μm to 600μm). After 48 hours a population of HDF cells have invaded deeper further through the gel which is now approximately 500μm thick. At the 72 hour time point the HDF cells within the gel have reached the bottom of the Transwell®, which has now contracted to a height of approximately 400μm.

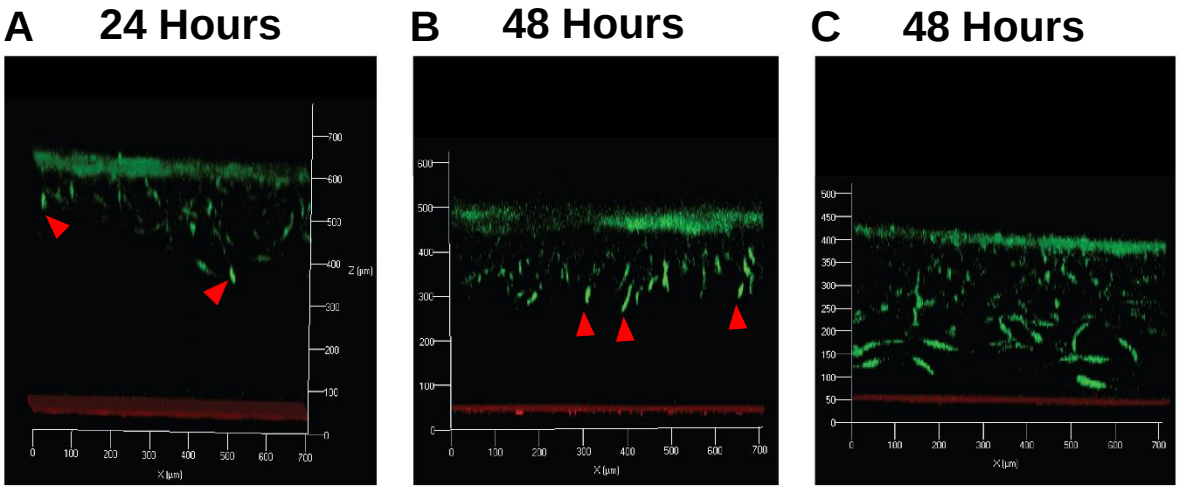

Figure 3.5: Fluorescently labelled HDF cells in mini-organotypic gels imaged at 24, 48 & 72 hour time points

The above images display HDF cells labelled with CellTracker™ Green (10µM) and plated on top of mini-organotypic gels. The same Transwell® was imaged every 24 hours for a total period of 72 hours. **A)** After 24 hours post plating, HDF cells become polarised and invade vertically through the mini-organotypic gel (indicated by red arrows), consequently instigating drastic gel shrinkage. Gel thickness ca. 600µm. **B)** 48 hours post plating, HDF cells invade further through the mini-organotypic gel. Gel thickness contacts to approximately 500µm. **C)** 72 hours post plating, HDF cells invade the entirety of the mini-organotypic gel. Gel thickness further contracts to approximately 400µm. Furthermore, there does not seem to be any significant increase in the total number of fibroblast cells. One representative image for each time point from triplicate gels belonging to one of three independent experiments.

3.3.3 Fluorescently labelled HDF & VB6 cancer cells in mini-organotypic gels imaged at 24, 48 & 72 hour time points

To examine the effects of fibroblast and cancer cell invasion simultaneously, HDF and VB6 cells were fluorescently labelled with CellTracker™ Green (10μM) and Red (5μM) and admixed in a 2:1 ratio of fibroblast (6.7×10^4 cells) to tumour (3.3×10^4 cells) and plated on top of mini-organotypic gels (**Figure 3.6**). This ratio was chosen because in previous work performed by our laboratory this gave the maximal invasion (data not shown). 24 hours post plating, growth medium underneath each Transwell® was replaced with fresh media and excess medium from the surface of the gel was carefully removed leaving the gels exposed.

3D *z*-stack images displayed enhanced cell invasion patterns and striking gel contraction. It is likely that the fibroblasts remodel the collagen: Matrigel® substrate by secreting enzymes that destroy matrix proteins. Thus invading into the gel, forcing their way down towards the chemoattractant. Closely behind, a mass of cancer cells appears to pursue the fibroblast trail. **Figure 3.4**, **Figure 3.5** and **Figure 3.6** are product of the Zen 2009 Software 3D Compiler Tool (Carl Zeiss, Germany), images were saved as tagged image file format (.tiff) files.

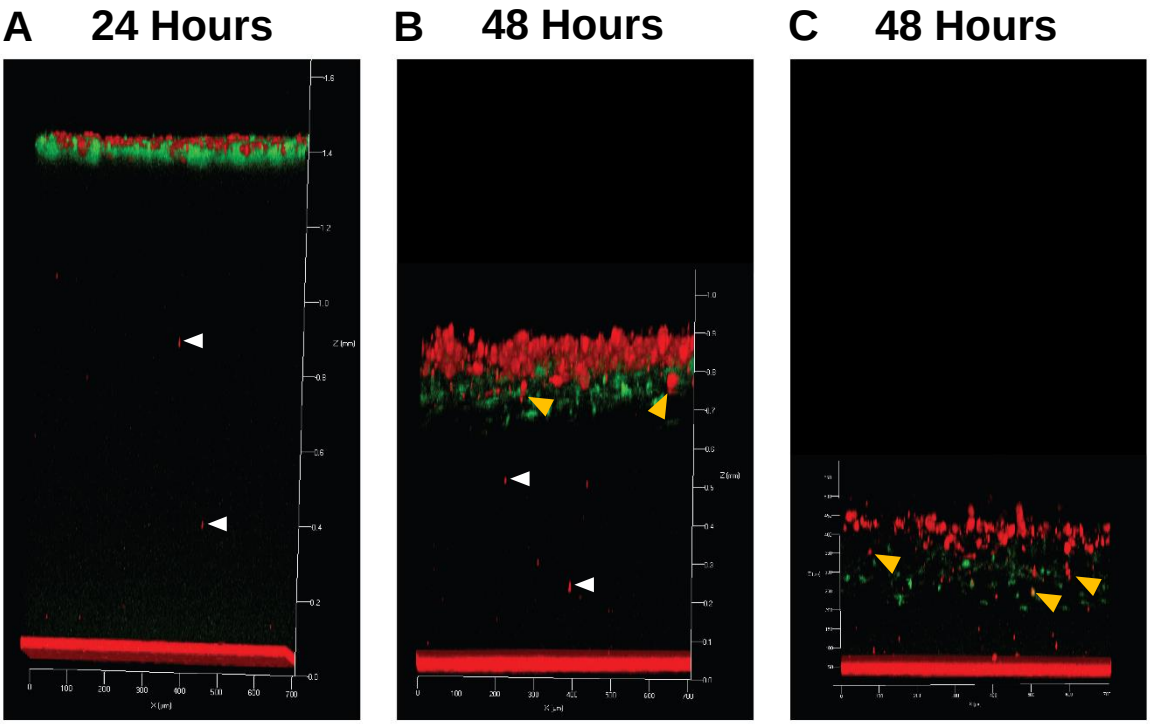

Figure 3.6: Fluorescently labelled VB6 cancer and HDF cells in mini-organotypic gels imaged at 24, 48 & 72 hour time points

The above images display HDF and VB6 cancer cells labelled with CellTracker™ Green (10µM) and Red (5µM) respectively and plated on top of mini-organotypic gel. The same Transwell® was imaged every 24 hours for a total period of 72 hours**. A)** After 24 hours post plating, HDF and VB6 cells form multi-cell layers on top of the mini-organotypic gel. Gel height is approximately 1400µm. HDF and VB6 cells do not appear to invade, however what appear to be single cells or artefacts within the gel are observed (indicated by white arrows). **B)** 48 hours post plating, it is clear that both the VB6 cells and the HDF cells have polarised. A population of HDF cells appear to have invaded further in to the gel than the VB6 cells. The HDF cells probably remodel the mini-organotypic gel, creating channels, though which the VB6 cells follow closely behind (indicated by yellow arrow). HDFs appear to be the primary invading cell type, however what appear to be single cells or artefacts within the gel are observed (indicated by white arrows) and will be identified via image analysis. Gel contracts to approximately 800µm. **C)** 72 hours post plating, HDF cells continue to invade ahead of the VB6 cells, followed by an increased population of VB6 cells (indicated by yellow arrows). Gel further contracts to approximately 400µm. One representative image for each time point from triplicate gels belonging to one of three independent experiments.

3.4 Image analysis & construction of 3D volumes from raw data

In order to analyse the 3D *z*-stack results it was necessary to find; (1) a suitable software that could handle 3D data; (2) a software that would accept .lsm files; (3) a commercially available and affordable program; (4) a software that was uncomplicated, easily operated and user friendly. I discussed using Definiens with their technical sales representatives (Definiens AG, Germany), however, the costs were prohibitive (totalling over £14,000 for the base software, annual licence and a custom made CPU workstation), moreover, 3D image analysis modules would have been an additional cost. As discussed below, I eventually chose the image analysis software Imaris (Bitplane AG, Switzerland) on account of its ease of use and moderately priced software (£10,000).

Confocal imaging accumulates distortion and image quality is therefore directly affected by signal-to-noise background; consequently raw data files were rendered and smoothened using Imaris 8.2 image analysis software (basic software, Bitplane AG). Imaris is a modular software tool purposely suited for multi-dimensional data from the confocal imaging variety, regardless of the method used for image capturing. The software provides a variety of modules to inspect the 3D arrangement of various cell types and other components native to tissue. Multiple spots, surfaces and volumes can be segmented and rendered to customised specifications set by the user.

Sections were acquired at different *z*-positions and assembled into a 3D volume of data. Each pixel from the 2D section becomes a voxel (a 3D pixel) and computer aided 3D reconstruction of the gels enables visualisation of the fluorescently labelled cells throughout each of the individual focal planes.

3.4.1 Quantification of 3D volumes

In order to validate and quantify 3D cell distribution, I purchased an additional module called Imaris XTensions (XT) (Bitplane AG, Switzerland). This module is a programmable interface that contains a package of add-on plug-ins that enable quantitative analysis data from 3D volumes. Imaris XT is interfaced with MatLab® (Matrix Laboratory, MathWorks Inc, USA) and uses custom algorithms for image processing and segmentation. This permits the 3D measurement of cells without a

pre-defined shape or with inconsistent fluorescent components. Imaris XT segments objects and generates data for every single particle within the obtained field of view (defined by user).

Data for individual cells or cell clusters were exported as .csv files into Microsoft Excel for further quantification. The organotypic specimens (typically a volume of 700µm x 700µm x 1400µm) were examined regarding number of projections, fluorescence intensity and position via Distance Transformation measurements. Data were exported into Microsoft Excel software and processed using Prism 5. The *z*-position of each fluorescent particle within the gels, in relation to the bottom membrane of the Transwells® was extrapolated and plotted. Creating a 'bee swarm' plot displaying the collective invasive depth of the each cell population within the 3D field of view.

3.5 Imaris image analysis at 24, 48 & 72 hour time points

Mini-organotypic gels containing fluorescently labelled red VB6 cells alone, green HDF cells alone and HDF: VB6 co-cultures were observed over a 72 hour time period. Confocal *z*-stack images were acquired at 24, 48 and 72-hour time points post seeding from the same Transwell®. The raw .lsm data files were processed and rendered using Imaris XT image analysis software (**Figure 3.7A-C**, **Figure 3.8A-C** and **Figure 3.9A-C**).

A pre-written MatLab® algorithm within Imaris XT called 'Distance Transformation' allows the quantification of distances between objects in different channels. This is performed by the creation of a new channel measuring distances from the centre of spots to the edge of additional volumes within the field of interest. The invasive depth data were collect and plotted in Prism (**Figure 3.7D**, **Figure 3.8D** and **Figure 3.9D**). Mini-organotypic gels were fixed in formalin and processed to paraffin before sections were stained with H&E (**Figure 3.7E-G**, **Figure 3.8E-G** and **Figure 3.9E-G**).

3.5.1 Construction of 3D volumes and distance quantification: VB6 cancer cells alone at 24, 48 & 72 hour time points

VB6 cells were labelled with CellTracker™ Red (5μM), plated alone on top of mini-organotypic gels and imaged every 24 hours for three days via CLSM 710, producing *z*-stack volumes (**Figure 3.4**). Using Imaris XT image analysis software a rendered, smoothened 3D representation of the raw .lsm confocal *z*-stack was generated for the 24, 48 and 72-hour time points (**Figure 3.7A-C**). Distance Transformation analysis was performed on the rendered 3D volumes producing .csv data files. Graphical plots of invasive depth were generated in Prism using data extrapolated from the .csv files (**Figure 3.7D**). Mini-organotypic gels containing VB6 cells were fixed in formalin and processed to paraffin before sections were stained with H&E (**Figure 3.7E-G**).

After 24 hours the VB6 cells appear adhered and homogeneously spread on to the surface of the gel. At the 72 hour time point the VB6 cells do not exhibit signs of invasion into the collagen: Matrigel® substrate. **Figure 3.7D** shows a graphical bee swarm plot displaying distance away from the PET membrane in micrometres (*y*-axis) against time in hours (*x*-axis).

The *z*-positions of each particle (in this case a cell) were generated in relation to their distance away from the red porous PET membrane at the bottom of the Transwell® (Position 0). The graph suggests that after 72 hours VB6 cells are invading through

the gel towards the bottom of the Transwell®, however this does not appear to be the circumstance when observing the images in **Figure 3.7A-C.** The reduction in gel height from approximately 1400µm at the 24 hour time point, to 1100µm by the 72 hour time point, may possibly be due to evaporation. As the surface of the gel was left exposed, evaporation during incubation may be a result of gel contraction. The VB6 cells maintain a tightly packed layer arranged within a proximity of <100µm of each other. To confirm the data obtained by fluorescence *in situ* imaging at each time point, a gel from each time point was fixed and stained with H&E. The image in **Figure 3.7E-G** show the VB6 cells growing on the surface of the gel. At 72 hours the cells look less healthy than at the earlier time points, possibly due to desiccation. For similar reasons evaporation of the gels during incubation is highly likely to be responsible for the change in gel height.

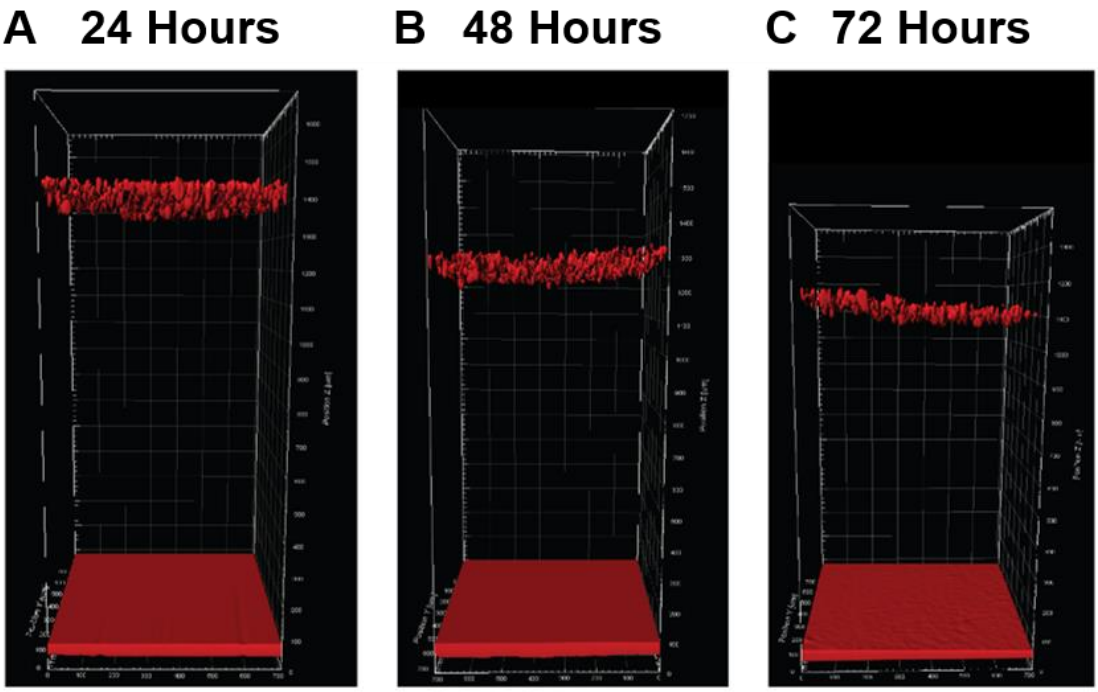
A 24 Hours
B 48 Hours
C 72 Hours

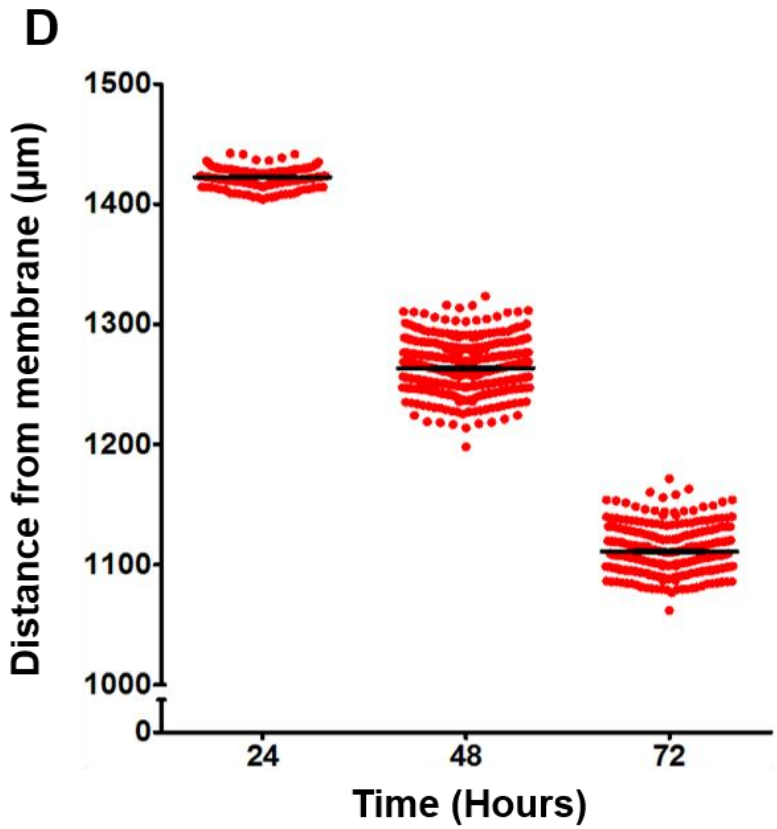
D
Distance from membrane (µm)
1500
1400
1300
1200
1100
1000
0
24
48
72
Time (Hours)

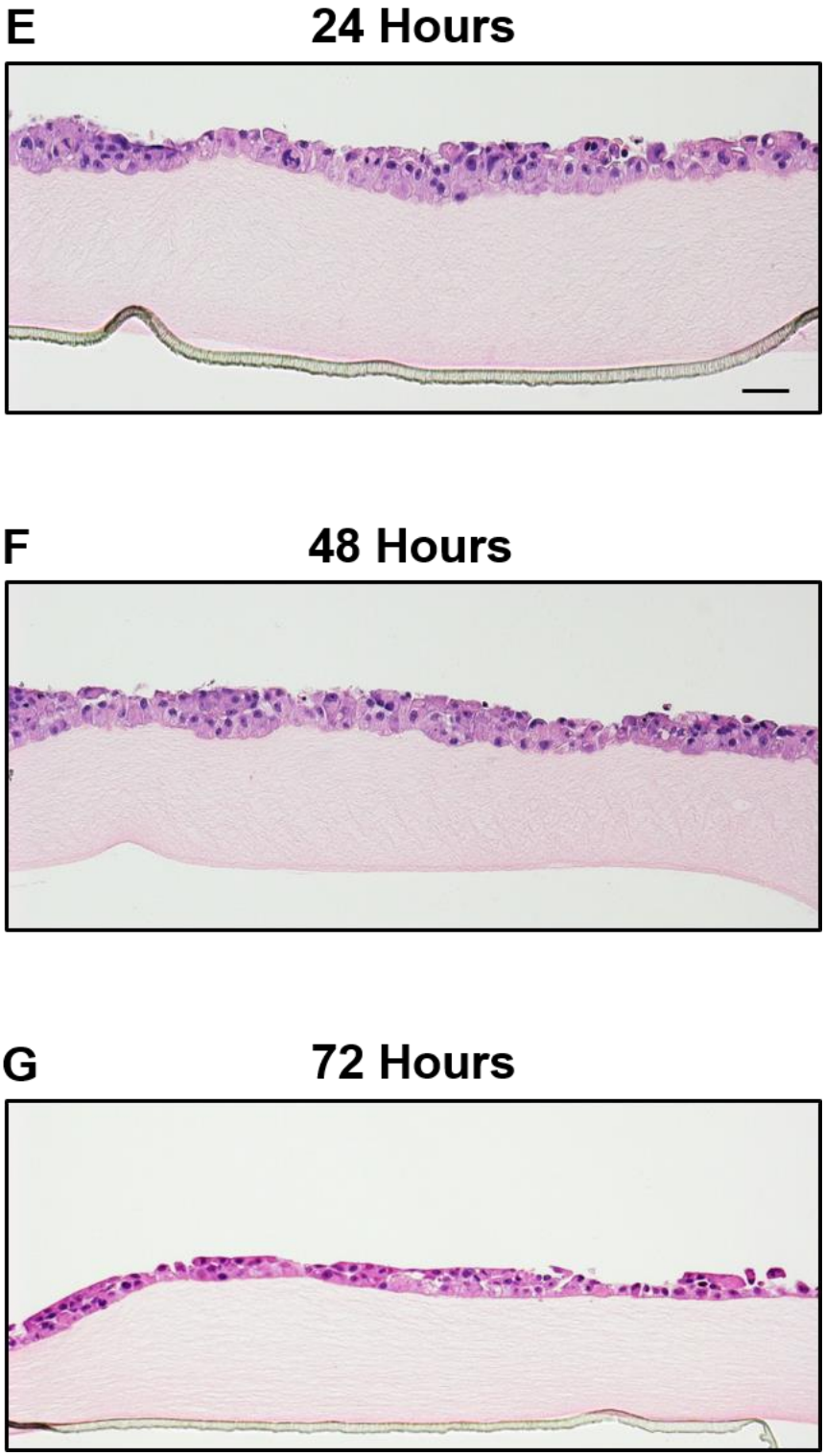

Figure 3.7: 3D rendered and quantified z-stacks of fluorescently labelled VB6 cancer cells plated alone on top of mini-organotypic gels with H&E stained sections

Figure 3.7; 3D rendered and quantified z-stacks of fluorescently labelled VB6 cancer cells plated alone on top of mini-organotypic gels with H&E stained sections

The figure displays Imaris XT rendered and analysed mini-organotypic gels plated with CellTracker™ Red labelled VB6 cancer cells (5µM). Samples were fixed in formalin, processed to paraffin and H&E stained were sections obtained. The confocal microscope *z*-stacks data files were segmented, rendered and analysed by Imaris XT. Images were rendered using a surface segmentation tool that accurately detects particles of specific diameters and intensity. Distance Transformation calculations were performed via Imaris XT and plotted in Prism. **A, B, C)** 24, 48 and 72 hour time point rendered images. VB6 cells appear vibrant with colour and are easily identifiable. VB6 cells do not invade throughout the mini-organotypic gel over a 72 hour period. However the average height of the gels reduces. This contraction is probably due to evaporation during incubation. Serum-free medium was not placed above each gel when incubated, thus exposing the upper surface of the gels. **D)** Graphical depiction of individual VB6 cells *z*-position in relation to the PET membrane (position 0). Each red dot represents one cell within the 700µm square field of view. The cells stack tightly together and on top of each other in a layer that is <100µm in depth. **E-G)** H&E stained sections of VB6 cells plated on top of mini-organotypic gels and harvested at 24, 48 and 72 hour time points. Scale bar: 100µm. One representative image for each time point from triplicate gels belonging to one of three independent experiments.

3.5.2 Construction of 3D volumes and distance quantification: HDF cells alone at 24, 48 & 72 hour time points

HDF cells were labelled with CellTracker™ Green (10μM), plated alone on top of mini-organotypic gels and imaged every 24 hours for three days via CLSM 710, producing *z*-stack volumes (**Figure 3.5**). Using Imaris XT image analysis software a rendered, smoothened 3D representation of the raw .lsm confocal *z*-stack was generated for the 24, 48 and 72-hour time points (**Figure 3.8A-C**). Distance Transformation analysis was performed on the rendered 3D volumes producing .csv data files. Graphical plots of invasive depth were generated in Prism using data extrapolated from the .csv files (**Figure 3.8D**). Mini-organotypic gels containing HDF cells were fixed in formalin and processed to paraffin before sections were stained with H&E (**Figure 3.8E-G**).

Image analysis revealed invasion of HDF cells after 24 hours. I also observed dramatic gel contraction at this time point (**Figure 3.8A**). By 48 hours post plating, HDF cells have fully polarised, changed their morphology and orientation to favour a vertically downward invasion through the gel, presumably toward a serum derived gradient (**Figure 3.8B**). This invasive behaviour has advanced further by the 72 hour time point and a large population of HDF cells invade through the gel at different positions, filling the entirety of the field of view (**Figure 3.8C**).

The gels appeared diminished and withered compared with observations of VB6 cells alone (**Figure 3.7**). The possible reason for this occurrence are several fold; (1) enzymes secreted from the HDFs may have degraded the ECM within the mini-organotypic gel, thus facilitating rapid invasion of the HDF cells; (2) as with VB6 gels, evaporation of exposed gel surface during incubation may have resulted in increased gel shrinkage; (3) the HDFs may have physically contracted the collagen: Matrigel® substrate.

Figure 3.8D displays the distance between the centres of each cells in relationship to the bottom of the Transwell®; over a 72 hour period the HDF cells produce a much steeper invasive gradient to that observed with VB6 cells (**Figure 3.7D**). Additionally the cells are not as tightly packed together as with VB6 cells. Furthermore the HDF cells are spread throughout the span of the gel, ranging an invasive depth between 600-200μm. This could imply that HDF cells are more invasive than VB6 cells over a 72 hour period and that some HDF cells within a population could be more invasive than others. Interestingly, in 24 hour time point image (**Figure 3.8A**) the gel height is around 600μm, and remains consistent throughout the course of the 48 and 72 hour time points (**Figure 3.8B** and **C**) whereas the VB6 gels contract over time.

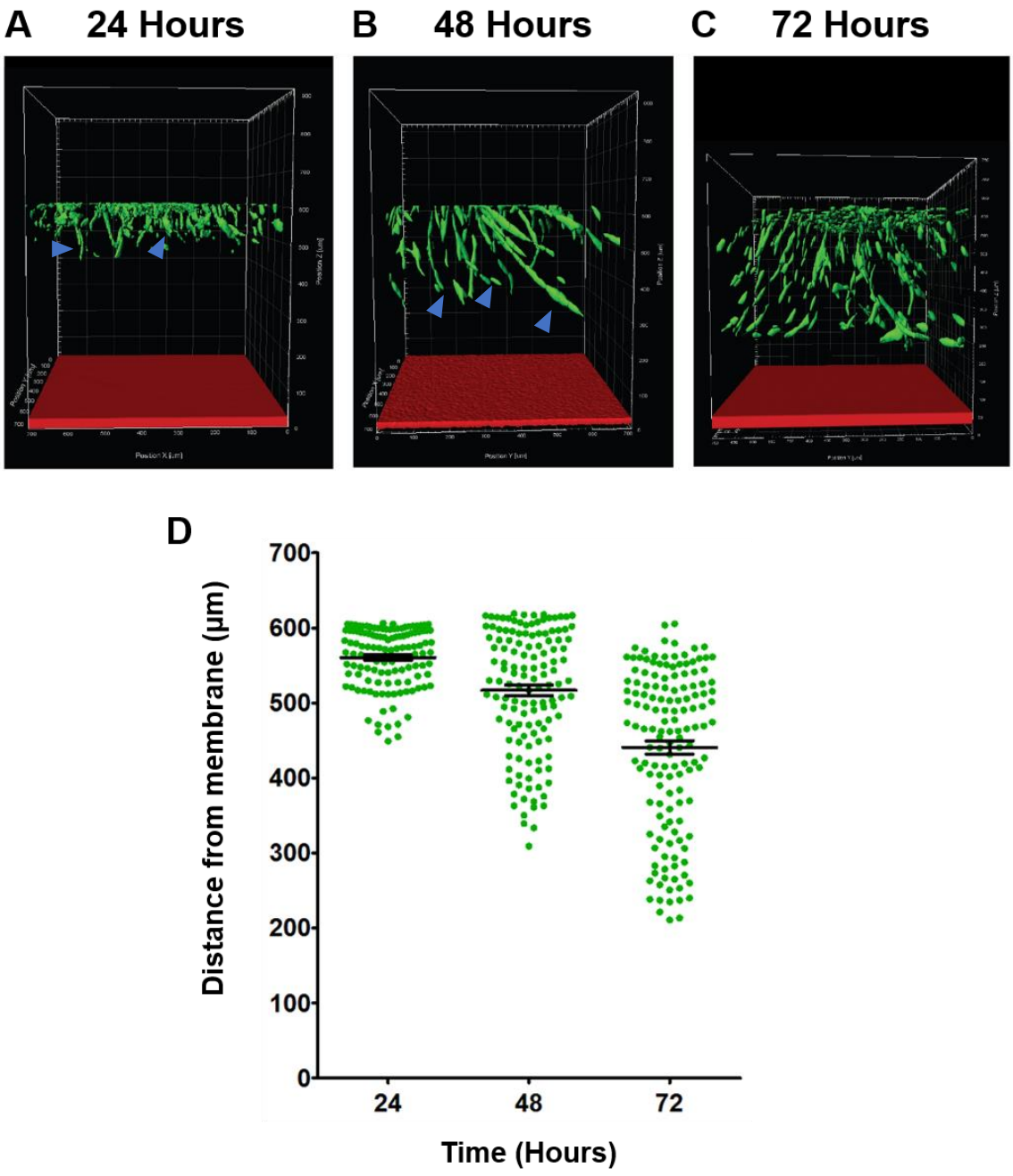
A 24 Hours
B 48 Hours
C 72 Hours
D
Distance from membrane (µm)
700
600
500
400
300
200
100
0
24
48
72
Time (Hours)

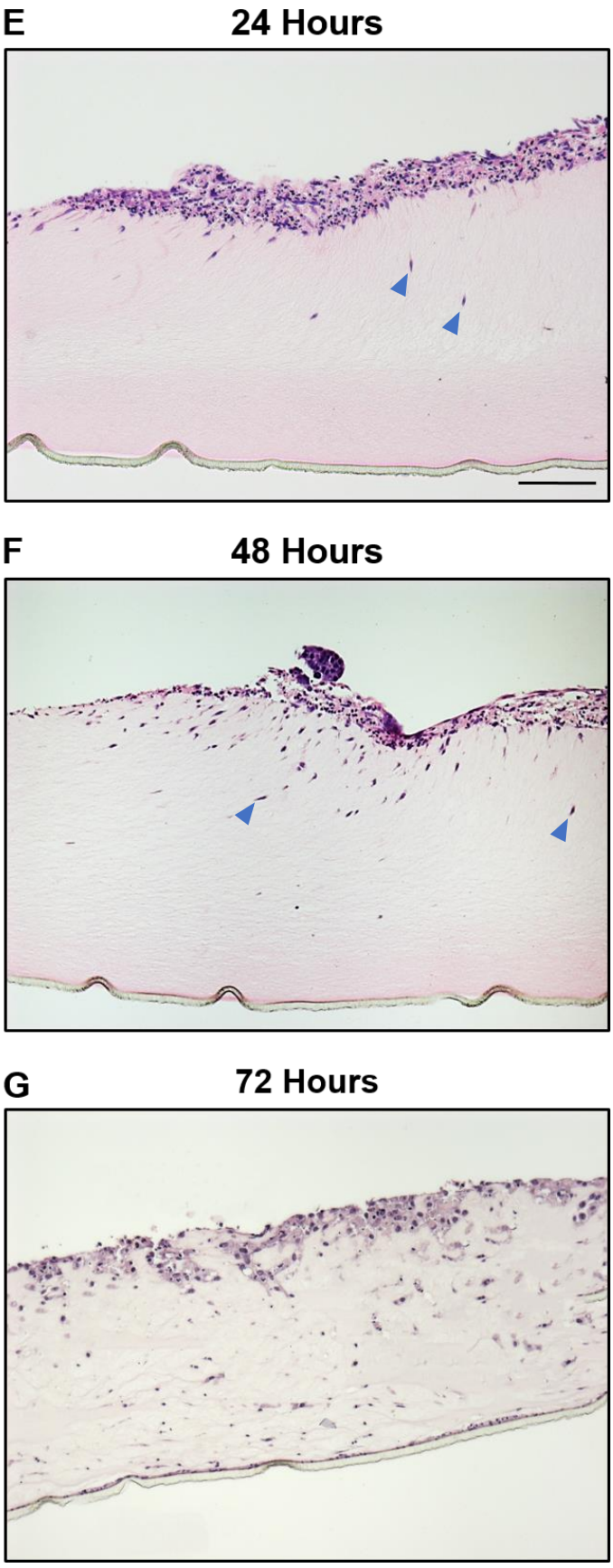

Figure 3.8: 3D rendered and quantified *z*-stacks of fluorescently labelled HDF cells plated alone on top of mini-organotypic gels with H&E stained sections

Figure 3.8: 3D rendered and quantified *z*-stacks of fluorescently labelled HDF cells plated alone on top of mini-organotypic gels with H&E stained sections

The figure displays Imaris XT rendered and analysed mini-organotypic gels plated with CellTracker™ Green labelled HDF cells (10µM). Samples were fixed in formalin, processed to paraffin and H&E stained sections were obtained. The confocal microscope *z*-stacks data files were segmented, rendered and analysed by Imaris. Images were rendered using a surface segmentation tool that accurately detects particles of specific diameters and intensity. Distance Transformation calculations were performed via Imaris XT and plotted in Prism. **A)** After 24 hour post cell seeding, HDF cells are vibrant with colour and easily identifiable. Cells become polarised, changing their morphology and orientation to favour a vertical downward invasion approach (indicated by blue arrows). At this time point we observe the dramatic gel contraction, possibly due in part to evaporation of the mini-organotypic gel during incubation. Additionally, the fibroblasts may have physically contracted the collagen: Matrigel® substrate, thus, further reducing overall gel height. Furthermore, additional contraction may be caused by degradation of the ECM proteins by enzymatic secretions from the HDF cells. Gel thickness is approximately 600µm. **B)** After 48 hours the mini-organotypic gel housing the HDF cells is approximately the same height as the 24 hour time point (ca 600µm). However the leading invasive cell reaches a depth of around 300µm. interestingly a mass of cells are seen invading vertically through the gel toward the bottom of the Transwell® (indicated by blue arrows). It is assumed that this invasion is driven by chemotaxis from the serum underneath the Transwell®. **C)** At the 72 hour time point a battalion of HDF cells has invaded the entirety of the mini-organotypic gel. The gel height remains at 600µm. **D)** Graphical depiction of individual HDF cells *z*-position in relation to the PET membrane (position 0). Each green dot represents one cell within the 700µm square field of view. The cells vastly spread throughout the gel, however still within close enough proximity to transmit and receive signalling information. **E-G)** H&E stained sections of HDF cells plated on top of mini-organotypic gels and harvested at 24, 48 and 72 hour time points. The blue arrows indicate HDF cells invading vertically through the mini-organotypic gels. Scale bar: 100µm. One representative image for each time point from triplicate gels belonging to one of three independent experiments.

3.5.3 Construction of 3D volumes and distance quantification: HDF: VB6 cells co-cultured cells at 24, 48 & 72 hour time points

HDF and VB6 cells were labelled with CellTracker™ Green (10µM) and Red (5µM) respectively and co-cultured in a 2:1 ratio on top of mini-organotypic gels. CLSM *z*-stacks images were acquired every 24 hours for three days (**Figure 3.9**). Using Imaris XT image analysis software a rendered, smoothened 3D representation of the raw .lsm confocal *z*-stack was generated for the 24, 48 and 72-hour time points (**Figure 3.9A**-**C**). Distance Transformation analysis was performed on the rendered 3D volumes producing .csv data files. Graphical plots of invasive depth were generated in Prism using data extrapolated from the .csv files (**Figure 3.9D**). Mini-organotypic gels containing VB6 admixed with HDF cells were fixed in formalin and processed to paraffin before sections were stained with H&E (**Figure 3.9E-G**).

The 24 hour image revealed both cell types appear to have attached and spread uniformly on the surface of the gel and display no signs of invasion at this time point. The data in **Figure 3.8** indicated that, when plated alone, HDFs are highly invasive, changing their polarity and appointing a vertical invasive position. This suggests that the rate of invasion of the HDF cells when co-cultured with VB6 is affected and results in a slower initial rate of invasion. After 48 hours I observed both populations of cells invading through the collagen: Matrigel® substrate and at the same time noticed gel contraction. I consistently observed that the most advanced invasive cell type was a fibroblast often followed closely behind by VB6 tumour cells.

The data appear to suggest the VB6 cells migrate into remodelled matrix channels generated by the fibroblasts. Again, H&E analysis of fixed and section samples of these mini-organotypic gels confirm that some tumour cells have invaded almost to the PET membrane. However the H&E images fail to reveal that the fibroblasts are truly the invasive phenotype.

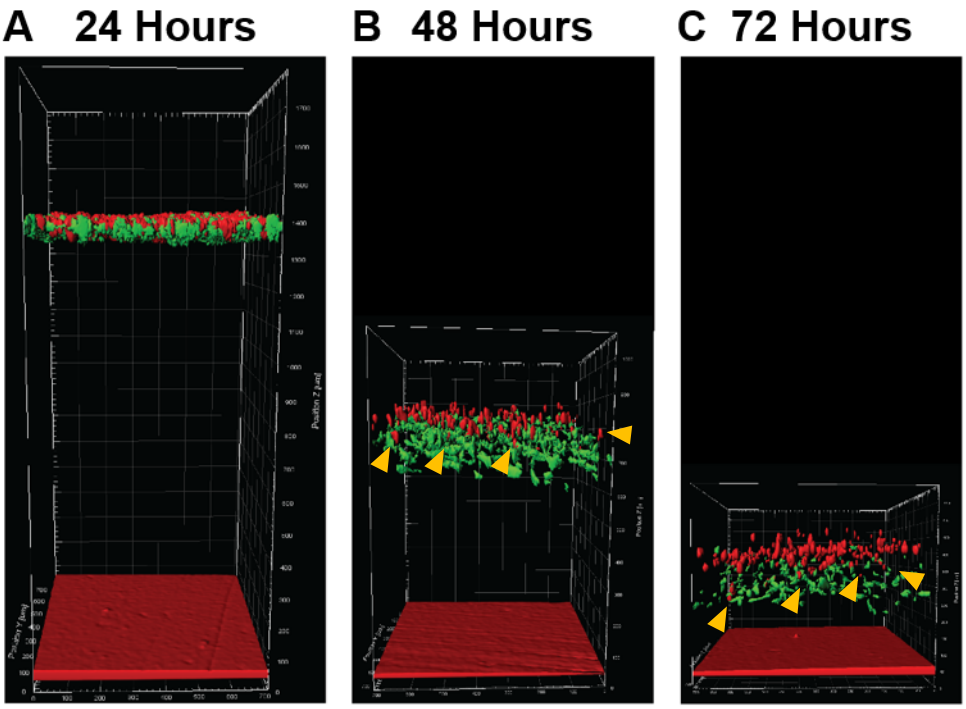
A 24 Hours
B 48 Hours
C 72 Hours

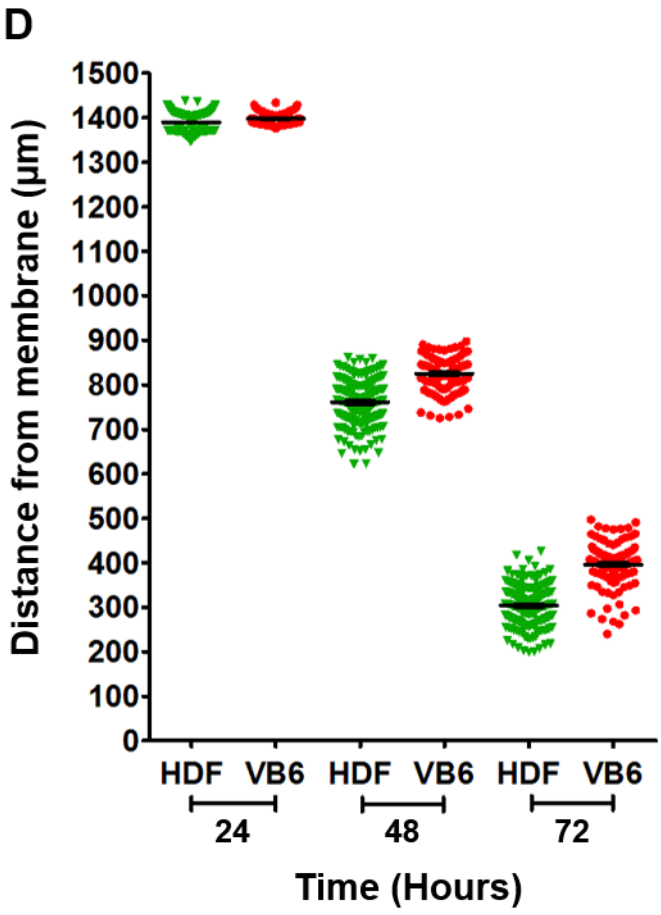
D
Distance from membrane (µm)
1500
1400
1300
1200
1100
1000
900
800
700
600
500
400
300
200
100
0
HDF VB6 HDF VB6 HDF VB6
24
48
72
Time (Hours)

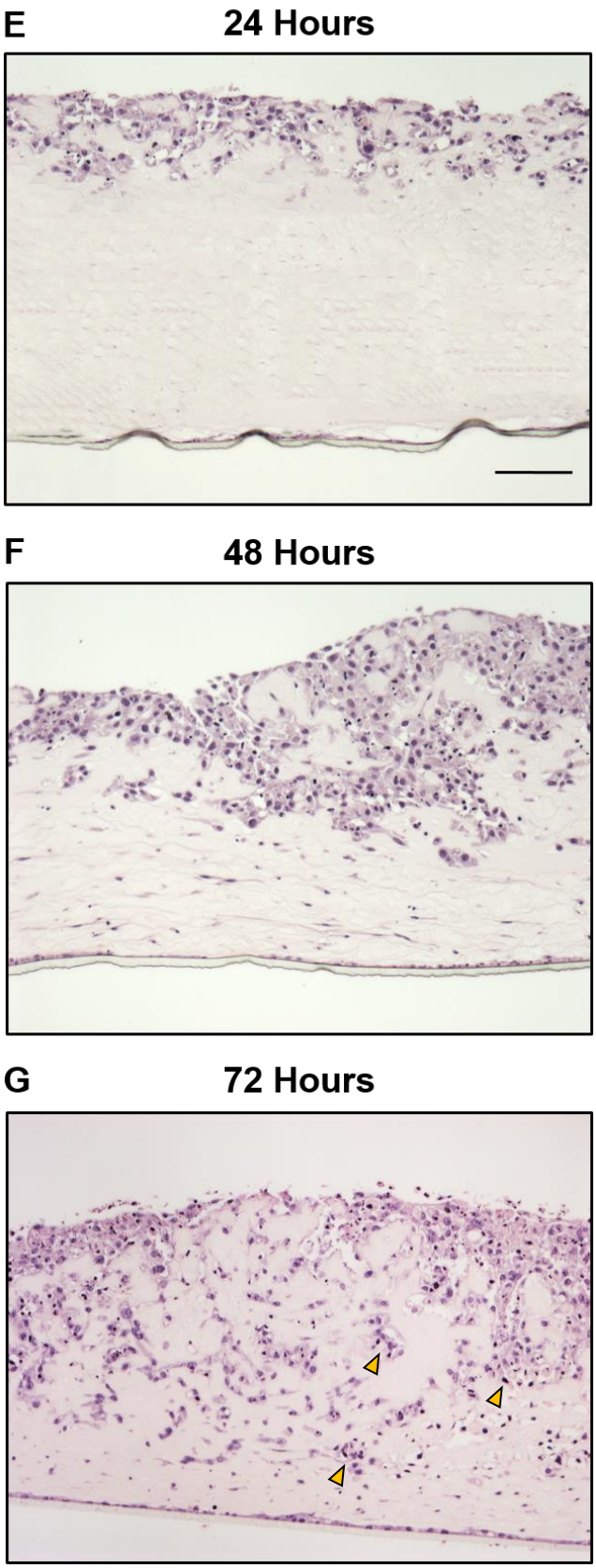

Figure 3.9: 3D rendered and quantified *z*-stacks of fluorescently labelled HDF & VB6 cells plated in co-culture on top of mini-organotypics gels with H&E stained sections

Figure 3.9: 3D rendered and quantified *z*-stacks of fluorescently labelled HDF & VB6 cells plated in co-culture on top of mini-organotypics gels with H&E stained sections

The figure displays Imaris XT rendered and analysed mini-organotypic gels co-cultured with CellTracker™ Green and Red labelled HDF (10µM) and VB6 (5µM) respectively. Samples were fixed in formalin, processed to paraffin and H&E stained sections were obtained. The confocal microscope *z*-stacks data files were segmented, rendered and analysed by Imaris. Images were rendered using a surface segmentation tool that accurately detects particles of specific diameters and intensity. Distance Transformation calculations were performed via Imaris XT and plotted in Prism. **A)** After 24 hour post cell seeding, HDF and VB6 cells are vibrant with colour and easily identifiable. Gel thickness is approximately 1400µm. Both cell populations appear to be settled and spread on to the surface of the gel. **B)** After 48 hours the mini-organotypic gel housing the HDF and VB6 co-cultures is approximately 850µm thick. However a population of HDF cells closest to the surface of the gel appear to become polarised and as observed previously, change their morphology and orientation, thus beginning to invade through the gel. the leading invasive cell (HDF) reaches a depth of around 600µm. HDF cells appear to be the leading invasive cell type as observed in **Figure 3.8**, however VB6 cells can be identified within the HDF invasive layer (indicated by yellow arrows). **C)** At the 72 hour time point a mass of HDF cells has arrived at the bottom of the Transwell® accompanied by VB6 cells. At this stage I also observed drastic gel contraction thus producing a gel thickness of approximately 400µm. **D)** Graphical depiction of HDF and VB6 cells *z*-position in relation to the PET membrane (position 0). Each dot represents one cell within the 700µm square field of view. **E-G)** H&E stained sections of VB6 admixed with HDF cells in a 1:2 ratio plated on top of mini-organotypic gels and harvested at 24, 48 and 72 hour time points. VB6 cells are observed invading through the gel with HDF cells (indicated by yellow arrows). Scale bar: 100µm. One representative image for each time point from triplicate gels belonging to one of three independent experiments.

3.6 Fibroblasts embedded within mini-organotypic gels

Throughout the previous experiments, HDF cells were always plated on top of the mini-organotypic gel. The organotypic invasion protocol described by Nystrom and colleagues states that stromal fibroblasts were embedded within the gel prior to polymerisation (Nystrom et al., 2005). This enables fibroblasts to become settled, creating a comfortable niche within a 3D environment prior to addition of cancer cells. Other groups within our institute similarly adopted the 'pre-embedding' step, for example, embedding pancreatic stellate cells to produce a pancreatic organotypic model (Coleman et al., 2014b; Froeling et al., 2009).

In the mini-organotypic assay used here, fibroblast cells are cultured on the same day as cancer cells and both cell types are plated on top of a polymerised gel. This method does not allow fibroblast cells to settle within the 3D environment. Therefore, fibroblast cells were labelled with CellTracker™ Green (10μM) and embedded into the mini-organotypic gel and plated into the Transwell® prior to polymerisation. Once polymerised, VB6 cells labelled with CellTracker™ Red (5μM) were plated on top of the mini-organotypic gel and imaged over a 48 hour period via CLSM 710.

Using Imaris XT image analysis software a rendered, smoothened 3D representation of the raw .lsm confocal *z*-stack was generated for the 24 and 48 hour time points (**Figure 3.10A** & **B**). Distance Transformation analysis was performed on the rendered 3D volumes producing .csv data files. Graphical plots of invasive depth were generated in Prism using data extrapolated from the .csv files (**Figure 3.10C**). Mini-organotypic gels embedded with HDF cells and surface plated VB6 cells were fixed in formalin and processed to paraffin before sections were stained with H&E (**Figure 3.10D** & **E**).

The results obtained display interesting outcomes, suggesting that HDF cells descend to the bottom of the gel during the pre-embedding step, possibly whilst the gel is polymerising. Furthermore, the morphology of the HDF cells remains spherical and the cells do not exhibit the same degree of polarisation and spreading as previously observed. One possibility of this occurrence, may be due to the mechanisms involved during the formation of collagen fibrils. The gel probably polymerises slowly during incubation, thus, the embedded cells descend to the bottom instead of being dispersed throughout the entire gel. The VB6 cells attach and spread to the surface of the gel 24 hours post seeding and appear to proliferate.

However invasion of VB6 cells through the mini-organotypic gel was not observed. This may be due to the fact that the fibroblast cells have not remodelled or degraded the upper part of the gel, but rather sunk down during gel cross-linking. Note that the gel height continued to shrink over the 48 hour period as previously observed, but to a lesser degree than observed when cells were co-cultured on top of the gels (see **Figure 3.9**). For these reasons I chose not to embed fibroblasts within the mini-organotypic gels for the remainder of my studies.

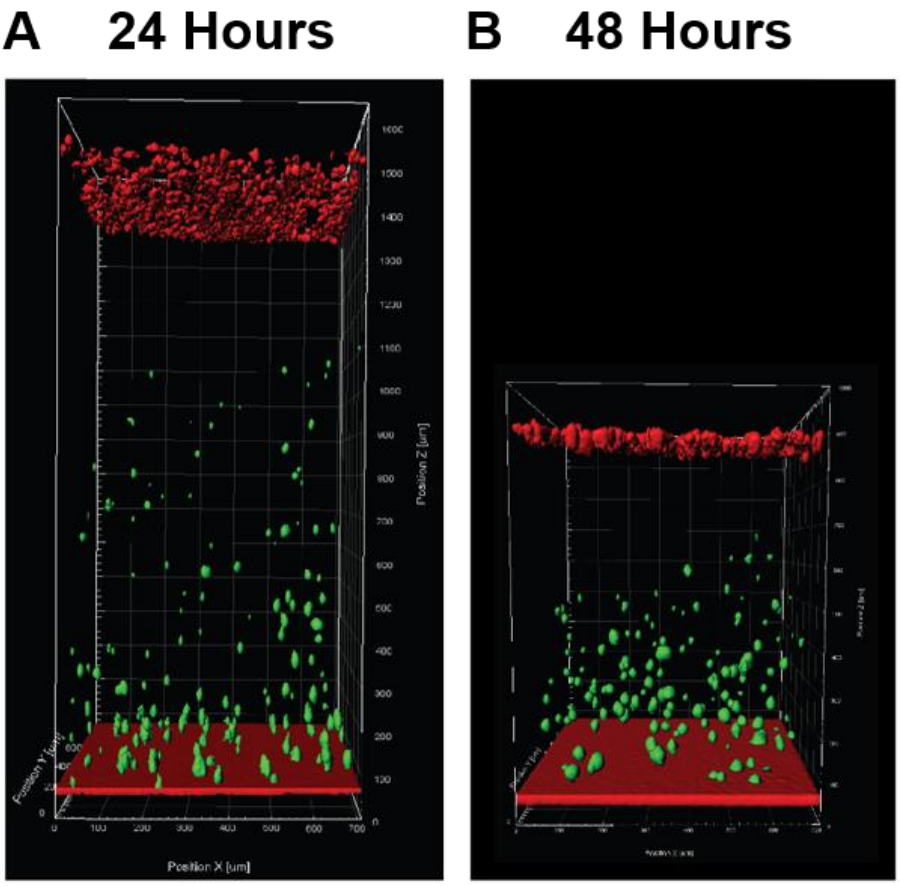
A 24 Hours
B 48 Hours
Position X [um]
Position Z [um]

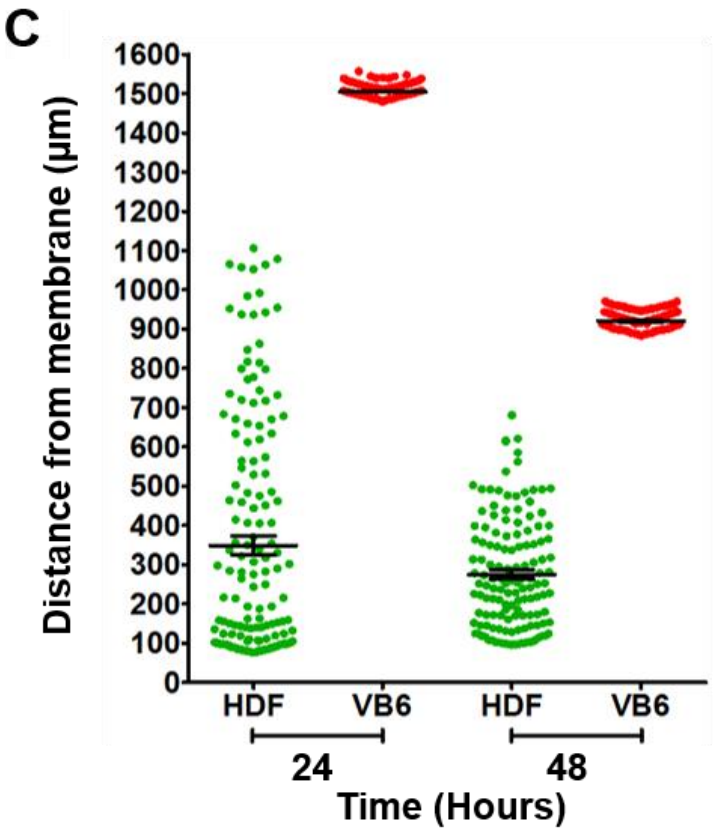
C
Distance from membrane (µm)
1600
1500
1400
1300
1200
1100
1000
900
800
700
600
500
400
300
200
100
0
HDF
VB6
HDF
VB6
24
48
Time (Hours)

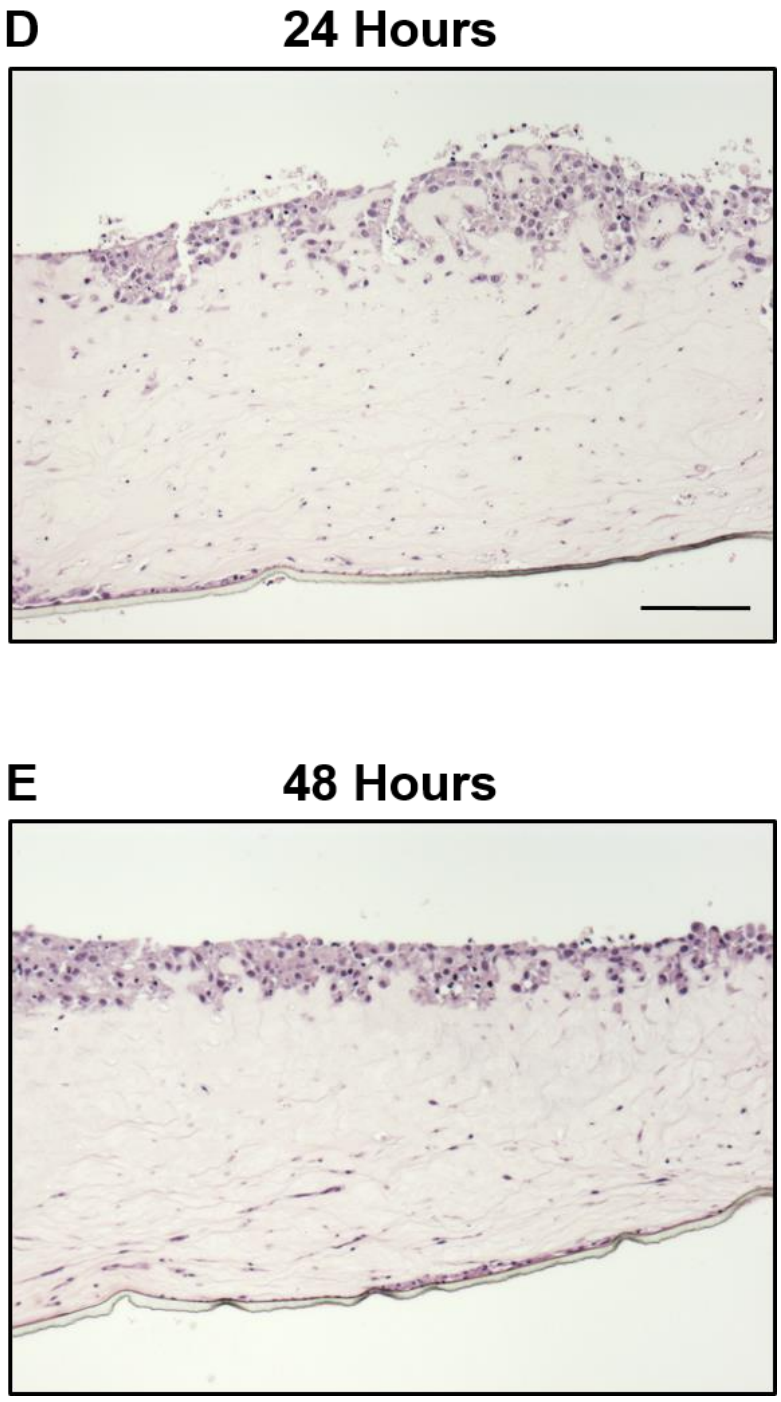

Figure 3.10: 3D rendered and quantified *z*-stacks of fluorescently labelled HDF cells embedded within mini-organotypic gels with H&E stained sections

Figure 3.10: 3D rendered and quantified *z*-stacks of fluorescently labelled HDF cells embedded within mini-organotypic gels with H&E stained sections

The figure displays Imaris XT rendered and analysed mini-organotypic gels embedded with CellTracker™ Green labelled HDF cells (10µM) and CellTracker™ Red labelled VB6 cancer cells (5µM). HDF cells were embedded within mini-organotypic gels and incubated until polymerised. Red labelled VB6 cells were plated on top of the solidified gel surface. Samples were fixed in formalin, processed to paraffin and H&E stained sections were obtained. **A)** 24 hours post cell seeding, HDF cells appear rounded and do not exhibit the previously observed polarised morphology (as displayed in **Figure 3.8** and **Figure 3.9**). Additionally the HDF cells have dispersed throughout the mini-organotypic gel. However mostly accumulating at the bottom of the gel. VB6 cells were plated once the gel had polymerised, the cells appear adhered and spread on to the surface of the gel. VB6 cells are vibrant with colour, easily identifiable and exhibit no signs of invasion. Gel thickness was approximately 1500µm. **B)** After 48 hours the mini-organotypic gel housing the embedded HDF cells has shrunk approximately to 900µm thick. The HDF population appears to have clustered closer together, possibly as a result of gel shrinkage. Their morphology remains spherical, where as previously; observations to their morphology and orientation were clearly evident. At this stage I can only make suggestion as to why the HDF cells gather at the bottom of the gel, do not take shape and do not appear to invade. Gel shrinkage appears to be a common factor observed here and in previous experiments, possibly due to evaporation during incubation. **C)** Graphical depiction of HDF and VB6 cells *z*-position in relation to the PET membrane. Each dot represents one cell within the 700µm square field of view. **D, E)** H&E stained sections of HDF cells embedded into gel prior to polymerisation step and VB6 plated on top of gels. HDF cells are observed at the bottom of the gel and VB6 remain at the surface. Scale bar: 100µm. One representative image for each time point from duplicate gels belonging to one of two independent experiments.

3.7 Investigating the invasiveness of different fluorescently labelled cell types within mini-organotypic gels

I have confirmed that the new *in situ* invasion assay works reliably, reproducibly and that the software can generate 3D images and quantitative data allowing suitable analysis. However the previous results have only examined one fibroblast: tumour pair; HDFs and VB6 cells. To investigate the invasive capability of different cell types within the mentioned 3D assay, three cancer cell lines; (1) VB6 – OSCC; (2) NCI-H1299 – human NSCLC (denoted as H1299 from this point forward); and (3) MDA-MB-468 – human breast adenocarcinoma (denoted as MDA-468 from this point forward) and three human fibroblast cell lines; (1) HDF – adult derived human dermal fibroblasts; (2) FSF – neonatal human foreskin fibroblasts; and (3) MRC5 – human foetal isolated lung fibroblasts were plated alone (**Figure 3.11** and **Figure 3.12** respectively) and co-cultured in combinations of; (1) HDF, FSF and MRC5 with H1299 (**Figure 3.13**); (2) HDF, FSF and MRC5 with MDA-468 (**Figure 3.14**); (3) HDF, FSF and MRC5 with VB6 (**Figure 3.15**).

H1299 and MDA-468 cancer cell lines were fluorescently labelled using the same concentration of CellTracker™ Red previously used for labelling the VB6 cancer cells (5µM). Similarly, FSF and MRC5 fibroblast cell lines were fluorescently labelled using the same concentration of CellTracker™ Green used for labelling the HDF cells (10µM). Once labelled, cells were plated on top of mini-organotypic gels in a 2:1 ratio of fibroblasts to tumour cells. Transwells® were imaged 72 hours post plating to determine which cell line pairs invaded the furthest by this time point. A preliminary time lapse fluorescence internalisation study (as displayed in **Figure 3.1** and **Figure 3.2**) was not performed on the H1299, MDA-468, FSF or MRC5 cell lines, as an IncuCyte™ ZOOM® microscope was not available.

3.7.1 Investigating the invasiveness of fluorescently labelled cancer cell lines; H1299, MDA-468 and VB6 in mini-organotypic gels

To investigate whether the cancer cell lines; H1299, MDA-468 and VB6 invaded through mini-organotypic gels; all three cell lines were fluorescently labelled with CellTracker™ Red (5µM) and plated on top of mini-organotypic gels. 24 hours post plating, growth medium underneath each Transwell® was exchanged and excess medium from the surface of the gel was carefully removed. Mini-organotypic gels containing H1299 and MDA-468 cells had their upper surface covered with a layer of serum-free medium, whereas, gels containing VB6 cells were left exposed.

Transwells® were imaged at an end point of 72 hours via CLSM 710 (**Figure 3.11**). Using Imaris XT image analysis software a rendered, smoothened 3D representation of the raw .lsm confocal *z*-stack was generated for each cancer cell line at the 72 hour time point (**Figure 3.11A-C**). Distance Transformation analysis was performed on the rendered 3D volumes producing .csv data files. Graphical plots of invasive depth were generated in Prism using data extrapolated from the .csv files (**Figure 3.11D**).

At the 72 hour time point, H1299, MDA-468 and VB6 cells appear to remain at the surface of the gel, homogeneously adhered and spread. None of the cell lines exhibited signs of invasion into the collagen: Matrigel® substrate. Previous observations from **Figure 3.7** (VB6 alone) suggested that mini-organotypic gels with an exposed surface contract over time, the initial gel height at the 24 hour time point was approximately 1400µm and contracted to approximately 1100µm by the 72 hour time point. This may be due to evaporation of the exposed gel surface during incubation. However all three samples in (**Figure 3.11**) display signs of gel contraction to a similar degree, despite H1299 and MDA-468 containing an overlay of serum-free medium. These data suggest that the serum-free layer in this instance made no or very little difference. Perhaps the serum-free layer needed to be replaced frequently at regular intervals.

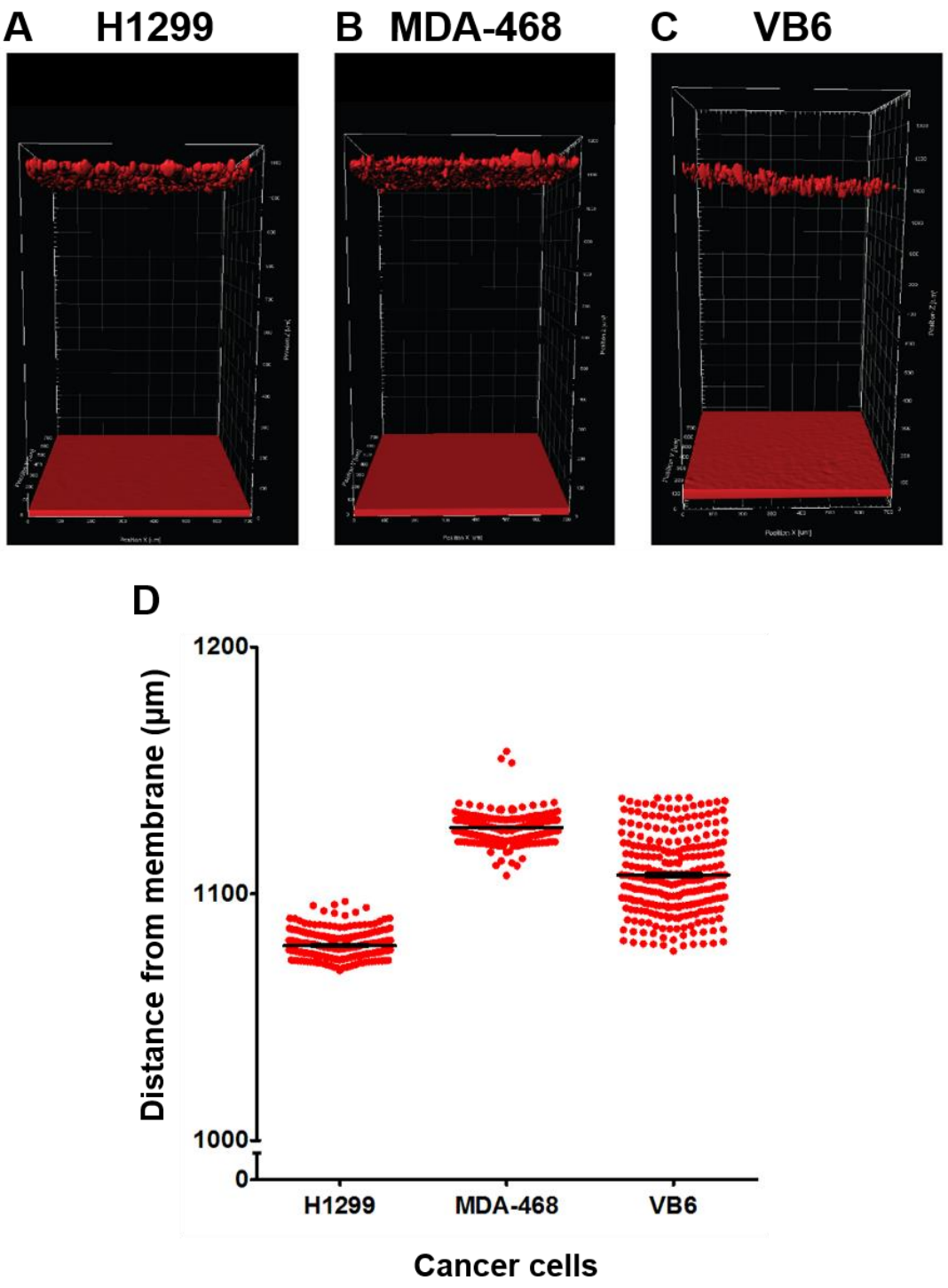

Figure 3.11: 3D rendered and quantified *z*-stacks of fluorescently labelled cancer cell lines; H1299, MDA-468 and VB6 in mini-organotypic gels imaged 72 hours post plating

Figure 3.11: 3D rendered and quantified *z*-stacks of fluorescently labelled cancer cell lines; H1299, MDA-468 and VB6 in mini-organotypic gels imaged 72 hours post plating

The figure displays Imaris XT rendered and analysed 3D *z*-stack images of fluorescently labelled red VB6, MDA-468 and H1299 cancer cells. Images were obtained via CLSM 710 72 hours post plating on top of mini-organotypic gels. After 72 hours post cell seeding, all cells type have adhered and spread out on to the surface of the gel. **A)** H1299 cells do not appear to invade through mini-organotypic gels. Gel thickness is approximately 1100µm. **B)** MDA-468 cells also show no signs of invasion after 72 hours post plating. Gel thickness is approximately 1140µm. **C)** VB6 cells display no signs of invasion. Gel thickness approximately 1100µm. **D)** Graphical bee swarm plot of invasive depth of all three cell types after 72 hours. Each dot represents one cell within the 700µm square field of view. One representative image for the 72 hour time point from triplicate gels belonging to one of two independent experiments.

3.7.2 Investigating the invasiveness of fluorescently labelled fibroblast cell lines; HDF, FSF and MRC5 in mini-organotypic gels

To determine whether the fibroblast cell lines; HDF, FSF and MRC5 invaded through mini-organotypic gels; all three cells were labelled with CellTracker™ Green (10µM) and plated on top of mini-organotypic gels. 24 hours post plating, growth medium underneath each Transwell® was exchanged and excess medium from the surface of the gel was carefully removed before being replaced with a serum-free medium layer.

Transwells® were imaged via CLSM 710 and *z*-stacks were obtained at an end point of 72 hours (**Figure 3.12**). Using Imaris XT image analysis software a rendered, smoothened 3D representation of the raw .lsm confocal *z*-stack was generated for each fibroblast cell line at the 72 hour time point (**Figure 3.12A-C**). Distance Transformation analysis was performed on the rendered 3D volumes producing .csv data files. Graphical plots of invasive depth were generated in Prism using data extrapolated from the .csv files (**Figure 3.12D**).

Image analysis revealed, when plated alone, that all three fibroblast cell lines invade through mini-organotypic gels, however, all at variable rates. In **Figure 3.12A** the HDF cells appear to have polarised and become activated at a faster rate, invading deeper into the gel by the 72 hour time point, in comparison to FSFs and MRC5s (**Figure 3.12B** and **C**). A large population of HDF cells are observed invading though the gel at different positions, filling the entirety of the field of view, presumably toward a serum derived gradient. Interestingly, the FSF and MRC5 cells do appear to become invasive, however, at a slower rate than the HDF cells.

A large population of both FSF and MRC5 cells are observed attached at the surface of the gels. A small population of FSF cells have begun to polarise and change their morphology, invading vertically downward through the mini-organotypic gel. Furthermore, an even smaller population of MRC5 cells are observed displaying signs of early invasive behaviour. Additionally, the gel containing the HDF cells (approximately 600µm thick) appears to be diminished and withered compared with observations of FSF and MRC5 gels (both approximately 800µm thick). The possible reasons for these occurrences may be due to; (1) enzymes secreted by the HDF cells may have degraded the collagen: Matrigel® substrate faster than the secretions from the FSF and MRC5 cells, thus, invading deeper through the gel; (2) the HDF cells may possess a more activated phenotype compared to the FSF and MRC5 cells, also leading to an increase in invasive activity and matrix degradation; (3) the FSF and

MRC5 cells may be slower at activating on 3D substrata, therefore, require more time to become fully activated and polarised.

Figure 3.12D displays the distance between the centres of each cell in relationship to the bottom of the Transwell®. Over a 72 hour period the HDF cells produce a much steeper invasive gradient to that observed of the FSF and MRC5 cells. Additionally the HDF cells are not as tightly packed as the FSF and MRC5 cells. In fact, the HDF cells are spread through the span of the gel, ranging and invasive depth between 600-200µm, on the contrary, FSF and MRC5 cells appear to be stacked on top of each other, producing a cell layer of 200µm in depth with only a small population of each cell line invading into the gels. This implies that the HDF cells are more invasive than FSF and MRC5 cells when plated alone over a 72 hour period and that some HDF cells within a population could be more invasive than others. Interestingly all three fibroblast cell lines display varying signs of activation and all appear to have changed their morphology to favour a vertical downward invasion through the mini-organotypic gel, albeit at different rates.

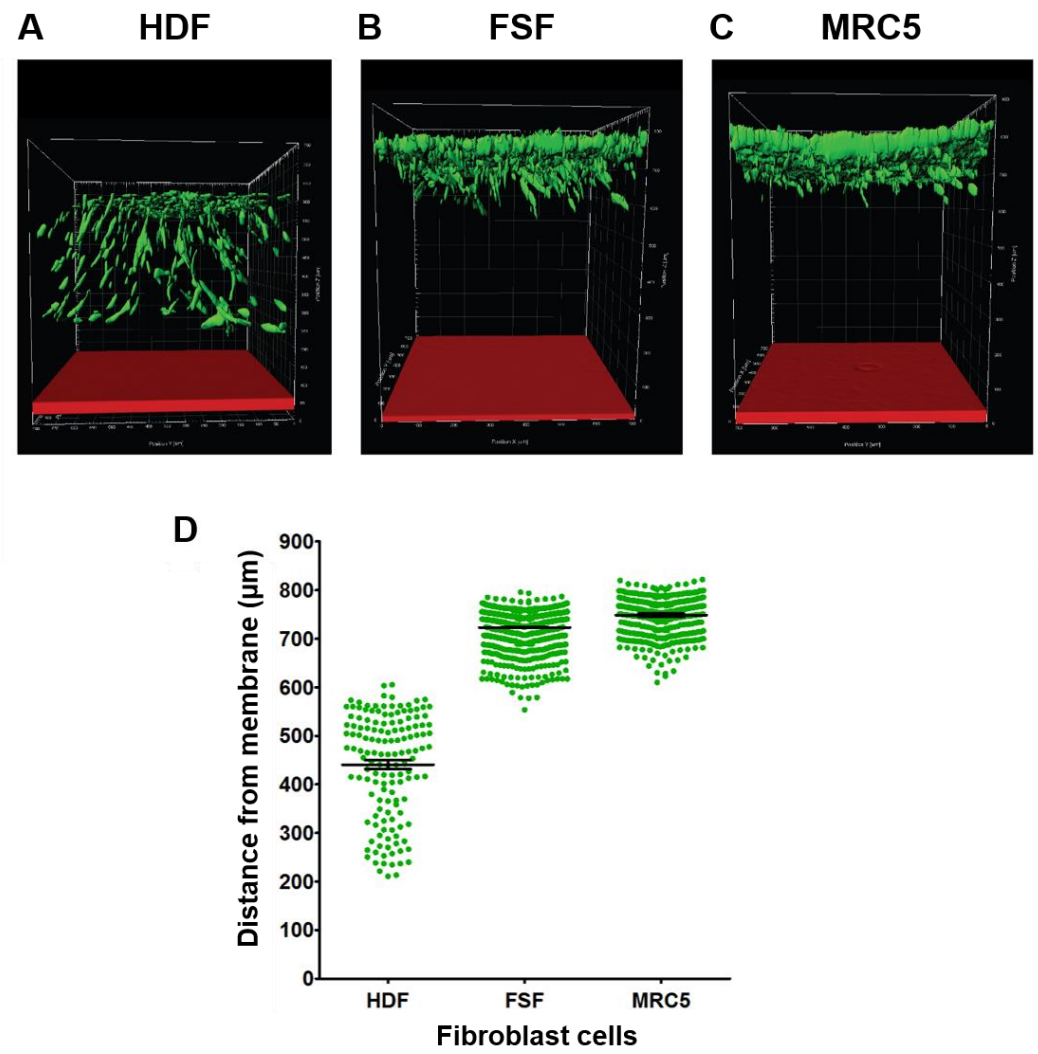

Figure 3.12: 3D rendered and quantified *z*-stacks of fluorescently labelled fibroblasts cell lines; HDF, FSF and MRC5 in mini-organotypic gels imaged 72 hours post plating

The figure displays Imaris XT rendered and analysed 3D *z*-stack images of fluorescently labelled green HDF, FSF and MRC5 fibroblast cells. After 72 hours post cell seeding, all cells type are vibrant with colour and easily identifiable. **A)** At the 72 hour time point a large population of HDF cells has invaded the entirety of the gel. HDF cells have changed their polarity and morphology, favouring a downward vertical invasion. Ranging and invasive depth between 600-200µm. Gel thickness is approximately 600µm. **B)** FSFs appear attached and very much settled on the surface of the gel. A small population of FSF cells can be observed initially invading. The level of invasive depth reached is far less than the HDF cells. Perhaps with more time the FSF cells would invade further through the gel. Gel thickness is approximately 800µm. **C)** MRC5 cells also appear to be settled on the surface of the gel. Similar to that of the FSF cell, some MRC5 cells appear to have begun invading. Gel thickness is approximately 800µm. **D)** Graphical bee swarm plot of invasive depth of all three cell types after 72 hours. Each dot represents one cell within the 700µm square field of view. One representative image for the 72 hour time point from triplicate gels belonging to one of two independent experiments.

3.7.3 Investigating the invasiveness of fluorescently labelled HDF, FSF, and MRC5 fibroblast cells co-cultured with H1299, MDA-468 or VB6 cancer cells in mini-organotypic gels

To identify which fibroblast: tumour cell pair displayed the maximum invasion after 72 hours post plating; HDF, FSF and MRC5 fibroblast cells were labelled with CellTracker™ Green (10µM) and co-cultured with fluorescently labelled CellTracker™ Red; H1299, MDA-468 or VB6 cancer cells (5µM) (**Figure 3.13**, **Figure 3.14** and **Figure 3.15**). Transwells® were imaged via CLSM 710 and *z*-stacks were obtained at an end point of 72 hours. Using Imaris XT image analysis software a rendered, smoothened 3D representation of the raw .lsm confocal *z*-stack was generated for each fibroblast and tumour cell line pair at the 72 hour end point (**Figure 3.13A-C**, **Figure 3.14A-C** and **Figure 3.15A-C**). Distance Transformation analysis was performed on the rendered 3D volumes producing .csv data files. Graphical plots of invasive depth were generated in Prism using data extrapolated from the .csv files (**Figure 3.13D**, **Figure 3.14D** and **Figure 3.15D**).

3.7.3.1 Investigating the invasiveness of fluorescently labelled HDF, FSF and MRC5 fibroblast cells: co-cultured with H1299 lung cancer cells in mini-organotypic gels

To determine which fibroblast cell line displayed maximum invasion after 72 hours when co-cultured with lung H1299 cells, HDF, FSF and MRC5 cells were labelled with CellTracker™ Green and plated in co-culture on top of mini-organotypic gels with CellTracker™ Red labelled H1299 cells. 24 hours post plating, growth medium underneath each Transwell® was exchanged and excess medium from the surface of the gel was carefully removed before being replaced with serum-free medium. Transwells® were imaged via CLSM 710 and *z*-stacks were rendered, smoothened and quantified at an end point of 72 hours post plating (**Figure 3.13**).

Image analysis revealed, when H1299 cells were plated in co-culture with three different fibroblast cell lines, cell invasion in to the mini-organotypic gels was diverse in each combination. **Figure 3.13A** displays fluorescently labelled HDF and H1299 cells 72 hours post plating. Both cell types appear to have adhered and spread homogeneously on the surface of the gel. HDF cells appear to have become polarised, changed their morphology and orientation and invaded into the gel, as similarly observed in **Figure 3.12A** (HDF cells alone). However, the HDF cells have not reached the same invasive depth when co-cultured with H1299 cells compared to when plated alone. The bee swarm plot suggests that the H1299 cells have settled on the surface of the gel and produced a layer, approximately 80µm in depth. Interestingly, the plot also reveals a small population of H1299 cells residing beneath this layer, located deep within the core of the invading HDFs, with a secondary wave following closely behind. This may be a result of the H1299 cells migrating closely behind the HDFs, possibly through the channels produced by the fibroblasts. Conversely, observations from **Figure 3.11A**, suggested H1299 cells do not migrate through mini-organotypic gels when plated alone.

Figure 3.13B displays fluorescently labelled populations FSF and H1299 cells attached and evenly spread on the surface of the gel 72 hours post plating. The bee swarm plot suggest that the H1299 cells produce a cell layer approximately 80µm in depth. A small cluster of FSF cells have begun to polarise and change their morphology, invading vertically downward through the gel. Similar observations were noted in **Figure 3.12B** (FSF cells alone).

However in that experiment, FSF cells expand over an invasive depth between 700-550µm, whereas when co-cultured with H1299 cells, the rate of invasion appears to have decreased, with FSF cells only ranging an invasive depth between 850-750µm. This reduction in invasive capability may be due to the presence of the H1299 cells, competing for space or potentially supressing, temporarily, the FSFs capability to polarise and invade.

Figure 3.13C displays large populations of fluorescently labelled MRC5 and H1299 cells attached and uniformly spread to the surface of the gel 72 hours after plating. Neither cell type are seen invading through the gel. The MRC5 cells do not appear to become polarised or change their morphology, unlike the observations displayed with the HDF and FSF cells (**Figure 3.13A** and **B** respectively).

In **Figure 3.13A**, the mini-organotypic gel appears to have contracted to approximately 600µm in depth. In comparison, gels in **Figure 3.13B** and **C** appear to have contracted less and appeared more robust (approximately 850µm and 1200µm respectively). This may be due to enzymatic secretions from the HDF cells increasing the rate of gel degradation and remodelling, compared to the gels containing FSF and MRC5 cells.

The 3D rendered images and bee swarm plot data suggest that HDF cells polarise and invade further into the gel after 72 hours compared to FSF and MRC5 fibroblast cells when co-cultured with H1299 cancer cells. These data suggest that H1299 cell migration may be co-dependant on the fibroblasts ability to invade and remodel the mini-organotypic gels, and additionally, the invasive capability of fibroblast cells may be due to specific genotypes.

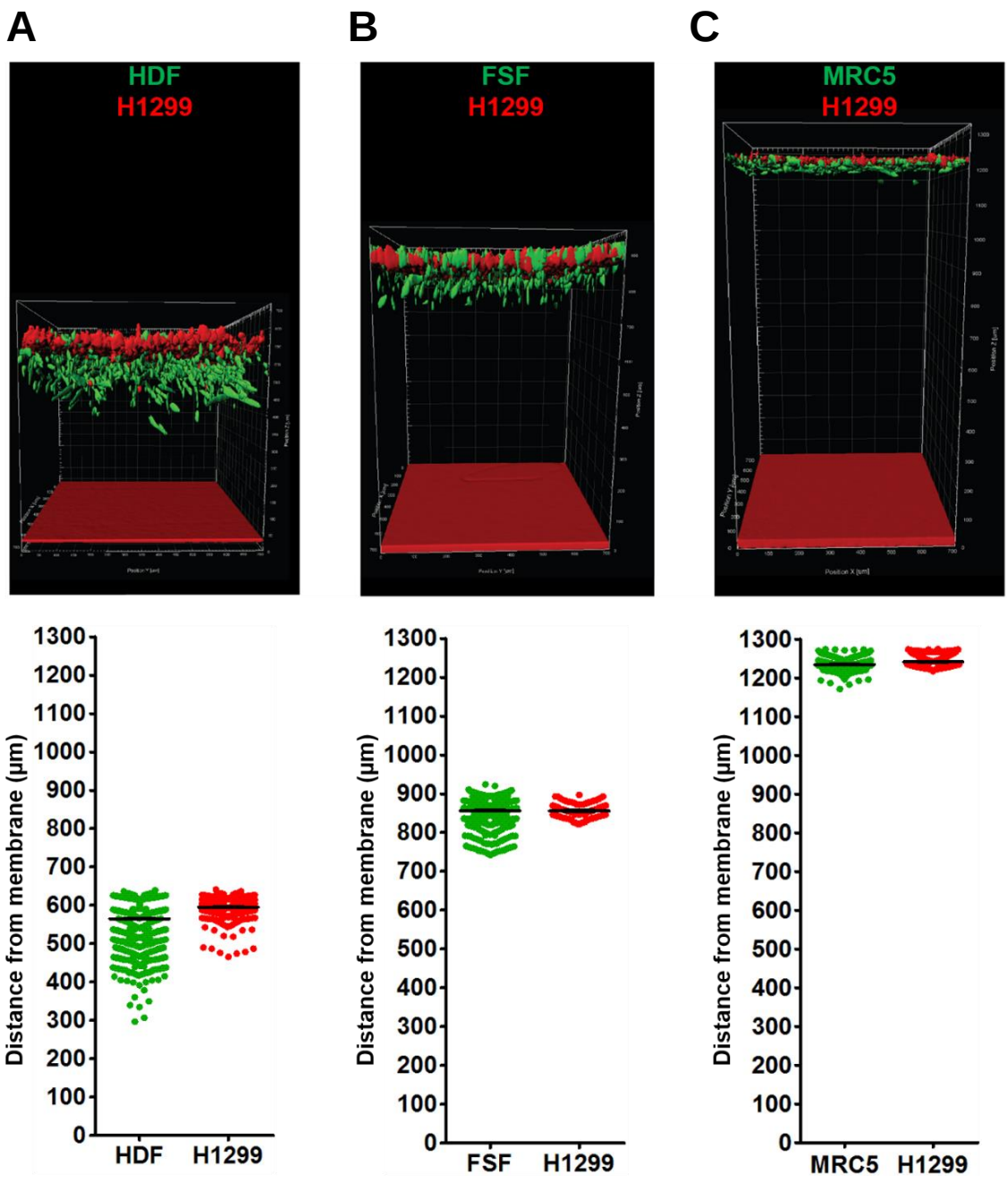

Figure 3.13: 3D rendered and quantified *z*-stacks of fluorescently labelled HDF, FSF and MRC5 cells co-cultured with fluorescently labelled H1299 cells in mini-organotypic gels imaged 72 hours post plating

Figure 3.13: 3D rendered and quantified *z*-stacks of fluorescently labelled HDF, FSF and MRC5 cells co-cultured with fluorescently labelled H1299 cells in mini-organotypic gels imaged 72 hours post plating

The figure displays Imaris XT rendered and analysed 3D *z*-stack images of fluorescently labelled green HDF, FSF and MRC5 fibroblast cells co-cultured with fluorescently labelled red H1299 lung cancer cells. After 72 hours post cell seeding, all cells type are vibrant with colour and easily identifiable. **A)** At the 72 hour time point HDF cells have changed their polarity to that favouring a downward vertical invasion. H1299 cells appear attached and spread on the surface of the gel. A small population of H1299 cells can be observed migrating in to the gels. Gel thickness is approximately 600 µm. **B)** FSFs appear attached and very much settled on the surface of the mini-organotypic gel. A small population of FSF cells can be observed initially invading. The level of invasive depth reached is far less than the HDF cells. H1299 cells appear attached and spread on the surface of the gel, with no signs of invasion after 72 hour. Gel thickness is approximately 850µm. **C)** Large populations of MRC5 and H1299 cells appear to be settled, attached and spread on the surface of the mini-organotypic gel. Both cell types appear densely packed together in a layer no more than 90µm in thickness. Overall gel thickness is approximately 1250µm. One representative image for the 72 hour time point from triplicate gels belonging to one of two independent experiments.

3.7.3.2 Investigating invasiveness of fluorescently labelled HDF, FSF and MRC5 fibroblast cells: co-cultured with MDA-468 breast cancer cells in mini-organotypic gels

To determine which fibroblast cell line displayed maximum invasion after 72 hours when co-cultured with MDA-468 cells, HDFs, FSFs and MRC5s were labelled with CellTracker™ Green and plated in co-culture on top of mini-organotypic gels with CellTracker™ Red; labelled MDA-468 cells. 24 hours post plating, growth medium underneath each Transwell® was exchanged and excess medium from the surface of the gel was carefully removed before being replaced with serum-free medium. Transwells® were imaged via CLSM 710 and *z*-stacks were rendered, smoothened and quantified at an end point of 72 hours post plating (**Figure 3.14**).

Image analysis revealed, when MDA-468 cells were plated in co-culture with three different fibroblast cell lines, cell invasion into mini-organotypic gels was different in each combination, as previously observed (**Figure 3.13**). **Figure 3.14A** displays fluorescently labelled HDF and MDA-468 cells 72 hours post plating. Both cell types appear to have attached and spread equally on the surface of the gel. The HDF cells appear to have become polarised, changed their morphology and invaded into the gel. However, HDF cells co-cultured with MDA-468 cells have not reached the same invasive depth as when plated alone (**Figure 3.12A**) or when plated with H1299 cells (**Figure 3.13A**). This could imply that the MDA-468 cells may have decreased the rate at which HDF cells become polarised and activated, thus, slowing down the depth of invasion reached by the 72 hour time point. The bee swarm plot suggests that the MDA-468 cells have formed a cell layer approximately 80µm in depth.

Additionally, a small number of MDA-468 cells are residing underneath this layer buried deep within the invading fibroblasts, as previously observed in **Figure 3.13A** (HDF cells co-cultured with H1299). Suggesting that a small population of MDA-468 cells may have migrated into the channels in the gel, created by HDF cells, during matrix remodelling. Interestingly, observations from **Figure 3.11B**, suggest that MDA-468 cells do not migrate through mini-organotypic gels when plated alone.

Figure 3.14B displays fluorescently labelled populations of FSF and MDA-468 cells attached and homogenously to the surface of the gel 72 hours post plating. FSF cells appear to have become polarised, changed their morphology and started to invade downward through the mini-organotypic gel. The level of invasive depth reached by the FSF cells in **Figure 3.14B** (between 800-650µm) resembles similar observations

identified in **Figure 3.12B** (FSF cells alone, invasive depth between 700-550µm). The MDA-468 cells appear to have formed a layer of cells at the surface of the gel approximately 50µm thick. The bee swarm plot suggests that three individual MDA-468 cells have drifted away from the main layer and possibly migrated into the channels created by the FSF cells. Potentially with more time FSF cells could invade further through the mini-organotypic gels, thus, enabling MDA-468 cells to follow closely behind.

Figure 3.14C displays a large population of fluorescently labelled MRC5 and MDA-468 cells attached and spread evenly on the surface of the gel 72 hours post plating. As observed in **Figure 3.13C** (MRC5 co-cultured with H1299), neither cell type are seen invading through the gel. The MRC5 cells do not appear to become polarised or change their morphology however a few rounded cells have started to invade.

The 3D rendered images and bee swarm plot data suggest that HDF and FSF cells become polarised and invade through mini-organotypic gels when co-cultured with MDA-468 cells. Contrarily, MRC5 cells displayed no signs of invasion when co-cultured with MDA-468 cells, as similar previous observations (**Figure 3.13C**). All gels appear to experience some level of contraction, **Figure 3.14B** and **C** display greater contraction compared with observation of **Figure 3.14A**.

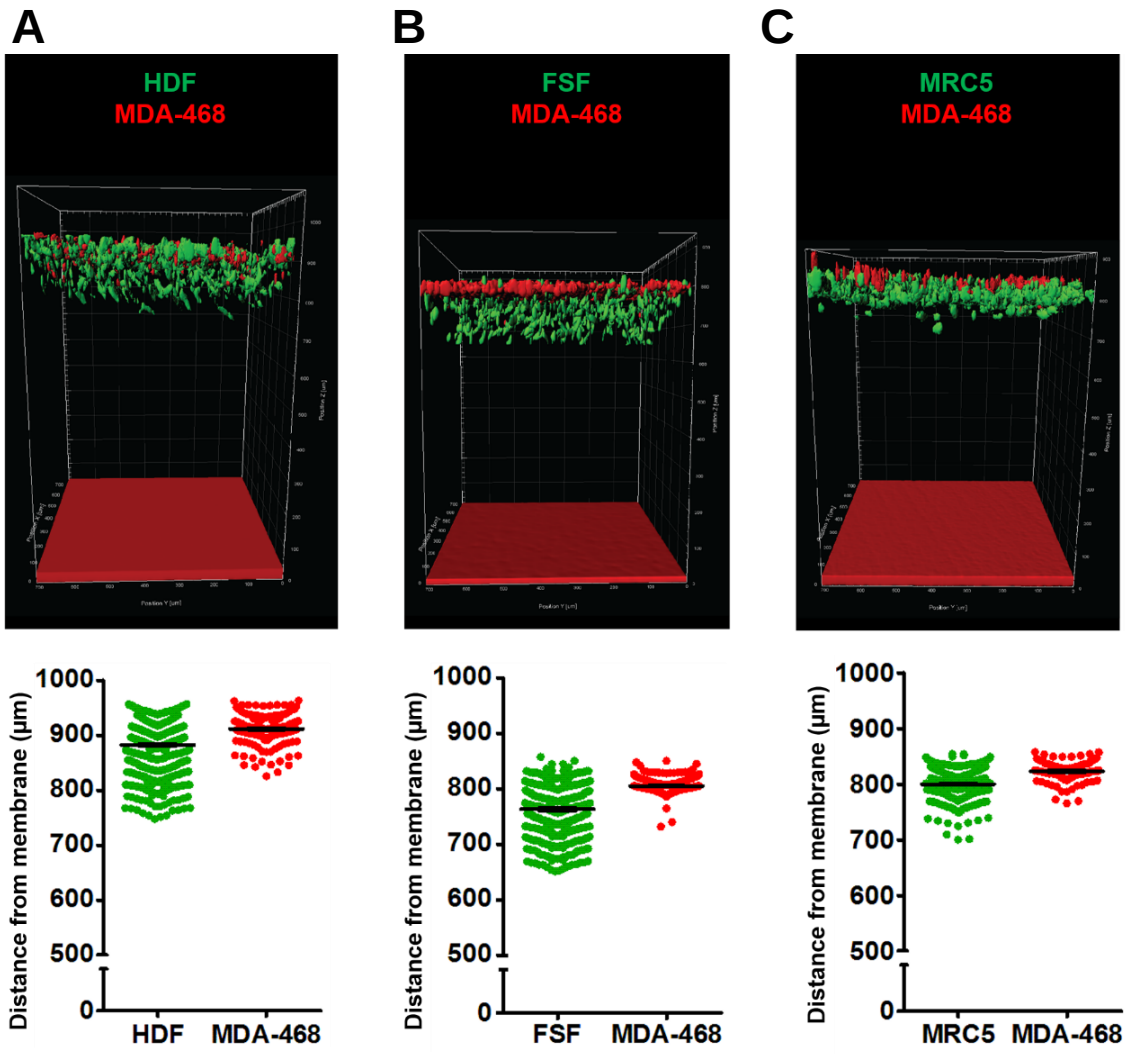

Figure 3.14: 3D rendered and quantified *z*-stacks of fluorescently labelled HDF, FSF and MRC5 cells co-cultured with fluorescently labelled MDA-468 cells in mini-organotypic gels imaged at 72 hours post plating

Figure 3.14: rendered and quantified *z*-stacks of fluorescently labelled HDF, FSF and MRC5 cells co-cultured with fluorescently labelled MDA-468 cells in mini-organotypic gels imaged at 72 hours post plating

The figure displays Imaris XT rendered and analysed 3D *z*-stack images of fluorescently labelled green HDF, FSF and MRC5 fibroblast cells co-cultured with fluorescently labelled red MDA-468 breast cancer cells. After 72 hours post cell seeding, all cells type are vibrant with colour and easily identifiable. **A)** HDF and MDA-468 cells appear attached and spread on to the surface of the gel. HDF cells have changed their polarity to that favouring a downward vertical invasion. The bee swarm plot displays a small population of MDA-468 cells migrating in to the gels. Gel thickness is approximately 900 µm. **B)** FSF and MDA-468 cells appear attached and spread on the surface of the gel. A small population of FSF cells appear to become polarised and can be observed initially invading. The bee swarm plot displays three MDA-468 cells migrating away from main cell layer in to the gel. Gel thickness is approximately 800µm. **C)** Large populations of MRC5 and MDA-468 cells appear to be settled, attached and homogenously spread on the surface of the gel. Neither cell type display signs of invasion. Both cell types appear densely packed together in a layer no more than 100µm in thickness. Overall gel thickness is approximately 1250µm. One representative image for the 72 hour time point from triplicate gels belonging to one of two independent experiments.

3.7.3.3 Investigating invasiveness of fluorescently labelled HDF, FSF and MRC5 fibroblast cells; co-cultured with VB6 OSCC in mini-organotypic gels

To examine which fibroblast cell line displayed maximum invasion after 72 hours when co-cultured with VB6 cells, HDFs, FSFs and MRC5s were labelled with CellTracker™ Green and plated in co-culture on top of mini-organotypic gels with CellTracker™ Red labelled VB6 cells. 24 hours post plating, growth medium underneath each Transwell® was exchanged and excess medium from the surface of the gel was carefully removed leaving the surface of the gels exposed for the remainder of the assay. Transwells® were imaged via CLSM 710 and *z*-stacks were rendered, smoothened and quantified at an end point of 72 hours post plating (**Figure 3.15**).

Image analysis revealed, when VB6 cells were plated in co-culture with three different fibroblast cell lines, cell invasion into mini-organotypic gels was uniquely different in each combination, as previously observed (**Figure 3.13** and Figure **3.14**). **Figure 3.15A** displays fluorescently labelled HDF and VB6 cells 72 hours post plating. Both cell types appear to have attached and spread on the surface of the gel. The HDF cells appear to have become polarised, changed their morphology and invaded deeply into the gel. Interestingly, the HDF cells co-cultured with VB6 cells reached an invasive depth, similar to that observed when HDF cells were plated alone (**Figure 3.12A**) and greater than when plated with H1299 cells (**Figure 3.13A**) and MDA-468 cells (**Figure 3.14A**). The bee swarm plot suggests that the VB6 cells have formed a cell layer approximately 100µm in depth. Additionally, a population of VB6 cells are residing underneath this layer buried deep within the invading fibroblasts, as previously observed in **Figure 3.13A** (HDF cells co-cultured with H1299). Again, as indicated previously, this suggests that a small population of VB6 cells probably migrate into the channels in the gel, created by HDF cells. Interestingly, observations from **Figure 3.11C**, suggest that VB6 cells do not migrate through mini-organotypic gels when plated alone. After 72 hours I observed both populations of cells invading through the collagen: Matrigel® substrate and at the same time notice gel contraction.

Figure 3.15B displays fluorescently labelled populations of FSF and VB6 cells attached and homogenously to the surface of the gel 72 hours post plating. FSF cells do not appear to show the same levels of polarity or invasiveness as observed in **Figure 3.15A**.

Additionally the gel appear more robust. The bee swarm plot suggests that the FSF and VB6 cells are tightly packed together in an area no greater than 50µm in depth.

Figure 3.15C displays large population of fluorescently labelled MRC5 and VB6 cells attached and spread evenly on the surface of the gel 72 hours post plating. Similar observation in **Figure 3.13C** (MRC5 co-cultured with H1299) and **Figure 3.14C** (MRC5 co-cultured with MDA-468) were seen with neither cell type invading through the gel. The MRC5 cells do not appear to become polarised or change their morphology and exhibit no signs of gel contraction.

The 3D rendered images and bee swarm plot data suggest that HDF cells become polarised and invade through mini-organotypic gels when co-cultured with VB6 cells. Contrarily, FSF and MRC5 cells displayed no or little signs of invasion when co-cultured with VB6 cells. The HDF: VB6 combination exhibits a large degree of gel contraction (gel height approximately 400µm thick), compared to the gels containing FSF (800µm) and MRC5 cells (1050µm).

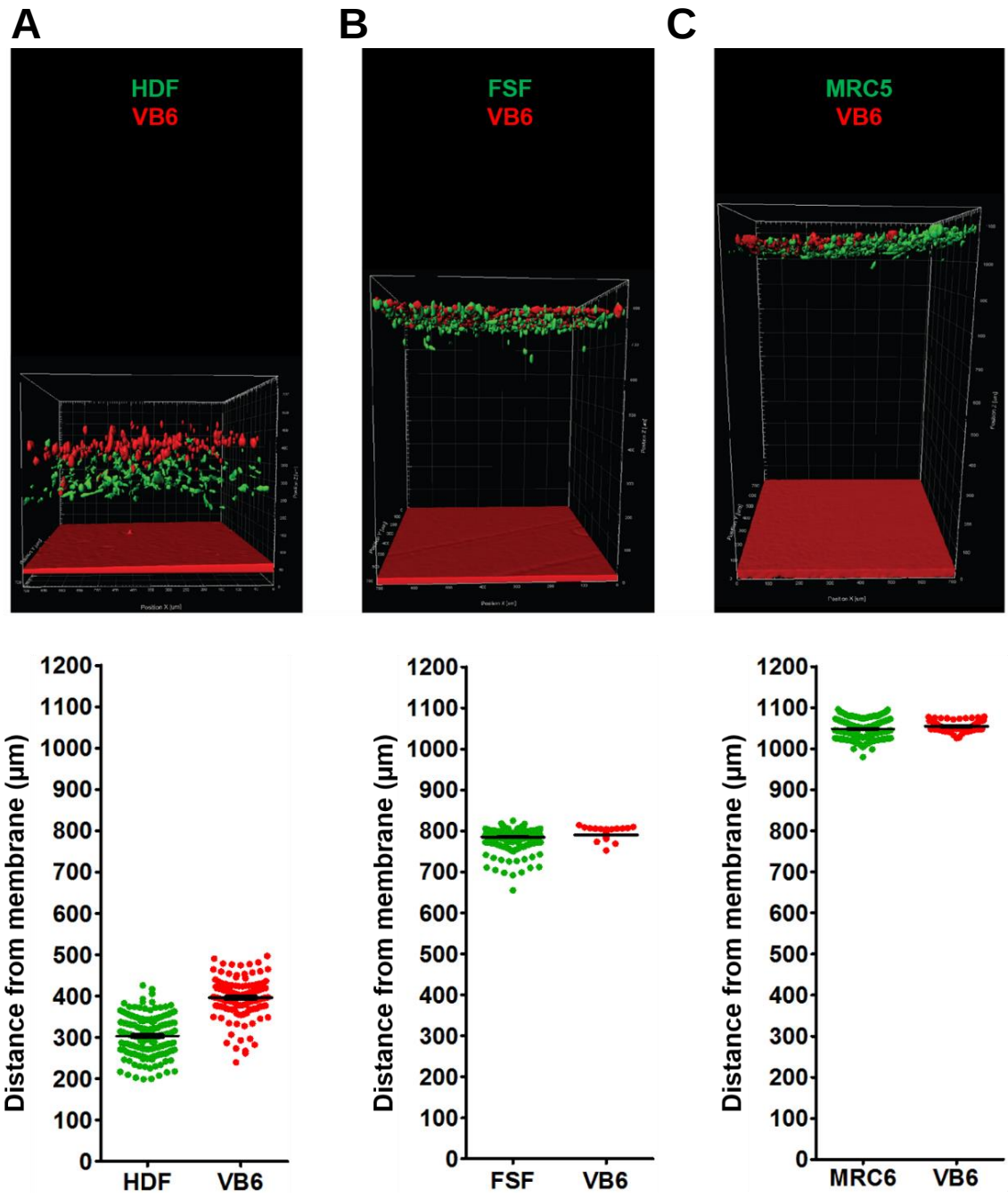

Figure 3.15: 3D rendered and quantified *z*-stacks of fluorescently labelled HDF, FSF and MRC5 cells co-cultured with fluorescently labelled VB6 cells in mini-organotypic gels imaged at 72 hours post plating

Figure 3.15: rendered and quantified *z*-stacks of fluorescently labelled HDF, FSF and MRC5 cells co-cultured with fluorescently labelled VB6 cells in mini-organotypic gels imaged at 72 hours post plating

The figure displays Imaris XT rendered and analysed 3D *z*-stack images of fluorescently labelled green HDF, FSF and MRC5 fibroblast cells co-cultured with fluorescently labelled red VB6 OSCC cancer cells After 72 hours post cell seeding, all cells type are vibrant with colour and easily identifiable. **A)** HDF and VB6 cells appear attached and spread on to the surface of the gel. HDF cells have changed their polarity to that favouring a downward vertical invasion. The bee swarm plot displays a population of VB6 cells migrating in to the gels. Gel thickness is approximately 400µm. **B)** FSF and VB6 cells appear attached and spread on the surface of the gel. FSF cells do not appear to become polarised or invade into the gel. Gel thickness is approximately 800µm. **C)** MRC5 and VB6 cells appear to be settled, attached and homogenously spread on the surface of the gel. Neither cell type display signs of invasion. Both cell types appear densely packed together in a layer no more than 100µm in thickness. Overall gel thickness is approximately 1050µm. One representative image for the 72 hour time point from triplicate gels belonging to one of two independent experiments.

3.8 Discussion

The primary aim of this study was to develop a novel 3D organotypic invasion model aided by fluorescence to capture, monitor and study live cancer cell invasion. This was achieved by combining use of transient cellular dyes, Transwell® inserts with optically clear PET membranes, a long working distance 20x objective and confocal microscopy. Thus, I have developed a new reproducible robust method to visualise tumour cells interacting with stromal fibroblasts within a 3D microenvironment *in situ*. Furthermore with the aid of image analysis we have found a suitable representation to measure and quantify cellular invasion. This assay will speed up the analysis of tumour-stromal interactions that have previously required many days of histological processing. However the assay has revealed much more about the dynamic behaviour and interactions between tumour and fibroblast cells within mini-organotypic gels.

Many labs now use the *in vitro* organotypic gel assay systems (Coleman et al., 2014b; Froeling et al., 2010; Froeling et al., 2009; Gaggioli et al., 2007; Mackenzie, 2004; Schneider et al., 2008) as they are meant to more closely mimic the *in vivo* invasive tumour front. Almost all other groups use histology to assess the invasiveness of the tumour cell component of the organotypic gel and then do so at a pre-determined end-point. However, here with the aid of confocal microscopy, we have attempted to quantify tumour and fibroblast cell invasion within a 3D gel. A similar imaging technique was used by Vial and colleagues to examine colon carcinoma cell invasion through Matrigel®-coated 8µm pore size Transwell® inserts (Vial et al., 2003). Few groups have examined the inherent invasiveness of the fibroblasts used in the assay. The data in this chapter shows that one must be very careful to monitor the invasive activity of the fibroblasts in isolation as they may be the principal determinant of cancer cell invasiveness.

Observations from this study suggest that some stromal fibroblasts cells are highly invasive through the collagen: Matrigel® substrate, in particular our HDFs (**Figure 3.8**), whereas, VB6 cancer cells are not (**Figure 3.7**). Only when combined with HDFs, do VB6 cells have the ability to ‘invade’ (**Figure 3.9**). This capacity to follow into the fibroblast pre-modelled matrix has been reported to occur *in vivo* during collective cell invasion (Alexander et al., 2008; Hegerfeldt et al., 2002). A study in 2007 described co-cultures containing carcinoma cells and stromal fibroblasts resulted in the leading cells always to be a fibroblast (Gaggioli et al., 2007). The authors used multi-photon microscopy to examine invasion through large organotypic

gels (designed by Nystrom et al., 2005). Gaggioli and colleagues reported that carcinoma cells move through the tracks and channels in the ECM behind the fibroblasts, such tracks required protease- and force- mediated matrix remodelling.

The data presented here are consistent with that of Gaggioli, that the fibroblast cells within our 3D model create tracks and channels through the mini-organotypic gel, perhaps by use of enzymes. It is widely established that MMPs have a key role in matrix degradation and remodelling by fibroblast cells (Egeblad et al., 2005; Egeblad and Werb, 2002; Raeber et al., 2007; Rhee, 2009; Yamaguchi et al., 2014). Stromal fibroblasts have been shown to participate in tumour invasion by secretion of matrix-degrading enzymes (Sreenath et al., 1992; Wernert, 1997). However the Gaggioli study failed to acknowledge the dynamic signalling between cancer cells and fibroblasts that modifies this invasive response.

Thus combining the highly invasive HDF cells with the poorly invasive MDA-468 resulted in only a moderately invasive co-culture. The HDF cells have not invaded as deeply as they are able when plated on their own and the MDA-468s have shown evidence of invasion in contrast to when they are plated on their own (compare **Figure 3.11B** and **Figure 3.14A**).

The combination of H1299 and HDF cells appears to have had an intermediate effect in-between that of the MDA-468 and HDF co-culture. When one examines the other tumour; fibroblast combinations, again there is a distinct difference in behaviour of the combined cells. This can be seen clearly in the quantitation data. It appears that, when plated alone, the FSFs and MRC5s polarise and invade slower compared to HDFs (**Figure 3.12**). Moreover, FSFs and MRC5s cell combinations with H1299, MDA-468 and VB6 cancer cells show little and in some cases, no signs of invasion, at least within the initial 72 hours (**Figure 3.13B** & **C**, **Figure 3.14B** & **C** and **Figure 3.15B** & **C**).

Initial interpretation of the VB6: HDF data might be that this is just an assay that measures fibroblast invasion, however, the assay is measuring the dynamic interactions between cancer cells and stromal fibroblasts that result in a modified behaviour of both cell types. Which signals are exchanged between the cancer cells and fibroblasts to result in these specific 3D behaviours remain unknown but are likely to be valuable to identify since they can completely change the behaviour of an invasive front. Moreover, it is likely that modifying the extracellular matrix gel composition may also modify the behaviour observed in the experiments displayed in

this chapter. Both suggestions will have to be investigated by others as it is beyond the scope of this study.

As mentioned earlier, the large organotypic gels which were previously used (Nystrom et al., 2005) are more time consuming, expensive and arduous to create than the mini-organotypic gels. However there are significant differences between the Nystrom large organotypic gels and the *in situ* analysed fluorescent mini-organotypic gels described here. Plating gels into a Transwell® insert may exert additional mediated forces on to the gel, changing its overall stiffness which could feedback and change the motility, migration and invasive capabilities of cells (Ehrbar et al., 2011; Lang et al., 2015; Zaman et al., 2006).

Additionally the large organotypic gels had fibroblasts embedded within the gel prior to the polymerisation incubation step, however **Figure 3.10** displays fluorescently labelled HDF cells residing at the bottom of the gel post polymerisation. This could be due to collagen fibril formation and mechanism. Collagen fibrils are a homogenous collection of thin rod shaped molecules before polymerisation. Polymerisation generates heterogeneous cross-linked lattice-like structures when conditions are adjusted to near physiological values (i.e., between temperatures 20-37°C and pH 6.5-8.5) producing collagen fibres >200nm wide (McPherson et al., 1985; Sung et al., 2009; Wood, 1960). Additionally, studies have reported the kinetics of *in vitro* collagen fibril development is effected by temperature, pH and integrins (Gelman et al., 1979; Velling et al., 2002; Williams et al., 1978). Perhaps the collagen fibres form at a greater rate than the rate of HDF cell polarisation and spreading.

Moreover, in the large organotypic gels, the plated tumour cells would not physically encounter as many fibroblasts as they do in the mini-organotypic assay and therefore would not have such a high cross-talk. However, as cancer cells *in vivo* do encounter fibroblasts at their invasive front the mini-organotypic gels might be considered as exaggerating the tumour: fibroblast interaction.

Overall the fluorescent mini-organotypic gels offers a reproducible, robust, and quantitative assay that allows researchers to investigate tumour-stroma interactions of any cell type in an affordable manner. Furthermore, measurable changes can be observed within 72 hours. This opens doors to conduct drug and gene library screens in 3D and this is what I have developed in the forthcoming chapters.

CHAPTER IV: RESULTS PART II

AN siRNA SCREEN INVESTIGATING THE ROLE OF FIBROBLAST PROTEASES IN REGULATING TUMOUR CELL INVASION USING A NOVEL 3D FLUORESCENT MINI-ORGANOTYPIC INVASION ASSAY

4.0 An siRNA screen investigating the role of fibroblast proteases in regulating tumour cell invasion using a novel 3D fluorescent mini-organotypic invasion assay

4.1 Background

4.1.1 Small interfering RNA (siRNA)

Gene silencing through a sequence specific manner is triggered by the introduction of double stranded RNA via a post-transcriptional process (known as RNA interference (RNAi)) (Elbashir et al., 2001). Since the discovery of genetic interference in 1998 (Fire et al., 1998), siRNA technology has become a powerful tool for temporarily silencing the expression of any target gene.

Studies have revealed that RNAi induced signalling is a two-step mechanism; (1) the first step involves the degradation of double stranded RNA (dsRNA) into siRNA (approximately 20-25 nucleotides long) by the enzyme Dicer (DCR); (2) the second step involves the siRNA being incorporated into a RNA-induced silencing complex (RISC), which subsequently identifies and silences complementary messenger RNA (mRNA) (Agrawal et al., 2003; Hannon and Rossi, 2004).

Several factors can affect the efficiency of RNAi, one of the major factor determine silencing efficiency is the length of the siRNA duplex. It was reported that a 17-nucldeotide duplex was not effective in silencing the target, however a 19-nucleuotide duplex mediated efficient silencing (Czauderna et al., 2003). Additionally, the amount of siRNA that is delivered to the host cells can effect siRNA transfection efficiency and reduce knockdown rates. Usually the siRNA duplexes are transfected using standard techniques and become diluted due to cell proliferation, thus only effective when concentration levels are sufficient (Alshamsan et al., 2009; Kim et al., 2007).

To achieve stable gene targeting is it possible to use a viral or non-viral transduction of short-hairpin (shRNA) nucleic acid that encodes the dsRNA that is then cut with DCR. Once inserted into genome each insert should produce siRNA for the life span of the cell (Huang et al., 2015).

4.1.2 Uses of siRNA technology in 2D screening methods

In published reports, siRNA and RNAi screens have been widely performed for a variety of biological studies using 2D adherent cell culture systems. Some examples include, the identification of novel targets for effective treatment of triple negative breast cancer (Lee et al., 2015), regulators of cell invasion and migration (Smolen et al., 2010) and mechanisms of resistance to drugs in liver cancer (Rudalska et al., 2014). However, the detriment of such assays lies within their incapacity to mimic a physiological microenvironment similar to that of native tissue. 3D cultures display a higher degree of structural complexity, analogous to native tissue (Hess et al., 2010) and are currently used in biological studies of tumour biology (Pampaloni et al., 2007).

High throughput siRNA screening using 2D microplate based methods are not hindered by readout limitations and are compatible with many liquid handling instruments typically available in most HTS laboratories. 2D high-throughput siRNA screens have been performed in 96-well plates (Ovcharenko et al., 2005), to 384-well microplates (Chung et al., 2008; Petrocca et al., 2013) and impressively, 1536-well nanoplates (Chung et al., 2010). However, all lacking the important significance of the third dimension (*z*-plane).

The appeal of screening in 3D is due to the ability to produce a variety of phenotypic data that are more physiologically relevant than those obtained in 2D screens. To ensure access of siRNA reagents to all cells within a 3D culture, they are typically transfected on a 2D substrate before being introduced into the 3D scaffold of choice. Current technological advances have enabled gene silencing of cancer cells in 3D models using BioChip (Abbud-Antaki et al., 2012; Marhefka and Abbud-Antaki, 2012), microfluidic platforms (Chen and Yoon, 2017) and implemented via 96-well hanging drop spheroids (InSphero AG, Switzerland) (Thoma et al., 2013). The abundance of diverse studies using RNAi technology illustrates how popular this silencing method has become over the past 20 years.

Development of a 3D screening system can be problematic in comparison to its 2D counterpart, caused by various factors, such as; (1) appointing a scaffold material and assay design that suitably represents an ECM environment with regards to the experimental question; (2) optimising an appropriate plate format to ensure optimal throughput with minimal experimental variations; (3) taking into consideration costs of consumables and reagents; (4) sourcing an appropriate microscope system, capable of imaging through *z*-depths with speed and consistency to produce high content phenotypic data for image analysis; and (5) data management; having a

system in place whereby high content multiple parameter data can be analysed via batch processing from an integrated software.

Cancer cells, have been the principal target cell of interest for the majority of *in vitro* cancer related drug and gene screens. Such screens include, targeting cancer stem cells via chemotherapeutic agents (Dragu et al., 2015), discovering potential cancer drug targets by clustered regularly interspaced short palindromic repeats (CRISP-Cas9) screening (Shi et al., 2015) or determining correlations between drug sensitivity and mutation by means of screening lung cancer cell lines for an EGFR kinase inhibitor (McDermott et al., 2008).

However, a dominant and yet often neglected component of the tumour stroma environment are the fibroblasts. Studies have suggested the prominent functional roles of these cells in cancer metastasis and progression (Gaggioli et al., 2007; Kalluri and Zeisberg, 2006; Liao et al., 2009). In this section, my aim was to investigate any changes in phenotypic behaviour of fibroblast and cancer cells when transfecting fibroblasts with siRNA that targeted proteases.

In the previous chapter, I screened three strains of fibroblasts and showed that HDFs are the most invasive cell type within 3D mini-organotypic gels, more so when plated alone, however also when co-cultured with cancer cells. Here, I focus especially on HDF cells, to perform a loss of function (LOF) siRNA screen, to observe and record any phenotypic changes when a single protease is knocked-down.

4.2 SMARTpool siRNA screen – targeting a panel of proteases in HDF cells

To examine whether gene silencing in HDF cells had any effect on invasion and matrix degradation, HDF cells were transfected with a custom library of SMARTpool siRNA and plated in co-culture with non-treated VB6 cells on to mini-organotypic gels. The custom SMARTpool siRNA library (listed in **Table 2.5**) was delivered within the inner 60 wells of a 96-well U-bottomed plate.

The siRNA transfection screen was conducted in 15 individual experiments; each experiment contained triplicate samples of four pooled siRNAs with the addition of a siGENOME non-targeting siRNA control (denoted as NT) and a transfection reagent-only treated control (listed in **Table 2.6** and displayed in **Appendix Figures 7.1 – 7.15**). The detailed experimental method is described in **Section 2.6.1**, but briefly, the concept was to use the newly optimised fluorescent 3D mini-organotypic invasion assay to identify which, if any, siRNAs inhibited HDF and VB6 cell invasion when the protease was knocked down solely in HDF cells.

HDF cells were plated into 6-well plates (1.5 x 10^5 cells/well) and the next day transfected with SMARTpool siRNA (20nM final concentration). Three days post transfection, HDF and VB6 cells were fluorescently labelled with CellTracker™ Green (10µM) and Red (5µM) respectively, counted and seeded in a 2:1 ratio of fibroblast: tumour cells on top of mini-organotypic gels. Three days post plating (six days post transfection) end point analysis *z*-stack images were acquired via CLSM. A smoothened, rendered 3D representation of the raw .lsm confocal *z*-stack was generated for each of the samples via Imaris XT image analysis software. Distance Transformation analysis was performed on the rendered 3D volumes producing .csv data files. Graphical plots of invasive depth were generated in Prism using data extrapolated from the .csv files (as described in **Section 2.5**).

Due to the cost of consumables, reagents and limited confocal microscopy usage time, the primary siRNA knockdown screen could only be conducted once and on one strain of fibroblasts (HDFs).

4.2.1 SMARTpool primary siRNA screen

Here I investigated, the effects, of siRNA knockdown in fibroblast cells of intracellularly expressed proteases using the fluorescent 3D mini-organotypic invasion assay. The series of figures that follow display 3D Imaris rendered images

of the 60 SMARTpool siRNA (arranged alphanumerically) compared against a non-targeting siRNA control (NT) at the end point of the assay (**Figure 4.1** - **Figure 4.5**). The invasive depth data, of HDF (**Figure 4.6A**) and VB6 cells (**Figure 4.6B**), was measured and plotted, compared against the NT control.

4.2.1.1 SMARTpool primary siRNA screen: calpains (CAPNs)

Calpains are a unique class of intracellular Ca^{2+} dependent cysteine proteases, with a wide array of functionalities, including, cytoskeletal remodelling, cellular signalling, cell survival and apoptosis. In mammals the calpain family is comprised of 15 members, of which nine are ubiquitously expressed in all tissues, specifically CAPN-1, -2, -4, -7 and -10 (Ono and Sorimachi, 2012; Storr et al., 2011). CAPN-3 has been identified within the skeletal muscles, whereas CAPN-5 has been expressed in the brain and CAPN-8 and -9 in the stomach (Sorimachi and Suzuki, 2001).

Figure 4.1 displays a series of 3D images containing fluorescently labelled HDF (green) cells transfected with SMARTpool CAPN-1, -2, -3, -5, -6, -7, -9, -10, -11, -13 and CAPN small subunit-1 (also known as CAPN-4) siRNA, co-cultured with fluorescently labelled VB6 cells (red). Transwells® were imaged six days post transfection via CLSM.

Image analysis shows that siRNA knockdown of CAPN-1, -2, -9, -10 and CAPNS-1 in HDFs reduces the invasion of the fibroblasts and contraction of the gels in relation to the NT sample. In contrast, HDF cells transfected with CAPN-3, -5, -6, -11 and -13 display more polarisation, changing their orientation and invading vertically through the gel, as similarly observed with the NT sample. Interestingly, CAPN-7 displays signs of gel contraction (gel height approximately 450µm), however, HDF and VB6 cells appear to be attached and spread out on to the gel. HDF cells exhibit no polarisation, change in morphology or invasion. The gel contraction displayed may be a product of matrix remodelling and evaporation of gels during incubation.

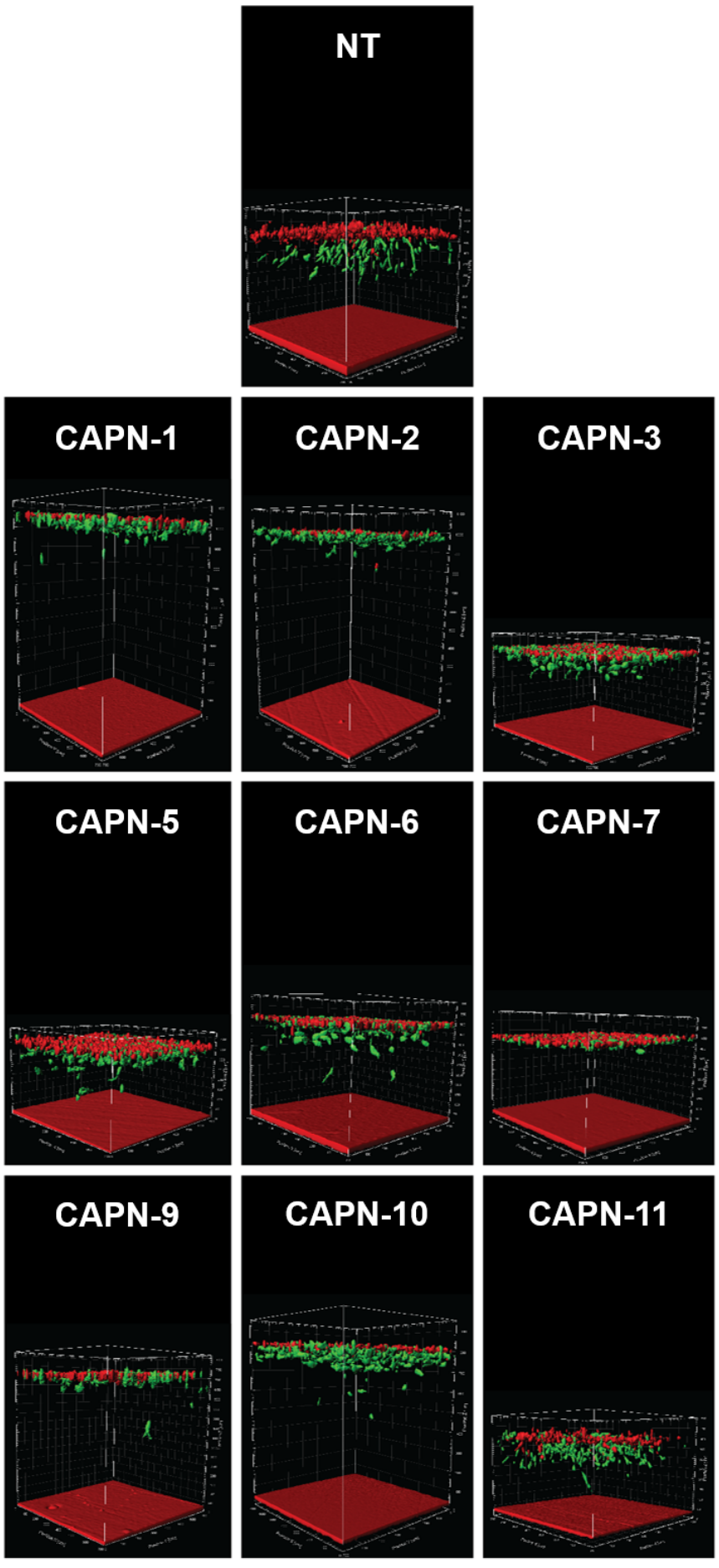
NT
CAPN-1
CAPN-2
CAPN-3
CAPN-5
CAPN-6
CAPN-7
CAPN-9
CAPN-10
CAPN-11

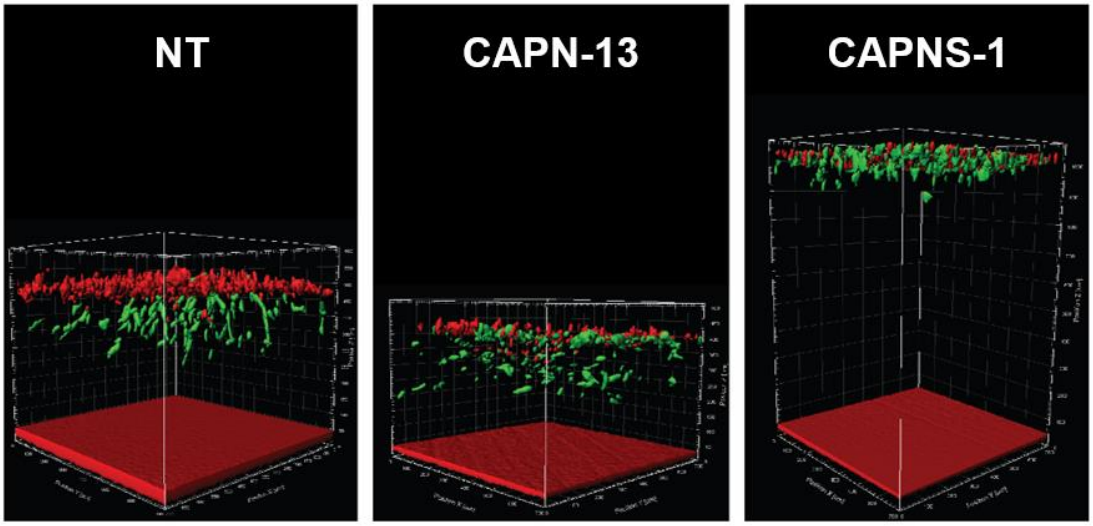

Figure 4.1: End point 3D rendered z-stacks of fluorescently labelled HDF cells transfected with siRNA to different calpains plated in mini-organotypic gels with fluorescently labelled VB6 cells

The series of images above displays 3D Imaris rendered *z*-stacks of mini-organotypic gels containing siRNA transfected HDF and non-transfected VB6 cells, six days post transfection. HDF cells were plated into a 6-well plate (1.5 x 10^5 cells/well) and after 24 hours, HDFs were transfected with siRNA (20nM) in triplicate wells. 72 hours post transfection, HDF and VB6 cells were fluorescently labelled with CellTracker™ Green (10µM) and Red (5µM) respectively. Next, HDF and VB6 cells were counted and plated (2:1 ratio of fibroblast: tumour in a suspension containing 10^5 cells in total) on to mini-organotypic gels and incubated. 72 hours post incubation (six days post transfection) *z*-stack volumes were obtained via CLSM. Images were rendered using Imaris image analysis software. Image analysis revealed HDF cells transfected with CAPN-1, -2, -10 and CAPNS-1 siRNA reduced gel contraction and HDF: VB6 cell invasion into the gel in relation to the non-targeting siRNA (NT) sample. Whereas, HDF cells transfected with CAPN-3, -5, -6, -7, -9, -11 and -13 polarised and invade into the gel. Gels appear diminished and contracted to a degree similar to that compared with observation from the NT sample. One representative image of triplicate gels belonging to one independent experiment.

4.2.1.2 SMARTpool primary siRNA screen: caspases (CASPs)

Caspases (cysteine-aspartic proteases) are a family of Ca^{2+} independent enzymes essential for maintaining homeostasis through programmed cell death (apoptosis, necrosis and pyroptosis) and are categorised as initiators or effectors based on their apoptotic signalling cascade positions (McIlwain et al., 2013; Zhivotovsky, 2003).

Figure 4.2 displays a series of 3D rendered images containing fluorescently labelled HDF (green) cells transfected with SMARTpool CASP-1, -2, -3, -4, -5, -6, -7, -8, -9, -10 and -14 siRNA, co-cultured with fluorescently labelled VB6 cells (red). Transwells® were imaged six days post transfection via CLSM.

Image analysis suggests that siRNA knockdown of CASP-1 and -8 in HDFs reduces the number of cells which that have become polarised, correlating with reduced invasion and gel contraction compared with the NT sample. Whereas, HDF cells transfected with CASP-2 and -5 display HDF cells polarising, changing their orientation and invading vertically through the gel, as similarly observed with the NT sample. Interestingly, CASP-7 displays signs of gel contraction (gel height approximately 450µm), however, HDF and VB6 cells appear to be attached and spread on to the surface of the gel. HDF cells display no signs of polarisation, change in morphology or invasion. The gel contraction observed may be products of matrix remodelling, gel contraction and evaporation during incubation. It's possible that knockdown of CASP-7 has inhibited invasion of fibroblasts cells. Furthermore, the VB6 cells plated alongside the CASP-9 and -14 transfected HDFs appear to have changed their morphology, from a spherical to an elongated form. The reasons for this are unknown and could possibly be due to signalling changes between the cells within the co-culture. Additionally, the VB6 cells in the CASP-9 and -14 samples appear less in number, suggesting that there is maybe cell death or diminished levels of the transient fluorescent dye.

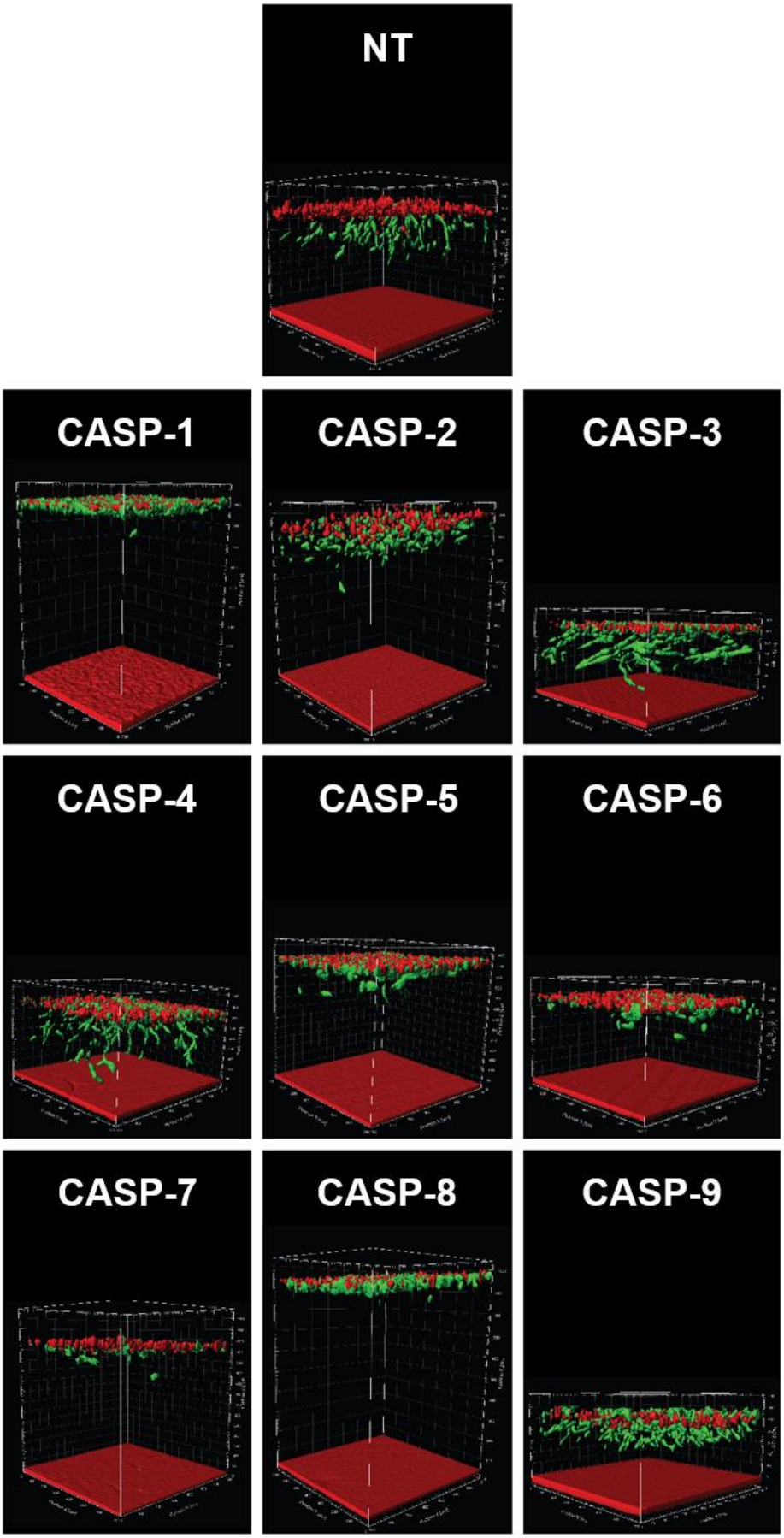
NT
CASP-1
CASP-2
CASP-3
CASP-4
CASP-5
CASP-6
CASP-7
CASP-8
CASP-9

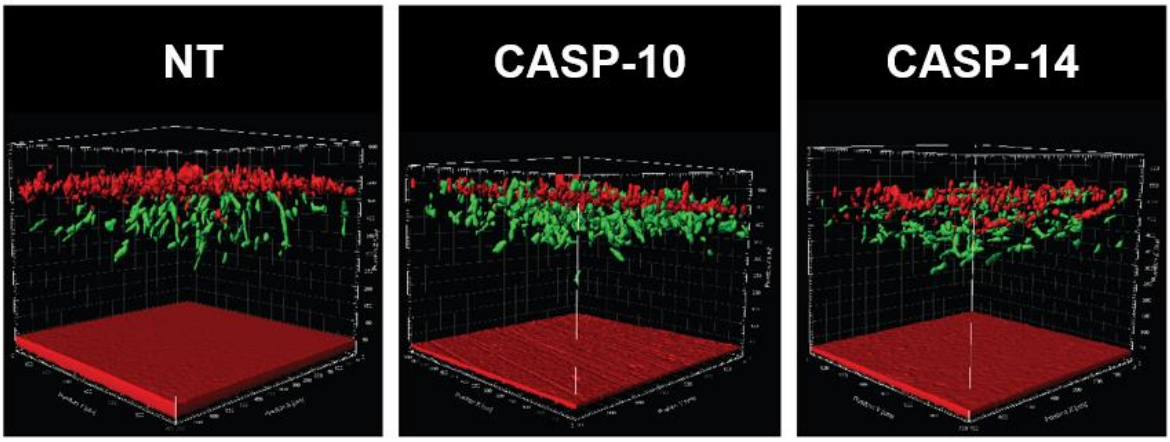

Figure 4.2: End point 3D rendered *z*-stacks of fluorescently labelled HDF cells transfected with siRNA to different caspases plated in mini-organotypic gels with fluorescently labelled VB6 cells

The series of images above displays 3D Imaris rendered *z*-stacks of mini-organotypic gels containing siRNA transfected HDF and non-transfected VB6 cells, six days post transfection. HDF cells were plated in to a 6-well plate (1.5 x 10^5 cells/well) and after 24 hours, HDFs were transfected with siRNA (20nM) in triplicate wells. 72 hours post transfection, HDF and VB6 cells were fluorescently labelled with CellTracker™ Green (10µM) and Red (5µM) respectively. Next, HDF and VB6 cells were counted and plated (2:1 ratio of fibroblast: tumour in a suspension containing 10^5 cells in total) on to mini-organotypic gels and incubated. 72 hours post incubation (six days post transfection) *z*-stack volumes were obtained via CLSM. Images were rendered using Imaris image analysis software. Image analysis revealed HDF cells transfected with CASP-1 and -8 siRNA reduced gel contraction and HDF: VB6 cell invasion into the gel in relation to the NT sample. Whereas, HDF cells transfected with CASP-3, -4, -5, -6, -7, -9, -10 and -14 show varying levels of polarisation and invasion into the gel. Gels appear diminished and contracted to a degree similar to that compared with observation from the NT sample. One representative image of triplicate gels belonging to one independent experiment.

4.2.1.3 SMARTpool primary siRNA screen: matrix metalloproteinases (MMPs)

Matrix metalloproteinases (or matrixins) are a family of zinc-containing metalloendopeptidase enzymes that are known to degrade and remodel various components of the ECM (Egeblad and Werb, 2002). Studies have identified a variety of functions and roles involving MMPs, such as, degradation of ECM proteins (Alexander et al., 1996), collagen production during wound healing (Saarialho-Kere et al., 1993) and in 2001 our laboratory revealed that the integrin αvβ6, upregulated MMP-9 and promoted migration of oral keratinocytes (Thomas et al., 2001c).

Figure 4.3 displays a series of 3D images containing fluorescently labelled HDF (green) cells transfected with SMARTpool MMP-1, -2, -3, -7, -8, -9, -10, -12, -13, -14, -15, -16, -17, -19, -20, -21, -24, -25, -26, -27 and -28 siRNA, co-cultured with fluorescently labelled VB6 cells (red). Transwells® were imaged six days post transfection via CLSM.

Image analysis suggests that siRNA knockdown of MMP-3, -9, -10, -11, -17, -20 and -21 in HDFs reduces the number of cells which become polarised, associated with reduced invasion and gel contraction in relation to the NT sample. HDF cells transfected with MMP-1, -2, -7, -12, -13, -19, -24 and -25 all display HDF polarisation, changing their orientation and invading vertically through the gel, as similarly observed with the NT sample.

Interestingly, HDF cells transfected with MMP-14, -15, -26 and -27 displays signs of gel contraction, however, HDF and VB6 cells appear to remain at the top of the gel. These HDF cells display no signs of polarisation, change in morphology or invasion. The gel contraction observed within these samples (MMP-14, -15, -26 and -27) may be products of matrix remodelling and evaporation of gels during incubation. Additionally, the knockdown of MMP-14, -15, -26 and -27 may have inhibited the ability of HDF cell to migrate or invade. In fact Stephen Weiss' group published the necessity of MMP-14 (MT1-MMP) to mediate cell invasion (Hotary et al., 2002). Furthermore, MMP-8, -16, and -28 exhibit medium levels of gel contraction, however also display signs of fibroblast cell polarisation and invasion into the gel. This may be due to diminishing siRNA effects or inefficient knockdown during the transfection process.

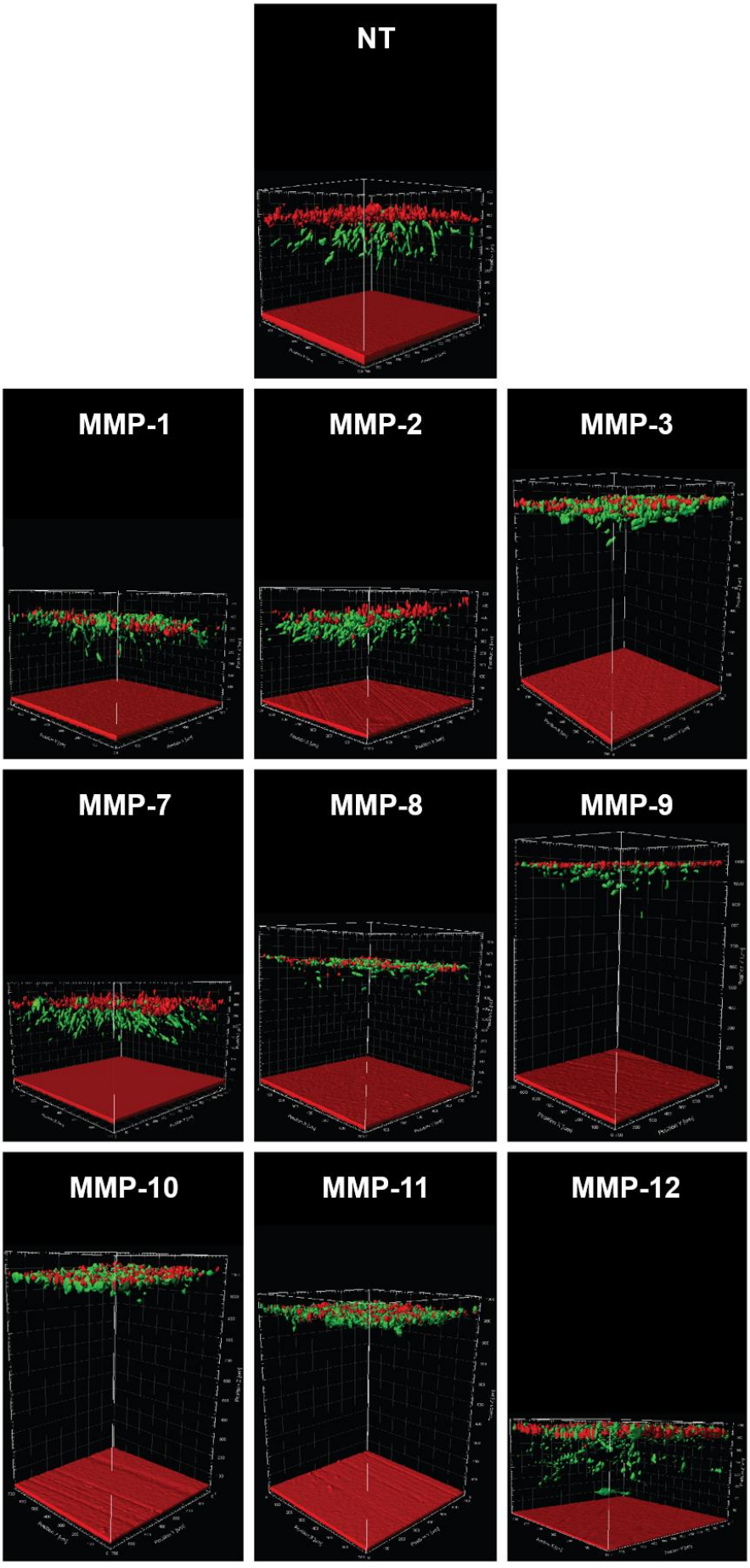
NT
MMP-1
MMP-2
MMP-3
MMP-7
MMP-8
MMP-9
MMP-10
MMP-11
MMP-12

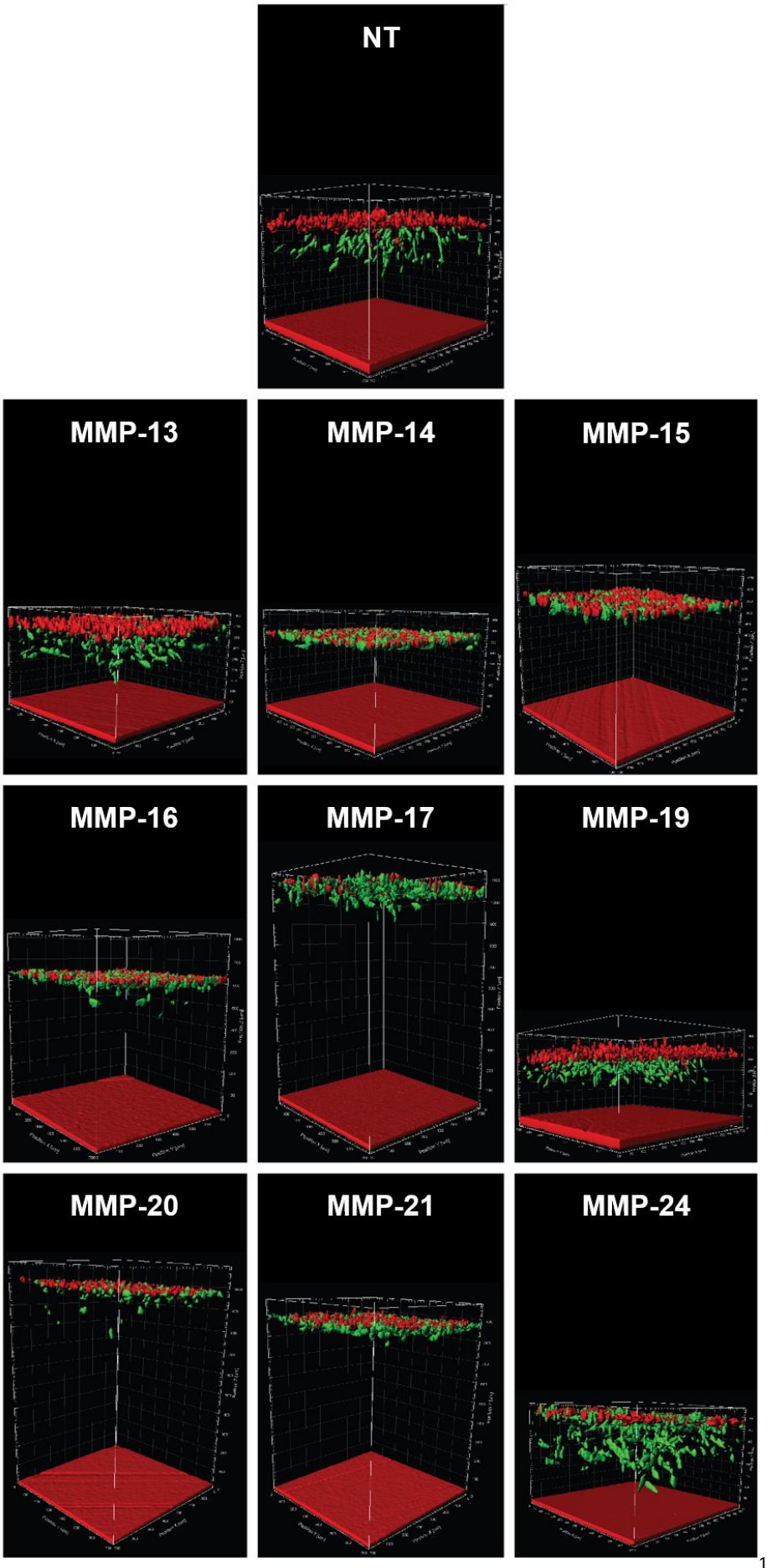
NT
MMP-13
MMP-14
MMP-15
MMP-16
MMP-17
MMP-19
MMP-20
MMP-21
MMP-24

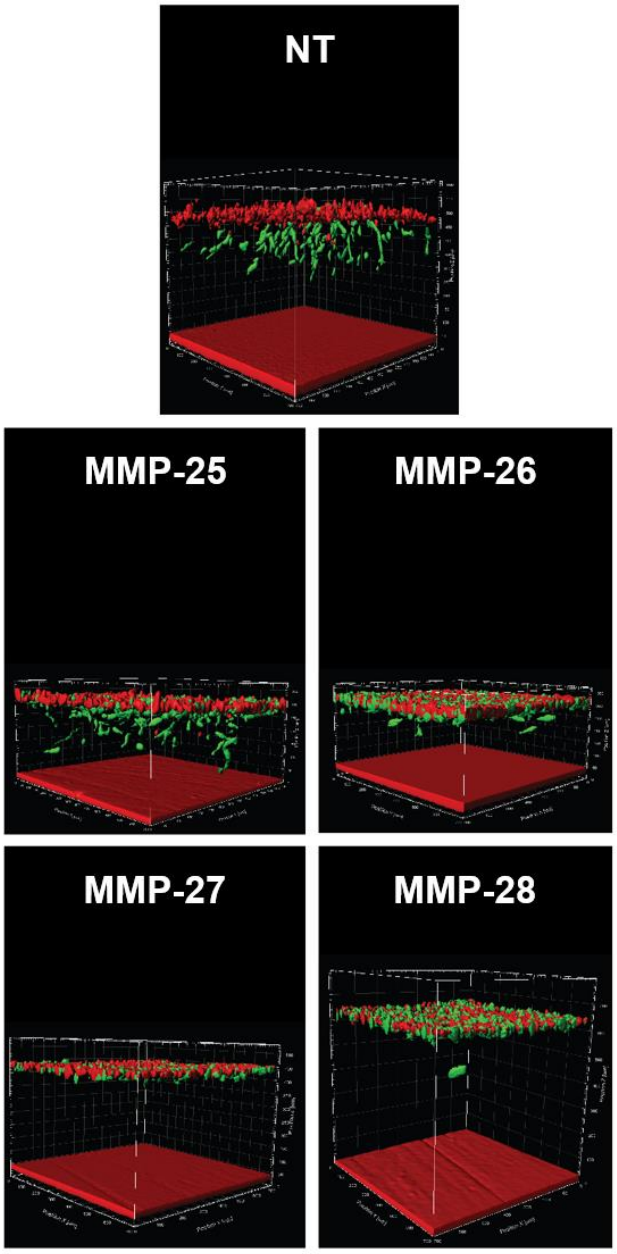

Figure 4.3: End point 3D rendered *z*-stacks of fluorescently labelled HDF cells transfected with siRNA to different matrix metalloproteinases plated in mini-organotypic gels with fluorescently labelled VB6 cells

Figure 4.3: End point 3D rendered *z*-stacks of fluorescently labelled HDF cells transfected with siRNA to different matrix metalloproteinases plated in mini-organotypic gels with fluorescently labelled VB6 cells

The series of images above displays 3D Imaris rendered *z*-stacks of mini-organotypic gels containing siRNA transfected HDF and non-transfected VB6 cells, six days post transfection. HDF cells were plated in to a 6-well plate (1.5 x 10^5 cells/well) and after 24 hours, HDFs were transfected with siRNA (20nM) in triplicate wells. 72 hours post transfection, HDF and VB6 cells were fluorescently labelled with CellTracker™ Green (10μM) and Red (5μM) respectively. Next, HDF and VB6 cells were counted and plated (2:1 ratio of fibroblast: tumour in a suspension containing 10^5 cells in total) on to mini-organotypic gels and incubated. 72 hours post incubation (six days post transfection) *z*-stack volumes were obtained via CLSM. Images were rendered using Imaris image analysis software. Image analysis revealed HDF cells transfected with MMP-3, -9, -10, -11, -17, -20 and -21 siRNA reduced gel contraction and HDF: VB6 cell invasion into the gel in relation to the NT sample. Whereas, HDF cells transfected with MMP-1, -2, -7, -12, -13,-14, -15, -19, -24, -25, -26 and -27 show varying levels of polarisation and invasion into the gel. Gels appear diminished and contracted to a degree similar to that compared with observation from the NT sample. One representative image of triplicate gels belonging to one independent experiment.

4.2.1.4 SMARTpool primary siRNA screen: serine protease inhibitors (SERPINs) and sonic hedgehog (SHH)

Serine protease inhibitors (known as SERPINs) are a superfamily of inhibitors that use a conformational change to inhibit target enzymes. Over 1,500 SERPIN-like genes have been identified in animals, bacteria, plants and poxviruses. However in humans, 36 SERPINs have been identified as extracellular molecules (Law et al., 2006).

SHH is one of three hedgehog homologues present in mammals, the others being Desert (DHH) and Indian (IHH). The SHH pathway has been reported during early embryonic cortical (Rash and Grove, 2007) and neuronal development (Lewis and Eisen, 2001). It has also been implicated with regulating stromal fibroblast behaviour in cancers (Fendrich et al., 2011; Thayer et al., 2003) and was the target for clinical trials in pancreatic cancer (Kim et al., 2014). It was included in the screen as a non-protease target likely to affect fibroblast promoted invasion.

Figure 4.4 displays a series of 3D images containing fluorescently labelled HDF (green) cells transfected with SMARTpool SERPIN-A1, -A3, -B2, -B12, -D1, E1, -F1 and SHH co-cultured with fluorescently labelled VB6 cells (red). Transwells® were imaged six days post transfection via CLSM.

Image analysis shows that siRNA knockdown of SERPIN-D1 and -F1 in HDFs reduces the number of HDF cells that become polarised, thus inhibiting invasion and gel contraction in relation to the NT sample. Whereas, HDF cells transfected with SERPIN-A3 and SHH display HDF cell polarisation, changing their orientation and invading vertically through the gel, as similarly observed with the NT sample. Interestingly, SERPIN-A1, -B2, -B12 and -E1 displays medium levels of gel contraction, however, also display early levels of fibroblast cell polarisation and invasion into the gel. This may be due to diminishing siRNA effects or inefficient knockdown during the transfection process.

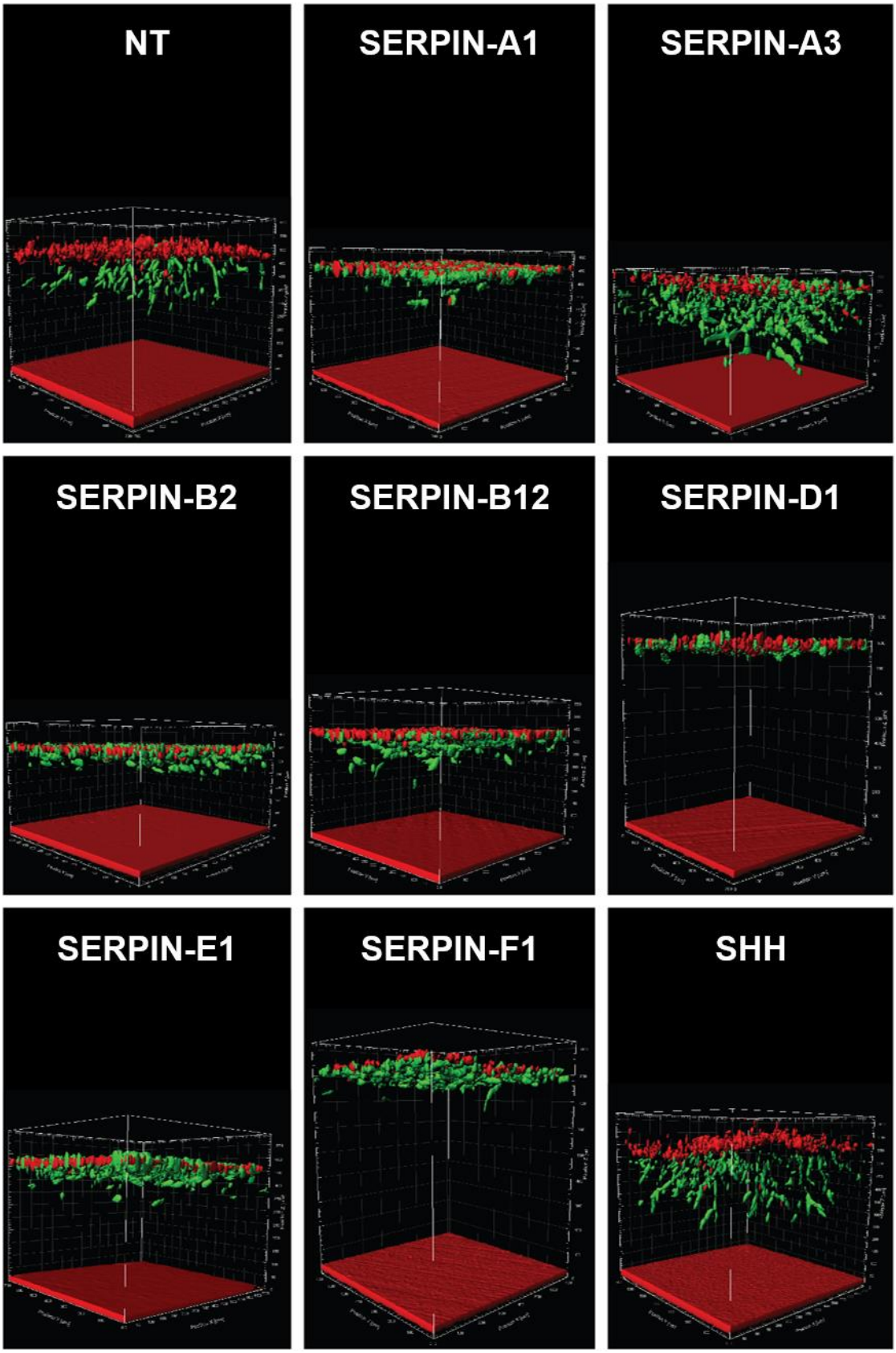

Figure 4.4: End point 3D rendered *z*-stacks of fluorescently labelled HDF cells transfected with siRNA to different serpins and sonic hedgehog in mini-organotypic gels with fluorescently labelled VB6 cells

Figure 4.4: End point 3D rendered *z*-stacks of fluorescently labelled HDF cells transfected with siRNA to different serpins and sonic hedgehog in mini-organotypic gels with fluorescently labelled VB6 cells

The series of images above displays 3D Imaris rendered *z*-stacks of mini-organotypic gels containing siRNA transfected HDF and non-transfected VB6 cells, six days post transfection. HDF cells were plated in to a 6-well plate (1.5 x 10^5 cells/well) and after 24 hours, HDFs were transfected with siRNA (20nM) in triplicate wells. 72 hours post transfection, HDF and VB6 cells were fluorescently labelled with CellTracker™ Green (10µM) and Red (5µM) respectively. Next, HDF and VB6 cells were counted and plated (2:1 ratio of fibroblast: tumour in a suspension containing 10^5 cells in total) on to mini-organotypic gels and incubated. 72 hours post incubation (six days post transfection) *z*-stack volumes were obtained via CLSM. Images were rendered using Imaris image analysis software. Image analysis revealed HDF cells transfected with SERPIN-D1 and -F1 siRNA reduced gel contraction and HDF: VB6 cell invasion into the gel in relation to the NT sample. Whereas, HDF cells transfected with SERPIN-A1, -A3, -B2, -B12, -E1 and SHH show varying levels of polarisation and invasion into the gel. Gels appear diminished and contracted to a degree similar to that compared with observation from the NT sample. One representative image of triplicate gels belonging to one independent experiment.

4.2.1.5 SMARTpool primary siRNA screen: transmembrane serine proteases (TMPRSSs)

Transmembrane serine proteases are a class of membrane-bound proteolytic enzymes, which have been identified to play roles in activation of virus entry within in acute respiratory syndromes (Shulla et al., 2011), hearing loss (Guipponi et al., 2008) and cancer (Tuhkanen et al., 2013).

Figure 4.5 displays a series of 3D images containing fluorescently labelled HDF (green) cells transfected with SMARTpool TMPRSS-2, -3, -4, -5, -6, -9, -11A and -13 co-cultured with fluorescently labelled VB6 cells (red). Transwells® were imaged six days post transfection via CLSM.

Results show that siRNA knockdown of TMPRSS-13 in HDFs reduces the number of cells that become polarised correlating with reduced invasion and gel contraction in relation to the NT sample. Whereas, HDF cells transfected with TMPRSS-2, -3, -5, -9 and -11A display HDF cells polarising, changing their orientation and invading vertically through the gel, as similarly observed with the NT sample. Interestingly, TMPRSS-4 and -6 displays medium levels of gel contraction, however, also display early levels of fibroblast cell polarisation and invasion into the gel. This may be due to diminishing siRNA effects or inefficient knockdown during the transfection process.

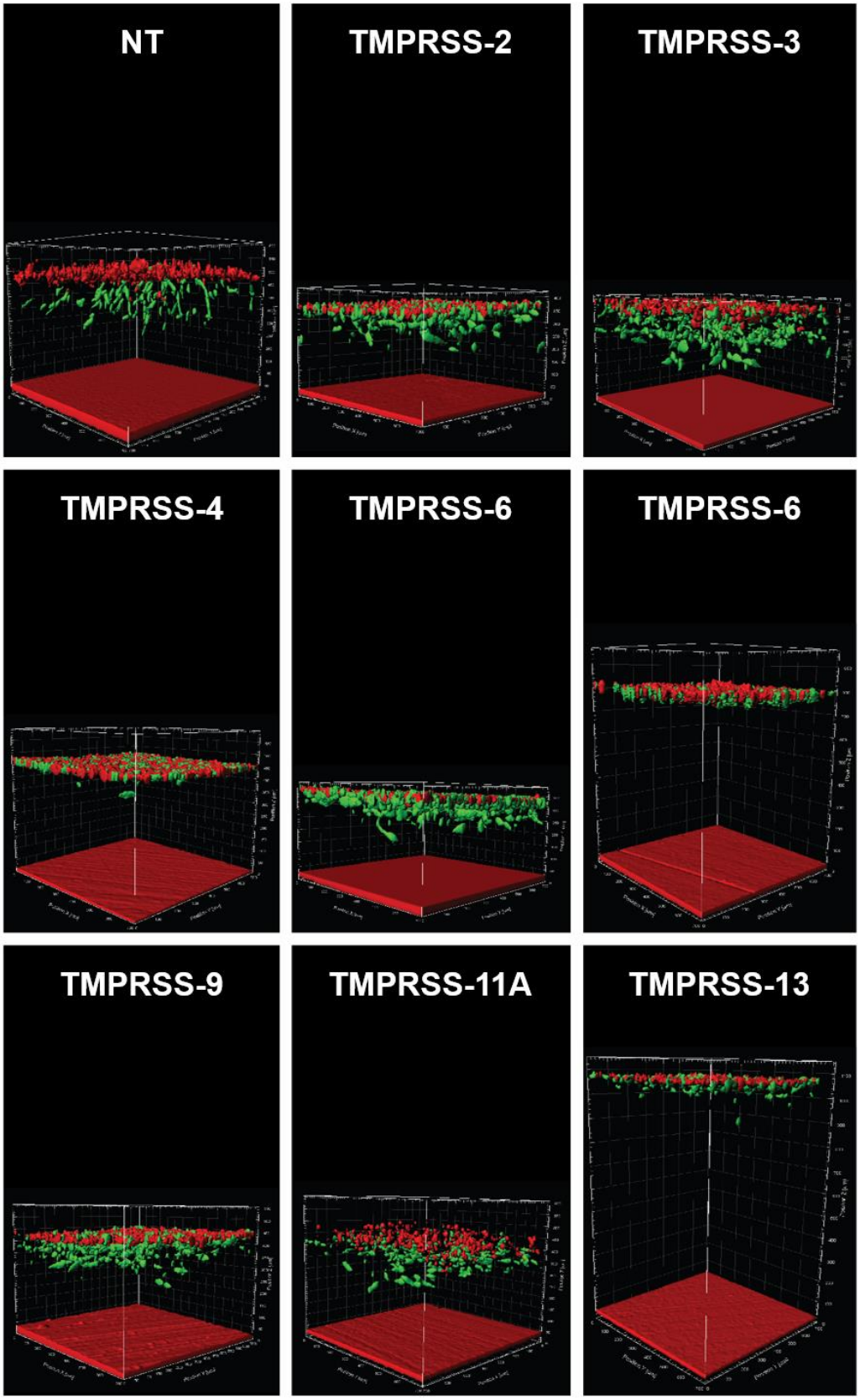

Figure 4.5: End point 3D rendered *z*-stacks of fluorescently labelled HDF cells transfected with siRNA to different transmembrane serine proteases in mini-organotypic gels with fluorescently labelled VB6 cells

Figure 4.5: End point 3D rendered *z*-stacks of fluorescently labelled HDF cells transfected with siRNA to different transmembrane serine proteases in mini-organotypic gels with fluorescently labelled VB6 cells

The series of images above displays 3D Imaris rendered *z*-stacks of mini-organotypic gels containing siRNA transfected HDF and non-transfected VB6 cells, six days post transfection. HDF cells were plated in to a 6-well plate (1.5 x 10^5 cells/well) and after 24 hours, HDFs were transfected with siRNA (20nM) in triplicate wells. 72 hours post transfection, HDF and VB6 cells were fluorescently labelled with CellTracker™ Green (10µM) and Red (5µM) respectively. Next, HDF and VB6 cells were counted and plated (2:1 ratio of fibroblast: tumour in a suspension containing 10^5 cells in total) on to mini-organotypic gels and incubated. 72 hours post incubation (six days post transfection) *z*-stack volumes were obtained via CLSM. Images were rendered using Imaris image analysis software. Image analysis revealed HDF cells transfected with TMPRSS-13 siRNA reduced gel contraction and HDF: VB6 cell invasion into the gel in relation to the NT sample. Whereas, HDF cells transfected with TMPRSS-2, -3, -4, -5, -6, -9 and -11A show varying levels of polarisation and invasion into the gel. Gels appear diminished and contracted to a degree similar to that compared with observation from the NT sample. One representative image of triplicate gels belonging to one independent experiment.

4.2.1.6 Identification of hits from SMARTpool primary siRNA screen

To determine whether knockdown of siRNA from the SMARTpool library had any significant effect on fibroblast cell invasion when compared against the NT sample, data were collected and plotted in prism. A waterfall histogram plot, displays the HDFs (**Figure 4.6A**) and VB6s (**Figure 4.6B**) average distance from the PET membrane for all 60 siRNAs relative to the NT control sample. Statistical analysis identified 16 gene candidates that reduced HDF and VB6 cell invasion when knocked down in HDF cells.

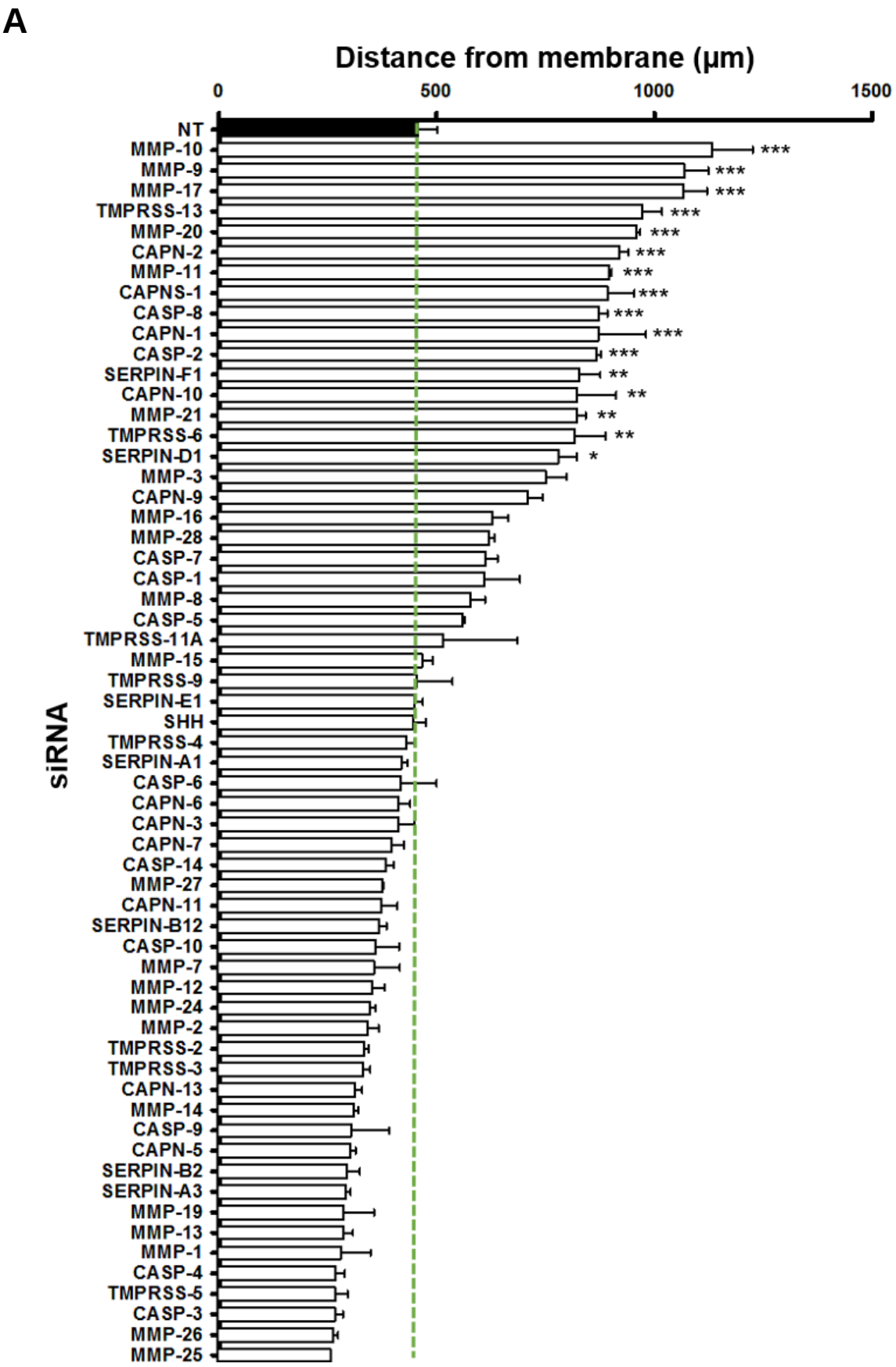
A
Distance from membrane (µm)
0
500
1000
1500
siRNA
NT
MMP-10
MMP-9
MMP-17
TMPRSS-13
MMP-20
CAPN-2
MMP-11
CAPNS-1
CASP-8
CAPN-1
CASP-2
SERPIN-F1
CAPN-10
MMP-21
TMPRSS-6
SERPIN-D1
MMP-3
CAPN-9
MMP-16
MMP-28
CASP-7
CASP-1
MMP-8
CASP-5
TMPRSS-11A
MMP-15
TMPRSS-9
SERPIN-E1
SHH
TMPRSS-4
SERPIN-A1
CASP-6
CAPN-6
CAPN-3
CAPN-7
CASP-14
MMP-27
CAPN-11
SERPIN-B12
CASP-10
MMP-7
MMP-12
MMP-24
MMP-2
TMPRSS-2
TMPRSS-3
CAPN-13
MMP-14
CASP-9
CAPN-5
SERPIN-B2
SERPIN-A3
MMP-19
MMP-13
MMP-1
CASP-4
TMPRSS-5
CASP-3
MMP-26
MMP-25
***
***
***
***
***
***
***
***
***
***
***
**
**
**
**
*

B

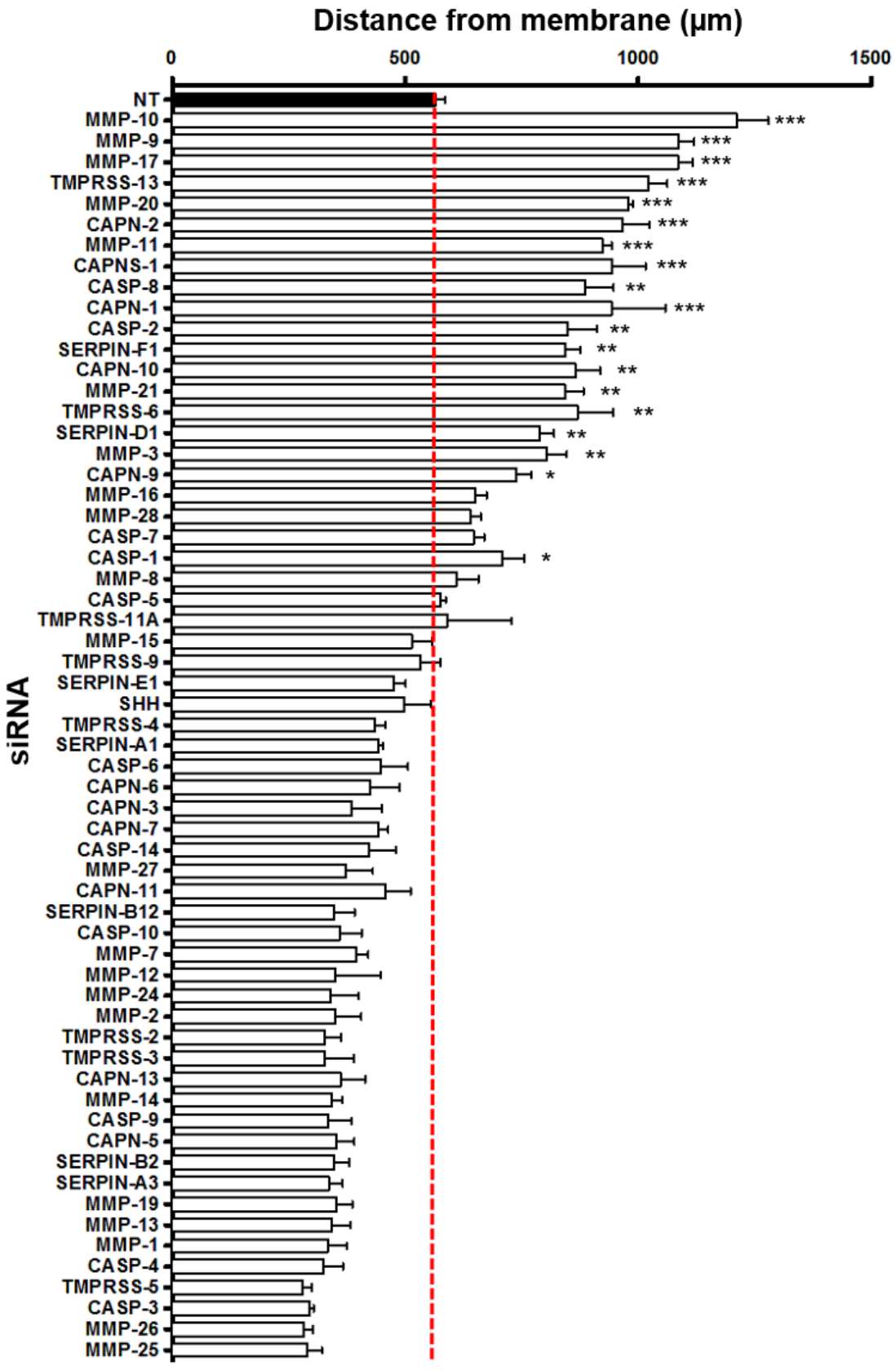
Distance from membrane (µm)
0
500
1000
1500
siRNA
NT
MMP-10 ***
MMP-9 ***
MMP-17 ***
TMPRSS-13 ***
MMP-20 ***
CAPN-2 ***
MMP-11 ***
CAPNS-1 ***
CASP-8 **
CAPN-1 ***
CASP-2 **
SERPIN-F1 **
CAPN-10 **
MMP-21 **
TMPRSS-6 **
SERPIN-D1 **
MMP-3 **
CAPN-9 *
MMP-16
MMP-28
CASP-7
CASP-1 *
MMP-8
CASP-5
TMPRSS-11A
MMP-15
TMPRSS-9
SERPIN-E1
SHH
TMPRSS-4
SERPIN-A1
CASP-6
CAPN-6
CAPN-3
CAPN-7
CASP-14
MMP-27
CAPN-11
SERPIN-B12
CASP-10
MMP-7
MMP-12
MMP-24
MMP-2
TMPRSS-2
TMPRSS-3
CAPN-13
MMP-14
CASP-9
CAPN-5
SERPIN-B2
SERPIN-A3
MMP-19
MMP-13
MMP-1
CASP-4
TMPRSS-5
CASP-3
MMP-26
MMP-25

Figure 4.6: Analysing the effects of siRNA knockdown of proteases in HDF cells within 3D mini-organotypic gels plated with fluorescent VB6 cells

The figure displays average cell distance from the PET membrane for all 60 siRNAs. The height of each bar signifies depth of invasion, therefore, the shorter the bar the great the invasion. *Z*-position data of HDF cells within the mini-organotypic gels six days post transfection were collected and plotted in Prism and compared to the NT siRNA control. **A)** HDF cell waterfall plot displaying average height of cells six days post transfection. The green dashed line represents the average for the NT sample HDF cells. **B)** VB6 cell average height plotted in the same arrangement HDF siRNA treatment. Red dashed line represents the average for the NT sample VB6 cells Results display the mean and s.d of triplicate samples from one biological experiment. One-way ANOVA, *** $p < 0.001$, ** $p < 0.01$, * $p < 0.05$.

4.2.2 Summary of hits from SMARTpool primary siRNA screen

The results of the siRNA screen identified 16 siRNAs that significantly reduced ($p<0.05$) HDF and VB6 cell invasion as well as gel shrinkage when knocked down in HDF cells (summarised in **Table 4.1**). **Figure 4.6** provides a unique insight to the five main protease families that comprise the screen (calpains, caspases, matrix metalloproteinases, serine peptidase inhibitors and transmembrane serine proteases).

The 16 hits comprise of; six matrix metalloproteinases (MMP-9, -10, -11, -17, -20 and -21); four calpains (CAPN-1, -2, -10 and sub-unit 1); two caspases (CASP-2 and -8); two serine peptidase inhibitors (SERPIN-D1 and -F1); and two transmembrane serine proteases (TMPRSS-6 and -13) (displayed in **Figure 4.7**). The data show multiple protease families appear to have a substantial role in fibroblast biology, which, in turn is having a direct effect on invasion and migration of cancer cells in 3D mini-organotypic gels.

Table 4.1: List of hits from primary SMARTpool siRNA screen

siRNA	Level of significance	References	Function in cancer
CAPN-1	***	(Al-Bahlani et al., 2017; Luo et al., 2016)	Apoptosis Proliferation Migration Adhesion Autophagy
CAPN-2	***	(Ho et al., 2012; Mamoune et al., 2003)	
CAPN-10	**	(Ling et al., 2009; Moreno-Luna et al., 2011)	
CAPNS-1	***	(Bertoli et al., 2009)	
CASP-2	***	(Ho et al., 2009; McIlwain et al., 2013; Shin et al., 2005)	Apoptosis Necrosis
CASP-8	***	(Kolenko et al., 1999; McIlwain et al., 2013; Shivapurkar et al., 2002)	
MMP-9	***	(P et al., 2000; Simon et al., 1998; Thomas et al., 2001a)	ECM degradation Metastasis Angiogenesis Wound healing Migration
MMP-10	***	(Regala et al., 2011; Zhang et al., 2014)	
MMP-11	***	(Kou et al., 2013)	
MMP-17	***	(Chabottaux et al., 2006)	
MMP-20	***	(Saxena et al., 2015)	
MMP-21	**	(Wu et al., 2013)	
SERPIN-D1	*	(Bosse et al., 2012)	Inflammation Supresses tumour growth Antiangiogenic
SERPIN-F1	**	(Dawson et al., 1999; Fitzgerald et al., 2012; Yang et al., 2009)	
TMPRSS-6	**	(Hartikainen et al., 2006; Tuhkanen et al., 2013)	Tumourigenesis
TMPRSS-13	***	-	

***** p < 0.001, ** p < 0.01, * p < 0.05**

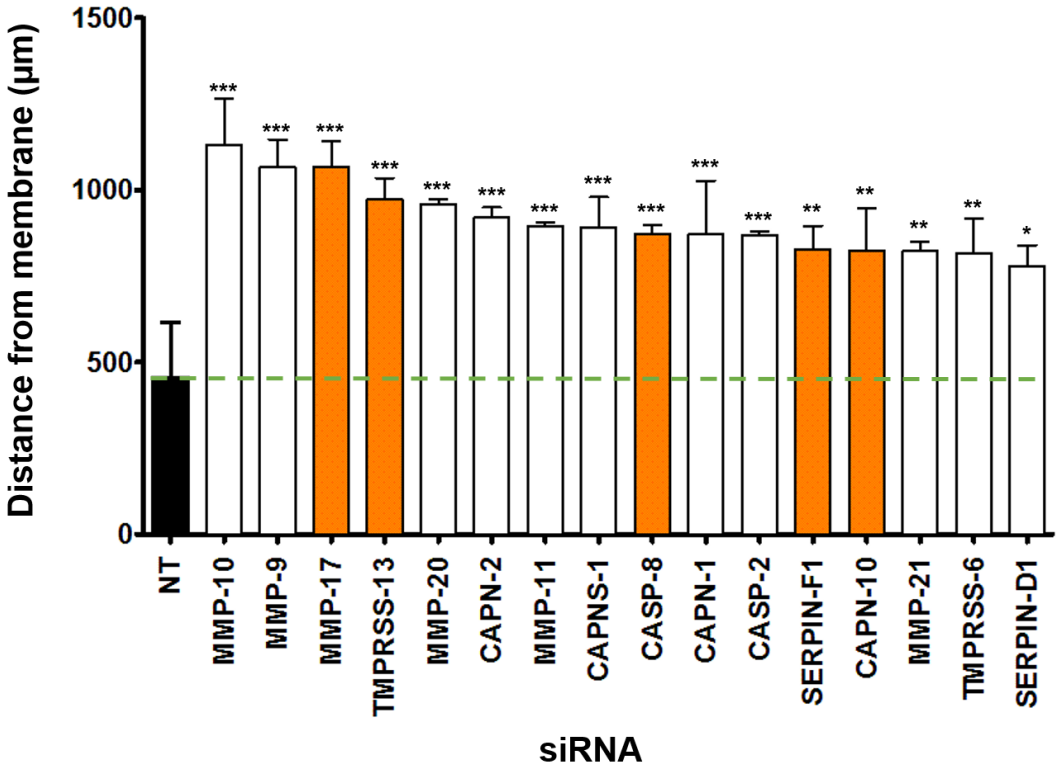

Figure 4.7: Summary of hits from primary SMARTpool siRNA screen

The figure displays the significant hits (One-way ANOVA, *** $p < 0.001$, ** $p < 0.01$, * $p < 0.05$) from the primary siRNA screen. The solid orange bars indicate the five selected siRNA hits I choose to follow up. The green dashed line represents the average for the NT sample. Results display the mean and s.d of triplicate samples.

4.3 Investigation of hits from primary SMARTpool siRNA screen

Due to cost and time factors, all of the 16 siRNA hits could not be investigated. Therefore five siRNA were chosen to pursue and validate based on; (1) their relevance, if any, towards cancer progression; (2) their novelty as potential targets; and (3) commercial availability of known working antibodies.

The chosen siRNA to pursue were calpain-10 (CAPN-10), caspase-8 (CASP-8), matrix metalloproteinase-17 (MMP-17), serine peptidase inhibitor clade-F (SERPIN-F1) and transmembrane protease, serine-13 (TMPRSS-13) (highlighted by orange filled bars in **Figure 4.7**).

To confirm observations from the SMARTpool primary screen, the five selected hits were re-tested. HDF cells were once again, plated, transfected with pooled siRNA, alongside a NT control and a transfection reagent-only treated control (denoted as Control) and imaged in the same manner as described above. Unfortunately, at the end point of the assay the confocal microscope was unavailable due to technical issues. Therefore mini-organotypic gels containing siRNA treated HDF cells were fixed and stained with H&E and the level of gene knockdown was confirmed via qPCR (**Figure 4.8**).

4.3.1 Repeating siRNA knockdown on pooled; CAPN-10, CASP-8, MMP-17, SERPIN-F1 and TMPRSS-13

The H&E stained images (**Figure 4.8A**) show HDF and VB6 cells invading as expected within the NT siRNA control and non-transfected HDF (denoted as Control) samples, with clear signs of both cell types invading through the mini-organotypic gel towards the bottom of the Transwell®. Conversely, the gels with siRNA treated HDFs appear not to have invaded in comparison to NT and Control samples. Thus, probably reducing the HDFs ability to remodel the gel and create channels which cancer cells migrate through.

The siRNA within the HDF cells may also have an effect on the surrounding VB6 cells when plated together on top of the gels. Within the siRNA treated samples, a small number of cells appear to start invading through the gel; I believe these could be fibroblast cells (due to their spindle-like appearance) that have polarised and started to initially invade. This could be due to low knockdown efficiency during transfection stage, or diminished siRNA effects. **Figure 4.8B** demonstrates at least 70% gene silencing was induced for all five pooled siRNA. Overall these results, firstly suggest

via H&E and qPCR data, that each of the selected siRNAs may have an effect on mediating fibroblast cell invasion in 3D gels. Secondly, the 24-well mini-organotypic invasion assay is a suitable, reliable and reproducible method for siRNA studies.

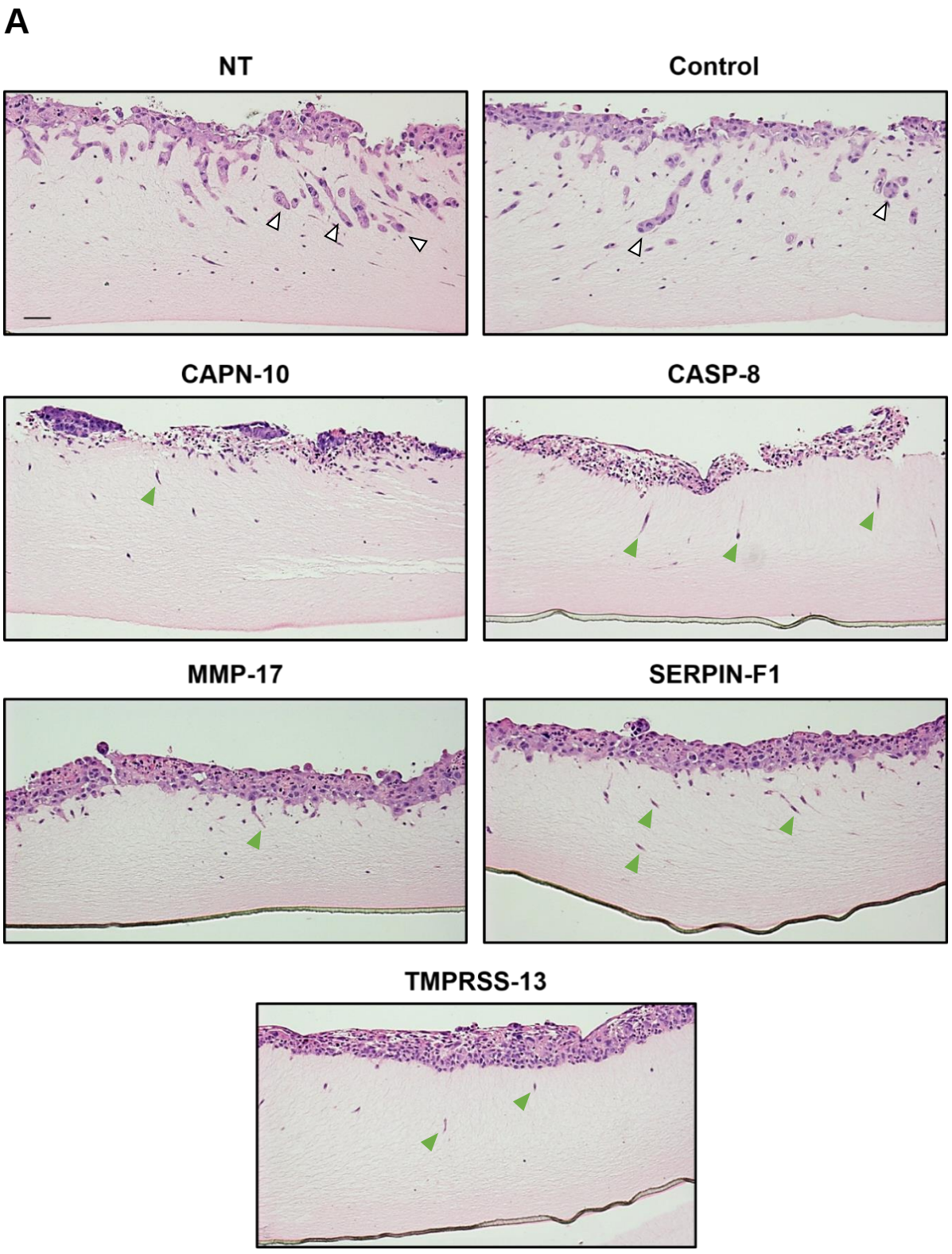
A
NT
Control
CAPN-10
CASP-8
MMP-17
SERPIN-F1
TMPRSS-13

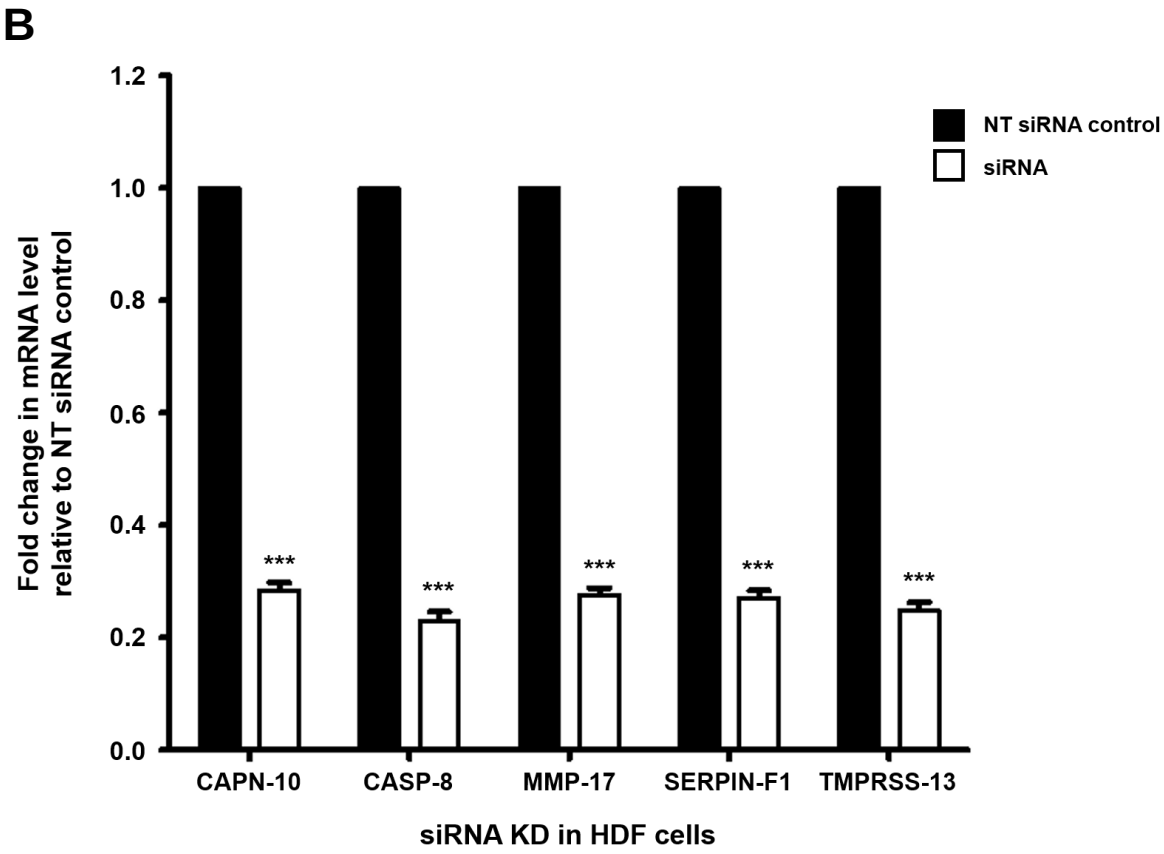

Figure 4.8: Representative H&E stained sections of 3D-miniorganotypic gels with siRNA knockdown HDF cells and confirmation via qPCR

A) HDF were pre-treated with five chosen pooled siRNA, 6 days post transfection, mini-organotypic gels were fixed and H&E stained. NT and Control (top left and right panel) display fibroblast and cancer cell collectively invading (indicated by white arrows). siRNA knockdown samples show reduced fibroblast and cancer cell invasion. A small number of fibroblast cells can be seen invading vertically (indicated by green arrows). One representative of triplicate samples. Scale bar 100µm, x20 objective. **B)** siRNA knockdown examined using qPCR (NT = non targeting siRNA control); *** $p<0.001$ students paired *t*-test. Data shown represents s.d from triplicate samples from one independent experiment.

4.4 Hit validation of SMARTpool siRNA using individual deconvoluted siRNAs

The approach to test pooled siRNA duplexes that can target a single given gene maximises resources and increases throughput. However pooled screens do not provide any insight into the activity of the individual siRNAs contributing to a given change in phenotypic behaviour. On the contrary, individual siRNA duplex experiments, do require considerable commitments in terms of consumables, however permitting stratification of the hits into groups based on particular phenotypic discoveries.

Here, investigation into the pooled siRNAs was performed, via LOF validation screen. Therefore each of the four individual siRNA duplexes of CAPN-10 (**Figure 4.9**), CASP-8 (**Figure 4.10**), MMP-17 (**Figure 4.11**), SERPIN-F1 (**Figure 4.12**) and TMPRSS-13 (**Figure 4.13**) were purchased and knocked down in HDF cells (summarised in **Table 2.7**).

(**Figure 4.9A** - **Figure 4.13A**) display 3D rendered Imaris images of the siRNA knocked down in HDF cells. Graphical bee swarm plots, indicating exact *z*-positions of HDF and VB6 cells within the gel were plotted to display invasive capability compared against the NT (**Figure 4.9B** - **Figure 4.13B**). At least two siRNA molecules are expected to recapitulate phenotypic changes induced by the pool and be confirmed by clear correlations in protein level depletion to establish a relationship between the gene and the response.

4.4.1 Hit validation of pooled siRNA using individual molecules to identify active species for CAPN-10

To determine which four, if any, of the individual CAPN-10 constituents (represented as 1, 2, 3 and 4) had any effect whatsoever on the phenotypic properties of HDF cells or gel integrity, HDF cells were, plated, transfected (in triplicate) with the single siRNA duplexes (after 24 hours), fluorescently labelled and co-cultured with fluorescent VB6 cells on to mini-organotypic gels (after 72 hours) and imaged via CLSM (after another 72 hours) as previously described in **Section 2.6.1** (**Figure 4.9**). **Figure 4.9A** displays a panel of 3D Imaris rendered images containing a NT siRNA control sample and the individual siRNA duplexes transfected into HDF cells.

Image analysis observations suggest the HDF cells do not become polarised or invade through the organotypic gel compared with the NT sample. With the exception

of siRNA number 1 and 2, a small number of HDFs can be identified breaking away from the main cluster of cells and invading into the gel in siRNA 3 and 4. This may be due to diminished siRNA effects. The NT sample displays large populations of HDF cells becoming polarised, changing their morphology to favour a vertical orientation, thus, invading downward through the gel. Additionally all gels appear to exhibit the same level of gel contraction as observed with the NT sample.

Figure 4.9B illustrates a graphical plot of each HDF and VB6 cells *z*-position within the mini-organotypic gel at the end point of the assay. The plot displays that HDFs within the NT sample cover an invasive range of approximately 250µm. Within the core of the invading HDF cells, a small cluster of VB6 cells are identified following closely behind. Perhaps migrating through the channels made by the HDF cells. Transfection of the four individual siRNAs for CAPN-10 in HDF cells demonstrated inhibition of HDF and VB6 cell growth and invasion compared with the NT control. However, the siRNA transfected gels have shrunk to the same height as the NT sample which was not expected.

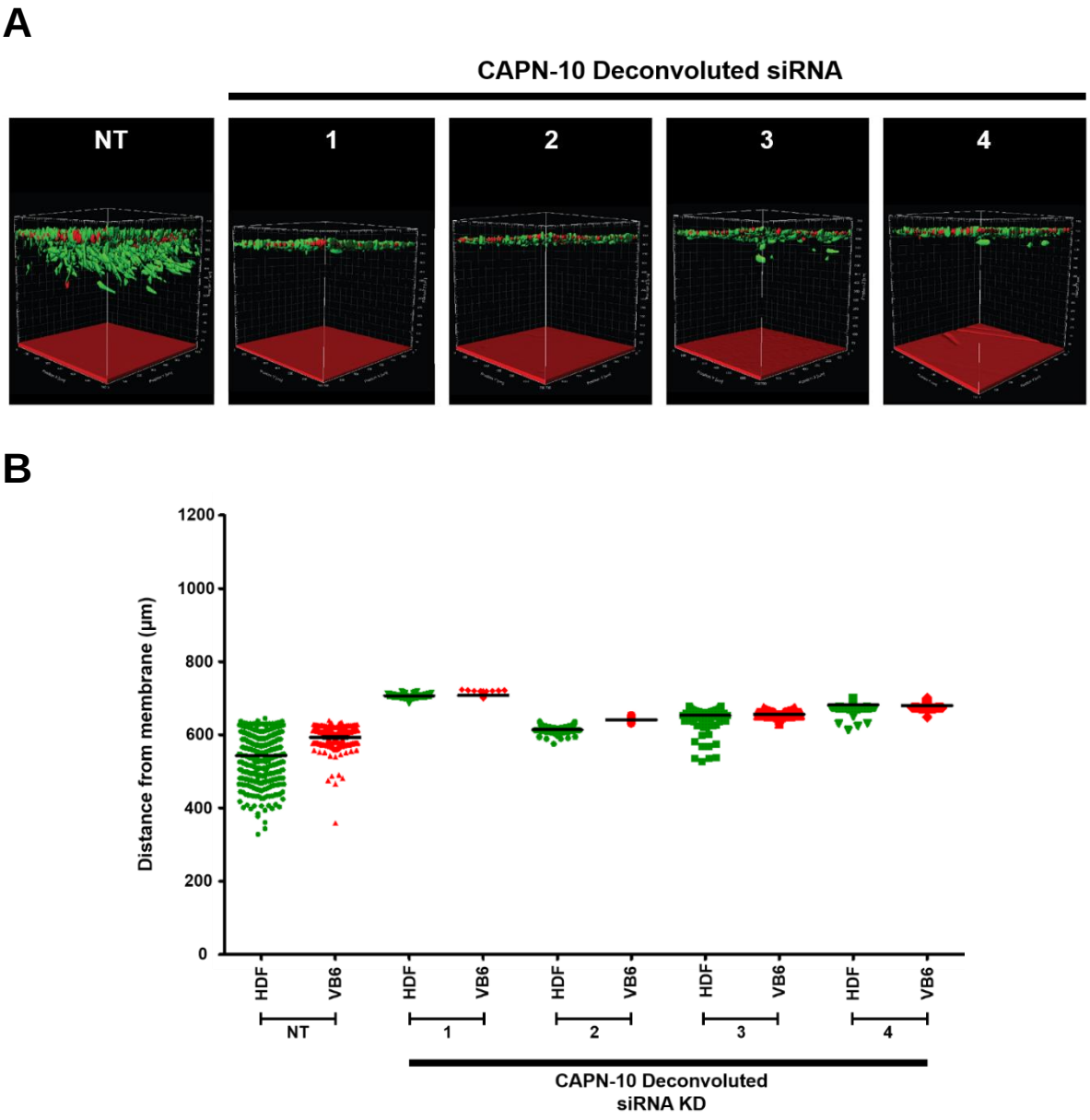

Figure 4.9: 3D rendered and invasion distance quantification of individual CAPN-8 siRNA knockdown in HDF cells

Figure 4.9: 3D rendered and invasion distance quantification of individual CAPN-8 siRNA knockdown in HDF cells

The series of images above displays 3D Imaris XT rendered and analysed *z*-stacks of mini-organotypic gels containing siRNA transfected HDF and non-transfected VB6 cells, six days post transfection. HDF cells were plated in to a 6-well plate (1.5 x 10^5 cells/well), after 24 hours, HDFs were transfected with individual oligonucleotides of CAPN-10 siRNA (denoted as 1, 2, 3 and 4) (20nM) in triplicate wells. 72 hours post transfection, HDF and VB6 cells were fluorescently labelled with CellTracker™ Green (10µM) and Red (5µM) respectively. Next, HDF and VB6 cells were counted and plated (2:1 ratio of fibroblast: tumour in a suspension containing 10^5 cells in total) on to mini-organotypic gels and incubated. **A)** 72 hours post incubation (six days post transfection) *z*-stack volumes were obtained via CLSM. Images were rendered using Imaris image analysis software. NT and siRNA samples 1, 2, 3 and 4 display brightly fluorescent populations of both cell types. HDFs and VB6 cells appear attached and spread on to the gel surface. Gel height for all samples is similar to observations of the NT sample (all samples approximately between 700-600µm in thickness). Image and distance quantification analysis show that HDF cells become polarised, change their morphology and invade vertically downward through the gel, whereas, siRNA 1 and 2 treated HDFs do not become polarised or invade. Analysis of siRNA 3 and 4 suggest a small population of HDF cells start to become polarised and begin their initial invasion. **B)** Invasion data were measured and plotted in Prism and compared against the NT control. One representative series of images from triplicate gels belonging to one of two independent experiments.

4.4.2 Hit validation of pooled siRNA using individual duplexes to identify active species for CASP-8

HDF cells were transfected with the individual CASP-8 constituents represented as 1, 2, 7 and 25. **Figure 4.10A** displays a panel of 3D Imaris rendered images containing a NT sample and the individual siRNA duplexes transfected into HDF cells.

Image analysis observations suggest HDF cells transfected with CASP-8 oligonucleotides appear to display minimal polarisation and changes in morphology, compared to the more polarised appearing HDFs within the NT sample. siRNA 1, 2 and 7 displayed a small number of HDF breaking away from the main cluster of cells, polarised and invading through the gel. This may be due to diminishing siRNA effects. Additionally all gels appear to exhibit the same level of gel contraction as observed with the NT sample, with gel heights for all samples approximately between 700-600µm.

Figure 4.10B illustrates a graphical plot of each HDF cells *z*-position within the mini-organotypic gel at the end point of the assay. Treatment of the four individual siRNA duplexes for CAPN-8 demonstrated an inhibition of growth and invasion of HDF and VB6 cells, relative to the NT control. However the gel has contracted to a height similar to that of the NT control (as observed in **Figure 4.9**).

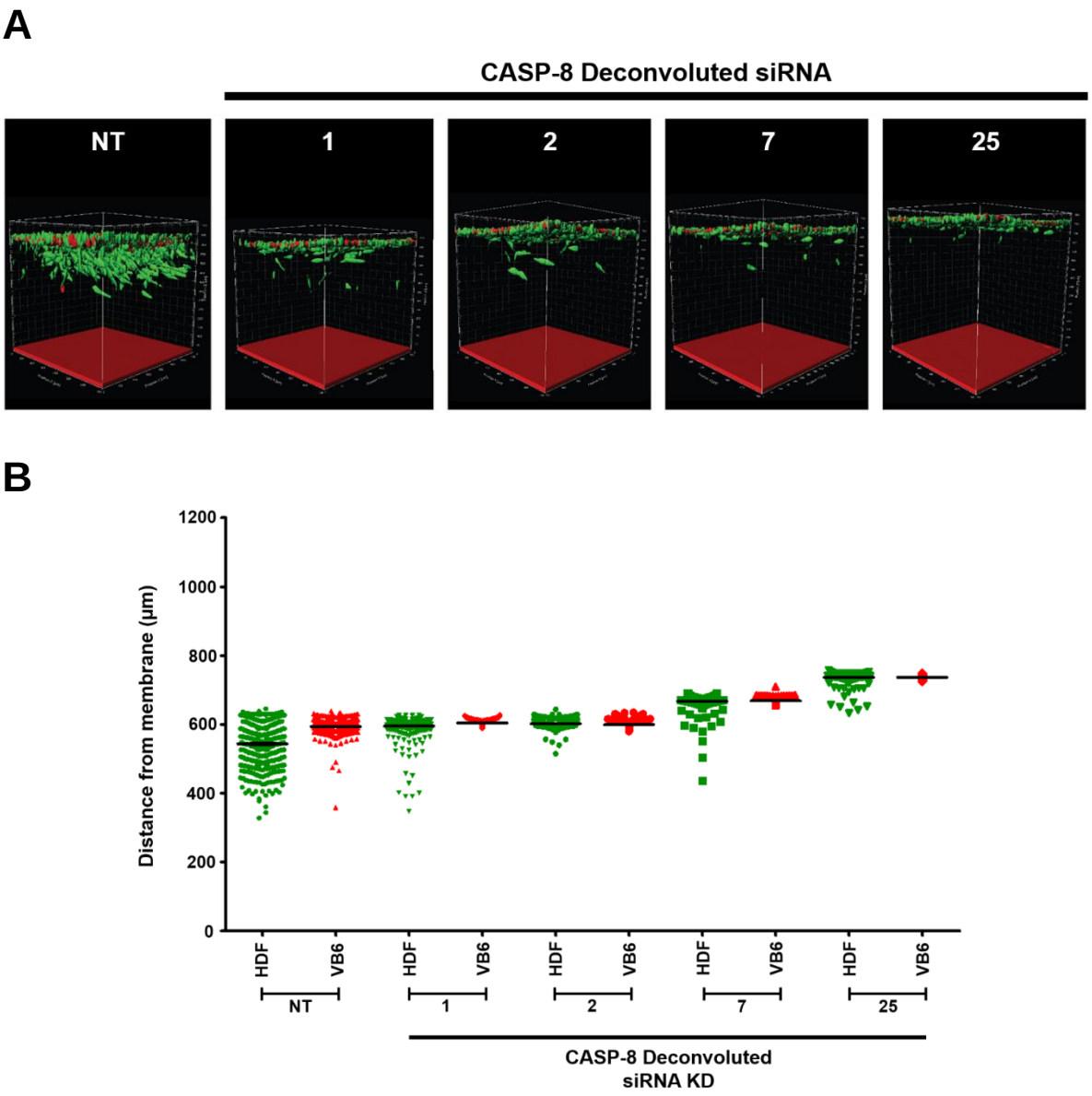

Figure 4.10: 3D rendered and invasion distance quantification of individual CASP-8 siRNA knockdown in HDF cells

Figure 4.10: 3D rendered and invasion distance quantification of individual CASP-8 siRNA knockdown in HDF cells

The series of images above displays 3D Imaris XT rendered and analysed *z*-stacks of mini-organotypic gels containing siRNA transfected HDF and non-transfected VB6 cells, six days post transfection. HDFs were transfected with individual oligonucleotides of CASP-8 siRNA (denoted as 1, 2, 7 and 25) (20nM) in triplicate wells. 72 hours post transfection, HDF and VB6 cells were fluorescently labelled with CellTracker™ Green (10µM) and Red (5µM) respectively. Next, HDF and VB6 cells were counted and plated (2:1 ratio of fibroblast: tumour in a suspension containing 10^5 cells in total) on to mini-organotypic gels and incubated. **A)** 72 hours post incubation (six days post transfection) *z*-stack volumes were obtained via CLSM. Images were rendered using Imaris image analysis software. NT and siRNA samples 1, 2, 3 and 4 display brightly fluorescent populations of both cell types. HDFs and VB6 cells appear attached and spread on to the gel surface. Gel height for all samples is similar to observations of the NT sample (all samples approximately between 700-600µm in thickness). Image and distance quantification analysis show that HDF cells become polarised, change their morphology and invade vertical downward through the gel. Whereas siRNA 1 and 2 treated HDFs do not come polarised or invade. Analysis of siRNA 3 and 4 suggest a small population of HDF cells start to become polarised and begin their initial invasion. **B)** Invasion data were measured and plotted in Prism and compared against the NT control. One representative series of images from triplicate gels belonging to one of two independent experiments.

4.4.3 Hit validation of pooled siRNA using individual duplexes to identify active species for MMP-17

HDF cells were transfected with MMP-17 constituents represented as 1, 4, 5 and 19. **Figure 4.11A** displays a panel of 3D Imaris rendered images containing a NT sample and the individual siRNA duplexes transfected into HDF cells.

Interestingly siRNA 1 and 4 displayed signs of increased gel thickness compared to the NT sample, which is approximately 600µm. siRNA 1 – approximately 1100µm thick with HDF cells covering an invasive range between 1100µm and 850µm, siRNA 2 – approximately 1000µm thick with HDF cells covering an invasive range between 1000µm and 700µm. Additionally within these two samples HDF cells have begun to start invading, however, have not reached the same invasive depth as siRNA 5 (300µm) and 19 (600µm). All samples exhibited increased gel thickness when compared with, not only, the NT sample but also the CAPN-10 (**Figure 4.9**) and CASP-8 (**Figure 4.10**) samples.

Figure 4.11B illustrates a graphical plot of each HDF cells *z*-position within the mini-organotypic gel at the end point of the assay. Treatment of the four individual siRNA duplexes for MMP-17 demonstrated an inhibition of HDF and VB6 growth and invasion for siRNA 1 and 4 with decreased levels of gel contraction, however, siRNA samples 5 and 19 display signs of increased gel contraction and HDF cell invasion, but not as extensively as observed with the NT control.

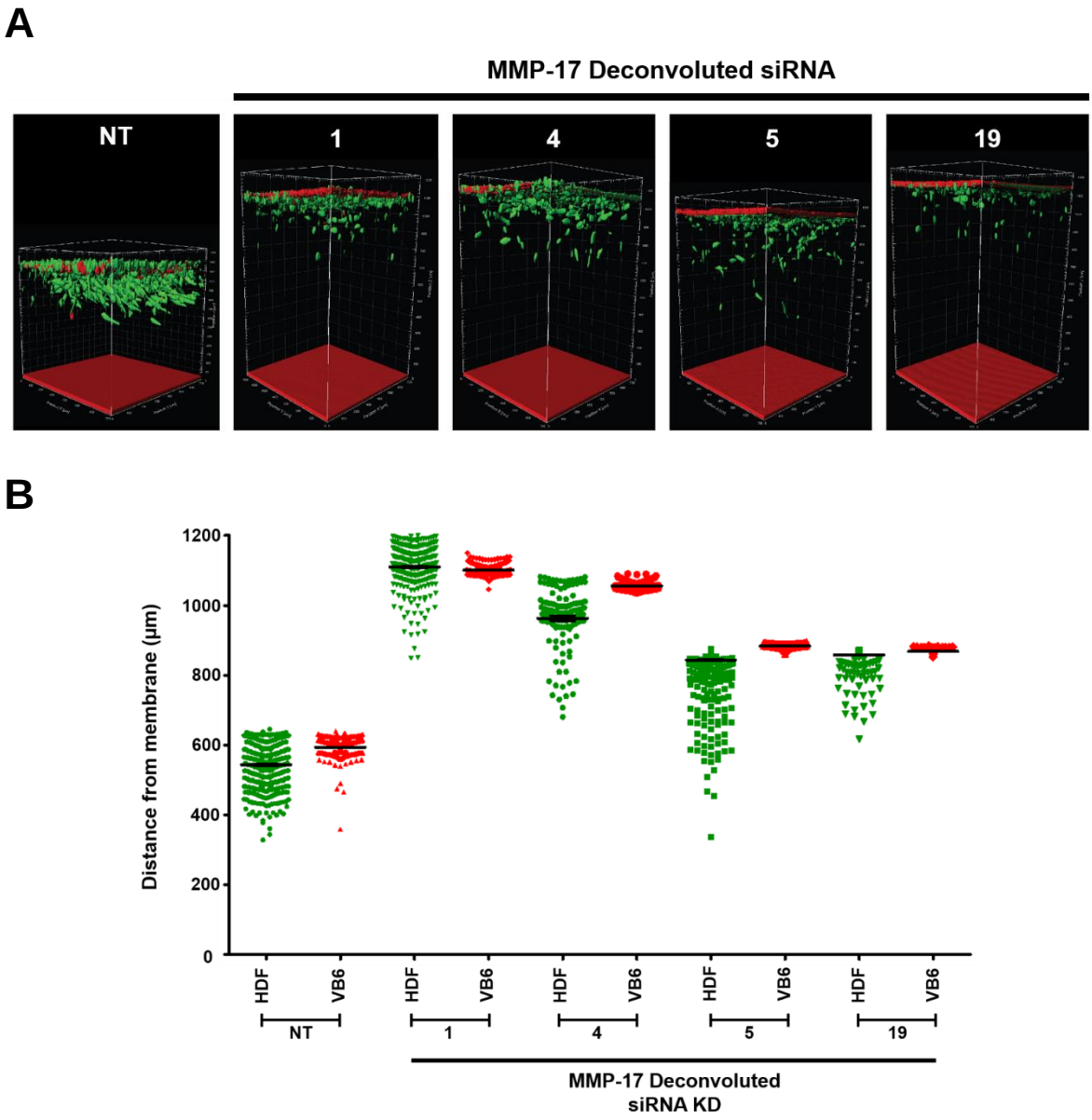

Figure 4.11: 3D rendered and invasion distance quantification of individual MMP-17 siRNA knockdown in HDF cells

Figure 4.11: 3D rendered and invasion distance quantification of individual MMP-17 siRNA knockdown in HDF cells

The series of images above displays 3D Imaris XT rendered and analysed *z*-stacks of mini-organotypic gels containing siRNA transfected HDF and non-transfected VB6 cells, six days post transfection. HDFs were transfected with individual oligonucleotides of MMP-17 siRNA (denoted as 1, 4, 5 and 19) (20nM) in triplicate wells. 72 hours post transfection, HDF and VB6 cells were fluorescently labelled with CellTracker™ Green (10µM) and Red (5µM) respectively. Next, HDF and VB6 cells were counted and plated (2:1 ratio of fibroblast: tumour in a suspension containing 10^5 cells in total) on to mini-organotypic gels and incubated. **A)** 72 hours post incubation (six days post transfection) *z*-stack volumes were obtained via CLSM. Images were rendered using Imaris image analysis software. NT and siRNA samples 1, 4, 5 and 19 display brightly fluorescent populations of both cell types. HDFs and VB6 cells appear attached and spread on to the gel surface. Image and distance quantification analysis suggest that HDF cells from all siRNA treated samples become polarised, change their morphology and invade vertical downward through the gel at different rates. Samples 1 and 4 gels have contracted much less than the NT sample and display signs of HDF cell invasion. Samples 5 and 19 shows a lesser degree of contraction when compared to samples 1 and 4, but possess thicker gels than the NT control. **B)** Invasion data were measured and plotted in Prism and compared against the NT control. One representative series of images from triplicate gels belonging to one of two independent experiments.

4.4.4 Hit validation of pooled siRNA using individual duplexes to identify active species for SERPIN-F1

HDF cells were transfected with SERPIN-F1 constituents represented as 1, 2, 3 and 4. **Figure 4.12A** displays a panel of 3D Imaris rendered images containing a NT siRNA control sample and the individual siRNA duplexes transfected into HDF cells.

Image analysis observations suggest the HDF cells treated with siRNA 1 and 2 do not become polarised or invade through the organotypic gel compared with the NT sample. However, siRNA samples 3 and 4, a small number of HDFs can be identified breaking away from the main cluster of cells and invading into the gel. This may be due to diminished siRNA effects. The NT sample displays large populations of HDF cells becoming polarised, changing their morphology to favour a vertical orientation, thus, invading downward through the gel. Additionally all gels appear to exhibit the same level of gel contraction as observed with the NT sample.

Figure 4.12B illustrates a graphical plot of each HDF cells *z*-position within the mini-organotypic gel at the end point of the assay. The plot displays that HDFs within the NT sample cover an invasive range of approximately 200µm. Within the core of the invading HDF cells, a small cluster of VB6 cells are identified following closely behind. Perhaps migrating through the channels made by the HDF cells. Transfection of the four individual siRNA duplexes for SERPIN-F1 in HDF cells demonstrated an inhibition of HDF and VB6 cell growth and invasion, compared with the NT control. As observed with CAPN-10 (**Figure 4.9**) and CASP-8 (**Figure 4.10**) the SERPIN-F1 siRNA treated gels have contracted vertically almost to the same thickness as the NT control samples.

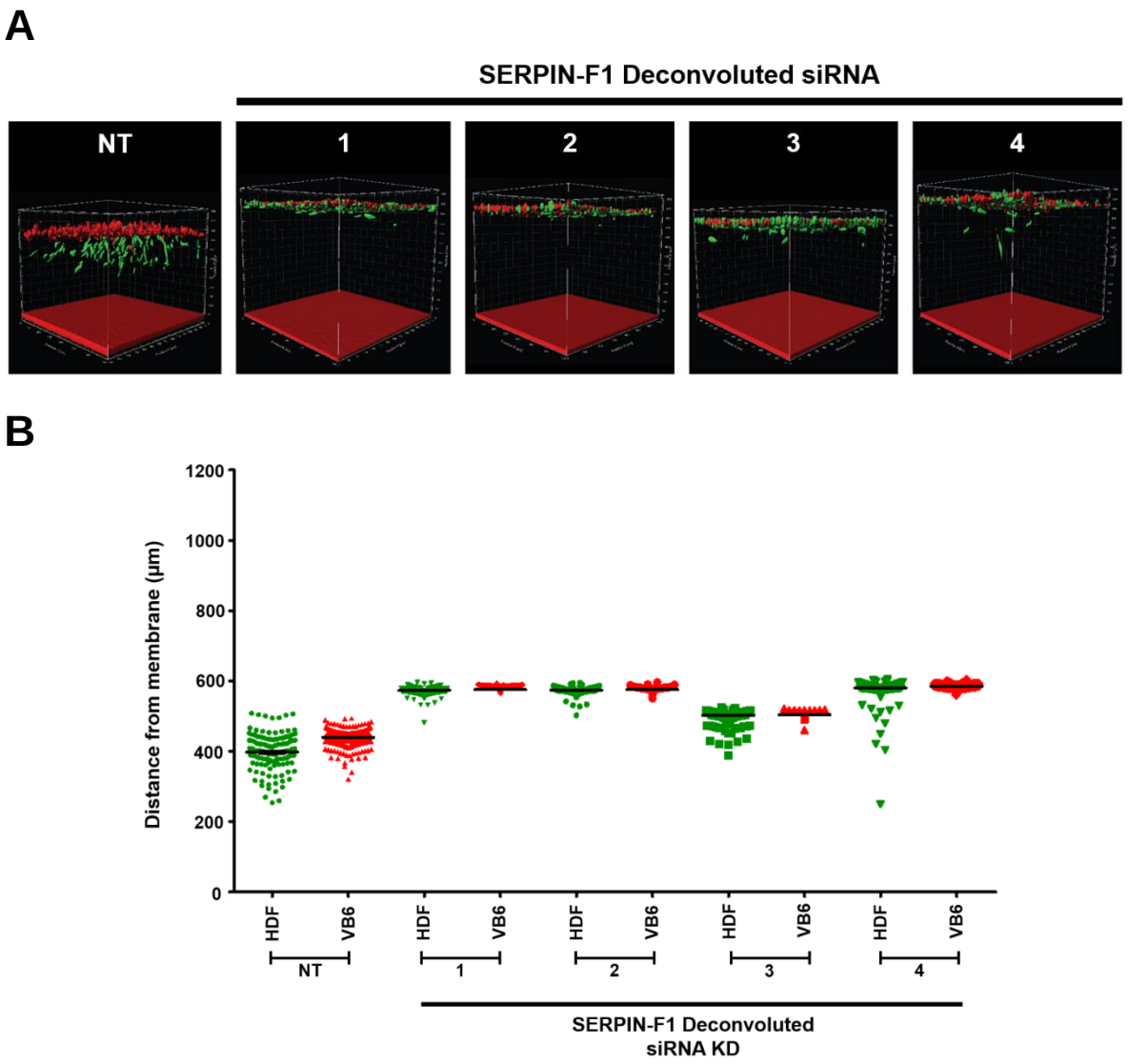

Figure 4.12: 3D rendered and invasion distance quantification of individual SERPIN-F1 siRNA knockdown in HDF cells

Figure 4.12: 3D rendered and invasion distance quantification of individual SERPIN-F1 siRNA knockdown in HDF cells

The series of images above displays 3D Imaris XT rendered and analysed *z*-stacks of mini-organotypic gels containing siRNA transfected HDF and non-transfected VB6 cells, six days post transfection. HDF cells were plated in to a 6-well plate (1.5 x 10^5 cells/well), after 24 hours, HDFs were transfected with individual oligonucleotides of SERPIN-F1 siRNA (denoted as 1, 2, 3 and 4) (20nM) in triplicate wells. 72 hours post transfection, HDF and VB6 cells were fluorescently labelled with CellTracker™ Green (10µM) and Red (5µM) respectively. Next, HDF and VB6 cells were counted and plated (2:1 ratio of fibroblast: tumour in a suspension containing 10^5 cells in total) on to mini-organotypic gels and incubated. **A)** 72 hours post incubation (six days post transfection) *z*-stack volumes were obtained via CLSM. Images were rendered using Imaris image analysis software. NT and siRNA samples 1, 2, 3 and 4 display brightly fluorescent populations of both cell types. HDFs and VB6 cells appear attached and spread on to the gel surface. Gel height for NT sample is approximately 450µm in thickness, whereas, samples 1-4 are approximately between 600-500µm in thickness. Image analysis of NT sample displays HDF cells become polarised, change their morphology and invade vertical downward through the gel. Whereas siRNA 1 and 2 treated HDFs do not come polarised or invade. Analysis of siRNA 3 and 4 suggest a small population of HDF cells start to become polarised and begin their initial invasion. **B)** Invasion data were measured and plotted in Prism and compared against the NT control. One representative series of images from triplicate gels belonging to one of two independent experiments.

4.4.5 Hit validation of pooled siRNA using individual duplexes to identify active species for TMPRSS-13

HDF cells were transfected with TMPRSS-13 constituents represented as 1, 2, 3 and 4. **Figure 4.13A** displays a panel of 3D Imaris rendered images containing a NT sample and the individual siRNA duplexes transfected into HDF cells.

NT control and all siRNA samples suggest HDF cells appear to become polarised and being invading through the gel. The NT sample shows large populations of HDF cells invading vertically downward through the gel and VB6 cells follow closely behind. Interestingly siRNA 1, 2 and 3 displayed signs of increased gel thickness compared to the NT sample, which his approximately 650µm. siRNA 1 and 2 are both approximately 900µm thick with HDF cells covering an invasive range between 900µm and 850µm, siRNA 3 being approximately 1000µm thick with HDF cells covering an invasive range between 1000µm and 850µm. siRNA 4 displays levels of contraction in between that of the NT control and its siRNA members. siRNA samples 1, 2 and 3 display similar levels of increased gel thickness compared with observation from MMP-17. The images also display reduced invasion and growth of HDF and VB6 cells when treated with siRNAs 1, 2 and 3 compared with the NT samples.

Figure 4.13B illustrates a graphical plot of each HDF cells *z*-position within the mini-organotypic gel at the end point of the assay. Treatment of the four individual siRNA duplexes for TMPRSS-13 demonstrated a slight inhibition of HDF and VB6 invasive capabilities for siRNA 1, 2 and 3 with decreased levels of gel contraction, however, siRNA sample 4 display signs of increased gel contraction and HDF cell invasion, but not as extensively as observed with the NT control.

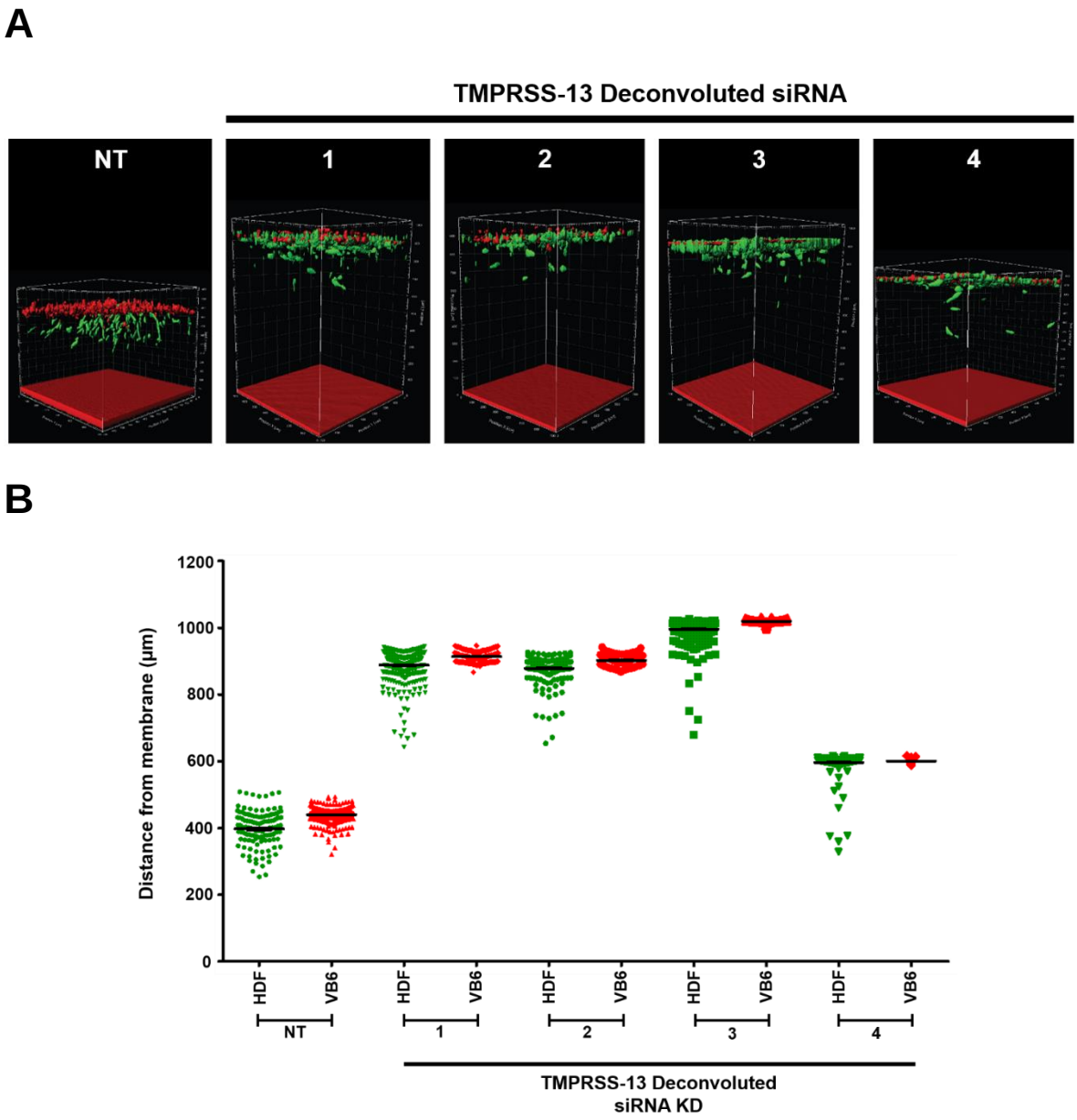

Figure 4.13: 3D rendered and invasion distance quantification of individual TMPRSS-13 siRNA knockdown in HDF cells

Figure 4.13: 3D rendered and invasion distance quantification of individual TMPRSS-13 siRNA knockdown in HDF cells

The series of images above displays 3D Imaris XT rendered and analysed *z*-stacks of mini-organotypic gels containing siRNA transfected HDF and non-transfected VB6 cells, six days post transfection. HDF cells were plated in to a 6-well plate (1.5 x 10^5 cells/well), after 24 hours, HDFs were transfected with individual oligonucleotides of TMPRSS-13 siRNA (denoted as 1, 2, 3 and 4) (20nM) in triplicate wells. 72 hours post transfection, HDF and VB6 cells were fluorescently labelled with CellTracker™ Green (10µM) and Red (5µM) respectively. Next, HDF and VB6 cells were counted and plated (2:1 ratio of fibroblast: tumour in a suspension containing 10^5 cells in total) on to mini-organotypic gels and incubated. **A)** 72 hours post incubation (six days post transfection) *z*-stack volumes were obtained via CLSM. Images were rendered using Imaris image analysis software. NT and siRNA samples 1, 2, 3 and 4 display brightly fluorescent populations of both cell types. HDFs and VB6 cells appear attached and spread on to the gel surface. Gel height for NT sample is approximately 450µm in thickness, whereas, samples 1 and 2 are approximately between 900µm in thickness. Sample 3 is approximately 1000µm and sample 4 being approximately 580µm. Image analysis of NT sample displays large populations of HDF cells become polarised, change their morphology and invade vertical downward through the gel. Whereas siRNA samples 1-4 display a varying degree of HDF cell polarisation and invasion. **B)** Invasion data were measured and plotted in Prism and compared against the NT control. One representative series of images from triplicate gels belonging to one of two independent experiments.

4.4.6 Summary of hit validation screen from individual siRNA

The knock down of CAPN-10, CASP-8 and SERPIN-F1 individual siRNA in HDF cells appears to have decreased the number of HDF cells that have polarised, change their morphology and invade into mini-organotypic gels. However there was a similar reduction in gel height which was not expected. These effects are unlikely to be just evaporation of gels during incubation, since other siRNA experiments run at the same time and biological repeats did not shrink. In contrast, individual siRNA from MMP-17 and TMPRSS-13 both displayed a similar responses to the SMARTpool.

Thus, invasion and growth of the HDFs and VB6 were reduced and gel thickness remained similar to the starting height. **Figure 4.14** displays a summarised plot of individual siRNA invasion data. As we could not deduce why the CAPN-10, CASP-8 and SERPIN-F1 samples displayed reduced growth and invasion, but still displayed a high degree of gel contraction, I choose to concentrate on MMP-17 and TMPRSS-13.

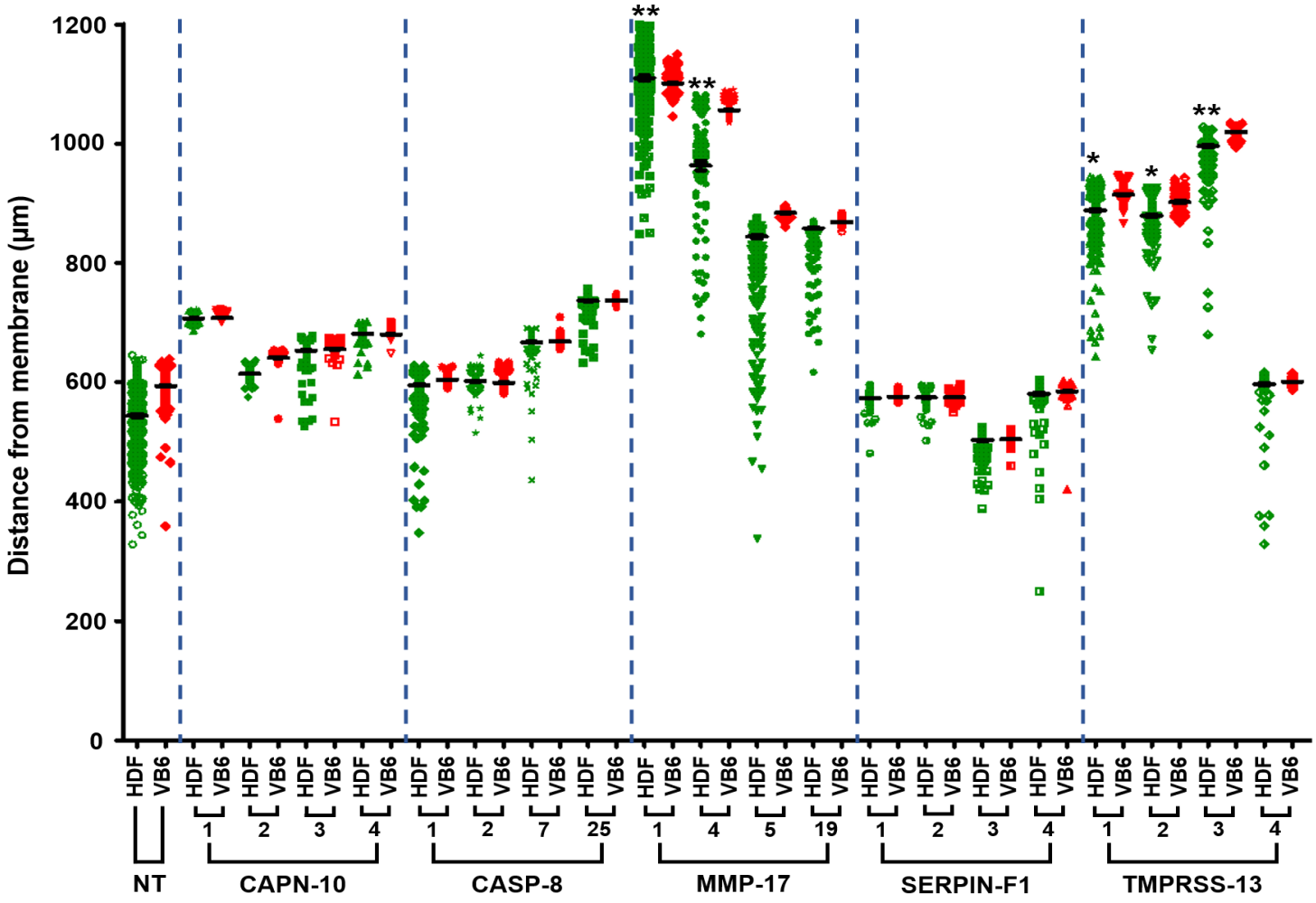

Figure 4.14: Invasion distance quantification of individual siRNA

Figure 4.14: Invasion distance quantification of individual siRNA

The bee swarm plot displays invasive spread of HDF and VB6 cells of the individual siRNA from the five chosen hits identified from the primary screen. *Z*-position data of HDF and VB6 cells within the mini-organotypic gels six days post transfection were collected and plotted in Prism and compared to the NT control. Results display the mean and s.d of triplicate repeats from one of two biological experiments. One-way ANOVA, ** $p < 0.01$, * $p < 0.05$.

4.5 Protein expression of selected siRNA targets

Western blotting was conducted to determine the protein expression level of the individual oligonucleotides from MMP-17 and TMPRSS-13. HDF cells were plated and transfected as previously described, before protein lysates were collected and samples were prepared for western blotting (as described in **Section 2.2**). Western blots were quantified by densitometry analysis of three independent biological experiments, relative to non-targeting siRNA control (denoted at NT).

4.5.1 Protein expression level of MMP-17 in response to siRNA

Figure 4.15 suggests that HDF cells transfected with the individual MMP-17 siRNA, numbers 5 and 19, produced higher levels of MMP-17 protein expression when compared to the NT sample. However, on the contrary, numbers 1 and 4, significantly reduced MMP-17 expression six days post transfection, relative to the NT.

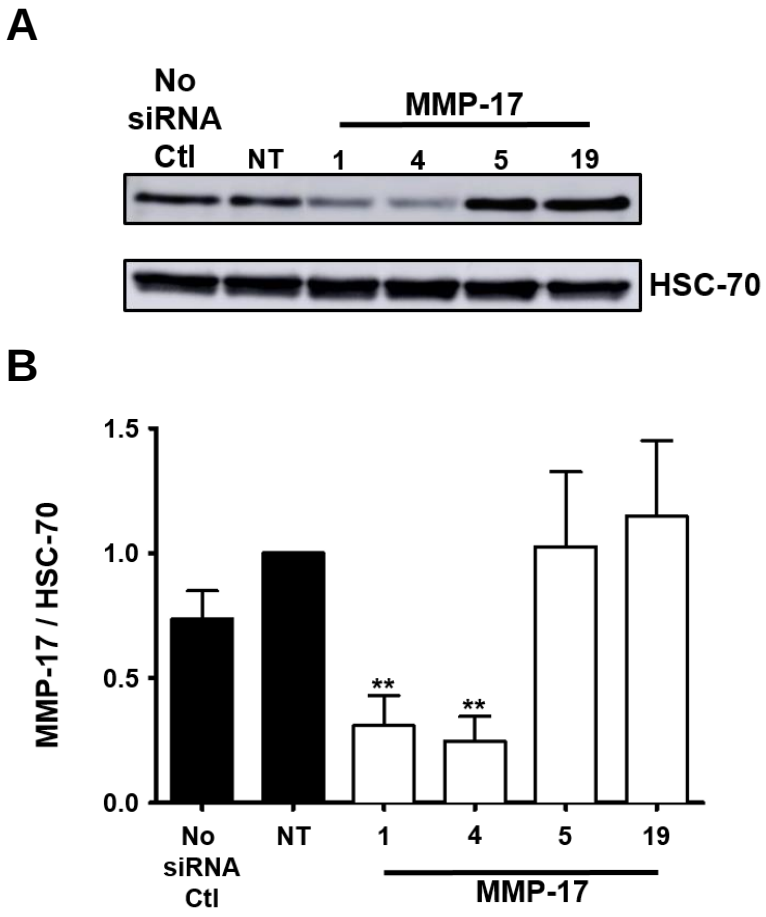

Figure 4.15: Western blot analysis of HDF cells transfected with MMP-17 individual oligonucleotides

Figure 4.15: Western blot analysis of HDF cells transfected with MMP-17 individual oligonucleotides

The four individual siRNA constituents of MMP-17 were knocked down in HDF cells (20nM), alongside a non-targeting (NT) siRNA control and a transfection reagent only treated sample (No siRNA Ctl). 6 days post transfection lysates were collected and blotted for MMP-17 protein expression. **A)** Cell lysates from HDF cells transfected with MMP-17 individual siRNA (numbered 1,4, 5 and 19), NT, and No siRNA Ctl were analysed for MMP-17 expression (MMP-17 antibody) and HSC-70 loading control by western blotting. **B)** Triplicate western blot samples were analysed by densitometry and data were normalised to NT. Data display the mean and s.d of three independent biologically repeated experiments. Student *t*-test, ** $p<0.01$.

4.5.2 Protein expression level of TMPRSS-13 oligonucleotides

Figure 4.16 suggests that HDF cells transfected with the individual TMPRSS-13 siRNA, numbers 1-4, had no significant effect on protein expression of TMPRSS-13 when compare to the NT. Conversely, increasing protein expression level in siRNA numbers 1 and 3.

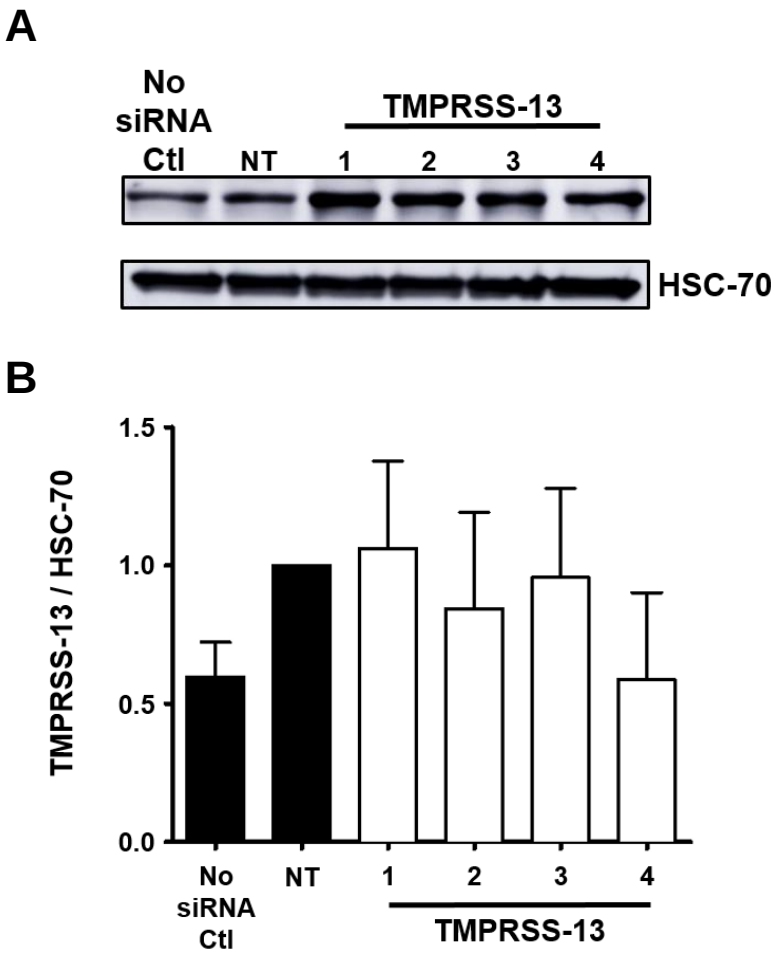

Figure 4.16: Western blot analysis of HDF cells transfection with TMPRSS-13 individual oligonucleotides

The four individual siRNA constituents of TMPRSS-13 were knocked down in HDF cells (20nM), alongside a non-targeting (NT) siRNA control and a transfection reagent only treated sample (No siRNA Ctl). 6 days post transfection lysates were collected and blotted for TMPRSS-13 protein expression. **A)** Cell lysates from HDF cells transfected with TMPRSS-13 individual siRNA (numbered 1,2, 3 and 4), NT, and No siRNA Ctl were analysed for TMPRSS-13 expression (TMPRSS-13 antibody) and HSC-70 loading control by western blotting. **B)** Triplicate western blot samples were analysed by densitometry and data were normalised to NT. Data display the mean and s.d of three independent biologically repeated experiments.

4.6 Summary of data

Here, I have validated the robustness, reproducibility and reliability of the fluorescent mini-organotypic invasion assay by performing a primary siRNA SMARTpool library screen. Image and data analysis identified 16 hits that significantly reduced gel contraction and cancer and fibroblast invasion. From those 16 hits, five were selected to follow up. Repetition of the five SMARTpool hits confirmed observations and results obtained from the primary screen.

Validation of the selected hits was performed via individual deconvolution experiments which identified MMP-17 and TMPRSS-13 candidates for further investigation. Protein level expression of MMP-17 was significantly reduced in two of the four individual siRNA when knocked down in HDF cells. Conversely, protein levels reduction of TMPRSS-13 was not observed. It is possible that the antibody used was not specific for TMPRSS-13, despite the manufacturers' claims. With more time and funds I could have tested other reagents for TMPRSS-13 but this was not possible.

4.7 High-content multi-parameter data analysis

3D Image analysis of confocal *z*-stacks via Imaris XT produced .csv data files for a variety of parameters for every fluorescent particle (a cell or group of cells) within each colour channel (area, elipticity oblate and prolate, intensity, invasion, sphericity and volume). So far, I have investigated invasive depth against time and treatment parameters for HDF and VB6 cells. However, multi-parameter phenotypic analysis may provide important insights into assessing changes in cell dynamics and the biological responses to siRNA transfection on both HDF and VB6 cell behaviour.

Traditionally, from a screening point of view, the end point goal was to identify compounds or small molecules which had a desirable effect and eliminate those that did not. Primary screening assays were designed with a single read-out (commonly time-resolved fluorescence resonance energy transfer (TR-FRET)) to aid selection of active molecules. However, recently the pharmaceutical and biotechnology industry have adopted a multi-parameter high-content phenotypic screening and data analysis approach.

With the vast advances in high-content capturing automated microscopes, intelligent data management systems and automated batch and image processing analysis software; the rate of target identification of new therapeutic agents may increase. Therefore, screening of therapeutic interfering molecules (such as compounds or RNAi) along with efficient multi-parameter high-content data analysis has become an achievable and desirable objective (Hulkower and Herber, 2011).

Here, with the aid of MatLab® (Matrix Laboratory, MathWork, USA), an interactive, multi-paradigm mathematical programming language; manipulation, extrapolation and plotting of data was performed automatically via a custom designed script named ‘multi-parameter analysis algorithm’. Data for invasion vs sphericity, invasion vs volume and effect of elipticity prolate vs elipticity oblate were determined and plotted via MatLab®.

The customised script was developed in collaboration with Joseph Brook (Sosabowski group, Centre for Molecular Oncology – Barts Cancer Institute) who wrote the algorithm (**Appendix Figure 7.16**).

4.7.1 High-content multi-parameter data analysis: SMARTpool primary screen

As described previously in this chapter, HDFs were plated into 6-well plates, transfected with SMARTpool or NT siRNA control, fluorescently labelled with CellTracker™ Green and co-cultured into mini-organotypic gels containing CellTracker™ Red labelled VB6 cells. Six days post transfection gels were imaged via CLSM and *z*-stack data files (.lsm) were analysed and rendered using Imaris XT. Analysis of the 3D volumes produced multi-parameter data files (.csv), of which, each could be plotted and analysed in comparison against each other. To efficiently extract this data the custom MatLab® algorithm was used to collate and plot HDF and VB6 cell data from a range of phenotypic parameters (elipticity prolate, elipticity oblate, invasion, sphericity and volume).

Sphericity (ψ), defined by Wadell in 1932, is the measure of how mathematically spherical an object is on a scale of 0 to 1 (0 being flat to 1 being perfectly spherical) (Wadell, 1932). An example of multi-parameter analysis, shown below, displays invasion vs sphericity data for NT control siRNA transfected HDFs co-cultured with VB6 cells from three technical repeat samples (**Figure 4.17A**). In all three samples it is evident that the fibroblast cells with the deepest invasion have a spherical value between 0.55 – 1.0. This may suggest medium to high level spherical cells invade further into the gels, thus, potentially being the invasive cell type for tumour cells to follow.

Additionally, all samples appear to exhibit apparent signs of gel contraction (gel heights all within a range approximately between 380-500µm). Furthermore, the invading HDF and VB6 cells appear to have a greater sphericity value compared to the cells which do not appear to invade and remain at the surface of the gel. Thus suggesting that sphericity of fibroblast and tumour cells may affect their ability to invade within a 3D environment. Interestingly, all samples display different cell numbers, this may be due to differences in proliferative rates, cell death or dissipation of the transient fluorescent dye. Furthermore, cell number may be affected by sphericity, an increase in sphericity suggests a decrease in available surface area, thus prohibiting cell adhering and spreading.

Figure 4.17B displays invasion vs sphericity data for HDFs transfected with MMP-10 SMARTpool siRNA and co-cultured with VB6 cells. Each sample from three technical repeats is plotted alongside a NT siRNA control. Immediately, we observe differences not only, in gel height (MMP-10 treated gels are within a range approximately between

1100-1200µm in height) but also, level of invasion of both cell types. Suggesting, knockdown of MMP-10 in HDF cells effects the ability of these fibroblasts to polarise, remodel and invade through 3D gels, thus, also reducing invasiveness of the tumour cells. Similarly to **Figure 4.17A**, the number each cell type varies within all samples, probably due to the reasons mentioned above. However, this does not appear to influence or negate the possible deductions these data show as the sample size within every repeat is high.

I have focused on the five selected hits identified from the SMARTpool screen (CAPN-10, CASP-8. MMP-17, SERPIN-F1 and TMPRSS-13) to further analyse multi-parameter data for Invasion vs sphericity, volume and elipticity (**Figure 4.18**, **Figure 4.19** and **Figure 4.20** respectively).

A

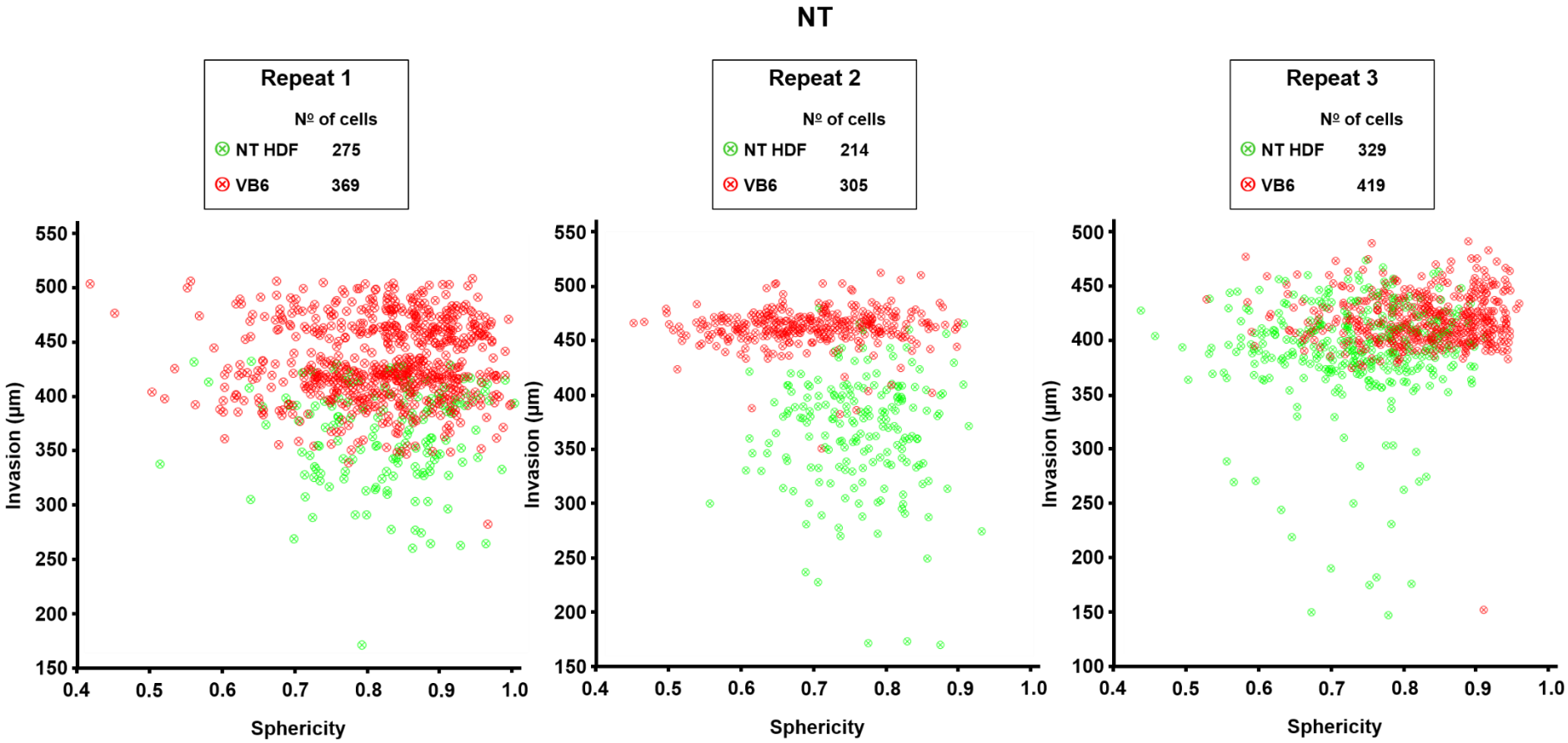
NT
Repeat 1
№ of cells
NT HDF 275
VB6 369
Repeat 2
№ of cells
NT HDF 214
VB6 305
Repeat 3
№ of cells
NT HDF 329
VB6 419
Invasion (µm)
Sphericity

B

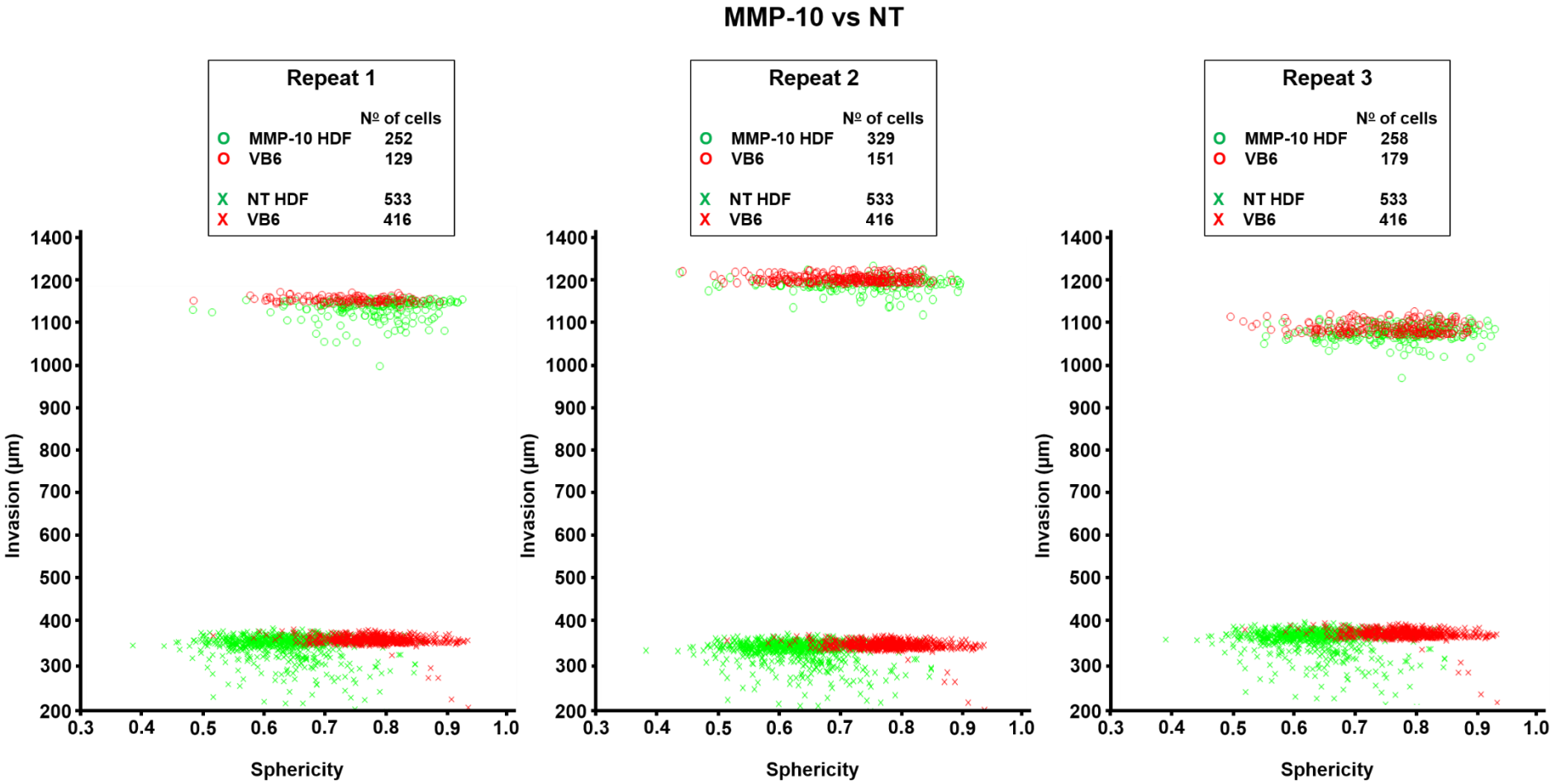

Figure 4.17: Multi-parameter analysis of HDFs transfected with NT control and MMP-10 siRNA co-cultured with VB6 cells: Invasion vs sphericity

Figure 4.17: Multi-parameter analysis of HDFs transfected with NT control and MMP-10 siRNA co-cultured with VB6 cells: Invasion vs sphericity

The figures above illustrate invasion vs sphericity data, which were compiled and plotted via the custom designed MatLab® algorithm. HDFs were transfected with SMARTpool MMP-10 or NT siRNA, fluorescently labelled green and co-cultured into mini-organotypic gels alongside fluorescently labelled red VB6 cells. *Z*-stacks were collected six days post transfection via CLSM and analysed by Imaris XT. **A)** HDFs transfected with NT control siRNA (⊗) co-cultured with VB6 cells (⊗). In all repeats HDF cells appear to become polarised and invade into the mini-organotypic gel. All gels exhibit signs of gel contraction to a similar degree (gel heights range between 380-500µm). All gels suggest invading HDF and VB6 cells have an increased spherical value. **B)** Combined plot of MMP-10 transfected HDFs (**O**) co-cultured with VB6 cells (**O**) and NT control siRNA transfected HDFs (**X**) co-cultured with VB6 cells (**X**) (NT sample is the same in all MMP-10 repeats). All gels appear to have contracted less compared to the NT sample. Additionally, HDFs and VB6s do not appear to invade throughout the gel. Series of invasion vs sphericity data from triplicate technical repeats from one independent experiment.

4.7.2 High-content multi-parameter data analysis of hits from primary screen

The five selected targets identified from the primary SMARTpool siRNA screen (CAPN-10, CASP-8, MMP-17, SERPIN-F1 and TMPRSS-13) significantly ($p<0.05$) reduced HDF and VB6 cell invasion and gel shrinkage relative to a NT siRNA control (**Figure 4.7**). However, to determine if siRNA knockdown had any effect on polarity, sphericity as well as invasion, data from Imaris XT was analysed using the 'multi-parameter analysis algorithm' via MatLab®.

Data from fluorescently labelled HDFs (transfected with target or NT control siRNA) and fluorescently labelled VB6 cells were extrapolated from .csv files and plotted for invasion vs sphericity (**Figure 4.18**), invasion vs volume (**Figure 4.19**) and invasion vs elipticity (oblate and prolate) (**Figure 4.20**).

In mathematical terms, a spheroid is a shape that closely resembles a sphere, but, is not perfectly spherical (also known as an ellipse). When the ellipse is rotated along its major axis, it produces an elongated 'pointy' shape, the extent of elongation is referred to as elipticity prolate. On the contrary, elipticity oblate is when an ellipse is rotated along its minor axis resulting in a compressed 'squashed' disk-like shape (Teitze, 1965). Effectively, oblate is more horizontal, whereas prolate favours the vertical plane.

Volume data for each cell type were filtered to background noise. The selection process involved excluding data that did not meet a specific criteria based on cell diameter of single and clusters of cells. Volumes between 1000 - 15000µm^3 on the basis that a single VB6 cell has a diameter of 18µm ± 2µm and a single HDF cell having a diameter of 15µm ± 2µm.

$$(V = \frac{4}{3}\pi r^3)$$

4.7.2.1 Multi-parameter data analysis: Invasion vs sphericity

Figure 4.18 shows plots of cell invasiveness versus sphericity for each of the hits against the NT siRNA control. In each case the data confirm that the NT control cells have all invaded further into the gels more than the CAPN-10, CASP-8, MMP-17, SERPIN-F1 and TMPRSS-13 siRNA transfected cells. One can also see that the depth of invasion varies in the NT control, with the surface of the VB6 cells varying

from 400-850µm. The change in sphericity of siRNA treated HDFs is predominantly between 0.6 – 0.9. Thus, these are mainly HDF cells that are near spherical, as well as those that have medium sphericity to be amongst the most invasive cell.

A similar spread of sphericity values are seen for most of the VB6 population within these samples. The data may suggest that HDFs exhibit both mesenchymal and amoeboid invasive migration patterns. The change in shape, sphericity and response to gene knockdown in HDFs appears different for each gene target. For example, CASP-8 (**Figure 4.18B**) and SERPIN-F1 (**Figure 4.18D**) show a wider range of change with a higher number of cells being less spherical (values at >0.5).

In contrast TMPRSS-13 knockdown (**Figure 4.18E**) shift the HDF population towards a more spherical nature. CAPN-10 (**Figure 4.18A**) and MMP-17 (**Figure 4.18C**) seem to have a similar shape distribution to that of the NT control cells. Since cell shape in 3D is a complex interplay between regulation of the cell cytoskeleton and the ECM, these data suggest that the effect of the siRNA targeting may be more complex than just modifying the ECM.

4.7.2.2 Multi-parameter data analysis: invasion vs volume

Figure 4.19 displays plots comparing invasiveness versus volume for each of the hits against a NT siRNA control. In each case the data confirm that NT HDFs have invaded further into the gel relative to the CAPN-10, CASP-8, MMP-17, SERPIN-F1 and TMPRSS-13 transfected HDFs. Additionally, the depth of invasion of the NT HDFs and VB6 cells varies with volume size, cells between 1000-5000µm^3 (probably single cells) appear to invade the deepest.

However NT HDFs and VB6 cell cover a broad range of volume between 1000-15,000µm^3, cells of a greater volume appear to remain at the surface of the gels. The siRNA treated HDFs, in general, the volume exhibits a broad range for all samples compared to the NT controls. The VB6 cells co-cultured with the siRNA HDFs also have a broad range of volumes.

4.7.2.3 Multi-parameter data analysis: invasion vs elipticity (oblate and prolate)

In **Figure 4.20** I compared invasiveness with oblate (horizontal, flattened shape) and prolate (vertical, elongated shape) elipticity. If we compare the NT control samples in each of the five pairs of data in **Figure 4.20**, In general, the trend is toward a more elongated (higher values for elipticity prolate) and a less flattened (lower values for elipticity oblate) polarisation in the invasive NT HDFs. Generally the VB6 cells show a spread of oblate and prolate elipticity values between 0.2 – 0.6. For the siRNA treated HDFs, in general, the elipticity values exhibit a broader range for both oblate and prolate for all samples compared with the NT control. The VB6 cells associated with the siRNA treated HDFs also have a broad range of elipticities.

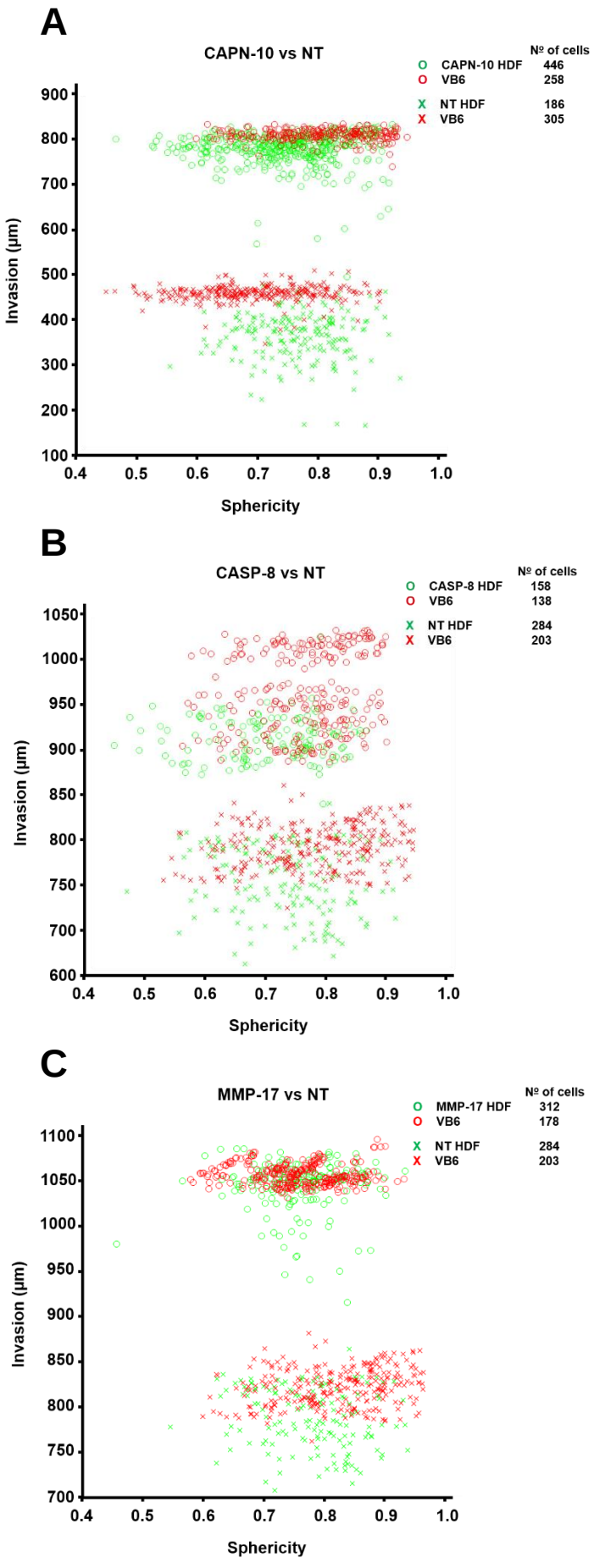
A
CAPN-10 vs NT
№ of cells
CAPN-10 HDF 446
VB6 258
NT HDF 186
VB6 305
Invasion (µm)
Sphericity
B
CASP-8 vs NT
№ of cells
CASP-8 HDF 158
VB6 138
NT HDF 284
VB6 203
Invasion (µm)
Sphericity
C
MMP-17 vs NT
№ of cells
MMP-17 HDF 312
VB6 178
NT HDF 284
VB6 203
Invasion (µm)
Sphericity

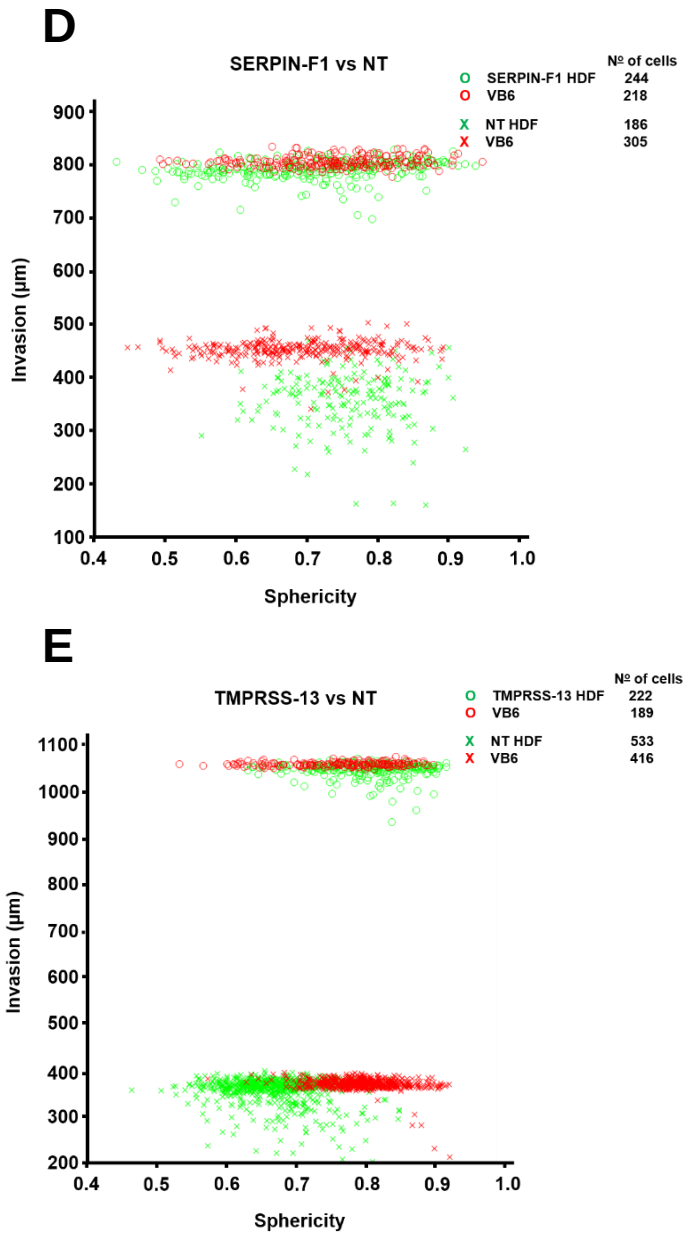

Figure 4.18: Multi-parameter analysis of the five selected siRNA targets: Invasion vs sphericity

The figure illustrates invasion vs sphericity data from the five chosen siRNA targets alongside a NT control. Fluorescently labelled HDF cells were transfected with SMARTpool target or NT siRNA control, co-cultured with fluorescently labelled VB6s and plated into mini-organotypic gels. *Z*-stacks were collected six days post transfection via CLSM and analysed by Imaris XT. A custom designed MatLab® algorithm extrapolated invasion and sphericity data from .csv files produced by Imaris XT. **O** represent fluorescent HDF cells transfected with target siRNA and **O** represent fluorescent VB6 cells co-cultured with target transfected HDFs. **X** represent fluorescent HDF cells transfected with NT siRNA control and **X** represent fluorescent VB6 cells co-cultured with NT transfected HDFs. **A)** CAPN10 vs NT. **B)** CASP-8 vs NT. **C)** MMP-17 vs NT. **D)** SERPIN-F1 vs NT. **E)** TMPRSS-13 vs NT. One representative plot of triplicate samples belonging to one independent experiment.

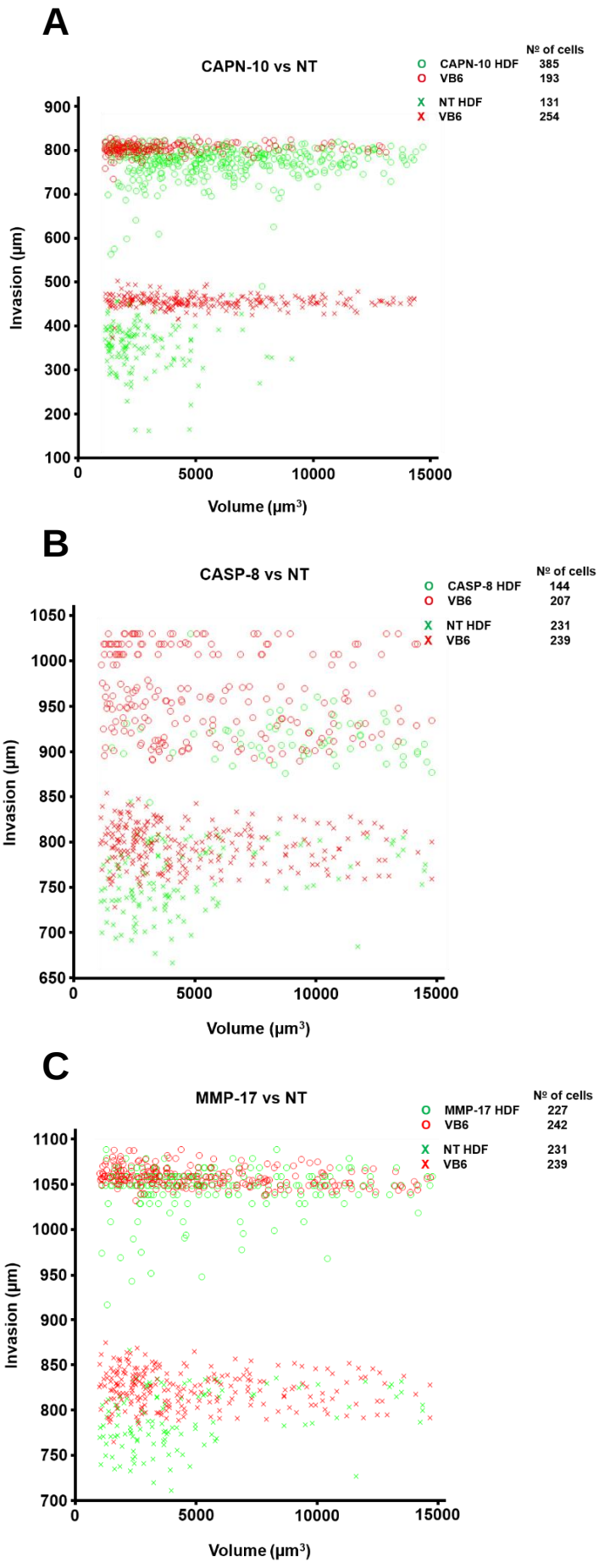
A
CAPN-10 vs NT
№ of cells
CAPN-10 HDF 385
VB6 193
NT HDF 131
VB6 254
Invasion (µm)
Volume (µm³)
B
CASP-8 vs NT
№ of cells
CASP-8 HDF 144
VB6 207
NT HDF 231
VB6 239
Invasion (µm)
Volume (µm³)
C
MMP-17 vs NT
№ of cells
MMP-17 HDF 227
VB6 242
NT HDF 231
VB6 239
Invasion (µm)
Volume (µm³)

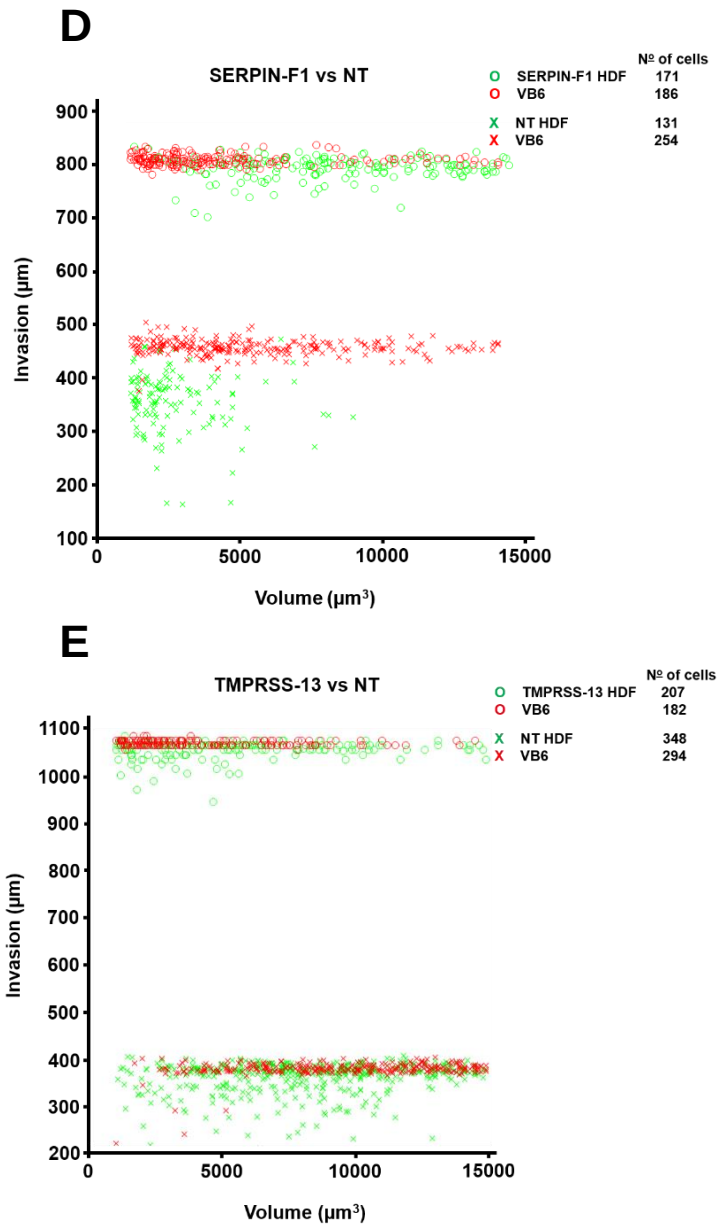

Figure 4.19: Multi-parameter analysis of the five selected siRNA targets: Invasion vs volume

The figure illustrates invasion vs volume data from the five chosen siRNA targets alongside a NT siRNA control. Fluorescently labelled HDF cells were transfected with SMARTpool or NT siRNA, co-cultured with fluorescently labelled VB6s and plated into mini-organotypic gels. *Z*-stacks were collected six days post transfection via CLSM and analysed by Imaris XT. A custom designed MatLab® algorithm extrapolated invasion and volume data from .csv files produced by Imaris XT. **O** represent fluorescent HDF cells transfected with target siRNA and **O** represent fluorescent VB6 cells co-cultured with target transfected HDFs. **X** represent fluorescent HDF cells transfected with NT siRNA control and **X** represent fluorescent VB6 cells co-cultured with NT transfected HDFs. **A)** CAPN10 vs NT. **B)** CASP-8 vs NT. **C)** MMP-17 vs NT. **D)** SERPIN-F1 vs NT. **E)** TMPRSS-13 vs NT. One representative plot of triplicate samples belonging to one independent experiment.

A

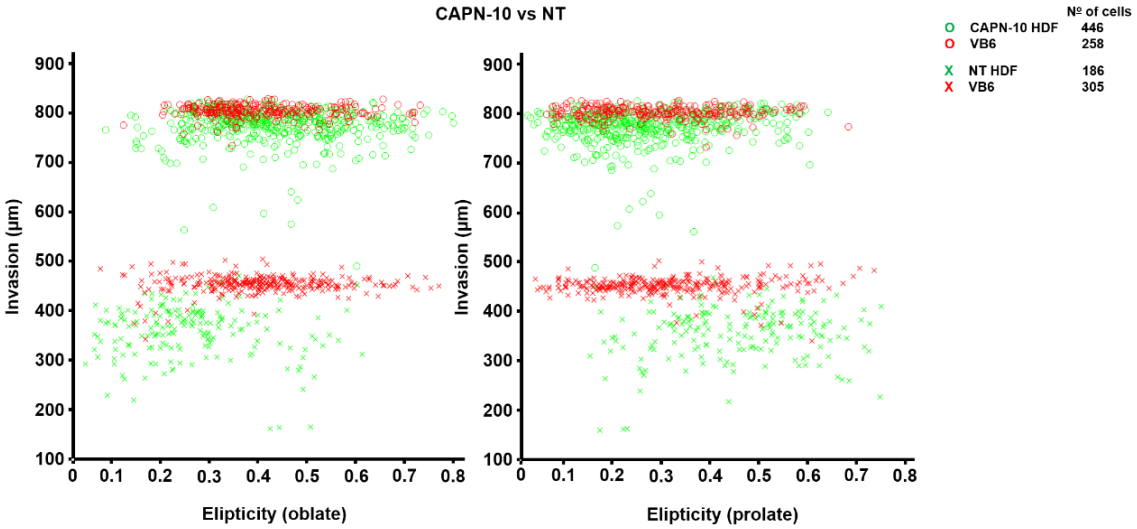
CAPN-10 vs NT
№ of cells
O CAPN-10 HDF 446
O VB6 258
X NT HDF 186
X VB6 305
Invasion (µm)
Elipticity (oblate)
Elipticity (prolate)

B

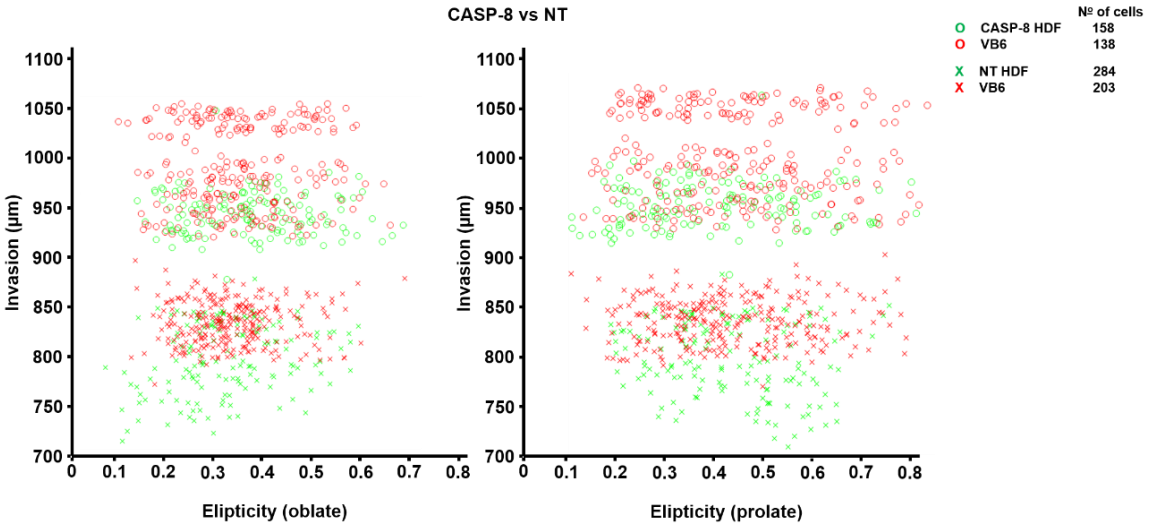
CASP-8 vs NT
№ of cells
O CASP-8 HDF 158
O VB6 138
X NT HDF 284
X VB6 203
Invasion (µm)
Elipticity (oblate)
Elipticity (prolate)

C

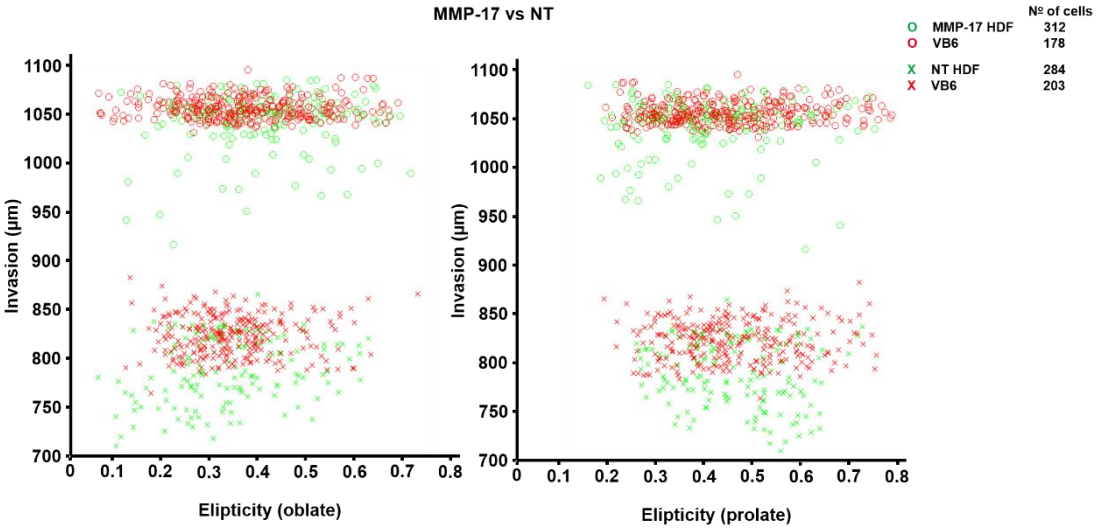
MMP-17 vs NT
№ of cells
O MMP-17 HDF 312
O VB6 178
X NT HDF 284
X VB6 203
Invasion (µm)
Elipticity (oblate)
Elipticity (prolate)

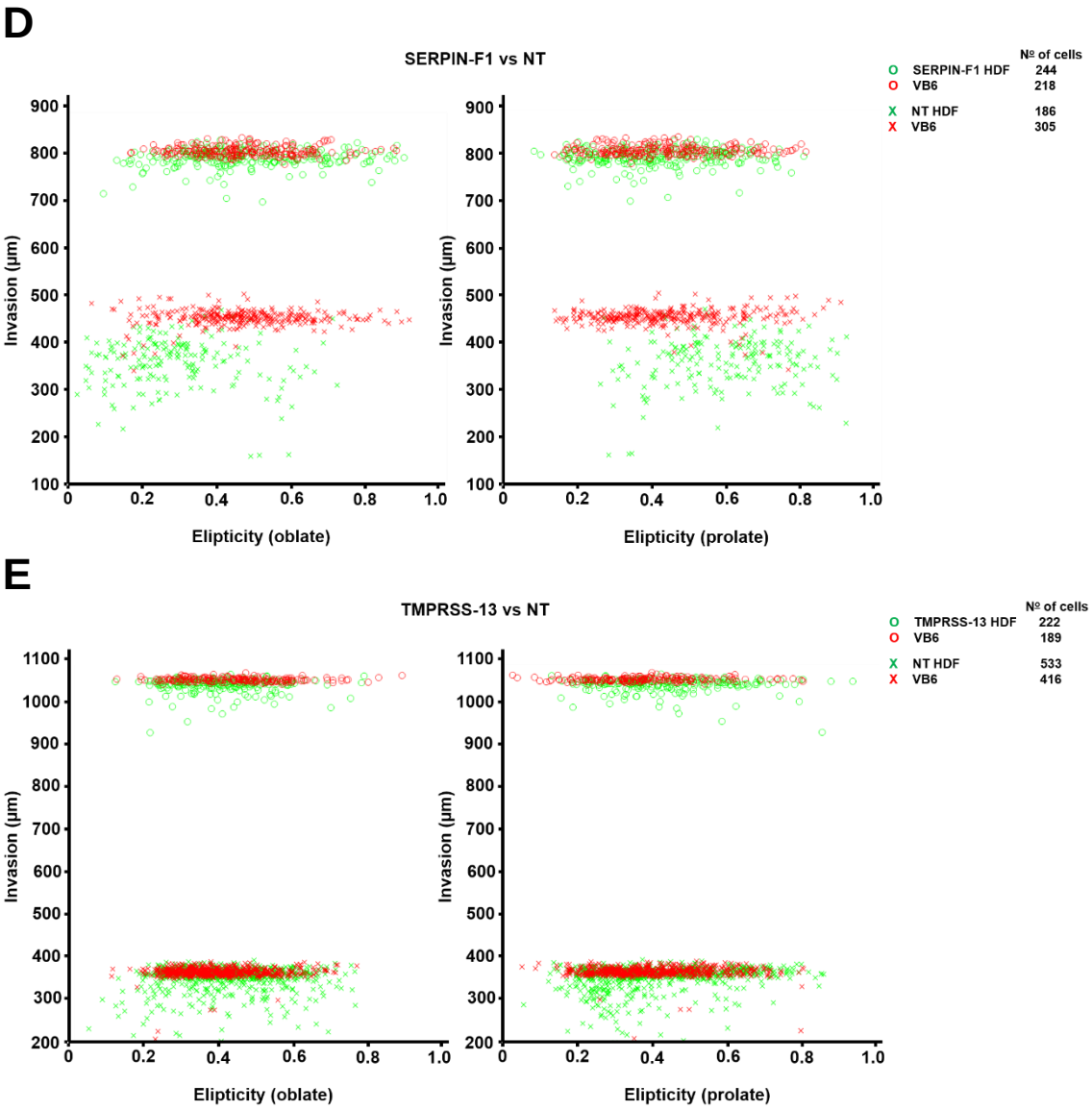

Figure 4.20: Multi-parameter analysis of the five selected siRNA targets: Invasion vs elipticity (oblate and prolate)

The figure illustrates invasion vs elipticity (oblate and prolate) data from the five chosen siRNA targets alongside an NT siRNA control. Elipticity oblate is a measure of compression of spherical objects when rotated along their minor axis, thus forming flattened disk-like shapes. Elipticity prolate is a measure of elongation of spherical objects when rotated along their major axis, thus, forming a rugby ball-like shape. A custom designed MatLab® algorithm extrapolated data from invasion and elipticity .csv files produced by Imaris XT. **O** represent fluorescent HDF cells transfected with target siRNA and **O** represent fluorescent VB6 cells co-cultured with target transfected HDFs. **X** represent fluorescent HDF cells transfected with NT siRNA control and **X** represent fluorescent VB6 cells co-cultured with NT transfected HDFs. **A)** CAPN10 vs NT. **B)** CASP-8 vs NT. **C)** MMP-17 vs NT. **D)** SERPIN-F1 vs NT. **E)** TMPRSS-13 vs NT. One representative plot of triplicate samples belonging to one independent experiment.

4.7.3 Summary of multi-parameter analysis

Here, I have presented the value of 3D multi-parametric phenotypic data that can be obtained from Imaris XT image analysis with aid of a custom designed MatLab® algorithm. Graphical data representation of invasion vs elipticity, sphericity and volume further suggests that siRNA knockdown of specific proteases on HDFs, co-cultured with VB6 tumour cells reduces cell polarisation, gel shrinkage and collective cell invasion into 3D gels.

With more time I could have developed an algorithm to perform statistical analysis in MatLab® on the multi-parameter data sets. For example, to determine any significance between cells within a sub-group of the majority population that may be more polarised. Additionally, to determine if there is any significance between the level of sphericity and invasion.

4.8 Discussion

Cancer cell metastasis *in vivo* can be influenced by an interactive 3D ECM. However, the majority of drug and RNAi primary and validation screens to identify potential therapeutic targets have been performed in 2D mono-layer culture systems (Chung et al., 2010; Jansen et al., 2017; Lee et al., 2015; Petrocca et al., 2013). A large number of studies have suggested that cellular cues, protein and gene expression, invasion and shape may all change in a 3D physiomimetic spatial architecture (Bissell et al., 2003; Nyga et al., 2011; Petersen et al., 1992; von der Mark et al., 1977).

Thus, 3D siRNA screening methods are becoming increasingly more prevalent; for example, the Cancer Biochip System has been used to study anchorage-independent breast cancer growth (Marhefka and Abbud-Antaki, 2012). Additionally, Bauer and colleagues used 3D mammospheres to perform an RNAi screen which identified several growth factors that increased breast cancer cells sensitivity to paclitaxel (Bauer et al., 2010). Furthermore, Thoma and colleagues developed a 3D hanging droplet spheroid assay to assess phenotypic growth effects of siRNA gene depletions in colon cancer cells (Thoma et al., 2013).

Here, I used the novel fluorescent 3D mini-organotypic co-culture invasion assay to perform a LOF siRNA screen from a custom library of intracellularly expressed proteases (**Figure 4.1** - **Figure 4.5**). Statistical analysis from the primary screen identified 16 hit targets which significantly ($p<0.05$) reduced fibroblast and cancer cell invasion six days post transfection compared to the NT control (**Figure 4.6**).

4.8.1 Investigation of hits from primary SMARTpool siRNA screen

The 16 hits from the primary screen (listed in **Table 4.1** and displayed in **Figure 4.7**) were categorised by their families and investigated for their relevance, if any, in cancer progression (described in detail below).

4.8.1.1 Investigation of proteases from primary SMARTpool siRNA screen – CAPNs

Investigations have highlighted the importance of several calpains in processes crucial to cancer development and progression. A study published in 2009 identified two splice variants of CAPN-3 that could be responsible for degrading cytoplasmic β-

catenin, thus having control on the translocation to the nucleus, where β-catenin regulates transcription factors involved in cell proliferation and motility in melanoma development (Moretti et al., 2009).

Additionally, increased expression of CAPN-6 was observed during progression of uterine cervical neoplasia (Lee et al., 2008b). Furthermore, the regulatory role of CAPNs has been identified in apoptotic death in malignant brain tumours (Ray et al., 2002) and induce apoptosis in human prostate cancer cells (Zhu et al., 1995). CAPN-10 expression is ubiquitous (Sorimachi and Suzuki, 2001) and has been associated with type 2 diabetes (Horikawa et al., 2000; Ling et al., 2009).

However there is very little evidence to suggest that CAPN-10 plays a role in cancer progression, with the exception of Moreno-Luna and colleagues, whom analysed the contribution of CAPN-10 alleles in laryngeal cancer survivors (Moreno-Luna et al., 2011). Furthermore, the study of an association between variants in the diabetes susceptibility gene (CAPN-10) with pancreatic cancer amongst smokers (Fong et al., 2010). Moreover, I did not identify evidence of CAPN-10 having been used in a 3D model, thus, making CAPN-10 an interesting target for further pursuit.

4.8.1.2 Investigation of proteases from primary SMARTpool siRNA – CASPs

During normal development (embryogenesis, angiogenesis and organogenesis) excess cells are eliminated by various cell death modalities, amongst them, apoptosis is the most investigated. In 1972 it was first described as a major defence strategy, preventing cells from acquiring tumourigenic potential (Kerr et al., 1972).

Caspases (cysteine-aspartic proteases) are a family of Ca^{2+} independent enzymes essential for maintaining homeostasis through programmed cell death (apoptosis, necrosis and pyroptosis) and are categorised as initiators or effectors based on their apoptotic signalling cascade positions. Caspases can be subdivided into three functional groups; executioner CASPs (-3, -6 and -7) initiator CASPs (-2, -8, -9 and -10) and inflammatory CASPs (-1, -4, -5, -11 and -12) (Zhivotovsky, 2003). Interestingly, the regulation of apoptosis is controlled by the initiator CASPs (-2, -8, -9 and -10) (Olsson and Zhivotovsky, 2011; Parrish et al., 2013).

Groups have investigated the role of CASP-8 within neuroendocrine lung carcinomas and suggested that loss of CASP-8 expression in lung cancer cells (NCI-H82) correlates with activation of the MYCN oncogene (Shivapurkar et al., 2002).

Additionally, inactivation of CASP-8 has been considered to be involved in the pathogenesis of childhood neuroblastoma tumours (Takita et al., 2000; Teitz et al., 2000).

Furthermore the loss of protein and mRNA CASP-8 expression and enzyme activity are common in rhabdomyosarcomas, medulloblastomas, retinoblastomas and neuroblastomas (Harada et al., 2002). Interestingly, CASP-8 activity has been suggested to promote cell invasion in neuroblastoma cells (NB7 and NB5) (Barbero et al., 2009) and inhibition of CASP-8 suppressed cell migration of breast cancer cells (Lopez et al., 2011). This evidence suggests CASP-8 may have function as a potential future therapeutic target, however, increased understanding of its molecular mechanisms would be desired, thus making CASP-8 a suitable candidate for further investigation.

4.8.1.3 Investigation of chosen proteases from siRNA screen – MMPs

MMPs are a clan within a larger metzincin superfamily, which include other members such as astacins, reprolysins (a disintegrin and metalloproteinase (ADAMs)) and serralysins (Page-McCaw et al., 2007; Ra and Parks, 2007). MMPs are widely expressed and cleave a variety of extracellular substrates including, but not limited to, proteoglycans and protein components of the ECM. Thus, MMPs catalyse hydrolysis of ECM proteins, including, collagens, fibronectin and laminins, thus modifying the integrity of the connective tissue (Nagase et al., 2006). Moreover, MMP activation is regulated by tissue inhibitors of metalloproteinases (TIMPs) (Brew and Nagase, 2010).

This protease family includes secreted and soluble MMPs, or membrane type MMPs (MT-MMP) that are anchored to the cell surface through transmembrane domains, called glycosyl-phosphatidyl inositol (GPI) anchors (Host et al., 2012). There are 25 distinct family members of MMPs, humans having 24 of the matrixin genes including the duplicated MMP-23 gene, which can be organised into six groups based on substrate preference: Collagenases (MMP-1, -8, -13 and -18), gelatinases (MMP-2 and -9), stromelysins (MMP-3, -10 and -11), matrilysin (MMP-7 and -26), membrane type (MT)-MMPs (MMP-14, -15, -16, -17, -24 and -25) and others include MMP-12, -19, -20, -21, -23A -23B, -27 and -28.

Several studies have described the presence of MMPs in many types of cancer, Kohrmann and colleagues identified increased expression of MMP-1, -2, -8, -9, -10, -11, -12, -13, -15, -19, -23, -24, -27, and -28 on human breast cancer tissue compared to normal breast tissue (Kohrmann et al., 2009). Additionally, MMP-10 was suggested to be more highly expressed in lung cancer tumours with high metastatic potential (Regala et al., 2011). Interestingly, MMP-2, -9 and -14 (MT1-MMP) have been reported to mechanistically become involved in tumour angiogenesis (Littlepage et al., 2010). Moreover, our laboratory reported MMP-2 and -9 promote invasion of OSCC when upregulated via an increased expression of the integrin αvβ6 (Thomas et al., 2001a).

The MT-MMPs are affixed to the plasma membrane via a GPI anchor, enabling these enzymes to contain a unique set of functional and regulatory mechanisms that distinguish them from the rest of the MMP family (Itoh et al., 1999). MMP-17 is a member of the MT subfamily (MT4-MMP), it was cloned from human breast carcinoma cDNA and its mRNA has been expressed in breast cancer tissue (Chabottaux et al., 2006; Puente et al., 1996). The role of MMP-17 is currently unknown and there is little literature evidence describing its roll its role in cancer, with the exception of its expression being observed in multiple breast cancers, suggesting it plays a role in tumour invasion and metastasis (Puente et al., 1996). Thus, making MMP-17 (MT4-MMP) an interesting target for further investigation.

4.8.1.4 Investigation of chosen proteases from siRNA screen – SERPINs

SERPINs are a broadly distributed superfamily of serine proteinase inhibitors that use a conformational change to inhibit target enzymes. Over 1,500 SERPIN-like genes have been identified in animals, bacteria, plants and poxviruses. However in humans, 36 SERPINs have been identified as extracellular molecules (13 members of Clade A) and intracellular molecules (13 members of Clade B) and play a significant role in inflammation and cancer metastasis (Law et al., 2006; Silverman et al., 2001). SERPIN-F1 (also known as pigment epithelium derived factor, PEDF) was discovered in the early 1990s as a differentiation factor for retinoblastoma cells (Steele et al., 1993; Tombran-Tink et al., 1991). Soon after it was reported that expression of PEDF is highly increased in young lung fibroblasts cells related to senescent cells and has since been associated with growth arrest and ageing in fibroblasts (Doggett et al., 1992; Pignolo et al., 1993).

Almost a decade after its initial discovery, PEDF was described as an inhibitor of angiogenesis (Dawson et al., 1999) and thereafter been reported, to delay tumour growth in retinoblastomas (Yang et al., 2009), inhibit tumour cell proliferation in prostate cancer (Zhang et al., 2007) and act as both, a metastatic suppressor and neuroprotectant in brain metastasis from breast tumours (Fitzgerald et al., 2012). These observations show that PEDF (SERPIN-F1) has been implicated within diverse biological processes and is prominently emerging as an area of interest as an anticancer target, thus, making an interesting target to pursue.

4.8.1.5 Investigation of chosen proteases from siRNA screen – TMPRSS13

TMPRSS are one of four sub-family groups under the umbrella of type II transmembrane serine proteases (TTSPs) family. Several members of the TTSPs family have been shown to play a critical role in cancer progression. Hepsin (sub-family member of TTSPs) a cell surface serine protease, has been reported to be upregulated in prostate cancer (Klezovitch et al., 2004; Wu and Parry, 2007). Matriptase, also known as membrane-type serine protease 1, is widely, but not ubiquitously expressed at the cell surface of epithelia and expression of this protease correlates with the progression of ovarian (Oberst et al., 2002) and head and neck cancer (Cheng et al., 2006).

Moreover, Matriptase-2 (TMPRSS-6) has been linked to breast cancer (Hartikainen et al., 2006; Tuhkanen et al., 2013). TMPRSS-13 is a splice variant of the mosaic serine protease large forms and is a member of the hepsin sub-family (Hashimoto et al., 2010; Kido and Okumura, 2008). However the precise physiological and pathological function of TMPRSS-13 and its role, if any, in cancer progression remain to be investigated.

A biological repeat of the siRNA SMARTpool knockdown and qPCR data from the five chosen hits (CAPN-10, CASP-8, MMP-17, SERPIN-F1 and TMPRSS-13) confirmed observations from the primary screen, whereby, knockdown of the target siRNA in HDF cells reduced gel contraction, HDF cell polarisation and HDFs and VB6 cell invasion (**Figure 4.8**). Thus overall with the exception of SERPIN-F1 the other hits have all been associated with cancer but not through expression in the mesenchymal cells. My data suggested that many fibroblast proteases represent important components of tumour progression and invasion.

4.8.2 Summary of multi-parametric phenotypic analysis

3D high-content phenotypic screens are being widely implemented within early stage drug discovery research. For example, Di and colleagues used a 3D micro tissue assay cultured with mouse breast cancer cells (4T1 cells) to perform a phenotypic drug screen profiling against 598 parameters via ImageJ analysis (Di et al., 2014). Additionally, earlier this year, Ott and colleagues used high content image analysis and automated liquid handling robotics to not only plate, but also to dose 3D liver spheroids to deduce drug-drug interactions in hepatotoxicity studies (Ott et al., 2017).

The success of such assays depend on a variety of factors, such as; (1) developing a repeatable, reliable and robust 3D assay; (2) producing a suitable 3D physiomimetic environment to address the experimental question; (3) sourcing an appropriate imaging platform to ensure, not only speed, but sufficient resolution of image capture; and (4) ease of data analysis, having an image analysis system in place whereby multi-parametric phenotypic profiling can be efficiently determined. Here, we have adopted an efficient, user friendly programmable interface to extrapolate and deduce multi-parametric data from previous image analysis.

In the previous chapter I described the development of a novel, physiomimetic fluorescent invasion assay which offers reproducible, robust and quantitative 3D analysis. Development of the assay identified that fibroblasts (in this case HDFs) appear to be the leading invasive cell type. However, cancer cells appear to follow closely behind, probably migrating through the channels created from matrix degradation and remodelling by enzymatic secretions from the HDFs.

These data fit with observations from other studies in which fibroblast invasion led to collective cancer cell invasion (Gaggioli et al., 2007). With this information, we thought rather than focusing solely on trying to reduce cancer cell invasion, we would focus on targeting fibroblast activity. Here, I have utilised the assay to perform a siRNA screen of proteases, targeting specifically the HDF cells.

The objective of this screen was to identify, if any, targets whose silencing by siRNA significantly reduced HDF and consequently VB6 cell collective invasion. Image and quantitative invasion analysis identified 16 hits which significantly ($p<0.05$) reduced fibroblasts (HDF) and cancer (VB6) cell invasion six days post transfection. Interestingly, I observed changes in phenotypic characteristics (cell shape and polarity) within each cell type from different treatments.

To further examine these characteristics, we employed aid of a high-performance mathematical programming language (MatLab®) to measure and plot multi-parameter high-content data produced during Imaris XT image analysis. Analysis of invasion vs elipticity, sphericity and volume suggests knockdown of specific proteases in our HDF cells may lead to reductions in gel contraction, HDF polarisation and ultimately HDF and VB6 cell collective invasion in 3D gels when compared to a NT control treated sample.

Interestingly, phenotypic multi-parametric data analysis has also revealed different levels of variation between triplicate repeats. Suggesting that the amount of variation between cells from one experiment to another (performed 1-2 weeks apart) could potentially effect cellular behaviour within the 3D gels (such as cell adhesion, shape, and polarity). This may be due to the passage number of the HDF and VB6 cells, although lower passages were continually used. Additionally, the degree of variation may also be related to position of each Transwells® within the 24-well source plate during incubation; those situated at the plate periphery could be subject to greater levels of evaporation thus changing cell morphology.

However, the use of high-content multi-parameter phenotypic data analysis via MatLab® has proved to be a useful ally in the 3D fluorescent mini-organotypic invasion assay, in terms of; (1) extracting and plotting large amounts of data efficiently; (2) diversity, the algorithm can be easily modified by users with an intermediate level of expertise; (3) integration, MatLab® can be partnered with batch analysis software (such as SnowPlow and Pipeline Pilot) to perform ‘on-the-fly’ data migration and analysis, thus increasing the rate of result delivery.

Further investigation into these data would require more time. However, the use of MatLab® to determine these data provides greater support to earlier observations, thus, further validating the reliability and robustness of the assay.

The challenge now was to miniaturise and optimise the 24-well assay, to a 96-well microtiter plate format, thus enabling higher-throughput of small molecules and increased high-content data capture, further described in the next chapter.

CHAPTER V: RESULTS PART III

DEVELOPMENT OF A FLUORESCENT 96-WELL MICRO-ORGANOTYPIC INVASION ASSAY

5.0 Development of a fluorescent 96-well micro-organotypic invasion assay

5.1 Background

Over the last 15 years the majority of *in vitro* cell based drug discovery screening has been performed within 2D culture systems on flat and rigid substrata. However, culturing cells in 2D conditions may not be physiologically relevant with translation *in vivo* for reasons previously mentioned. Tissue-specific spatial architecture and biochemical and biomechanical elements surrounding the stromal microenvironment are all essential components of a developing tumour microenvironment and can be, at least in part, recapitulated within 3D culture systems. Earlier I described (**Section 1.3**) and summarised (**Table 1.1**) the main differences between 2D and 3D culture systems.

For example, endometrial cancer cells (Ishikawa, KLE and RL95-2) displayed lower proliferative rates in 2D monolayer cultures, compared to 3D spheroids supplemented with Matrigel® (Chitcholtan et al., 2012). Additionally, Gudjonsson and colleagues showed that mammary epithelial cells can form functional acini as observed *in vivo* when cultured on 3D collagen type I: laminin-1 rich gels (Gudjonsson et al., 2002).

With this in mind, many groups around the world have pioneered 3D cancer models to recapitulate the tumour-stromal microenvironment. Some examples include the use of organotypic culture models to study progression of pancreatic ductal adenocarcinoma (PDAC) (Carapuca et al., 2016; Froeling et al., 2009). Multicellular tumour spheroids used investigate the invasion, proliferation and viability of NSCLC line (Colo699) dosed with Afatinib (a tyrosine kinase inhibitor which targets EGFR) (Huber et al., 2016); and more advanced technologies, such as, 3D organ-on-a-chip microsystems, which have been used to successfully recreate and mimic human lung function (Benam et al., 2016) and identify gene targets for breast cancer via siRNA screening (Marhefka and Abbud-Antaki, 2012).

As advanced and unique as these 3D technologies are, they all share one common drawback, which is their inability to be integrated into a HTS automated workflow. This may be due to several factors, such as; (1) their incapacity to be miniaturised; (2) the need for human input during the assay protocol; (3) the high cost of consumables and reagents per experiment prohibiting higher-throughput; and (4) the

amount of time needed to complete the assay, analyse the data and measure significant changes.

Previously, I described the development of a novel 3D fluorescent invasion assay which produced reproducible, robust quantitative analysis and was also utilised to perform a siRNA screen of proteases. The screen identified MMP-17 may be required for the promotion of cancer cell invasion. Here I sought to develop and miniaturise the 24-well 3D mini-organotypic invasion assay, to engineer a one-step assay system, whereby initial cell and gel seeding, live image capture and final analysis is not only within the same culture vessel, but also compatible with laboratory HTS automation and high-content data analysis.

5.2 96-well micro-organotypic Transwell® invasion assay

The fluorescent 24-well mini-organotypic invasion assay revealed that not only do certain types of fibroblasts become polarised and rapidly invade down through a collagen: Matrigel® substrate, but also that they are the most invasive cell type. Previously, I have shown that this assay was used to perform a siRNA protease screen and revealed that knockdown of MMP-17 in HDF cells changed cell shape, gel contraction and significantly reduced invasion of HDF and VB6 cells (relative to a non-targeting siRNA control).

However, the entire screen, from tissue culture, to image capture, image rendering and data analysis took over 18 months to complete. This was in part due to; (1) procuring the correct microscope parts (LWD objective and plate stage); (2) obtaining an appropriate image analysis software; (3) time lost during delivery of reagents and consumables; and (4) limited use of the confocal microscope. This highlights the need to develop a novel 3D organotypic based model which would allow for higher-throughput of samples. Thus, I aimed to downsize the assay by increasing sample numbers with the use of a 96-well plate format.

Described in **Section 2.10.1**, Corning produce a variety of 96-well Transwell® insert plates covering a range of pore sizes between 0.4-8.0µm. Each plate includes a Transwell® unit (96-well insert), a reservoir plate and 96-well receiver plate with oval shaped wells. However all of the Transwell® insert units possess an opaque polycarbonate membrane which not suitable for imaging purposes (**Figure 2.2A**).

During a secondment with my collaborators, AstraZeneca, I contacted Corning requesting the need of a 96-well Transwell® insert with 0.4µm pore sizes and a PET (transparent) membrane. Corning sent free samples to me (**Figure 2.2B**), presumably having specifically manufactured them and now commercially produce these plates at a cost of £884.61 per case (five plates) (Corning, #7369).

5.2.1 96-well vs 24-well Transwell® insert invasion assay

To determine if the 96-well Transwell® insert could be used in a higher-throughput manner, this plate type was used to perform a comparison study against the 24-well mini-organotypic Transwell® invasion assay. Organotypic gel was prepared as described in **Section 2.3.1** and added to wells of the 96-well Transwell® insert plate (50µl/well) before being placed into an incubator to polymerise. Meanwhile, HDF and VB6 cells were fluorescently labelled with CellTracker™ Green (10µM) and Red

(5µM) respectively (described in **Section 2.4**). The fluorescently labelled cells were counted and seeded on top of the polymerised organotypic gels in 50µl suspensions of VB6s or HDFs alone (5 x 10^3 cells total), or in a 2:1 co-culture ratio of fibroblast (3.3 x 10^3 cells) and tumour (1.7 x 10^3 cells). 3D *z*-stack images were obtained over a 72 hour period via CLSM and raw .lsm confocal *z*-stacks were rendered and analysed via Imaris XT (described in **Section 2.5**) (**Figure 5.1**, **Figure 5.2** and **Figure 5.3**).

5.2.1.1 96-well micro-organotypic Transwell® cultured with fluorescently labelled VB6 cells imaged at 24, 48 & 72 hour time points

To compare the 96-well micro-organotypic Transwell® assay against the 24-well mini-organotypic invasion assay (**Figure 3.7**); fluorescently labelled, CellTracker™ Red (5µM) VB6 cells were plated alone on top of the gels and imaged every 24 hours for three days via CLSM 710, producing *z*-stack volumes.

Using Imaris XT image analysis software a rendered, smoothened 3D representation of the raw .lsm confocal *z*-stack was generated for the 24, 48 and 72-hour time points (**Figure 5.1A-C**). Distance Transformation analysis was performed on the rendered 3D volumes producing .csv data files. Graphical plots of invasive depth were generated in Prism using data extrapolated from the .csv files (**Figure 5.1D**).

At the 24 hour time point image analysis revealed the VB6 cells appear adhered and homogeneously spread on to the surface of the gel. Throughout the 72 hour time points VB6s do not exhibit signs of invasion into the organotypic gel. Additionally, over a 72 hour period the VB6s display proliferation and reside within tightly packed layers spanning 80µm (24 hours), 100µm (48 hours) and 120µm (72 hours). Gel height does appear to reduce over the 72 hour period, possible due to evaporation of the exposed surface of the gels during incubation (gel height at 24 hours is approximately 1450µm, shrinking to approximately 1080µm by 72 hours).

These data are consistent with the observations from **Figure 3.7,** where VB6 cells were plated on top of organotypic gels housed within the 24-well Transwell® format. In the 24-well format, 100µl of organotypic gel was plated into each Transwell® and once polymerised, this produced a gel 1400-1500µm in thickness when imaged at the 24 hour time point. Similarly, the gel thickness within the 96-well format is also between 1400-1500µm in thickness despite only plating 50µl of gel. This is due to the

diameter differences between both Transwell® inserts. The 24-well Transwells® are wide, containing parallel vertical walls and a diameter of 6.5mm whereas, the 96-well Transwells® have narrow non-parallel walls and a diameter of 4.26mm. Both formats permit a 700µm x 700µm x 1500µm field of view and show increased proliferation, gel shrinkage and no invasion of VB6 cells over a 72 hour period.

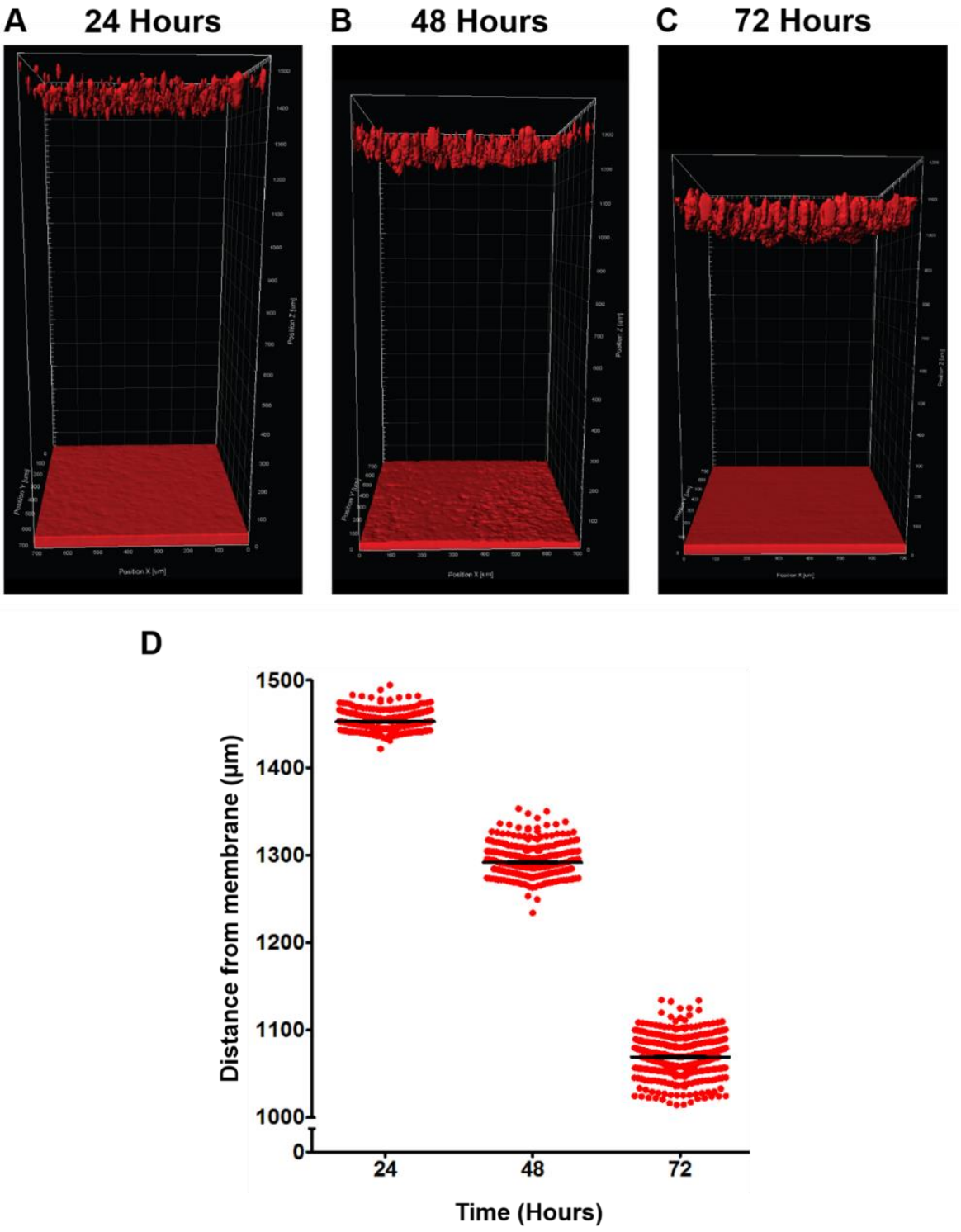

Figure 5.1: 3D rendered and quantified z-stacks of fluorescently labelled VB6 cells plated alone on top of 96-well Transwell® micro-organotypic gels

Figure 5.1: 3D rendered and quantified z-stacks of fluorescently labelled VB6 cells plated alone on top of 96-well Transwell® micro-organotypic gels

The figure displays Imaris XT rendered and analysed 96-well micro-organotypic gels plated with CellTracker™ Red labelled VB6 cells (5µM). Confocal microscope obtained *z*-stacks were segmented, rendered and analysed by Imaris XT. Images were rendered using a surface segmentation tool that accurately detects particles of specific diameters and intensity. Distance Transformation calculations were performed via Imaris XT and plotted in Prism. **A, B, C)** 24, 48 and 72 hour time point.VB6 cells appear vibrant with colour and are easily identifiable. VB6 cells do not invade throughout the micro-organotypic gel over a 72 hour period. However the average height of the gels reduces. This contraction is probably due to evaporation during incubation. Serum-free medium was not placed above each gel when incubated, thus exposing the upper surface of the gels. **D)** Graphical depiction of individual VB6 cells *z*-position in relation to the PET membrane (position 0). Each red dot represents one cell within the 700µm square field of view. The cells stack tightly together and on top of each other in a layer that is between 80-120µm in depth. One representative image for each time point from one of two independent experiments.

5.2.1.2 96-well micro-organotypic Transwell® cultured with fluorescently labelled HDF cells imaged at 24, 48 & 72 hour time points

To compare the 96-well micro-organotypic Transwell® assay against the 24-well mini-organotypic invasion assay (**Figure 3.8**); fluorescently labelled, CellTracker™ Green (10µM) HDF cells were plated alone on top of the gels and imaged every 24 hours for three days via CLSM 710, producing *z*-stack volumes.

Using Imaris XT image analysis software a rendered, smoothened 3D representation of the raw .lsm confocal *z*-stack was generated for the 24, 48 and 72-hour time points (**Figure 5.2A-C**). Distance Transformation analysis was performed on the rendered 3D volumes producing .csv data files. Graphical plots of invasive depth were generated in Prism using data extrapolated from the .csv files (**Figure 5.2D**).

At the 24 hour time point HDF cells appeared to be adhered and homogeneously spread on to the surface of the gel using image analysis. In addition, a number of HDF cells are seen to change their morphology and adopt a vertical orientation, thus invading vertically downward through the gel. At the 48 hour time point, increased numbers of HDFs have changed their orientation and invade further into the gel. This is probably due to enzymatic secretions from the fibroblasts which may have degraded the ECM proteins and remodelled the gels. Interestingly, at the 72 hour time point, the gel has drastically contracted vertically, however, there also appears to be signs of lateral contraction and the upper portion of the gel appears disfigured. This may be due to the narrowing walls of the 96-Transwell® insert exerting an inward force on to the gel and/or also the HDFs may have physically contracted the gel.

Between the 24 and 72 hour period the HDFs display increased proliferation and cover a *z*-range spanning 160µm (24 hours, **Figure 5.2A**), 250µm (48 hours, **Figure 5.2B**). Determining the range for the 72 hour time point (**Figure 5.2C**) accurately cannot be done due to the uneven surface. Gel height does appear to reduce over the 72 hour period, possible due to evaporation of the exposed surface of the gels during incubation and gel contraction via the fibroblasts (gel height at 24 hours is approximately 1700µm, shrinking to approximately 1000µm by 72 hours).

These data display some similarities with the observations from **Figure 3.8** where HDF cells were plated on top of organotypic gels housed within the 24-well Transwell® format. Both formats display levels of increased HDF proliferation and change in shape and orientation, resulting in invasion of HDFs into the gels. However, the 24-

well format displayed gel shrinkage 24 hours after cell-seeding (approximately 600µm, **Figure 3.8A**), whereas **Figure 5.2A** (96-well format 24 hour time point) gel height is 1700µm. This could be due to the rate of evaporation being less in the 96-well format than in the 24-well format, possibly to the reduced surface area of exposed gel.

Furthermore, data from **Figure 3.8C** suggest that HDFs polarise and invade very rapidly through 24-well mini-organotypic wells and by the 72 hour time have invaded into the entirety of the gel. However, the HDFs have not invaded as deeply into the gel by the 72 hour time point in this 96-well assay (**Figure 5.2C**). This may be due to the reduction in cell numbers plated per Transwell® (5×10^3 cells/well for 96-well, 10^5 cells/well for 24-well), or due to the fact that the volume of gel available for the cells to invade into is greatly reduced in the 96-well format, thus, not allowing them to invade as freely in all directions compared to the 24-well format.

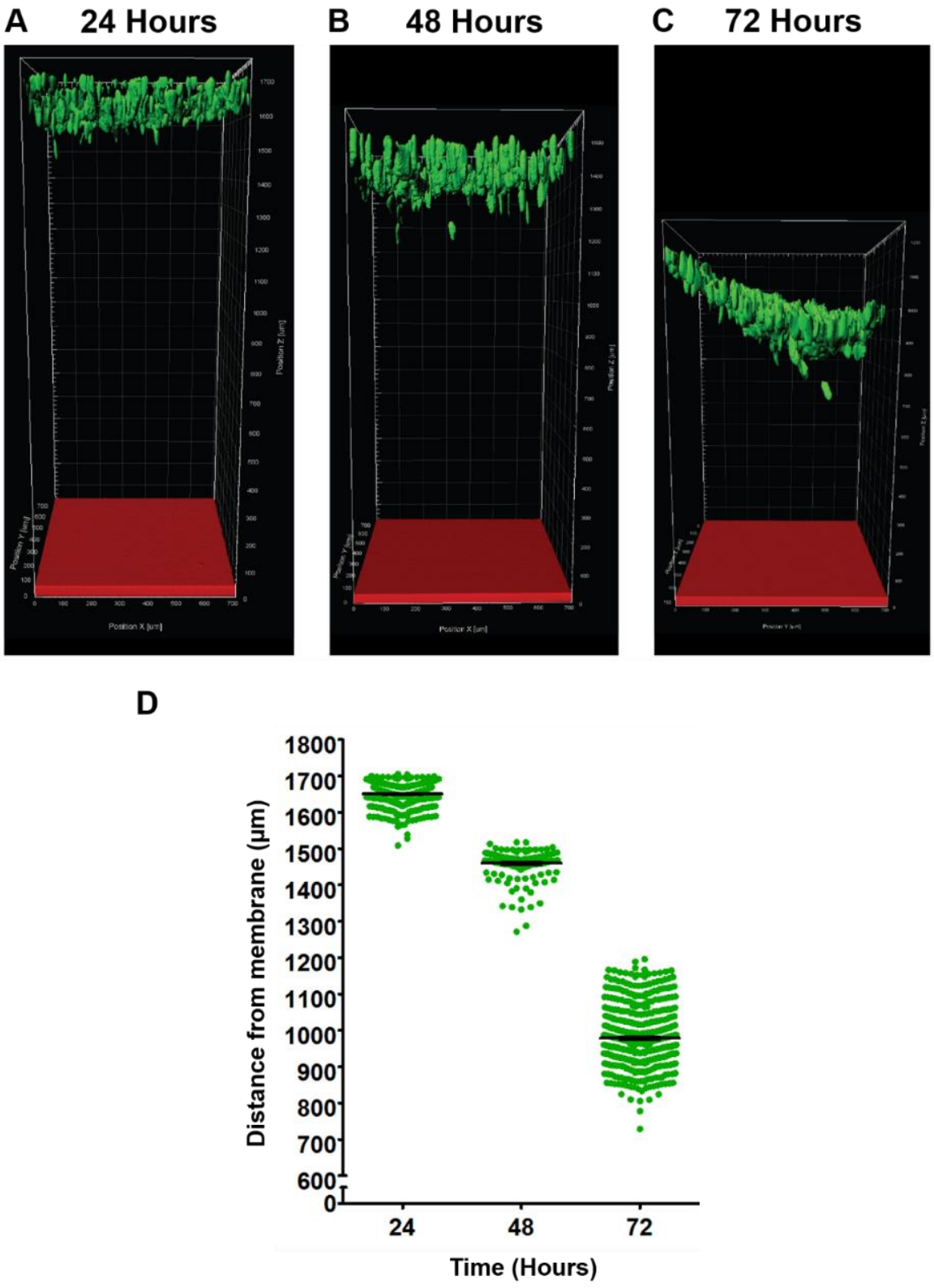

Figure 5.2: 3D rendered and quantified z-stacks of fluorescently labelled HDF cells plated alone on top of 96-well Transwell® micro-organotypic gels

Figure 5.2: 3D rendered and quantified z-stacks of fluorescently labelled HDF cells plated alone on top of 96-well Transwell® micro-organotypic gels

The figure displays Imaris XT rendered and analysed 96-well micro-organotypic gels plated with CellTracker™ Green labelled HDF cells (5µM). Confocal microscope obtained *z*-stacks were segmented, rendered and analysed by Imaris XT. Images were rendered using a surface segmentation tool that accurately detects particles of specific diameters and intensity. Distance Transformation calculations were performed via Imaris XT and plotted in Prism. HDF cells appear vibrant with colour and are easily identifiable. **A)** 24 hour time point, HDFs change shape and morphology and begin invading vertically downward through the gel. **B)** 48 hour time point, increased number of cells changing shape observed and cells invade further into the gel. **C)** After 72 hours gels display horizontal and perhaps lateral contraction and degradation, probably through evaporation during incubation and matrix remodelling from fibroblast secretions. **D)** Graphical depiction of individual HDF cells *z*-position in relation to the PET membrane (position 0). Each green dot represents one cell within the 700µm square field of view. One representative image for each time point from one of two independent experiments.

5.2.1.3 96-well micro-organotypic Transwell® co-cultured with fluorescently labelled VB6 and HDF cells imaged at 24, 48 & 72 hour time points

To compare the 96-well micro-organotypic Transwell® assay against the 24-well mini-organotypic invasion assay (**Figure 3.9**); HDF and VB6 cells were labelled with CellTracker™ Green (10µM) and Red (5µM) respectively and co-cultured in a 2:1 ratio on top of the gels and imaged every 24 hours for three days via CLSM 710.

Using Imaris XT image analysis software a rendered, smoothened 3D representation of the raw .lsm confocal *z*-stack was generated for the 24, 48 and 72-hour time points (**Figure 5.3A-C**). Distance Transformation analysis was performed on the rendered 3D volumes producing .csv data files. Graphical plots of invasive depth were generated in Prism using data extrapolated from the .csv files (**Figure 5.3D**).

After 24 hours both cell types appear to have attached and spread uniformly on the surface of the gel and display no signs of invasion at this time point. However, noticeably the HDF cells have started to change their shape and orientation to facilitate invasion.

At the 48 hour time point a large population of HDF and VB6 cell remain at the surface of the gel, however, a small number of HDFs are observed invading vertically through the gel and a small number of VB6 tumour cells are also observed breaking away the main layer. Gel height between these two time points is very similar, both approximately 1400µm, however, at the 72 hour time point, the gel has contracted vertically (now approximately 850µm) and HDF cells are observed invading through the gel. I also observed that the most invasive cell type was a fibroblast and often followed closely behind by VB6 tumour cells.

These data show resemblance similar to that of **Figure 3.9**, where HDF and VB6 cells were co-cultured into the 24-well format. In both formats, the leading invasive cell type always appears to be a fibroblast, which are followed by tumour cells probably migrating through the channels created by the fibroblasts during matrix remodelling. Additionally, data from **Figure 3.9** suggested that the rate at which the HDF cells invade through the gels when co-cultured with VB6 cells is reduced and results in a slower initial rate of polarisation and invasion when compared to HDFs plated alone (**Figure 3.8**).

This also appears to be a similar observation between **Figure 5.2** and **Figure 5.3**. Furthermore, I observed a large difference in gel contraction and invasion between the 48 and 72 hour time points, whereas, data from **Figure 3.9** suggests gradual gel shrinkage over 72 hours. This may be due to evaporation, matrix remodelling or even an inward force being exerting on to the gels from the 96-well format.

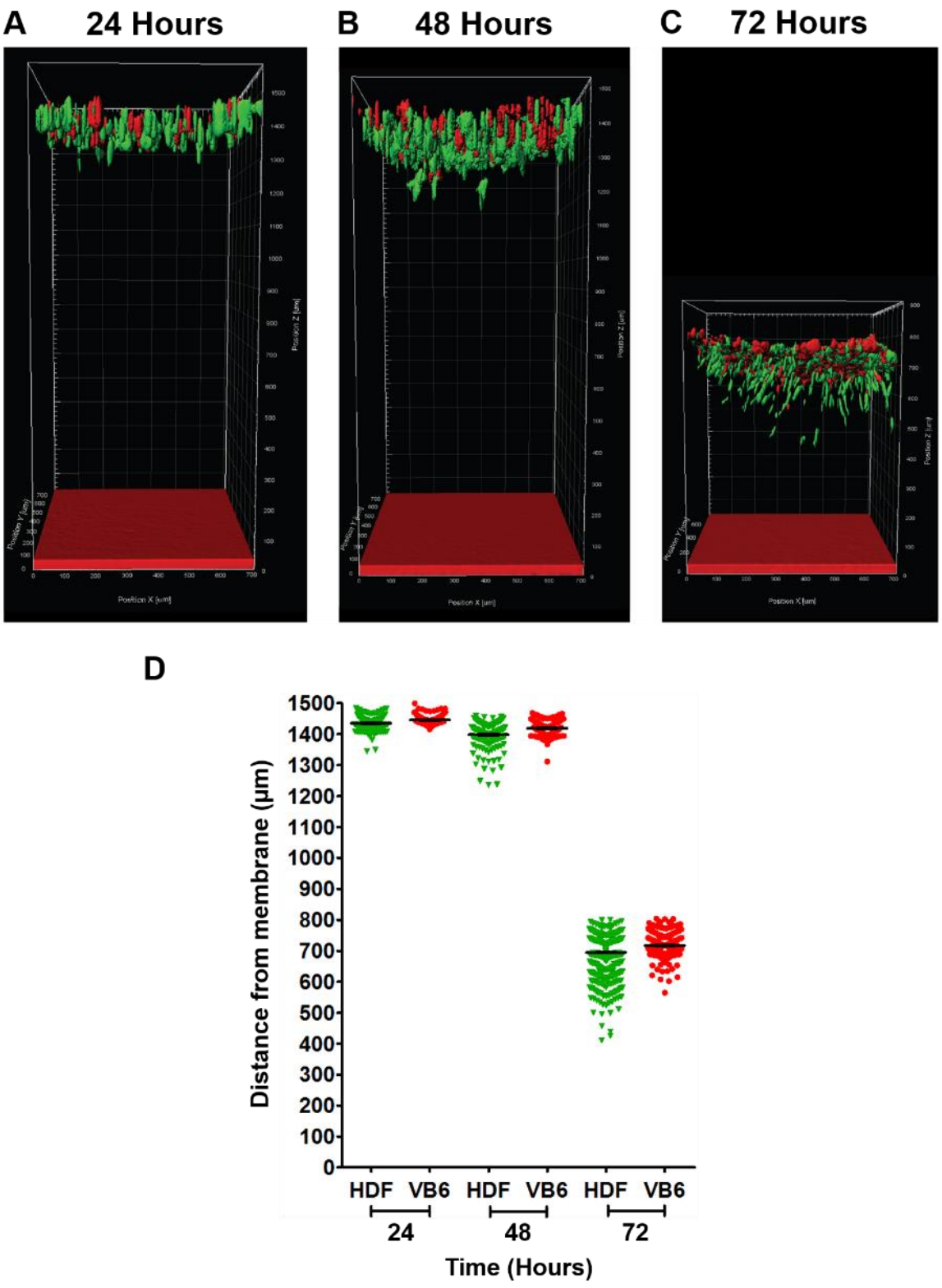

Figure 5.3: 3D rendered and quantified z-stacks of fluorescently labelled VB6s and HDF cells co-cultured in 96-well Transwell® micro-organotypic gels

Figure 5.3: 3D rendered and quantified *z*-stacks of fluorescently labelled VB6s and HDF cells co-cultured in 96-well Transwell® micro-organotypic gels

The figure displays Imaris XT rendered and analysed mini-organotypic gels co-cultured with CellTracker™ Green and Red labelled HDF (10µM) and VB6 (5µM) respectively. Confocal microscope obtained *z*-stacks were segmented, rendered and analysed by Imaris XT. Images were rendered using a surface segmentation tool that accurately detects particles of specific diameters and intensity. Distance Transformation calculations were performed via Imaris XT and plotted in Prism. HDF and VB6 cells appear vibrant with colour and are easily identifiable. **A)** At the 24 hour time point, HDFs show initial signs of polarisation and begin invading vertically downward through the gel. **B)** At the 48 hour time point, increased number of cells changing shape observed and cells invade further into the gel. A small number of VB6s can also be observed breaking away from the main cell layer. **C)** After 72 hours gels displays horizontal contraction and degradation, probably through evaporation during incubation and matrix remodelling from fibroblast secretions. **D)** Graphical depiction of individual HDF cells *z*-position in relation to the PET membrane (position 0). Each dot represents one cell within the 700µm square field of view. One representative image for each time point from one of two independent experiments.

5.2.1.4 Summary of 96-Transwell® insert

The 96 well Transwell® assay displays many similar features to the 24-well assay described in Chapter III, namely; both formats produce very similar 3D rendered images (red fluorescent PET membrane and 700µm x 700 µm x 1500 µm volumes) and quantitative data after 72 hours post cell seeding. Additionally, both assays revealed that VB6 OSCC do not invade through organotypic gels over a 72 hour period without the presence of HDFs. Furthermore, HDFs appear to be the most invasive cell type regardless of plate format or Transwell® size. Whilst, both formats display gel contraction and degradation, albeit to a varying degree in the 96-well assay I also observed lateral contraction of the gels.

The assay was set up with relative ease and advantageously requires less volume of expensive organotypic gel and a lower seeding density of cells. Image capture via CLSM was approximately the same time per gel as with the 24-well format (typically 20 minutes for gels approximately 1500µm in thickness), however, media replenishment without the use of liquid handling robotics was problematic.

Furthermore, the aim was always to develop an assay which was not only cost efficient to enable HTS within the pharmaceutical and biotechnology industry but also could be manually performed with ease by the majority of biological research laboratories. Owing to plate costs and technical difficulties of manual handling, this assay therefore is not suitable.

Thus, I asked the following; ‘is it possible to measure and quantify fibroblast and cancer cell 3D invasion without the use of a Transwell® organotypic culture system?’ To address this I began to develop a 96-well plate multicellular 3D invasion assay where the cells invaded upward through the gel toward a chemotactic gradient. In addition, for development of an HTS screen I needed to ensure that cells would be permanently fluorescent.

5.3 Generation of stable fluorescent cell lines via use of lentiviral particles

In the previous chapters, cancer cells (VB6, H1299 and MDA-468) and fibroblast cells (HDF, FSF and MRC5) were labelled with transient fluorescent dyes (CellTracker™ Red and Green, respectively). The advantage of such transient dyes is that they allow for multigenerational tracking of cellular movements, they are easy to use and compatible with almost all cell types. However, the disadvantages are that the fluorescent probes (supplied as a desiccated sample) must be dissolved in DMSO which although further diluted could affect the health of cells. Additionally, the dye is not permanent, the retention time is approximately 72 hours (dependent on concentration used and cell type) and effectively fluorescent intensity halves per each proliferation cycle.

Furthermore, there is no way of accurately confirming fluorescent efficiency, whilst sell sorting on fluorescent populations can be performed via FACs analysis, this process would take a few days in which the tracker would dissipate. Thus, to ensure permanent, stable and uniform fluorescence expression, a lentiviral transduction system was used to insert fluorescent proteins into the target cells.

5.3.1 Viral mediated generation of H2B-RFP expressing VB6 cells and H2B-GFP and EGFP expressing HDF cells

The lentiviral transduction system is based on the HIV and utilises a packaging, vehicle and vector plasmids (Dull et al., 1998). **Section 2.11** describes in detail the production of lentiviral particles encoding for fluorescent histone H2B-RFP, -GFP and whole cell EGFP. Briefly, HEK293T were seeded into a 6-well plate (10^5 cells/well) and grown to approximately 80% confluency before the lentiviral constructs (comprised of packaging plasmids pMD2.G and pCMVR8.74 with pLV-H2B-RFP or –GFP or EGFP vector and FuGENE transfection reagent) were added to the HEK293T cells and incubated for 48 hours. The resulting viral containing cell culture medium was collected and frozen at -80°C until use. VB6s were infected with virus carrying H2B-RFP (**Figure 5.4A**), whereas HDFs were infected with virus carrying H2B-GFP (**Figure 5.4B**) or EGFP (**Figure 5.4C**). Both cell types were sorted by FACS to recover and re-culture highly positive fluorescent populations.

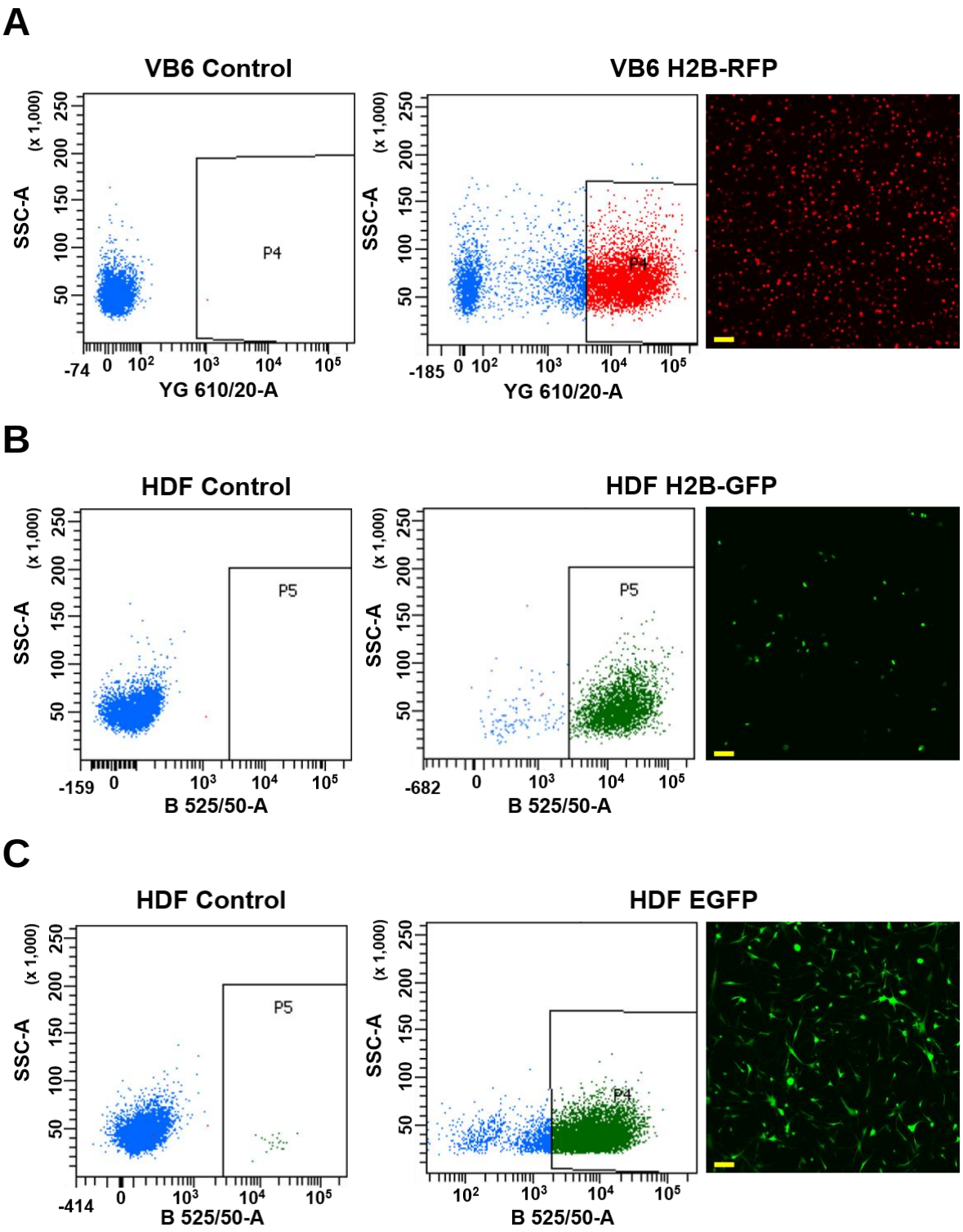

Figure 5.4: FACS analysis and expression of H2B-RFP infected into VB6 cells and H2B-GFP and EGFP infected into HDF cells

Figure 5.4: FACS analysis and expression of H2B-RFP infected into VB6 cells and H2B-GFP and EGFP infected into HDF cells

VB6 cells infected with lentivirus particles encoded for H2B-RFP and HDF cells infected with H2B-GFP or EGFP. FACS analysis was performed to select the highest expressing cells (>95% positive). Highly expressing cells were efficiently recovered and placed back into culture before another round of cell sorting was performed. **A)** Left panel displays VB6 control sample, middle panel gated region for H2B-RFP positive VB6 cells. Right panel displays a confocal microscopic image of live VB6 cells constitutively expressing nuclear histone H2B-RFP. **B)** Left panel displays HDF control sample, middle displays gated region of H2B-GFP positive HDF cells. Right panel displays a confocal microscopic image of live HDF cells constitutively expressing nuclear histone H2B-GFP. **C)** Left panel displays HDF control samples, middle panel displays gated region of EGFP positive HDF cells. Right panel displays a confocal microscopic image of live HDF cells constitutively expressing whole cell EGFP. FACS experiment was performed by the Flow Cytometry Department at BCI. Data shown is from the first of three rounds of FACS analysis. Scale bar 50µm.

5.4 96-well micro-organotypic reverse invasion assay

Due to the high cost and laborious process of preparing the 96-well Transwell® invasion assay, I sought to develop a 96-well micro-organotypic invasion assay that did not require the use of a Transwell® insert. In 2008, Sanz-Mareno and colleagues reported the use of a 3D 96-well invasion assay to examine roles of NEDD9-DOCK3-Rac and ROCK-ARHGAP22 signalling pathways, whereby cells were suspended in collagen type I and plated into 96-well plates coated with BSA. The plates were then centrifuged and incubated for 30 minutes before serum-containing media were added to each well. After 24 hours cells were fixed and stained with Hoechst before confocal *z*-slices were collected (Sanz-Moreno et al., 2008).

Like Sanz-Mareno, the assay described here uses a similar 96-well reverse invasion format, described in **Section 2.10.3**. Briefly, stably fluorescent HDFs expressing H2B-GFP and VB6s expressing H2B-RFP were suspended in organotypic gel and added to a low-binding 96-well plate either alone (7.5 x 10^3 cells/well in total) or in a 2:1 co-culture of fibroblast (5.0 x 10^3 cells) to tumour (2.5 x 10^3 cells) respectively. The plate was then centrifuged, forcing cells to the bottom of the gel before incubation at 37°C for one hour. Next, serum-containing media were added on top of the gels and returned for incubation. 3D live z-stack images were obtained daily over a period of 72 hours. Fluorescent microspheres (10µm diameter) were added to each well 20 minutes prior to imaging the 24 hour time point, thus identifying the surface of the gel.

5.4.1 96-well micro-organotypic reverse invasion assay cultured alone with stably expressing H2B-RFP VB6 cells imaged at 24, 48 & 72 hour time points

To examine whether VB6 tumour cells invade upward through micro-organotypic gels, VB6 cells stably expressing H2B-RFP were incorporated into organotypic gel before being plated alone into 96-well low binding plates and imaged every 24 hours for three days via CLSM 710. Using Imaris XT image analysis software a rendered, smoothened 3D representation of the raw .lsm confocal *z*-stack was generated and Distance Transformation analysis was performed on the rendered 3D volumes producing .csv data files. Graphical plots of invasive depth were generated in Prism using data extrapolated from the .csv files for the 24, 48 and 72-hour time points. The *z*-positions of each fluorescent microsphere were measured and averaged to determine approximate gel height (**Figure 5.5**).

At the 24 hour time point Image analysis revealed fluorescent red VB6 cells at the bottom of the gel forming a layer of cells approximately 30µm thick. The blue microspheres can be observed settled at the surface of the gel (approximately 450µm). At the 48 hour time point VB6 cell numbers appear to have increased and tightly packed together, now within approximately a 50µm layer. Additionally, VB6s do not appear to invade through the organotypic gel and gel height has remained similar to that observed at the 24 hour time point. By the 72 hour time point VB6 cell numbers appear to have increased further and produce a 100µm cell layer.

Interestingly gel height is now approximately 290µm, this may be due to evaporation and gel shrinkage. Throughout the three time points cell size does appear to vary, however, this may be due to groups or clusters of cells joined together or within close proximity of each other. Furthermore, these data are consistent with the observations from **Figure 3.7** and **Figure 5.1**, suggesting VB6 cells do not invade through organotypic gels when plated alone.

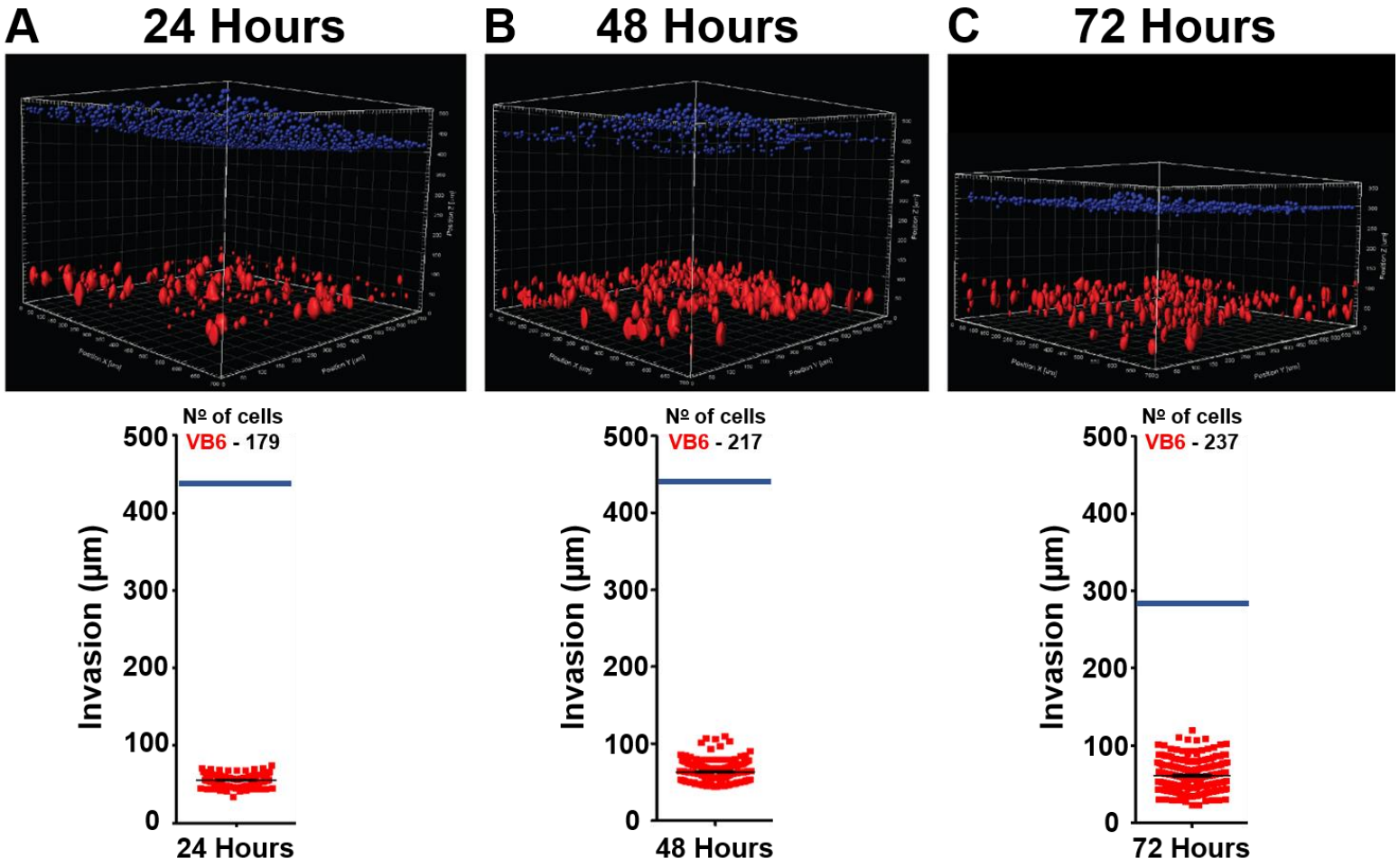

Figure 5.5: 3D rendered and quantified z-stacks of VB6 cells expressing H2B-RFP embedded alone in 96-well reverse micro-organotypic gels

Figure 5.5: 3D rendered and quantified z-stacks of VB6 cells expressing H2B-RFP embedded alone in 96-well reverse micro-organotypic gels

The figure displays Imaris XT rendered and analysed 96-well reverse invasion micro-organotypic gels embedded with VB6 cells stably expressing H2B-RFP. Confocal microscope obtained z-stacks were segmented, rendered and analysed by Imaris XT. Images were rendered using a surface segmentation tool that accurately detects particles of specific diameters and intensity. Distance Transformation calculations, relative to the base of the well, were performed using Imaris XT and plotted in Prism. **A**, **B**, **C)** 24, 48 and 72 hour time point images and quantified invasion distance plots. VB6 cells appear vibrant with colour and are easily identifiable. VB6 cells do not appear to invade throughout the micro-organotypic gel over a 72 hour period. However the average height of the gels reduces between 48 and 72 hour time points. This contraction is probably due to evaporation during incubation. One representative image for each time point from three independent experiments.

5.4.2 96-well micro-organotypic reverse invasion assay cultured alone with stably expressing H2B-GFP HDF cells imaged at 24, 48 & 72 hour time points

To examine whether HDF cells invade upward through micro-organotypic gels; HDFs stably expressing H2B-GFP were incorporated into organotypic gel before being plated alone into 96-well low binding plates and imaged every 24 hours for three days via CLSM 710.

Using Imaris XT image analysis software a rendered, smoothened 3D representation of the raw .lsm confocal *z*-stack was generated and Distance Transformation analysis was performed on the rendered 3D volumes producing .csv data files. Graphical plots of invasive depth were generated in Prism using data extrapolated from the .csv files for the 24, 48 and 72-hour time points. The *z*-positions of each fluorescent microsphere were measured and averaged to determine approximate gel height (**Figure 5.6**).

Image analysis from the 24 hour time point revealed fluorescently green labelled HDF cells at the bottom of the gel forming a layer of cells approximately 30-40µm thick. The blue microspheres can be observed settled at the surface of the gel (approximately 390µm). The graphical plot suggests one HDF cell is observed breaking away from the main population and invading through the organotypic gel (identified with a white arrow). At the 48 hour time point there notable differences to 24 hour time point, such as, a profuse increase in the number of HDF cells. Additionally, a large population of HDF cells can be observed invading almost through the entire gel. Thus, perhaps contributing to the reduction in gel height, which is now approximately 270µm thick. Furthermore, gel height reduction may be due to matrix remodelling from the HDFs. The 72 hour time suggests that HDF cells have now reached the top of the gel. Gel height appears to have slightly increased from 270µm to 305µm, this may be due to the fibroblast cells secretions at the top of the gel forcing the gel surface to expand.

Interestingly, the level of change between 24 and 48 hours is vast in comparison to 48 and 72 hours. Perhaps this may be due to a larger chemotactic effect between the initial few hours and the 48 hour time point. These data may suggest the chemotactic gradient is lost after 36-48 hours. However, these data are still consistent with observations from **Figure 3.8** and **Figure 5.2**, suggesting that HDF cells not only invade very quickly, but also effect gel shrinkage and contraction in organotypic gels.

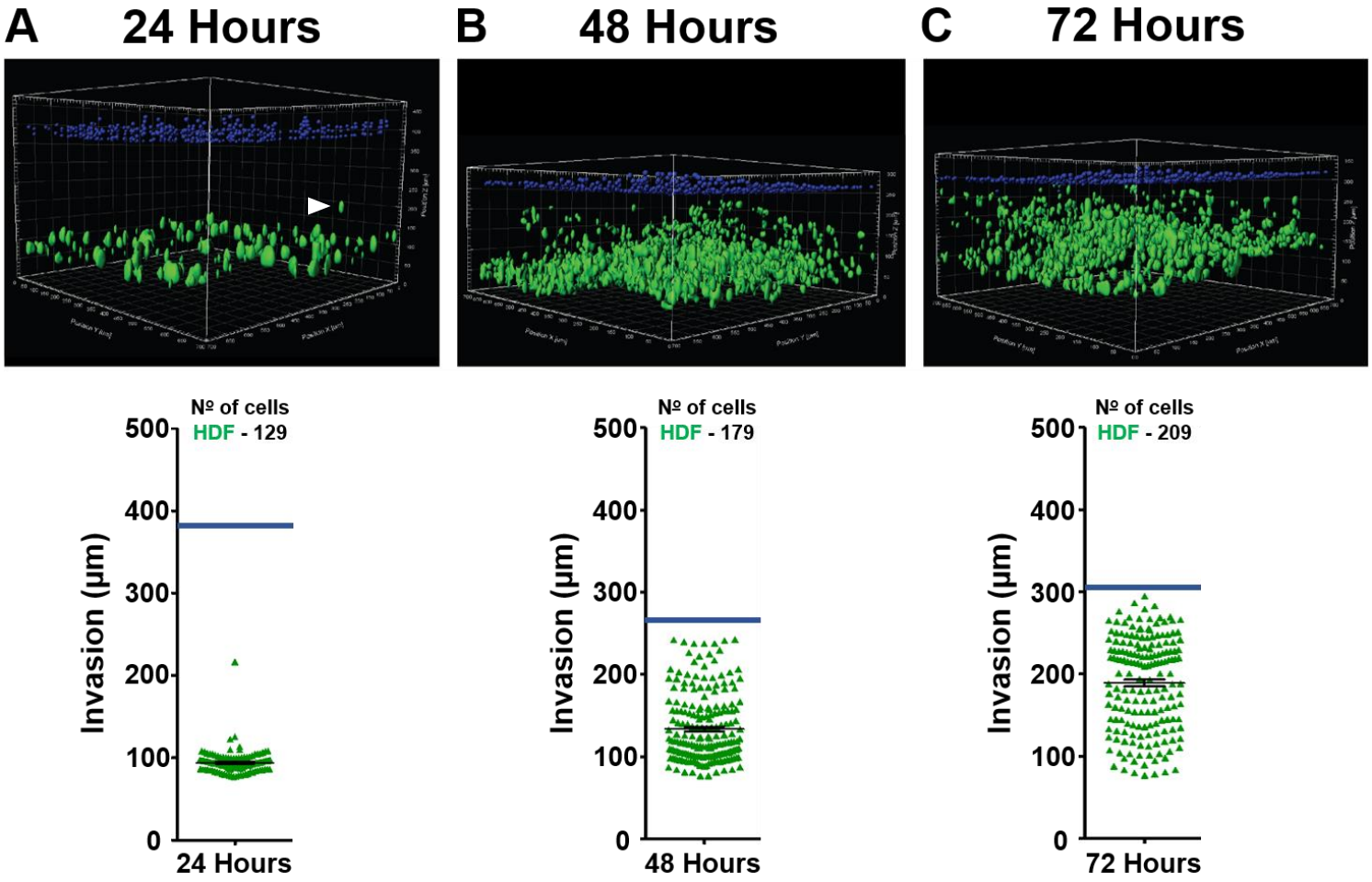

Figure 5.6: 3D rendered and quantified z-stacks of HDF cells expressing H2B-GFP embedded alone in 96-well reverse micro-organotypic gels

Figure 5.6: 3D rendered and quantified z-stacks of HDF cells expressing H2B-GFP embedded alone in 96-well reverse micro-organotypic gels

The figure displays Imaris XT rendered and analysed 96-well reverse invasion micro-organotypic gels embedded with HDF cells stably expressing H2B-GFP. Confocal microscope obtained z-stacks were segmented, rendered and analysed by Imaris XT. Images were rendered using a surface segmentation tool that accurately detects particles of specific diameters and intensity. Distance Transformation calculations, relative to the base of the well, were performed using Imaris XT and plotted in Prism. **A)** 24 hour time point displays vibrant HDF cells, distributed at the bottom of the gel. The 3D image and invasion distance graph displays one invading cell moving away from the main population towards the top of the gel. Gel height is approximately 390µm**. B)** 48 hour time point displays increased levels of cell number and invasion. HDF cells invade the entirety of the gel. In addition, gel height was reduced to approximately 270µm, probably due to gel contraction and degradation. **C)** The 72 hour time point displays similar features to that of the 48 hour time point, in that, HDFs have invaded the entire gel and increased in cell number. One representative image for each time point from three independent experiments.

5.4.3 96-well micro-organotypic reverse invasion assay co-cultured with stably expressing H2B-GFP HDFs and H2B-RFP expressing VB6 cells imaged at 24, 48 & 72 hour time points

To examine the invasion of VB6s in the presence of HDF cells in inverted micro-organotypic gels, HDFs expressing H2B-GFP and VB6s expressing H2B-RFP were incorporated into organotypic gel before being plated alone into 96-well low binding plates and imaged every 24 hours for three days via CLSM 710.

Using Imaris XT image analysis software a rendered, smoothened 3D representation of the raw .lsm confocal *z*-stack was generated and Distance Transformation analysis was performed on the rendered 3D volumes producing .csv data files. Graphical plots of invasive depth were generated in Prism using data extrapolated from the .csv files for the 24, 48 and 72-hour time points. The *z*-positions of each fluorescent microsphere were measured and averaged to determine approximate gel height (**Figure 5.7**).

Image analysis from the 24 hour time point revealed bright populations of both cell types forming layers approximately 30-40µm thick. The blue microspheres can be observed settled at the surface of the gel (approximately 390µm). The graphical plot suggests a small population of HDFs may have broken away from the main layer, followed by VB6 cells. At the 48 hour time point there are notable differences to the 24 hour time point, such as, increased cell numbers in both populations. Additionally, at the 48 hour time point, large populations of HDF cells can be observed invading through the entire gel. Followed closely by VB6 cells, which may have migrated into the channels created by the fibroblasts.

The graphical plot from the 48 hour time point suggests that the HDFs invade in a wave like pattern through the gel and both cell types appear to have a wide variation in the degree of invasive activity of individual cells. The gel height between the 24 and 48 hour time point does not change, thus suggesting that HDFs and VB6s invaded approximately 200µm in 24 hours. The 72 hour time point reveals increased cell numbers within both populations. Strikingly, the plot for the 72 hour time point suggests that HDFs and VB6 have retreated on themselves compared to the 48 hour time point, however I do not believe this to be the case. Rather, as the gel has contracted and degraded the overall gel height has reduced (now approximately 240µm), thus, bringing the cells closer in proximity to one another.

The level of change between the 24 and 48 hour time points is very informative and further suggests that, the invasive behaviour is largely based on chemotaxis. Similarly to the 72 hour HDF alone gel (**Figure 5.6C**) this sample also appears withered and contracted. This further suggests that quantitative behaviour changes can be collected and measured within the first 36, if not 24, hours of this experiment. These data are consistent with observations from **Figure 3.9** and **Figure 5.3**, suggesting that HDFs are the leading invasive cells type, probably degrading the organotypic gel, thus creating channels for the VB6 cells to follow closely behind.

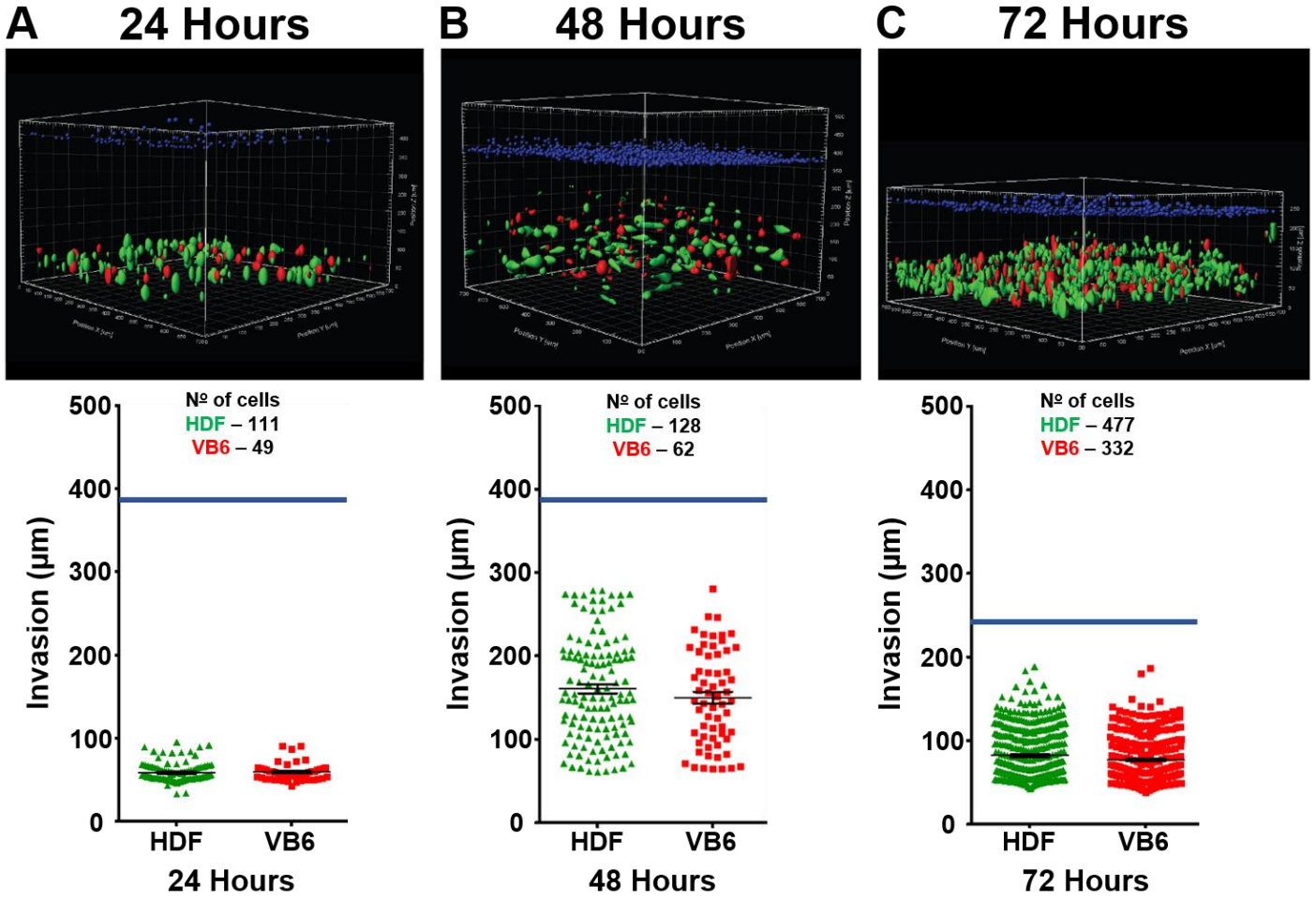

Figure 5.7: 3D rendered and quantified z-stacks of HDFs expressing H2B-GFP co-cultured with VB6s expressing H2B-RGP in 96-well reverse micro-organotypic gels

Figure 5.7: 3D rendered and quantified z-stacks of HDFs expressing H2B-GFP co-cultured with VB6s expressing H2B-RGP in 96-well reverse micro-organotypic gels

The figure displays Imaris XT rendered and analysed 96-well reverse invasion micro-organotypic gels co-cultured with embedded HDFs stably expressing H2B-GFP and VB6s stably expressing H2B-RFP. Confocal microscope obtained z-stacks were segmented, rendered and analysed by Imaris XT. Images were rendered using a surface segmentation tool that accurately detects particles of specific diameters and intensity. Distance Transformation calculations, relative to the base of the well, were performed using Imaris XT and plotted in Prism. **A)** 24 hour time point displays vibrant HDF and VB6 cells, distributed at the bottom of the gel. The invasion distance graph displays a small cluster of HDFs may have broken away from the main population, followed by VB6 cells. Gel height is approximately 390µm**. B)** 48 hour time point displays increased levels of cell proliferation of both cell types. HDFs have invaded further into the gel (200µm deeper than 24 hour time point) and appear to be followed closely by migrating tumour cells. Probably through the channels created by fibroblasts during matrix remodelling. Gel height remains similar to the previous time point (approximately 390µm). **C)** The 72 hour time point displays drastic gel contraction and degradation compared to the 48 hour time point. Gel is approximately 240µm in thickness. Both cell types display increased levels of proliferation. One representative image for each time point from three independent experiments.

5.4.4 siRNA knockdown of five selected hits from primary SMARTpool siRNA screen in 96-well reverse micro-organotypic invasion assay

To determine whether gene silencing in HDF cells had a similar or any effect on fibroblast/cancer cell invasion and gel contraction in the 96-well reverse format as observed in the 24-well format, HDFs were transfected with SMARTpool siRNA or non-targeting siRNA control (described in **Section 2.6.1**) and seeded into organotypic gels.

Briefly, HDF cells (H2B-GFP expressing) were plated into 24-well plates (2.0×10^4 cells/well) and the next day transfected with the five SMARTpool siRNA selected hits identified from the primary screen and NT siRNA control, described in **Section 4.3** (CAPN-10, CASP-8, MMP-17, SERPIN-F1, TMRPSS-13) (20nM). Three days post transfection, HDFs and VB6 cells (H2B-RFP expressing) were counted and incorporated into organotypic gel in a 2:1 ratio of fibroblast: tumour cells before being plated into 96-well low binding plates. The plate was then centrifuged at 4°C before being incubated. Post polymerisation, 100µl of serum-containing medium were added to each well and re-incubated. Three days post plating (six days post transfection), 10µm fluorescent microspheres were added to each well and end point *z*-stack images were acquired via CLSM 710.

Using Imaris XT image analysis software a rendered, smoothened 3D representation of the raw .lsm confocal *z*-stack was generated and Distance Transformation analysis was performed on the rendered 3D volumes producing .csv data files. Graphical plots of invasive depth were generated in Prism. The *z*-positions of each fluorescent microsphere were measured and averaged to determine approximate gel height (**Figure 5.8**).

Image analysis revealed vibrant populations of both cell types across all treatments. Interestingly, the NT sample displays similar levels of invasion of HDFs and VB6 cells and gel height (approximately 450µm) as observed in the 48 hour time point co-culture sample (**Figure 5.7B**).

The CAPN-10 and SERPIN-F1 images and invasion data from the invasion distance plots suggest similar levels of invasion to the NT sample, whereby HDFs are observed breaking away from the main population and begin to invade into the gels. As previously noticed, HDFs appear to be the leading invasive cell type and are closely followed by the VB6 tumour cells. The CAPN-10 (770µm) and SERPIN-F1 (660µm)

gel height is greater than that of the NT sample (450 µm). Furthermore, MMP-17 (1100µm) and TMPRSS-13 (1200µm) gels are even greater than CAPN-10, SERPIN-F1 and the NT sample. One possible explanation of the thicker gels might be via increased ECM secretions by the cells. I also considered whether it may be due to swelling of the gels from the medium placed above the gel but it was not observed in others treatments or in earlier experiments (**Figure 5.6** and **Figure 5.8**). The exact reasons for this increased size are yet to be identified.

To address the increase in gel size, I tested control wells where no cells were included, only the 10µm fluorescent beads were added to the top of the gel (**Figure 5.9**). Surprisingly the gel containing beads only (gel height 440µm) shrank to a similar height to that of the NT control (450µm). Since there were no cells, gel degradation and contraction may not be the explanation for the reduction in height, only evaporation. Thus explaining why the siRNA treated samples had taller gels remains unconfirmed.

The CASP-8 image and invasion plot reveal no evident signs of invasion of either cell type (**Figure 5.8**). More interestingly, the data displays the lowest numbers of both cell types compared against all samples, suggesting that CASP-8 knockdown in the HDFs may cause cell death or decrease proliferative rates. Gel height is similar to that of the NT sample (approximately 450µm).

Data from the invasion plot suggests samples containing HDFs with silenced MMP-17 and TMPRSS-13 do not appear to break away from the main population as observed with the NT, CAPN-10 and SERPIN-F1 transfected HDFs. Thus not invading into the gels but rather appear to settle in a large population at the bottom of the gel in a layer approximately 210µm thick. Secondly, the VB6 cells also remain at the bottom of the gel and do not invade into the gels. This may be due to the MMP-17 and TMPRSS-13 knockdown on the fibroblasts, thus, affecting the ability of matrix remodelling, motility or invasion to occur within the HDF population.

A consistent change that compares with the 24-well assay is the thickness of the gel at the end of the experiment. In both the 96-well and 24-well formats the gels containing MMP-17 and TMPRSS-13 treated HDF are thicker. In future improvements to this assay it would be ideal to use a fluorescent collagen or second-harmonic imaging to observe the distribution of collagen fibres within the gel.

Overall the fluorescent images in **Figure 5.8** show that there are large differences in the distribution and numbers of cells in each treatment, however given the

conclusions above, it was likely that chemotactic gradient had probably vanished by 36-48 hours and it may have been more informative to have analysed this assay in a shorter time frame. However, I did not have time to investigate this further.

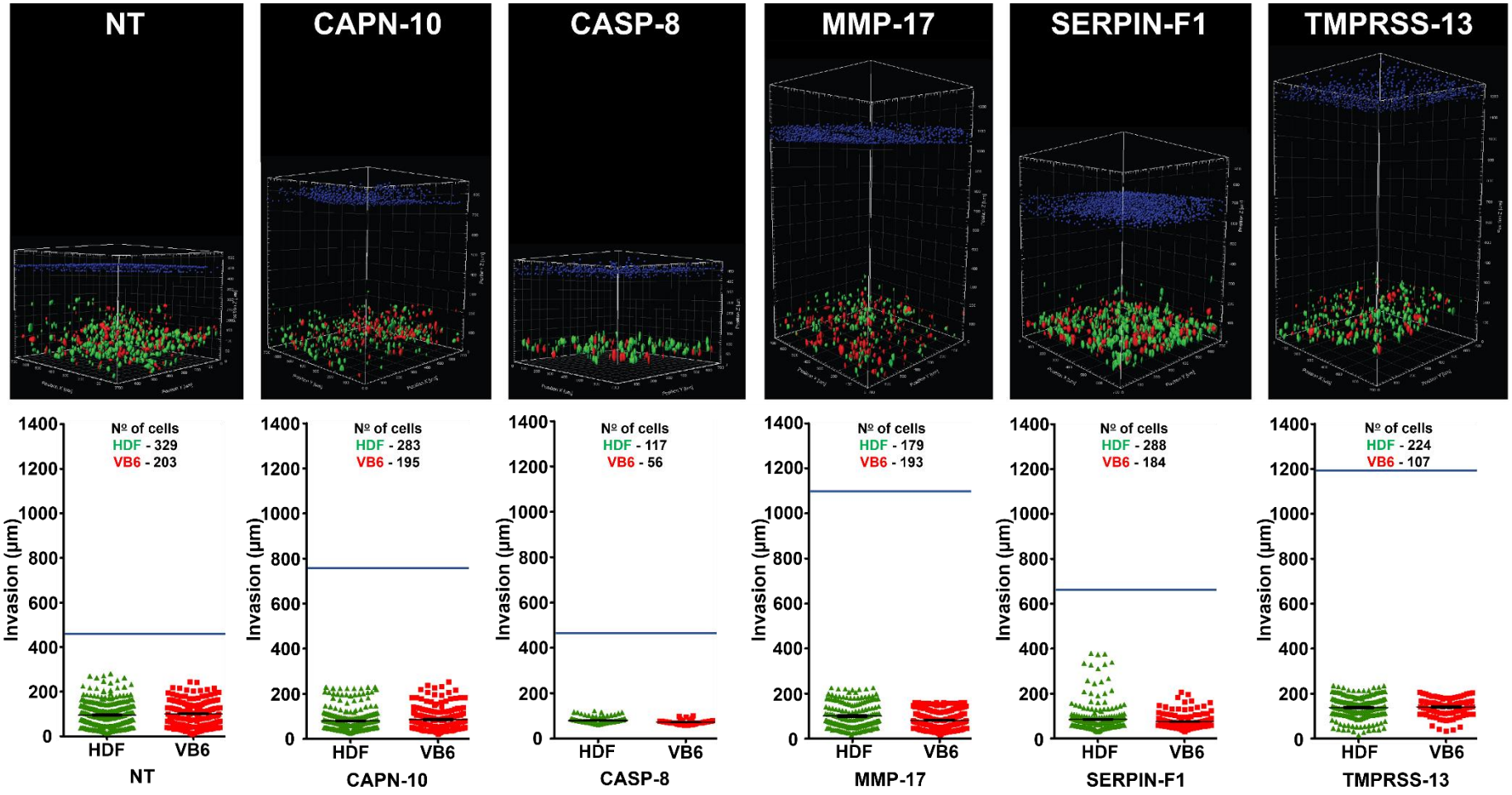

Figure 5.8: 3D rendered and quantified z-stacks of siRNA KD in HDFs expressing H2B-GFP co-cultured with VB6s expressing H2B-RGP in 96-well reverse micro-organotypic gels

Figure 5.8: End point 3D rendered and quantified z-stacks of siRNA KD in HDFs expressing H2B-GFP co-cultured with VB6s expressing H2B-RGP in 96-well reverse micro-organotypic gels

The figure displays Imaris XT rendered and analysed 96-well reverse invasion micro-organotypic gels co-cultured with embedded siRNA transfected HDFs (expressing H2B-GFP) and non-transfected VB6s (expressing H2B-RFP) six days post transfection. HDF cells were plated into a 24-well plate (2.0 x 10^4 cells/well) and after 24 hours transfected with the top five selected SMARTpool hits from the primary screen (CAPN-10, CASP-8, MMP-17, SERPIN-F1 and TMPRSS13) (20nM) along with a non-targeting siRNA control(NT) in triplicate wells. 72 hours post transfection HDF and VB6 cells were counted and embedded into organotypic gel before seeding into 96-well low binding plates and centrifuged at 4°C. The plate was incubated for one hour until polymerised before 100µl of serum media were added to each well. 72 hours post incubation (six days post transfection) *z*-stack volumes were obtained via CLSM. 20 minutes prior to imaging 10µm fluorescent (blue) microspheres were added in each well to identify the surface of the gel. Raw confocal data were segmented, rendered and analysed by Imaris XT and invasion data plotted in Prism. The NT sample displays similar results as observed with the 48 hour time point co-culture displayed in **Figure 5.7B**, whereby, the gel has not completely withered or diminished and HDFs can be observed invading through the gel followed closely by the VB6 cells. The CAPN-10 gel displays a degree of HDF and VB6 invasion similar to that of the NT sample, however, also exhibits and an increase in gel height (770µm). CASP-8 sample displays similar gel height to NT sample, however, both cell types appear lower in number compared with other samples. MMP-17 sample displays large populations of both cell types remain at the bottom of the gel in a layer approximately 210µm thick, moreover, the HDFs and VB6s show no signs of invasion as observed with the NT, CAPN-10 and SERPIN-F1 sample. SERPIN-F1 sample displays similar levels of invasion as observed with CAPN-10 and NT, however, also exhibits an increase in gel height (660µm). TMPRSS-13 sample displays similar features observed with MMP-17 sample, such as, increased gel thickness (1200µm) and no signs of HDF or VB6 invasion. One representative image for each treatment from one independent experiment.

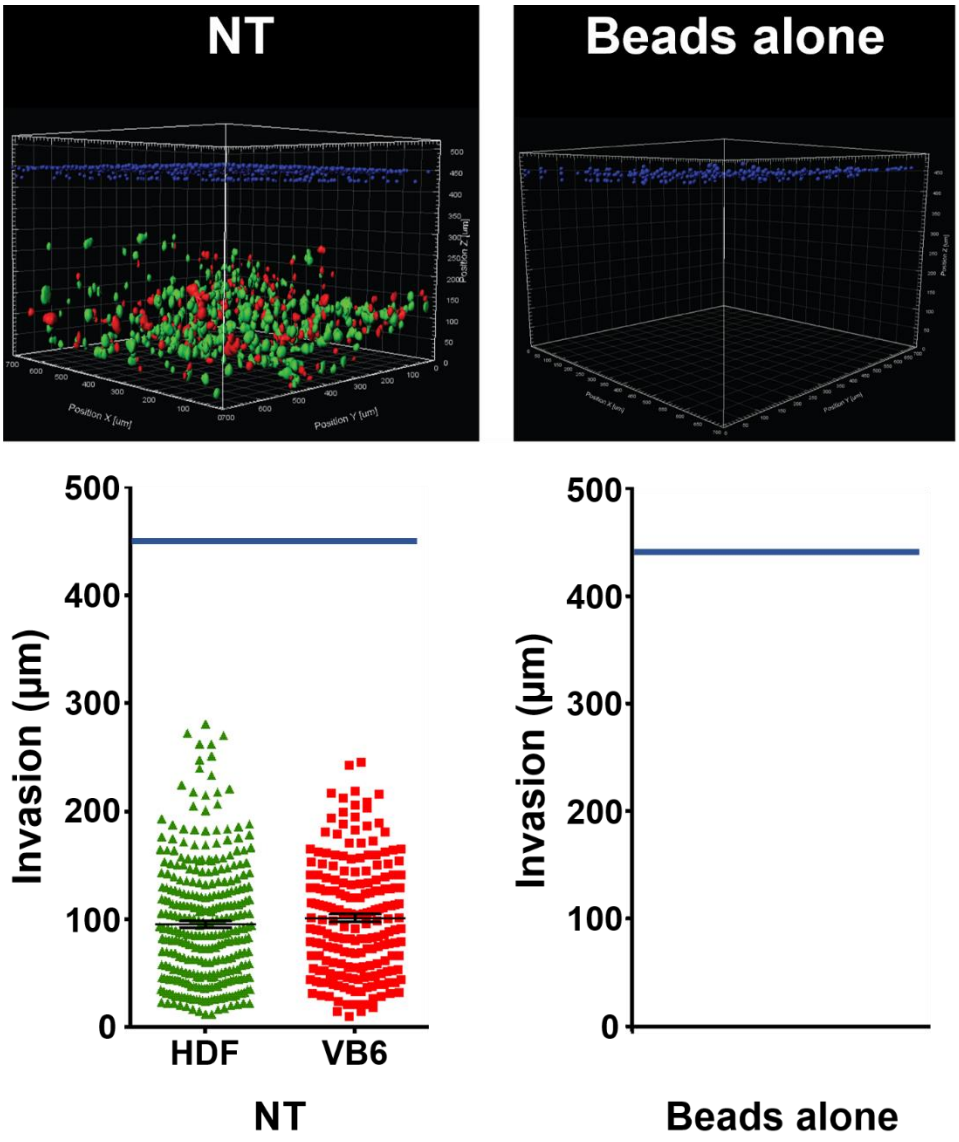

Figure 5.9: Comparison of gel height 72 hours post plating

Left figure displays Imaris XT rendered reverse invasion micro-organotypic gels co-cultured with embedded NT transfected HDFs (expressing H2B-GFP) and non-transfected VB6s (expressing H2B-RFP) at 72 hour end point (gel height 450 µm). Right panel displays 72 hours end point containing 10µm fluorescent (blue) microspheres only (gel height 440µm).

5.4.5 Summary – 96-well reverse

The 96-well reverse micro-organotypic invasion assay has revealed that not only are the fibroblast component of the ECM probably the most invasive but also one of the most crucial elements when trying to model *in vitro* tumour metastasis using organotypic cultures. Here I observed similarities between the reverse invasion format and the Transwell® insert formats, such as, the fibroblast component in both formats appear to be the leading invasive cell. In addition, regardless of well or insert size, the organotypic gels can experience contraction, degradation and/or evaporation. Furthermore, VB6 cells alone do not appear to invade through organotypic gels in either format, whereas, when co-cultured with HDFs, both cell types display signs of invasion and migration. Thus, both formats provide a robust method to monitor chemotaxis driven invasion.

However, the 96-well reverse format displayed increased gel thickness when cultured with MMP-17 and TMPRSS-13 siRNA transfected HDFs.

The 96-well reverse assay can be easily performed and is unique and versatile, producing 3D images and quantitative data for analysis. Nonetheless, regardless of the cost advantages and speed of the assay there are questionable observations which have been identified and discussed within the next section.

5.5 Discussion

It is recognised that 3D culture systems better reflect the *in vivo* behaviour of cellular characteristics in comparison to 2D monolayer cultures (Itano et al., 2003; Lee et al., 2007; McBeath et al., 2004). Additionally, the tumour microenvironment has been reported to play an important role within the process of metastasis and drug resistance (Correia and Bissell, 2012; Hanahan and Coussens, 2012; Quail and Joyce, 2013). However, HTS drug discovery programs still primarily use 2D cancer culture methods (Grozinger et al., 2006; Inglese et al., 2006) neglecting the importance of stromal cells and ECM components.

Therefore there is a desire for the pharmaceutical industry to implement 3D cancer screening assays for the identification of potential therapeutic targets. However, there is not a universal standardised 3D HTS model whereby manipulation, treatment, imaging and analysis can be up-scaled due to the vast focus on specific applications.

Some groups have reported the use of 3D single cell tumour spheroids as a potential 3D model to identify anticancer agents (Chen and Yoon, 2017; Huber et al., 2016; Ott et al., 2017; Zanoni et al., 2016). Although these models can recapitulate some aspects of cancer cell growth in 3D, their lack of stromal microenvironment components prohibits crucial *in vivo* interactions, thus making them an unsuitable 3D assay for industry. Thus, 3D multicellular spheroids have been developed to study the differences in drug sensitivity when comparing cancer cells grown in single and multi-cellular 3D cultures (Vorsmann et al., 2013).

5.5.1 Investigation of 96-well Transwell® invasion assay

The aim of this part of the study was to develop a higher-throughput novel 3D organotypic invasion model based on the previously described fluorescent 24-well mini-organotypic assay. This was achieved by miniaturising the 24-well assay via use of a 96-well Transwell® insert with optically clear PET membranes (**Figure 2.2B**), transient cellular dyes, a LWD 20x objective and confocal microscopy. Thus, I have developed and optimised a higher-throughput, reproducible and robust method to visualise fibroblast and tumour cell interaction within a 3D microenvironment.

Observations from the 96-well Transwell® pilot experiments revealed that when VB6 cancer cells are plated alone (**Figure 5.1**) there appear to be no signs of invasion when monitored over a 72 hour period. These observations are representative of the 24-well assay (**Figure 3.7**) and confirm that VB6 cells do not invade through

organotypic gels when plated alone. In addition, both formats display gel shrinkage over a 72 hour period, probably due to evaporation during incubation.

When HDFs were plated alone in the 96-well Transwell® format (**Figure 5.2**) they appear to change their morphology and orientation and invade into the organotypic gel within the first 48 hours as observed in the 24-well format (**Figure 3.8**). Thus confirming that HDFs can invade through collagen: Matrigel® based gels. However, the 72 hour time point images from the 96-well format display a reduction in invasion of the fibroblasts compared to that of the 24-well format and a disfigured gel. The 96-well data suggests that the gels experience vast contraction, horizontally and vertically. This may be due to the stiffness of the gels in the smaller inserts or possible degradation and remodelling of the gel through fibroblast secretions.

HDFs and VB6 cells co-cultured in the 96-well format (**Figure 5.3**) displayed reduced polarisation of the HDF cells and invasive depth reached was less than when plated alone. This may be result of signalling interference by the VB6 cells or also reduced cell numbers. Furthermore, invasive depth may have been prohibited by gel stiffness (Lang et al., 2015; Zaman et al., 2006), thus adding to the reduction in invasion. Nevertheless, the 72 hour time point image displays HDF cells invading through the gel followed by migrating tumour cells, as observed in the 24-well format (**Figure 3.9**).

The major differences between the both assay formats include; (1) differing surface area of exposed gel during incubation, thus, varying the rate and type of gel contraction and shrinkage (vertical and lateral); (2) 72 hour time point in the 96-well format appears to display physiologically disfigurement to gels, perhaps due to matrix remodelling action or gel contraction (perhaps performing this assay for 36-48 instead of 72 hour could be a solution); and (3) cost of consumables; one case (five plates) of the 96-well Transwell® Insert plates costs £884.61 (£1.84 per Transwell®), however one case (four plates, 12 inserts/plate) of the 24-well Transwell® inserts costs £271.60 (£5.69 per Transwell®). Thus per individual insert, the 24-well format is three times more expensive, excluding the cost of reagents. However, the advantage of the costlier 24-well format is that all of the Transwells® are individual, therefore, do not all need to be used at the same time.

The 96-well Transwell® micro-organotypic invasion assay has the potential to increase throughput and perform HTS, by reducing the volume of required reagents (collagen, Matrigel®, culture medium) and number of cells for those wishing to perform high-throughput assays. Interestingly, this plate format has been designed and can be integrated into an automated HTS workflow due to its barcoded plates and oval

shaped wells, thus facilitating medium exchange via liquid handling robotics, nonetheless, working by hand with this assay format proved to be very arduous and time consuming.

5.5.2 Investigation of 96-well reverse micro-organotypic invasion assay

In order to further reduce cost and decrease assay set up time, I developed 96-well reverse invasion assay similar to that used in 2008 (Sanz-Moreno et al., 2008). This group used A375M2 and WM1361 melanoma cells expressing GFP and measured invasion through collagen type I gels 24 hours post seeding, after fixation. Cells were cultured alone and those had invaded by 50µm from the base of the well were considered invasive. However, the assay described here uses two different stably fluorescent cell populations, imaged live via confocal microscopy.

The 96-well reverse assay pilot experiments displayed several similarities when compared to the 24- and 96-well Transwell® methods, such as, VB6 cells plated alone in the 96-well reverse assay (**Figure 5.5**) do not invade through organotypic gels over a period of 72 hours. Additionally, HDF cells plated alone (**Figure 5.6**) invade rapidly through organotypic gels, thus degrading the gels, causing them to shrink after 48 hours. Furthermore, HDFs and VB6s co-cultured (**Figure 5.7**) revealed that HDFs invade and remodel organotypic gels, thus, providing means of passage for migrating VB6 cells. Interestingly the 96-well reverse assay displays rapid behavioural changes. The 72 hour time point data shows that cell movement is not different between the siRNA treated wells and the cells in the non-targeting control wells.

These data suggested that the chemotactic gradient may be lost between 36-48 hours. Thus, ideally, microscope permitting, it may be of interest to image every hour for 24-36 hours.

The reverse invasion assay format has several advantages over the 96-well Transwell® assay, including; (1) reduced cost, the 96-well reverse format only requires 100µl of cell culture medium per well, whereas the 96-Transwell® format requires 150µl and the cost of an individual 96-well Transwell® plate is £176 whereas the low binding µClear® 96-well plates are £2.92 each; (2) overall assay set up time is reduced when using the reverse format due to the cells being embedded into the organotypic gel prior to polymerisation; (3) medium replenishment is simplified when using the reverse invasion assay, the process involves use of a multi-channel pipette

to exchange medium across all wells. Whereas, for the 96-well Transwell® format the user is required to manually remove the insert by hand and then replenish medium; (4) 3D image capture of the reverse assay gels is much faster as the gels are much thinner in comparison to those in the 96-well Transwell®, thus, reducing overall assay time.

Conversely, the data from (**Figure 5.8**) revealed that gel thickness increased after a 72 hour time period when gels were embedded with MMP-17 and TMPRSS-13 siRNA transfected HDFs. While the exact reasons for this are unclear, one suggestion may be due to the increased production of GAGs. Due to their strong hydrophilic properties, GAGs are highly negatively charged therefore attract osmotically active Na^+ ions, which in turn, draws large volume of water into surrounding ECM in which the GAGs reside. This influx of water can cause a form of swelling pressure (Frantz et al., 2010; Gandhi and Mancera, 2008), thus leading to an increased in gel thickness.

Additionally, perhaps the increase in gel thickness is a result of increased collagen production from HDF cells. For example, during fibrosis and wound healing, myofibroblasts are known to secrete exaggerated levels of ECM proteins (collagen type I and fibronectin) (Darby et al., 2014; Li et al., 2007b). With more time I would like to have investigated the secretome of the MMP-17 and TMPRSS-13 treated cells.

Overall, these results have demonstrated that miniaturisation of the 24-well mini-organotypic invasion does not compromise the value of the assay. Both formats are robust and reproducible despite differences in costs and 3D image readout. Whilst no 3D assay can fully mimic the *in vivo* tumour-stroma microenvironment, both 96-well versions have several important advances, such as; (1) modular design facilitates incorporation of any cell type; (2) permit live imaging and can produce measurable 3D data within 24 hours; (3) primary human and tumour cells can be integrated, thus, cultures can be customised to screen for target specific treatments; (4) ease of transfection or drug dosing during the experiment; and (5) integration into an automated screening work flow, thus, permitting HTS.

Whilst these data provide a useful insight into the development of a 3D micro-organotypic invasion assay, it should be noted that there remains much to validate and address. I have not performed siRNA transfection experiments within the 96-well Transwell® assay, nor repeated the top five siRNA knockdown in the 96-well reverse method. This was due to insufficient time and depletion of all siRNA reagents. Furthermore, I have not positively identified the mechanisms by which increased gel thickness occurs with some siRNA knockdowns and this is likely to be important in fully understanding the value of the organotypic assays.

CHAPTER VI: FINAL CONCLUSIONS

6.0 Final Conclusions

It has been estimated that number of globally reported cancer cases will rise to over 20 million per annum by 2025 (Bray and Soerjomataram, 2015). Cancer is becoming increasingly more prominent around the world, despite the progress being made towards reducing incidence and mortality rates. Metastases formation, the ability of cancer cells to spread to distant organs within the body, has been reported to be responsible for approximately 90% of cancer-related deaths (Chang et al., 2005). Thus, understanding the complex processes involved in tumour metastasis has been a major area of focus for over a century (Friberg and Nystrom, 2015; Hart and Fidler, 1980b; Paget, 1889; Paget, 1989; Rous, 1910).

With over 200 FDA approved anti-cancer drugs available for clinical application (Buffery, 2015), the majority of these drugs only target anti-proliferative properties of tumour cells and not their metastatic behaviour (migration and invasion). Metastasis still demands a high therapeutic focus, however major obstacles effect treatment of cancer patients who may develop or already have metastases, such as; (1) the heterogeneity of tumour cells, containing subpopulations of different geno- and phenotypic cells. Meaning each variation has its own invasive, migratory and proliferative properties, therefore could be uninhibited by drugs; (2) lack of standardised physiomimetic models which recapitulate the metastasis process. The pharmaceutical industry desire a 3D model that can be used to perform HTS for their potential anti-metastatic compound libraries (Fidler and Kripke, 2015).

Studies have attempted to inhibit various steps of the metastatic process, starting with Lance Liotta's earlier research, which reported the degradation of basement membrane by murine tumour cells (Liotta et al., 1977). Followed by the discovery of MMP-2 as a collagen type IV degrading enzyme (Liotta et al., 1979). In addition, the role of proteases within tumour cells to prohibit invasion was reported by Fayard and colleagues, who described a reduction in breast cancer cell invasion via inhibition of serine proteases (Fayard et al., 2009). Other proteases, such as MMPs have also been reported to have an inhibiting effect on tumour cell migration and proliferation. For example, Adachi and colleagues reported that MMP-7 overexpression in colon cancer cells (CHC-Y1) altered the invasive potential *in vivo* (Adachi et al., 1999). Adding further, up regulation of the integrin αvβ6 generated a tumour promoting function of myoepithelial cells in ductal carcinoma *in situ* (DCIS) through TGF-β upregulation of MMP-9 (Allen et al., 2014).

Additionally, inhibiting angiogenesis, more specifically VEGF, reduces the formation of blood vessels surrounding the tumour, thus blocking the supply of nutrients to cancer cells, leading to vascular collapse, hypoxia and eventually cell death (Bohn et al., 2017; Potente et al., 2011). However, cancer cells have the ability to proliferate around existing blood vessels in a process known as vessel co-option (Qian, 2013) thus antiangiogenic therapy is likely to be ineffective.

All of this is clearly not enough to prevent metastasis and perhaps this is an unpreventable occurrence. However, targeting a specific stage of the metastatic process with the use of a functional standardised assay is highly desirable. Moreover, focusing solely only on the cancer cells as a target completely neglects and misses the opportunity to manipulate the stromal host microenvironment. The host organ environment represents a stable target that could be manipulated *in vitro* and *in vivo* to produce an anti-invasive, uninhabitable environment for the unpredictable and unstable tumour cells.

Designing an *in vitro* 3D assay that provides a physiomimetic microenvironment to monitor and recapitulate the tumour-stromal interactions is highly required. To date, there are many different 3D cancer modelling methods, including spheroid cultures (Amann et al., 2014; Huber et al., 2016; Ott et al., 2017; Vorsmann et al., 2013; Ware et al., 2016), synthetic gels (DeVolder and Kong, 2012; Loessner et al., 2010; Sawhney et al., 1994) and organ-on-a-chip (Bhise et al., 2014; Huh et al., 2010; Marhefka and Abbud-Antaki, 2012).

In this study I have developed an *in vitro* 3D fluorescent mini-organotypic invasion assay based on the organotypic skin culture model originally developed by Fusenig (Fusenig et al., 1983). Adaptations of this model have been widely used (Carapuca et al., 2016; Froeling et al., 2011; Gaggioli et al., 2007; Mackenzie, 2004; Nystrom et al., 2005) to culture cancer cells (with or without fibroblast cells) in a polymerised collagen (type I) based gel. The assay (referred to as 'large organotypic gels') provides a unique scaffold to successfully cultivate cells on top of, or embedded, within the gel at an air-liquid interface to study cancer invasion. However, the assay lasts for 2-3 weeks, followed by several days of sample processing before being available for analysis. Additionally, the assay demands large volumes of costly reagents (collagen and Matrigel®) and large numbers of cells per experiment, therefore, prohibiting large scale functional drug or gene screening.

With the use of a transient fluorescent cell permeable dye (CellTracker™), a confocal microscope fitted with a LWD x20 objective and image analysis software; I produced

3D rendered *z*-stack volumes of cancer and fibroblast cell invasion within a 24-well mini-organotypic assay using Transwell® inserts. Data revealed that when fluorescently labelled (CellTracker™ Red) VB6 cancer cells were plated alone on top of mini-organotypic gels there were no signs of invasion over a 72 hour period (**Figure 3.7**). VB6 cells adhere and reside at the top of the gel, however, the gels displayed a slight reduction in gel height, suggesting that the exposed surface of the gel experiences evaporation. Probably during incubation thus causing the gels to shrink.

Conversely, 24 hours after our fluorescently labelled (CellTracker™ Green), HDFs were plated alone on top of the gels, fibroblasts became polarised, change their morphology to favour that of a vertical orientation and begin to invade downward through the gel (**Figure 3.8**). At the 72 hour time point large populations of spindle-shaped fibroblast cells were observed invading throughout the entirety of the gel probably towards a chemotactic gradient. Furthermore, the gel height has drastically reduced in comparison to observations with VB6 cells alone. The reduction in gel height maybe in part due to the evaporation witnessed with VB6 gels. However, I believe that it is also due to degradation and contraction of the gels via fibroblast cell activity. This is supported within the literature, that fibroblast cells remodel and destroy fibrous proteins in the ECM via enzymatic secretions (Frantz et al., 2010; Page-McCaw et al., 2007) and that fibroblast movement within the ECM can re-organise and contract collagen fibres in tissues *in vivo* (Ehrlich and Hunt, 2012). In addition, the discovery that stromelysin-3 promoted breast cancer but was located in the fibroblast component, further suggests that protease-dependent invasion of cancer cells may not require the cancer to express the protease (Basset et al., 1990).

When fluorescently labelled HDFs and VB6s were co-cultured into mini-organotypic gels (**Figure 3.9**); the 24 hour time point revealed that both cell types were homogenously spread and adhered on to the surface of the gel. However, HDFs did not display any signs of invasion as when plated alone after 24 hours. At the 48 hour time point, HDFs were observed invading through the gel in a polarised vertical morphology and VB6 cells appeared to follow closely behind. By the 72 hour time point the organotypic gel displayed signs of gel contraction, degradation and perhaps evaporation. Interestingly HDFs had invaded through the gel and were pursued by VB6 cells. This data suggests that not only are the HDFs the leading invasive cell type in this assay, but also, that when co-cultured, VB6 cells may slow down the rate at which HDFs polarise and invade. Furthermore, VB6 cells presumably migrate down through the channels created by the HDFs (**Figure 6.1**).

Furthermore, I examined different fibroblast and tumour cells to gather data on invasive behaviour and to test robustness of the assay. Breast (MDA-468) and lung (H1299) cancer cells were labelled using CellTracker™ Red and plated alone *z*-stacks obtained 72 hours post seeding (**Figure 3.11**). The data revealed that MDA-468, H1299 or VB6 cells invade into organotypic gels over a 72 hour time period.

Skin (FSF) and lung (MRC-5) fibroblasts were labelled using CellTracker™ Green and plated alone *z*-stacks obtained 72 hours post seeding (**Figure 3.12**). The data revealed that neither FSFs nor MRC-5s polarised or invaded into the gels to the extent observed with the HDF cells when plated alone. FSF cells do become polarised and displayed early signs of morphological changes and invasion after 72 hours. However, the reduced numbers of invading cells may be due to age and passage numbers of the fibroblast cells or that these cells possess a phenotype that has a slow rate of initial invasion. Thus longer time point images would be needed to confirm the extent of invasion.

HDF, FSF and MRC-5 fibroblast cells were co-cultured with either H1299, MDA-48 and VB6 cancer cells (**Figure 3.13 – Figure 3.15**) and imaged 72 hours post seeding. Data revealed that VB6 cancer cells co-cultured with HDF fibroblasts displayed the largest amounts of fibroblast and cancer cell invasion as well as the most amount of gel degradation and contraction.

Overall, these data showed that, the newly developed fluorescent *in vitro* 3D mini-organotypic invasion assay permits, live *in situ* imaging of 3D gels and the assay produces measurable changes within 72 hours. Furthermore, image analysis provides 3D rendered and smoothened images, along with quantifiable cellular invasion data. This will speed up the analysis of mini-organotypic samples compared to the lengthy time constraints of the large gels.

Furthermore, I identified that not only are fibroblasts the leading invasive cell type within 3D mini-organotypic gels, in particular HDFs, but also that they can facilitate invasion of cancer cells. Thus implying that the stromal fibroblasts are a key element in the invasion of certain types of cancers and may facilitate collective cell invasion, as was also reported by Gaggioli and colleagues (Gaggioli et al., 2007).

A

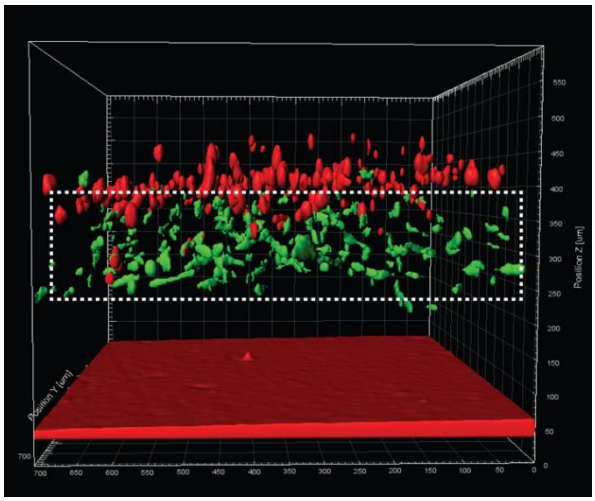

B

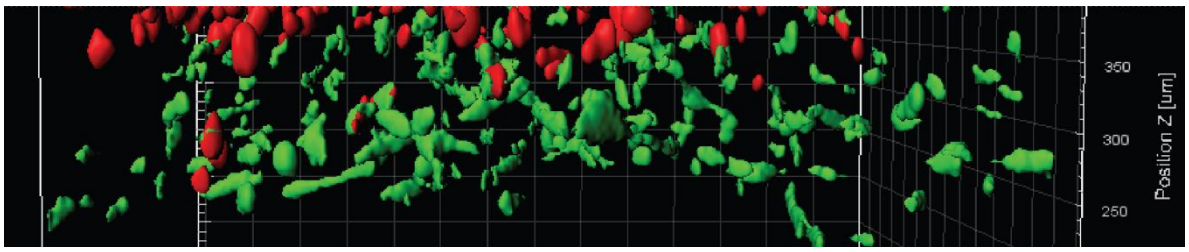

Figure 6.1: 3D rendered *z*-stack of 72 hour time point fluorescently labelled HDFs and VB6 cells co-cultured in mini-organotypic gels

The figure displays 72 hour time point Imaris rendered image of fluorescently labelled (CellTracker™ Green) HDFs co-cultured with fluorescently labelled (CellTracker™ Red) VB6 cells co-cultured in mini-organotypic gels. **A)** 72 hour time point image of co-culture. HDFs observed as leading invasive cell type followed by VB6 cells. **B)** Enlarged image of VB6 cells closely following behind HDF cells. One representative image from triplicate gels from one of three independent experiments.

To validate the 24-well fluorescent mini-organotypic invasion assay and examine gene silencing effects in 3D; I performed a siRNA SMARTpool library screen using a panel of proteases and targeted solely the fibroblast component of the tumour-stroma environment. Within the large organotypic gel studies, the tumour cells were predominantly the main cell of interest when performing data analysis and deducing conclusions. However, here I have chosen to focus on the often neglected fibroblast component of the stroma.

Since its original discovery in the late 90's (Fire et al., 1998), siRNA technology has become a powerful and commonly used tool for silencing the expression of target genes in many 2D *in vitro* siRNA screens (Lee et al., 2015; Rudalska et al., 2014; Smolen et al., 2010). Advances in liquid handling automation instruments, microscopy imaging platforms and plastics have made 2D siRNA HTS achievable in 384 (Petrocca et al., 2013) and even 1,536-well microtiter plates (Chung et al., 2010). However, all lacking the important significance of the 3D spatial architecture as observed *in vivo*.

Here, using a small protease target library, I focused on fibroblast component of the ECM via a SMARTpool siRNA knockdown. Target and NT siRNA control transfected fluorescently labelled HDFs were co-cultured with non-transfected fluorescently labelled VB6 cells, plated into mini-organotypic gels and imaged at a 72 hour end point. The purpose of this screen was to identify, if any, pooled proteases that show change in phenotypic behaviour of fibroblast and cancer cells via LOF screen.

The results of the siRNA screen (**Figure 4.6**) identified 16 genes that significantly ($p<0.05$) reduced fibroblast and cancer cell invasion as well as gel contraction, relative to a NT siRNA control. Image analysis revealed that fibroblast polarisation and changes in morphology were not observed and perhaps somewhat impeded or temporarily disengaged, thus, unable to invade through the gels. Therefore, ultimately leading to the reduction in cancer cell invasion. Furthermore, gel contraction and degradation was not as extensively observed.

Due to cost and time factors all 16 siRNA hits could not be investigated, thus, five siRNA were chosen to pursue and validate based on; (1) their relevance, if any, towards cancer progression; (2) their novelty as potential targets and; (3) the commercial availability of known working antibodies. The chosen genes of interest were CAPN-10, CASP-8, MMP-17, SERPIN-F1 and TMPRSS-13. A repeat transfection experiment confirmed that each of the selected siRNA reduced HDF and

VB6 cell invasion six days post transfection and was confirmed by H&E staining and qPCR (**Figure 4.8**).

SMARTpool siRNA of a single given gene consists of four siRNA duplexes that have been combined together. Thus, the individual siRNA of the five hits were purchased to investigate which, if any, of the individual siRNA duplexes provided any insight into the activity which contributed to the change in phenotypic behaviour.

The knockdown of CAPN-10 (**Figure 4.9**), CASP-8 (**Figure 4.10**) and SERPIN-F1 (**Figure 4.12**) individual siRNA in HDF cells decreased the number of polarising and invading HDF cells and reduction in gel height relative to a NT siRNA control. However, the individual siRNA of MMP-17 (constituent numbers one and two) (**Figure 4.11**) and TMPRSS-13 (constituent numbers 1 and 4) (**Figure 4.13**) significantly ($p<0.05$) showed limited change in gel height possible suggesting reduced gel degradation and contraction, as well as displaying reduced levels of HDF and VB6 cell invasion relative to a NT siRNA control. Therefore MMP-17 and TMPRSS-13 were further investigated. Western blotting confirmed reduction in protein level expression for MMP-17 (**Figure 4.15**). However, reduction in the protein expression of TMPRSS-13 was not observed via western blot. It is possible that the antibody used was not specific for TMPRSS-13 and would require further testing of other reagents. Further investigation included antibody staining on tissue sections, however, the results displayed large areas of non-specific staining and was not conclusive. Therefore alternative reagents would need to be identified and tested. The mechanism of how MMP-17 and TMPRSS-13 knockdown in HDFs reduced cancer and fibroblast cell invasion still needs to be identified.

In summary *in vitro* 3D fluorescent mini-organotypic invasion assay provided a reliable and repeatable method to perform a LOF siRNA screen via measurement of invasive depth. However, Imaris XT image analysis generated data for other measureable parameters from both cell types, such as volume, sphericity, and elipticity. These high-content phenotypic parameters may also be useful in providing information regarding fibroblast and cancer cell behaviour in 3D mini-organotypic gels.

With the use of a custom designed MatLab® algorithm (**Appendix 7.16**), phenotypic data of both cell types were extracted, organised and plotted to produce graphical plots for invasion vs sphericity of NT siRNA control samples (**Figure 4.17A**) and MMP-10 transfected HDF samples (**Figure 4.17B**). The data revealed that the leading invasive cells (mainly the HDFs) have a spherical value between 0.5-0.9. Suggesting

that in order to invade through the gels, the cells maybe slightly less spherical and possess a flatter shape. Invading VB6 cells display a similar range of spherical values suggesting that they may also change shape slightly if they are to migrate into and through the channel created by the HDFs. Resting VB6 cells (those at the surface of the gel) display a broad range of spherical values ranging from 0.4-1.0. Further MatLab® analysis was performed on the five SMARTpool selected siRNA hits; Invasion vs sphericity (**Figure 4.18**), Invasion vs volume (**Figure 4.19**) and invasion vs elipticity (oblate and prolate) (**Figure 4.20**). Data revealed that not only do smaller volume, but also, less oblate and more prolate shaped cells invade further into organotypic gels.

Overall, with the use of a novel *in vitro* 3D fluorescent mini-organotypic invasion assay and image analysis, I have performed and validated a siRNA screen that identified 16 SMARTpool hit proteases which significantly reduced cancer and fibroblast cell invasion. Further investigation revealed that two of these hits significantly reduced invasion when performing a validation screen using the individual siRNA. Furthermore, with the aid of MatLab® we have shown that this assay can provide 3D high-content multi-parametric data analysis. Thus further increasing the rate of result delivery and making this assay format a relatively easy 3D invasion assay for other laboratories to use.

The need to identify potential therapeutic targets using *in vitro* 3D HTS platforms has become increasingly more desirable within drug discovery (Mayr and Fuerst, 2008). Academic and industrial labs are developing 3D HTS assays which they feel can provide a suitable *in vitro*-like model. Here, I presented two potential HTS models that can be adopted by both academia and industry to perform HTS drug or gene screening in a 3D physiomimetic *in vitro* organotypic based model.

The 96-Transwell® insert micro-organotypic invasion assay has revealed similarities in invasive behaviour of VB6 and HDF cells and also shown to be more cost efficient than its 24-well counterpart. With oval shaped wells, for ease of medium exchange via integration with liquid handling systems and barcoded plates, this assay format would be fully supported on an automated platform. However working manually with this format was cumbersome.

The 96-well reverse assay, provides a simpler assay format which requires less preparation time and is more cost efficient than the 96-Transwell® method. Here I have shown that both assays can be performed manually from preparation to data

analysis, however going forward the 96-well reverse assay would be a more cost efficient model to use but it still requires further optimisation.

Despite these reservation, to investigate whether the 96-well reverse invasion assay could be used to; (1) perform a manually prepared drug screen; (2) deliver high-content multi-parameter data analysis; (3) be integrated into a robotic imaging system. I performed a manual small preliminary drug screen consisting of an ALK5, ERK and MEK inhibitors as well as two known MMP inhibitors (Doxycycline (Stechmiller et al., 2010) and Marimastat, which has been reported to prevent fibroblast-mediated collagen contraction (Scott et al., 1998).

The experiment, which took place in August 2017 at AstraZeneca (Cambridge) involved the manual preparation of organotypic gels containing transiently labelled fluorescent HDFs and VB6 cells. 24-hours post seeding compound dosing was performed automatically using a Bravo™ Velocity 11 liquid handling platform (Agilent, USA) before being incubated in an automated microplate carousel incubator (SteriStore, HighRes biosolutions, USA). 24-hours post drug dosing, plates were imaged automatically using a high-content screening confocal microscope system (Cell Voyager 7000 (CV7000), Yokogawa, Japan) (**Figure 6.2**).

Overall the process of plate preparation was the most time consuming aspect, compound dosing was quick and automated plate imaging was even more rapid. A *z*-stack of one well, with four field of views, containing a 500µm gel in three colours took approximately between 1-2 minute to scan. Unfortunately the experiment experienced some technical issues and even though high-content data were captured, complete analysis could not be completed. However the most important aspect is that the 96-well reverse assay can deliver high-content data for multi-parameter analysis aided by integration into an automated screening and imaging platforms.

Table 6.1: Comparison of *in vitro* 3D organotypic gel assays

Assay Format	Cost/plate	Nº cells required/ well	Volume of gel required/ well	Scanning method and time/well	Duration
24-well Transwell®	£137	100,000	100-120µl	CLSM 710 – 20-23 mins SD – 9-11 mins	Up to 14 days
96-well Transwell®	£176	5000	50µl	CLSM 710 – 10-12 mins SD – 5-6 mins	Up to 4 days
96-well reverse	£2.92	7500	50µl	CLSM 710 – 10-12 mins SD – 5-6 mins CV7000 – 1-2 mins	Up to 4 days

A

B

Figure 6.2: CV7000 – high content screening automated confocal scanner unit

A) CV7000 main confocal scanning unit, temperature and CO_2, controlled with built-in liquid handler to enable long term live cell image and rapid kinetic analysis. **B)** CV7000 set up at AstraZeneca. Integrated with SteriStore microplate incubator and plate hotel with loading robotic arm. Images provided by AstraZeneca.

My studies have allowed me to develop a novel and robust *in vitro* fluorescent 3D mini-organotypic invasion assay which can be used to perform siRNA screens and produce quantitative high-content phenotypic data for analysis. Furthermore, the miniaturisation has produced two smaller assays which can be integrated into a HTS platform. However there are several experiment that could be addressed to further validate this work:

1) Introduction of CAFs into the organotypic invasion assays order to further assess cancer and fibroblast cell invasion, but also to mimic more closely the tumour-stromal microenvironment. While the HDFs probably behaved has CAFs (high invasive) they were not derived from a tumour.

2) Gel contraction assays with fibroblast and cancer cell combinations, in the presence of pan-protease inhibitors may help to identify how much reduction in gel size is due to physical contraction by cells versus enzyme destruction.

3) To examine organotypic gel degradation and invasion of cancer and fibroblast cells, future work should involve the use of fluorescent collagen or second-harmonic imaging. Additionally, regular imaging of the gels (every few hours rather than once per day) via confocal or spinning disk microscopy, to understand the dynamic changes in collagen: Matrigel® gel remodelling.

4) To confirm the value of MMP-17 and TMPRSS-13 as targets for suppressing the pro-invasive activity of HDFs, these genes should be knocked-down in a series of CAFs from multiple cancers within the fluorescent 3D organotypic model described here. Furthermore, we could make cell line models which contain a more efficient knockdown of MMP-17 and TMPRSS-13. Thus future work may involve the development CRISPR-Cas9 cell lines.

5) The mechanisms of MMP-17 and TMPRSS-13 suppression of fibroblast and thus cancer cell invasion are not known. It is not established whether degradation of one or more proteins in the extracellular collagen: Matrigel® matrix is the target, or a consequence of siRNA knockdown within some other aspect of the fibroblast biology is affected. Some groups have established mass spectrometry methods for identifying protease degradome (Butler et al., 2009; Shen et al., 2012) and such studies may determine if the target is extracellular. We could perform mass spectrometry protease degradome analysis to identify the specific targets of MMP-17 and TMPRSS-13.

Advances in 3D culturing systems have enabled rapid development of an array of new *in vitro* tumour models and also variations of existing traditional models, through new innovations (detailed in **Section 1.3**). 3D models can partly recapitulate the *in vivo* tumour-stromal microenvironment, thus having the potential to reduce the number of animal experiments. In 2013 the EU banned the use of animal models within the cosmetics industry and experts stated that it would take at least 7-10 years to replace the current *in vivo* animal tests (Leist et al., 2014). Thus driving engineers and researchers to innovate new *in vitro* 3D modelling techniques.

To summarise, I have developed an *in vitro* 3D fluorescent organotypic invasion assay that not only mimics the *in vivo* tumour-stromal microenvironment and allows live *in situ* imaging of fluorescently labelled cell populations, but also produces quantitative multi-parametric data. The assay was used to perform a siRNA library screen and revealed promising avenues for potentially new therapeutic targets. Furthermore, the assay was miniaturised in to two different assay methods, having the potential to be suitable for higher-throughput studies of drug and gene therapies within academia and industry.

As no 3D *in vitro* assay can ever fully mimic the *in vivo* host environment; I believe the assays developed in this study provide an affordable and reliable model to produce a clearer insight to the early stages of cancer metastasis by means of targeting the stromal fibroblasts in order to reduce cancer cell invasion and migration. The assay can be used to rapidly identify potential targets and may be considered a positive aspect of the 3Rs (reduction, replacement, refinement) for *in vivo* studies. I believe the next generation of *in vitro* models will need to incorporate infiltrating cells from the innate and immune systems to move closer to mimicking the true *in vivo* microenvironment. However, our current technologies make this a technically challenging goal.

CHAPTER VII: APPENDIX

7.0 Appendix

7.1 Protease library primary SMARTpool siRNA screen

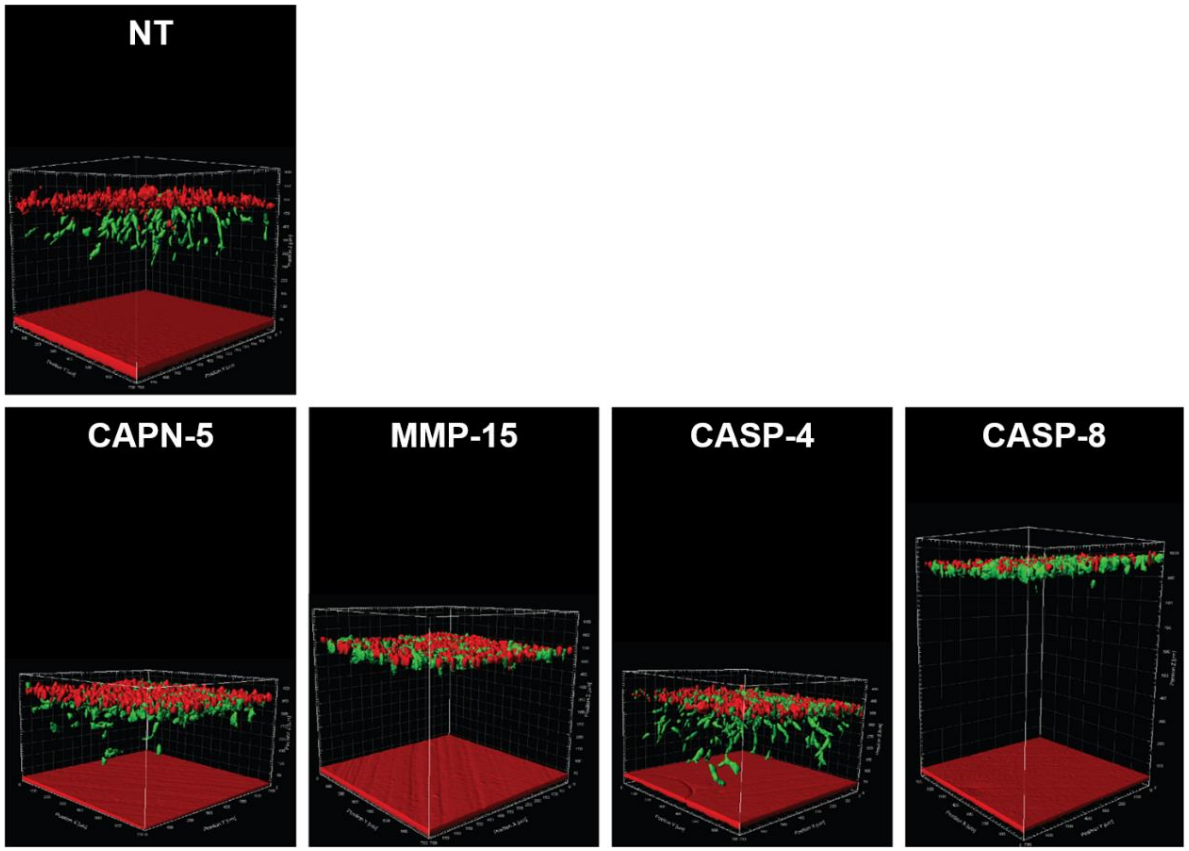

Appendix Figure 7.1: Primary SMARTpool siRNA screen; fluorescently labelled HDFs transfected with NT siRNA control, CAPN-5, MMP-15, CASP-4 and CASP-8 SMARTpool siRNA co-cultured with fluorescently labelled VB6 cells in mini-organotypic gels

3D Imaris rendered *z*-stacks of mini-organotypic gels containing fluorescently labelled HDFs (CellTracker™ Green) transfected with NT siRNA control, CAPN-5, MMP-15, CASP-4 and CASP-8 SMARTpool siRNA (20nM), co-cultured with fluorescently labelled VB6 cells (CellTracker™ Red). *Z*-stacks were obtained via CLSM 72 hours post seeding (six days post transfection). One representative image of triplicate gels belonging to one independent experiment.

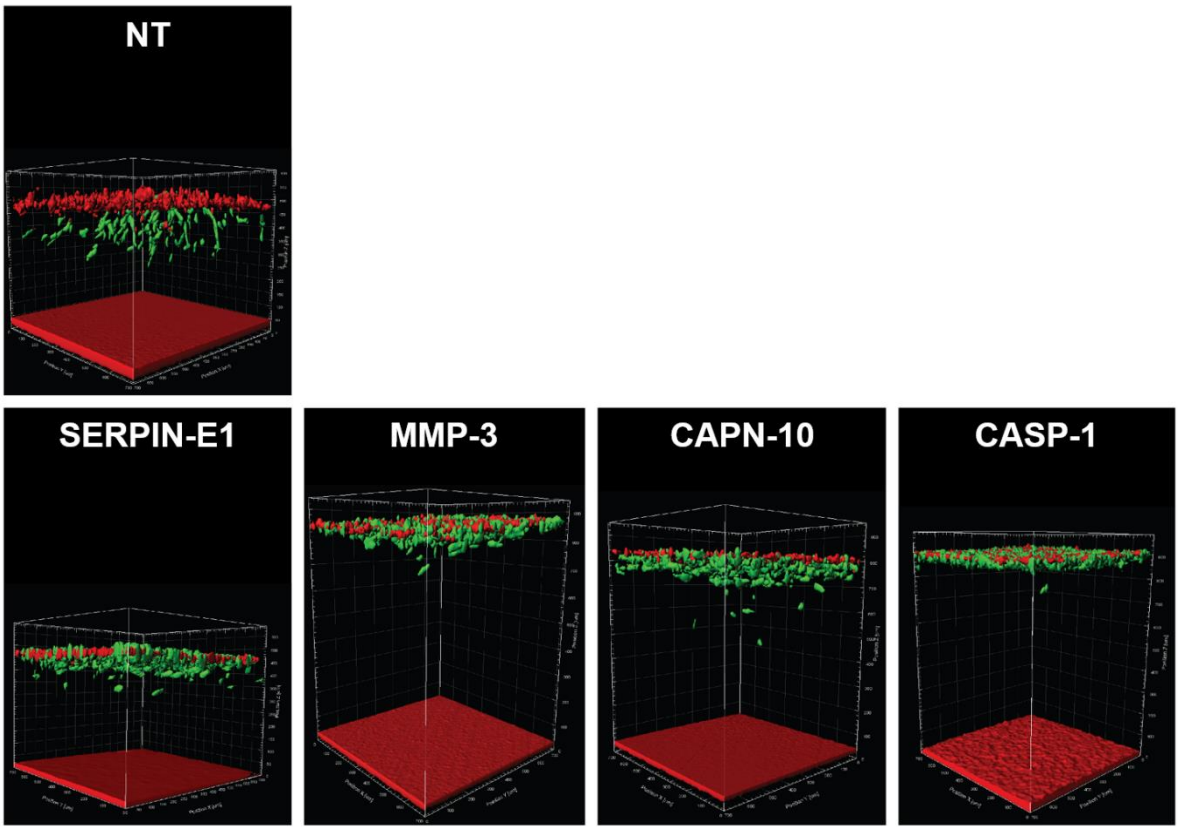

Appendix Figure 7.2: Primary SMARTpool siRNA screen; fluorescently labelled HDFs transfected with a NT siRNA control, SERPIN-E1, MMP-3, CAPN-10 and CASP-1 SMARTpool siRNA co-cultured with fluorescently labelled VB6 cells in mini-organotypic gels

3D Imaris rendered *z*-stacks of mini-organotypic gels containing fluorescently labelled HDFs (CellTracker™ Green) transfected with NT siRNA control, SERPIN-E1, MMP-3, CAPN-10 and CASP-1 SMARTpool siRNA (20nM), co-cultured with fluorescently labelled VB6 cells (CellTracker™ Red). *Z*-stacks were obtained via CLSM 72 hours post seeding (six days post transfection). One representative image of triplicate gels belonging to one independent experiment.

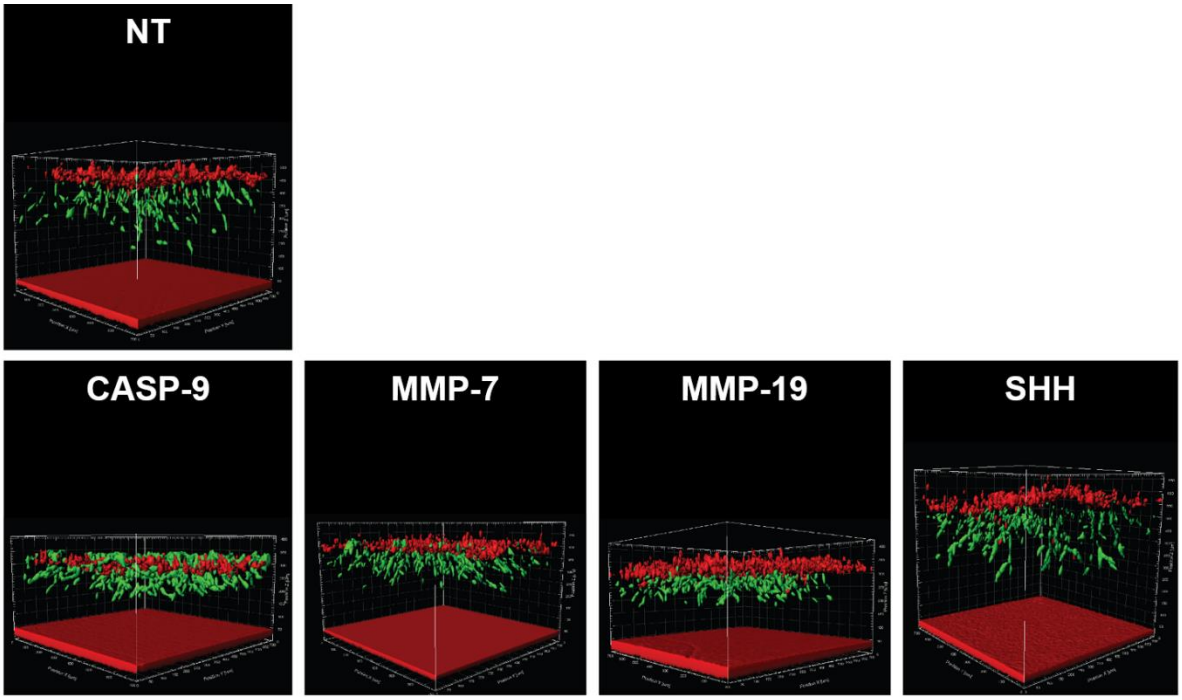

Appendix Figure 7.3: Primary SMARTpool siRNA screen; fluorescently labelled HDFs transfected with a NT siRNA control, CASP-9, MMP-7, MMP-19 and SHH SMARTpool siRNA co-cultured with fluorescently labelled VB6 cells in mini-organotypic gels

3D Imaris rendered *z*-stacks of mini-organotypic gels containing fluorescently labelled HDFs (CellTracker™ Green) transfected with NT siRNA control, CASP-9, MMP-7, MMP-19 and SHH SMARTpool siRNA (20nM), co-cultured with fluorescently labelled VB6 cells (CellTracker™ Red). *Z*-stacks were obtained via CLSM 72 hours post seeding (six days post transfection). One representative image of triplicate gels belonging to one independent experiment.

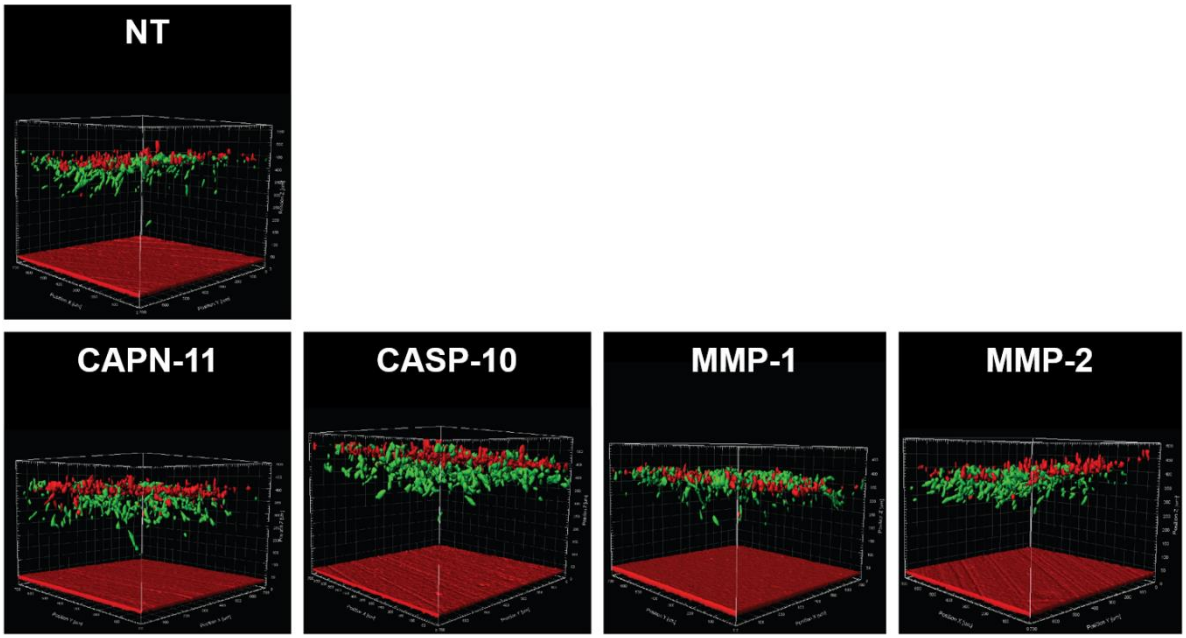

Appendix Figure 7.4: Primary SMARTpool siRNA screen; fluorescently labelled HDFs transfected with a NT siRNA control, CAPN-11, CASP-10, MMP-1 and MMP-2 SMARTpool siRNA co-cultured with fluorescently labelled VB6 cells in mini-organotypic gels

3D Imaris rendered *z*-stacks of mini-organotypic gels containing fluorescently labelled HDFs (CellTracker™ Green) transfected with NT siRNA control, CAPN-11, CASP-10, MMP-1 and MMP-2 SMARTpool siRNA (20nM), co-cultured with fluorescently labelled VB6 cells (CellTracker™ Red). *Z*-stacks were obtained via CLSM 72 hours post seeding (six days post transfection). One representative image of triplicate gels belonging to one independent experiment.

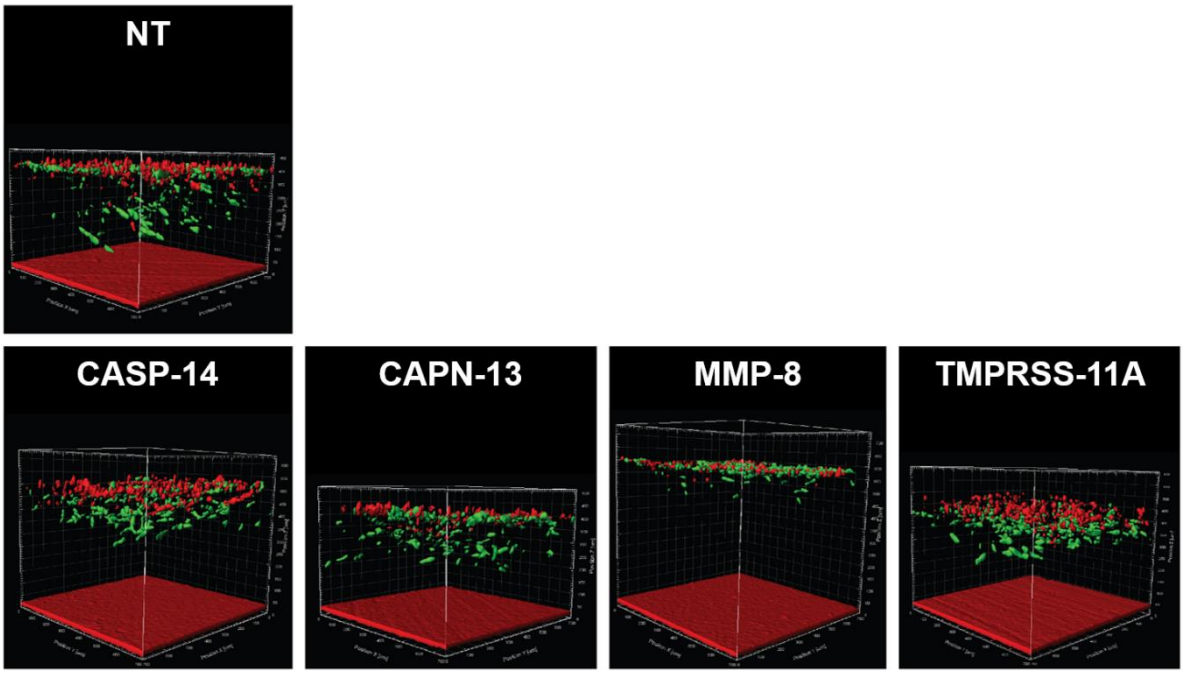

Appendix Figure 7.5: Primary SMARTpool siRNA screen; fluorescently labelled HDFs transfected with a NT siRNA control, CASP-14, CAPN-13, MMP-8 and TMPRSS-11A SMARTpool siRNA co-cultured with fluorescently labelled VB6 cells in mini-organotypic gels

3D Imaris rendered *z*-stacks of mini-organotypic gels containing fluorescently labelled HDFs (CellTracker™ Green) transfected with NT siRNA control, CASP-14, CAPN-13, MMP-8 and TMPRSS-11A SMARTpool siRNA (20nM), co-cultured with fluorescently labelled VB6 cells (CellTracker™ Red). *Z*-stacks were obtained via CLSM 72 hours post seeding (six days post transfection). One representative image of triplicate gels belonging to one independent experiment.

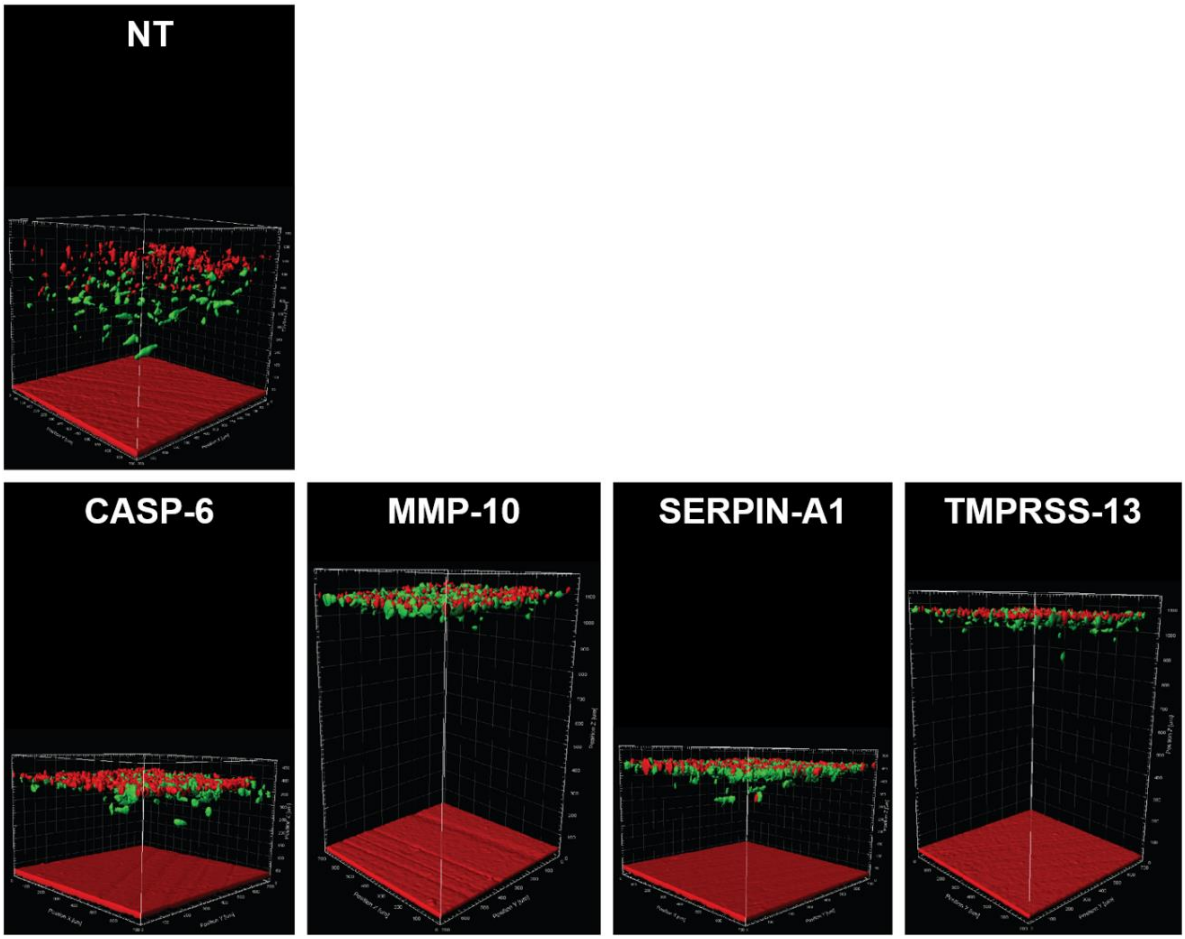

Appendix Figure 7.6: Primary SMARTpool siRNA screen; fluorescently labelled HDFs transfected with a NT siRNA control, CASP-6, MMP-10, SERPIN-A1 and TMPRSS-13 SMARTpool siRNA co-cultured with fluorescently labelled VB6 cells in mini-organotypic gels

3D Imaris rendered *z*-stacks of mini-organotypic gels containing fluorescently labelled HDFs (CellTracker™ Green) transfected with NT siRNA control, CASP-6, MMP-10, SERPIN-A1 and TMPRSS-13 SMARTpool siRNA (20nM), co-cultured with fluorescently labelled VB6 cells (CellTracker™ Red). *Z*-stacks were obtained via CLSM 72 hours post seeding (six days post transfection). One representative image of triplicate gels belonging to one independent experiment.

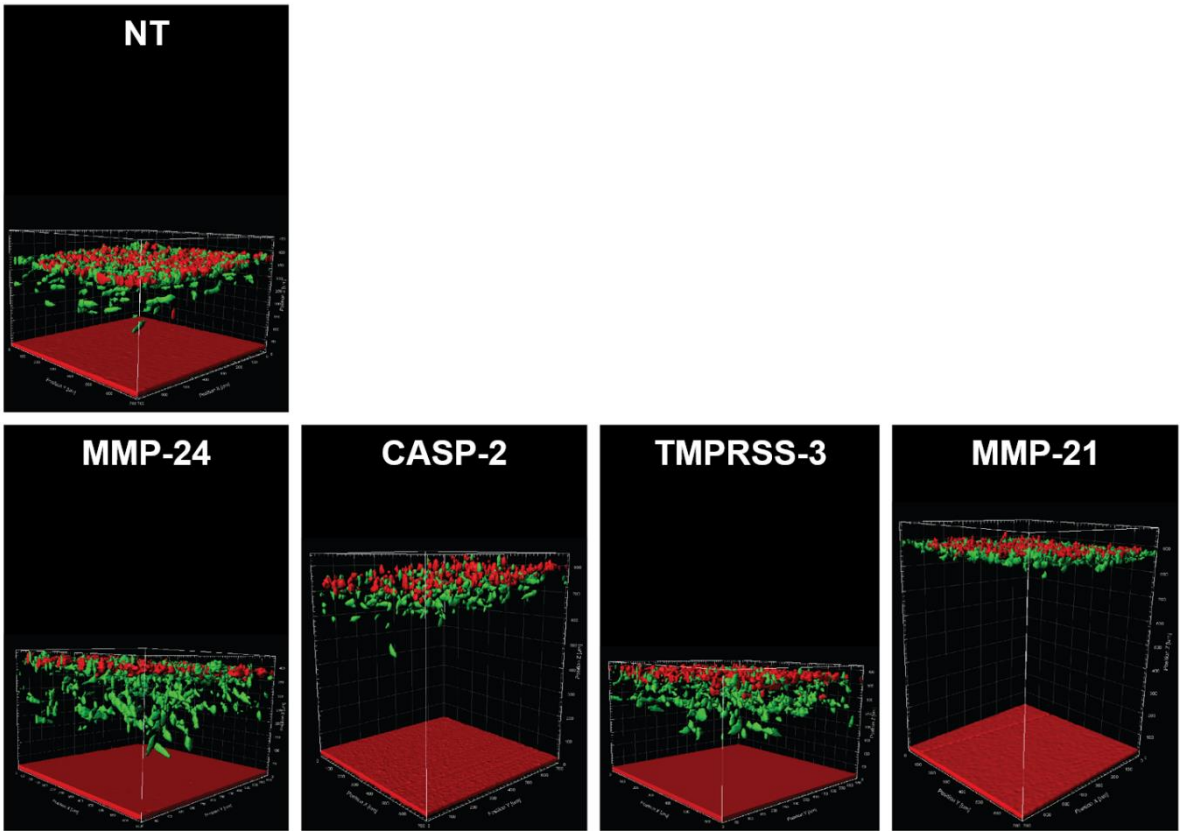

Appendix Figure 7.7: Primary SMARTpool siRNA screen; fluorescently labelled HDFs transfected with a NT siRNA control, MMP-24, CASP-2, TMPRSS-3 and MMP-21 SMARTpool siRNA co-cultured with fluorescently labelled VB6 cells in mini-organotypic gels

3D Imaris rendered *z*-stacks of mini-organotypic gels containing fluorescently labelled HDFs (CellTracker™ Green) transfected with NT siRNA control, MMP-24, CASP-2, TMPRSS-3 and MMP-21 SMARTpool siRNA (20nM), co-cultured with fluorescently labelled VB6 cells (CellTracker™ Red). *Z*-stacks were obtained via CLSM 72 hours post seeding (six days post transfection). One representative image of triplicate gels belonging to one independent experiment.

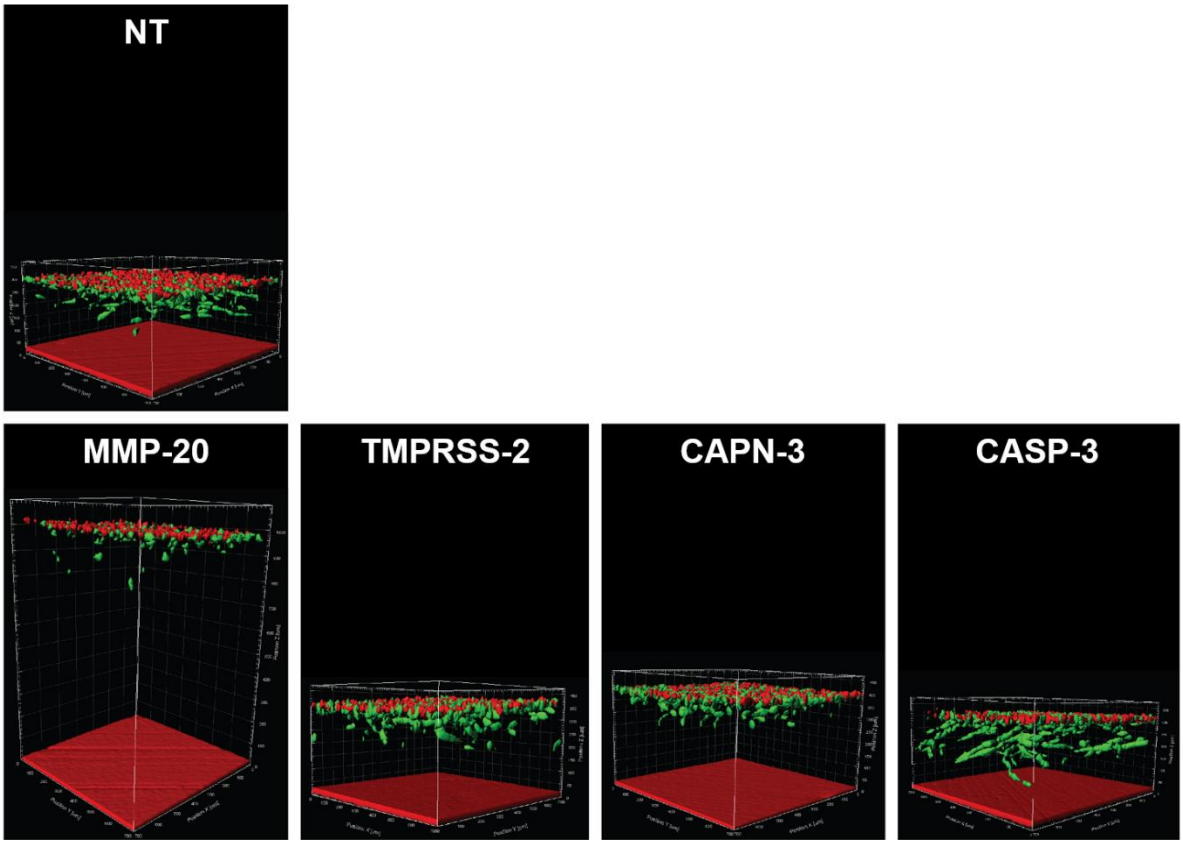

Appendix Figure 7.8: Primary SMARTpool siRNA screen; fluorescently labelled HDFs transfected with a NT siRNA control, MMP-20, TMPRSS-2, CAPN-3 and CASP-3 SMARTpool siRNA co-cultured with fluorescently labelled VB6 cells in mini-organotypic gels

3D Imaris rendered *z*-stacks of mini-organotypic gels containing fluorescently labelled HDFs (CellTracker™ Green) transfected with NT siRNA control, MMP-20, TMPRSS-2, CAPN-3 and CASP-3 SMARTpool siRNA (20nM), co-cultured with fluorescently labelled VB6 cells (CellTracker™ Red). *Z*-stacks were obtained via CLSM 72 hours post seeding (six days post transfection). One representative image of triplicate gels belonging to one independent experiment.

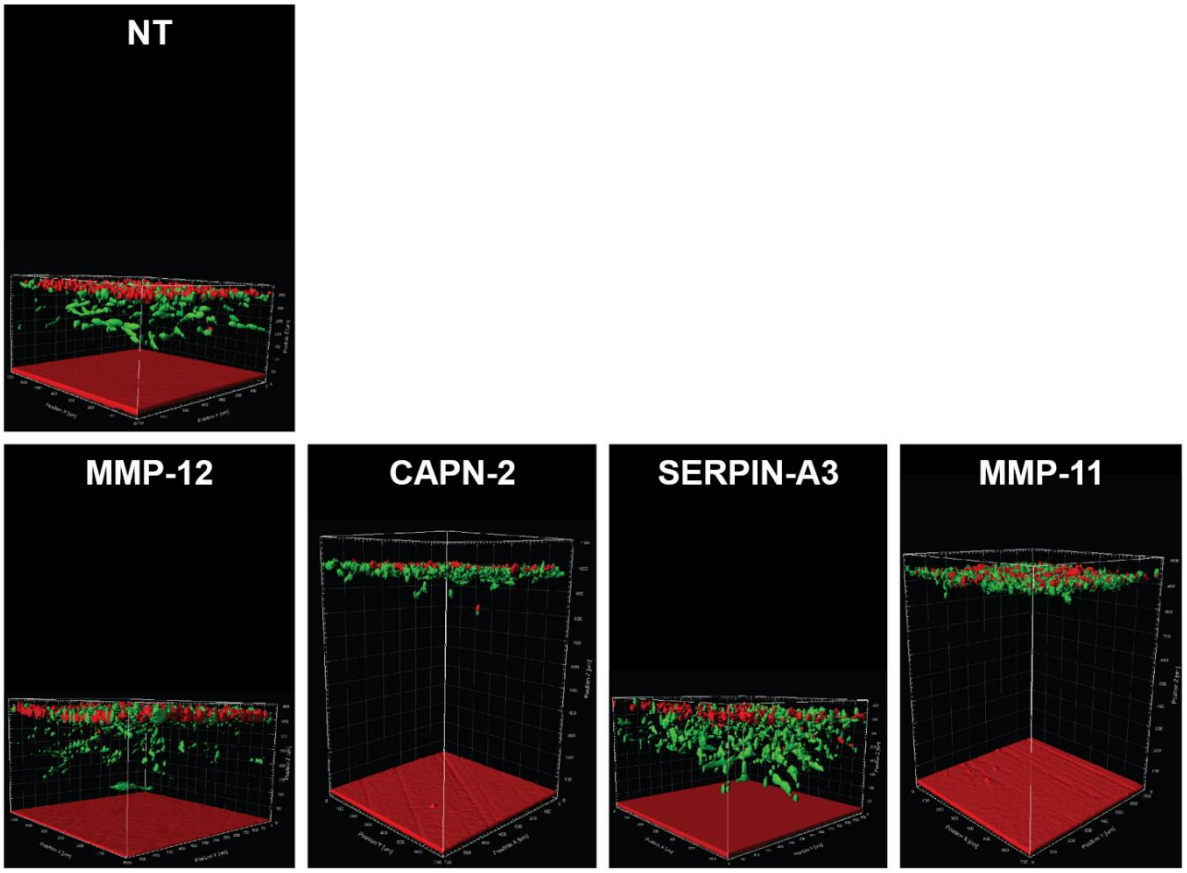

Appendix Figure 7.9: Primary SMARTpool siRNA screen; fluorescently labelled HDFs transfected with a NT siRNA control, MMP-12, CAPN-2, SERPIN-A3 and MMP-11 SMARTpool siRNA co-cultured with fluorescently labelled VB6 cells in mini-organotypic gels

3D Imaris rendered *z*-stacks of mini-organotypic gels containing fluorescently labelled HDFs (CellTracker™ Green) transfected with NT siRNA control, MMP-12, CAPN-2, SERPIN-A3 and MMP-11 SMARTpool siRNA (20nM), co-cultured with fluorescently labelled VB6 cells (CellTracker™ Red). *Z*-stacks were obtained via CLSM 72 hours post seeding (six days post transfection). One representative image of triplicate gels belonging to one independent experiment.

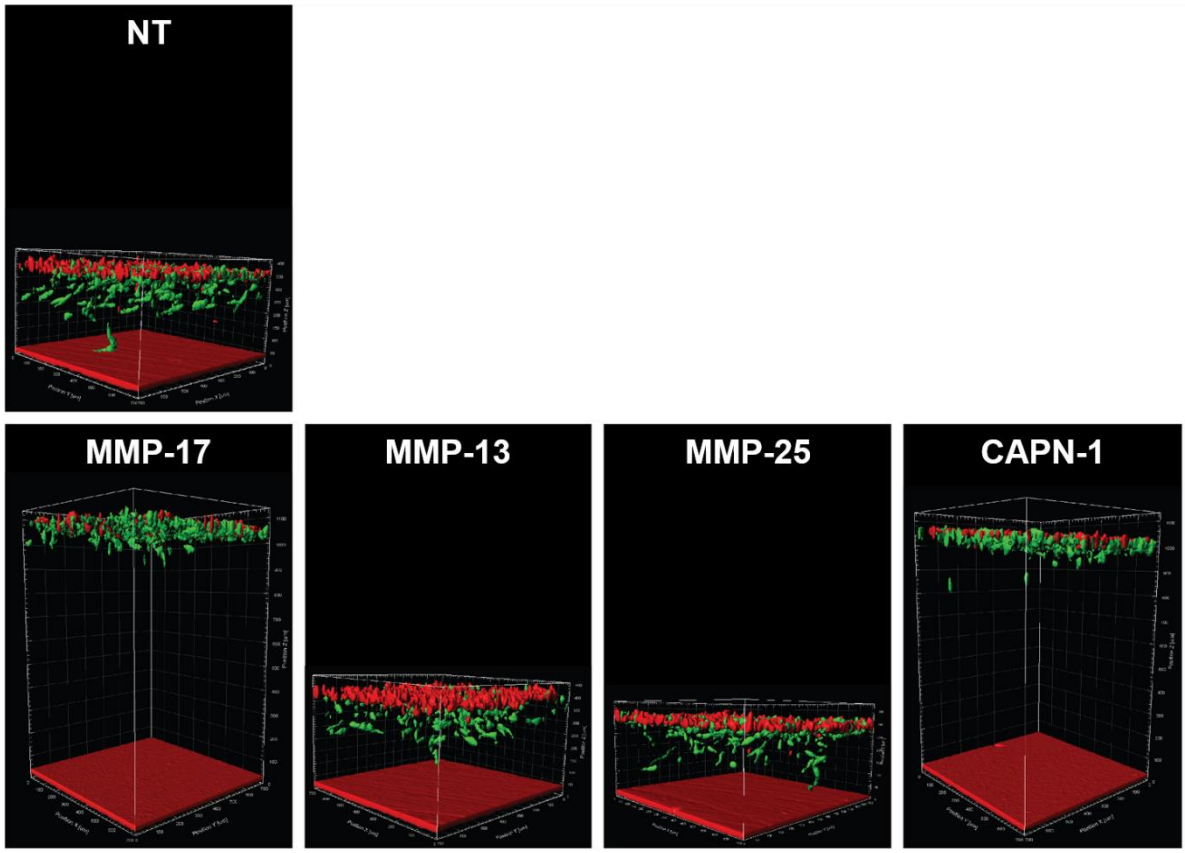

Appendix Figure 7.10: Primary SMARTpool siRNA screen; fluorescently labelled HDFs transfected with a NT siRNA control, MMP-17, MMP-13, MMP-25 and CAPN-1 SMARTpool siRNA co-cultured with fluorescently labelled VB6 cells in mini-organotypic gels

3D Imaris rendered z-stacks of mini-organotypic gels containing fluorescently labelled HDFs (CellTracker™ Green) transfected with NT siRNA control, MMP-17, MMP-13, MMP-25 and CAPN-1 SMARTpool siRNA (20nM), co-cultured with fluorescently labelled VB6 cells (CellTracker™ Red). Z-stacks were obtained via CLSM 72 hours post seeding (six days post transfection). One representative image of triplicate gels belonging to one independent experiment.

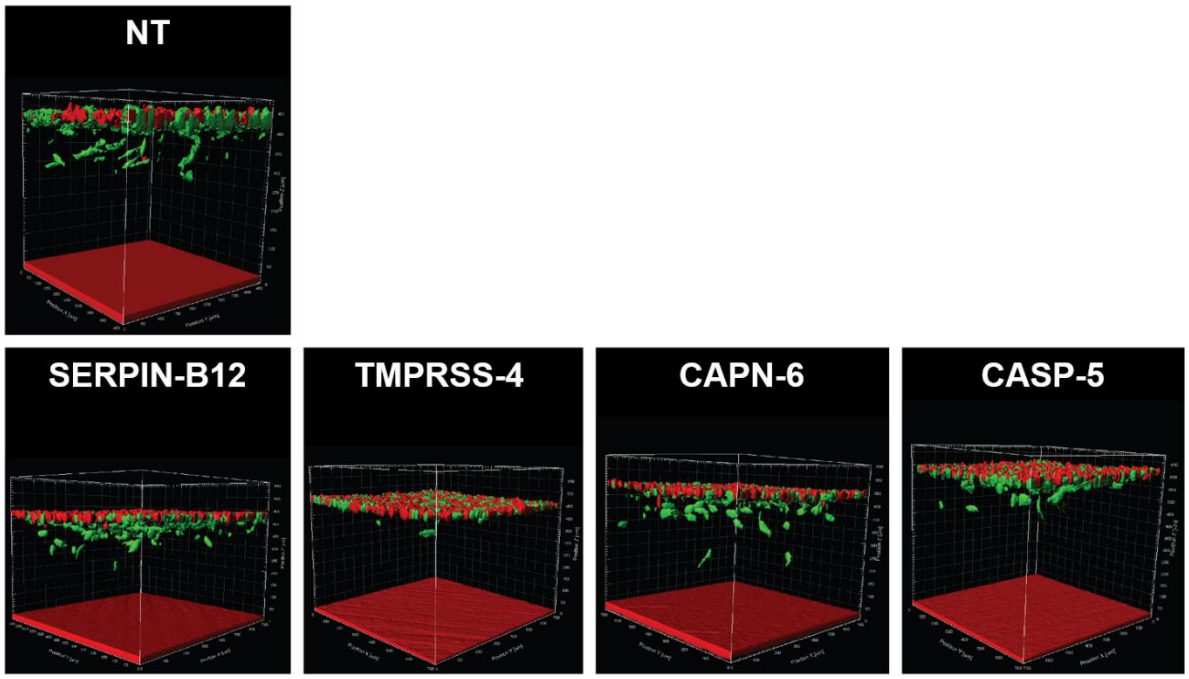

Appendix Figure 7.11: Primary SMARTpool siRNA screen; fluorescently labelled HDFs transfected with a NT siRNA control, SERPIN-B12, TMPRSS-4, CAPN-6 and CASP-5 SMARTpool siRNA co-cultured with fluorescently labelled VB6 cells in mini-organotypic gels

3D Imaris rendered z-stacks of mini-organotypic gels containing fluorescently labelled HDFs (CellTracker™ Green) transfected with NT siRNA control, SERPIN-B12, TMPRSS-4, CAPN-6 and CASP-5 SMARTpool siRNA (20nM), co-cultured with fluorescently labelled VB6 cells (CellTracker™ Red). Z-stacks were obtained via CLSM 72 hours post seeding (six days post transfection). One representative image of triplicate gels belonging to one independent experiment.

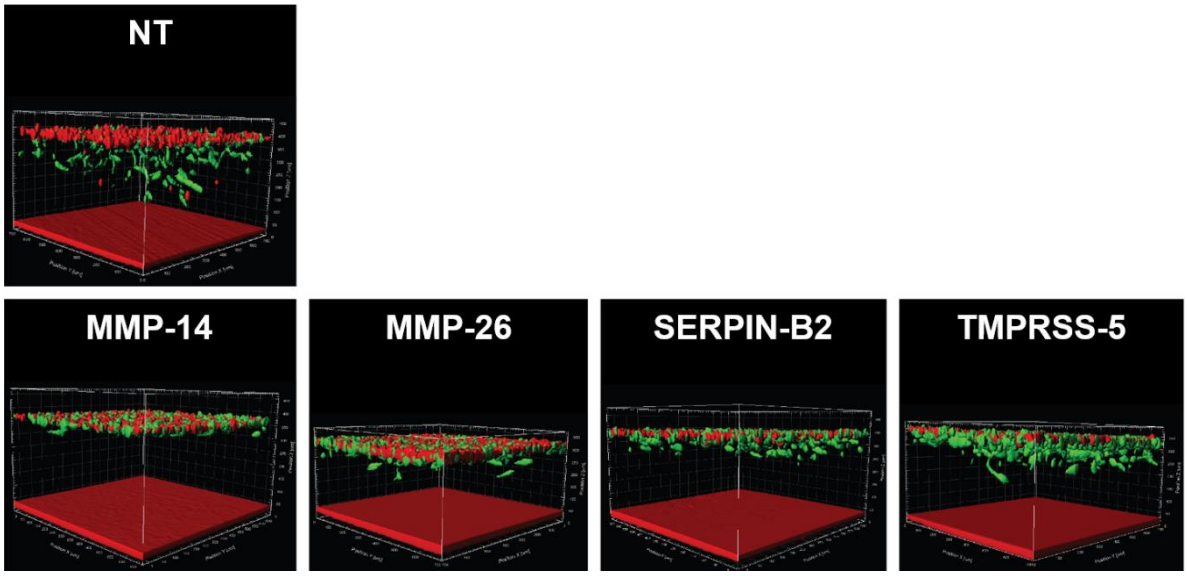

Appendix Figure 7.12: Primary SMARTpool siRNA screen; fluorescently labelled HDFs transfected with a NT siRNA control, MMP-14, MMP-26, SERPIN-B2 and TMPRSS-5 SMARTpool siRNA co-cultured with fluorescently labelled VB6 cells in mini-organotypic gels

3D Imaris rendered z-stacks of mini-organotypic gels containing fluorescently labelled HDFs (CellTracker™ Green) transfected with NT siRNA control, MMP-14, MMP-26, SERPIN-B2 and TMPRSS-5 SMARTpool siRNA (20nM), co-cultured with fluorescently labelled VB6 cells (CellTracker™ Red). Z-stacks were obtained via CLSM 72 hours post seeding (six days post transfection). One representative image of triplicate gels belonging to one independent experiment.

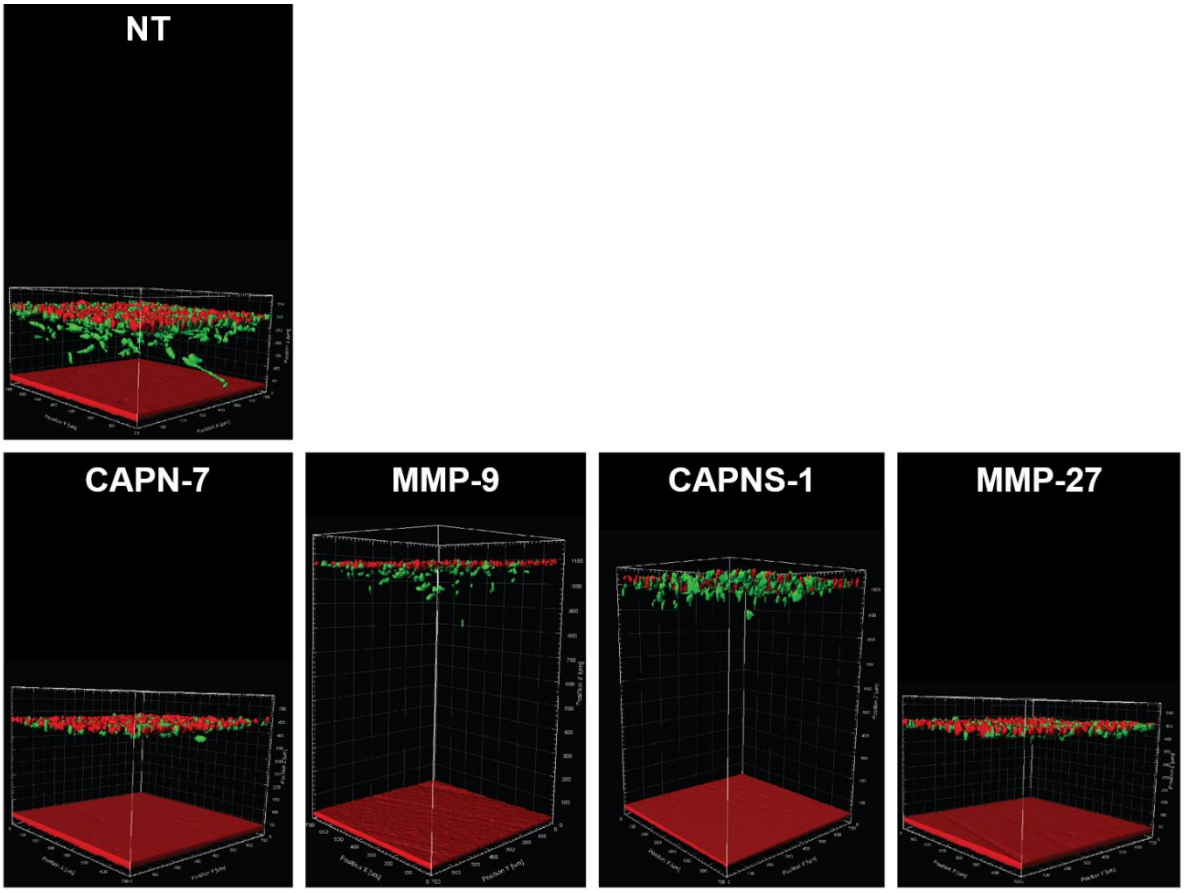

Appendix Figure 7.13: Primary SMARTpool siRNA screen; fluorescently labelled HDFs transfected with a NT siRNA control, CAPN-7, MMP-9, CAPNS-1 and MMP-27 SMARTpool siRNA co-cultured with fluorescently labelled VB6 cells in mini-organotypic gels

3D Imaris rendered z-stacks of mini-organotypic gels containing fluorescently labelled HDFs (CellTracker™ Green) transfected with NT siRNA control, CAPN-7, MMP-9, CAPNS-1 and MMP-27 SMARTpool siRNA (20nM), co-cultured with fluorescently labelled VB6 cells (CellTracker™ Red). Z-stacks were obtained via CLSM 72 hours post seeding (six days post transfection). One representative image of triplicate gels belonging to one independent experiment.

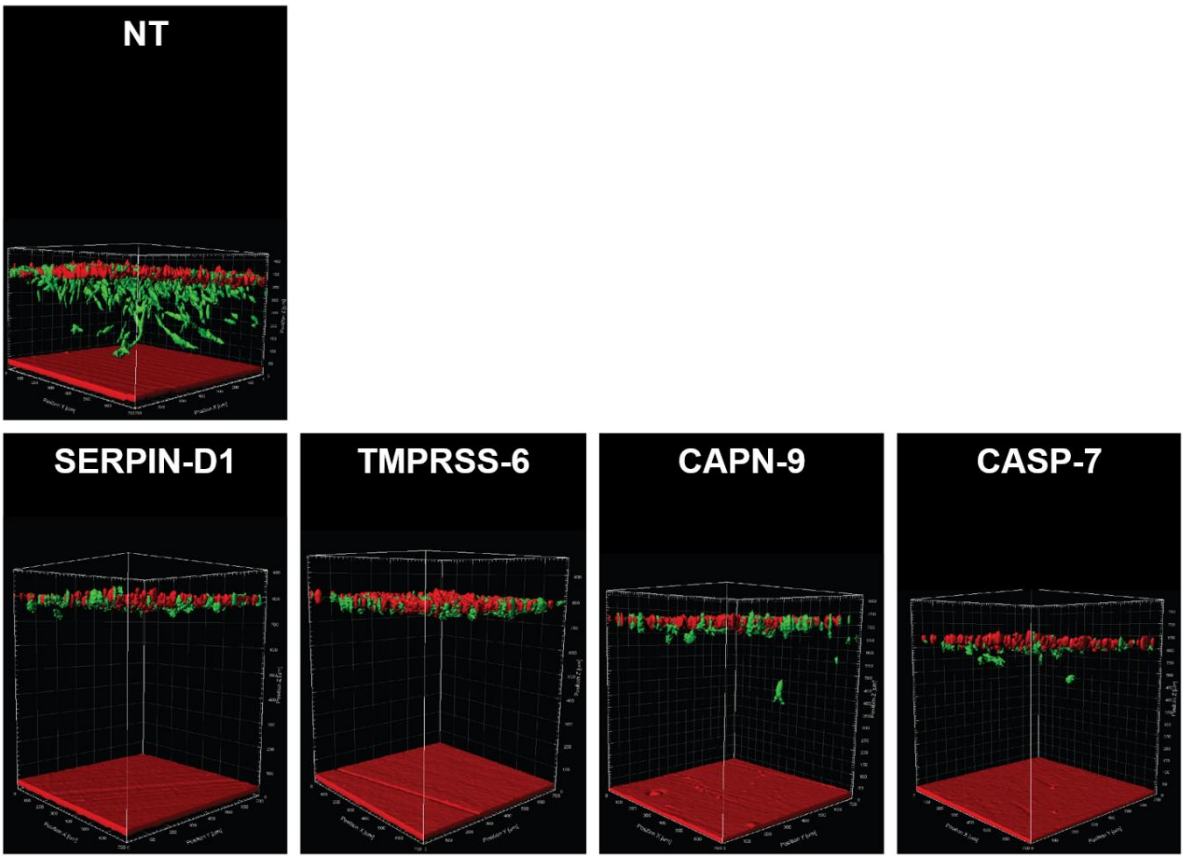

Appendix Figure 7.14: Primary SMARTpool siRNA screen; fluorescently labelled HDFs transfected with a NT siRNA control, SERPIN-D1, TMPRSS-6, CAPN-9 and CASP-7 SMARTpool siRNA co-cultured with fluorescently labelled VB6 cells in mini-organotypic gels

3D Imaris rendered z-stacks of mini-organotypic gels containing fluorescently labelled HDFs (CellTracker™ Green) transfected with NT siRNA control, SERPIN-D1, TMPRSS-6, CAPN-9 and CASP-7 SMARTpool siRNA (20nM), co-cultured with fluorescently labelled VB6 cells (CellTracker™ Red). Z-stacks were obtained via CLSM 72 hours post seeding (six days post transfection). One representative image of triplicate gels belonging to one independent experiment.

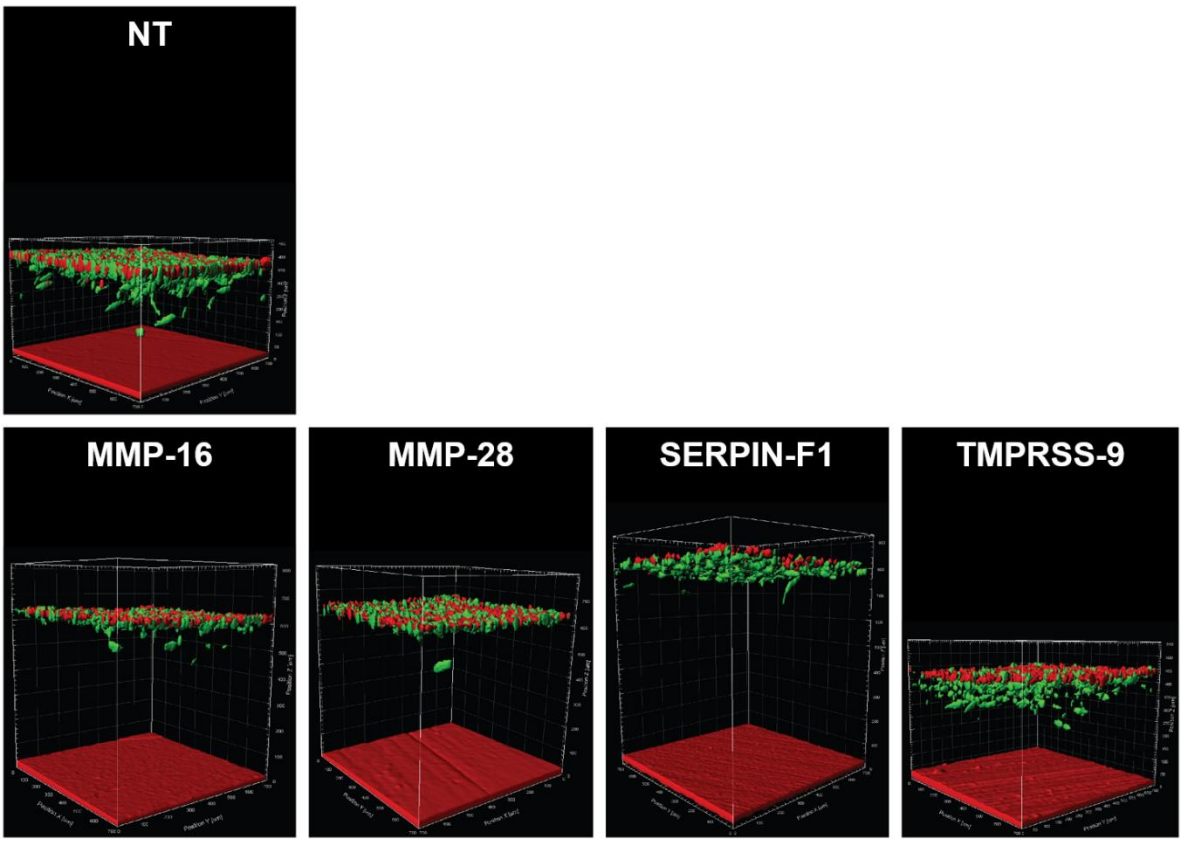

Appendix Figure 7.15: Primary SMARTpool siRNA screen; fluorescently labelled HDFs transfected with a NT siRNA control, MMP-16, MMP-28, SERPIN-F1 and TMPRSS-9 SMARTpool siRNA co-cultured with fluorescently labelled VB6 cells in mini-organotypic gels

3D Imaris rendered z-stacks of mini-organotypic gels containing fluorescently labelled HDFs (CellTracker™ Green) transfected with NT siRNA control, MMP-16, MMP-28, SERPIN-F1 and TMPRSS-9 SMARTpool siRNA (20nM), co-cultured with fluorescently labelled VB6 cells (CellTracker™ Red). Z-stacks were obtained via CLSM 72 hours post seeding (six days post transfection). One representative image of triplicate gels belonging to one independent experiment.

7.2 MatLab® algorithm for high-content multi-parameter analysis

```
//multi-parameter analysis algorithm

function [ContGreenOut,ContRedOut,IDgrOut,IDreOut]= CompPlot(
input1,input2 )
% Scatter plots of siRNA transfected HDF cells and non-treated VB6
cancer cells and non targeting siRNA control
% input1 and input2 are the choice of filter
% the choices are in order:
%   Area, Elipticity_(oblate), Elipticity_(prolate),Invasion,
Sphericity, Volume,
%  The outputs are the from the plots
close all

d = '*.csv'; %find csvs in directory
D = dir(d);
Key = {'Area', 'Elipticity (oblate)', 'Elipticity (prolate)',
'Sphericity', 'Volume', 'Invasion'}; %Names of the filters

%% Find the names of the compounds
for i = 1:size(D,1)
    place = regexp(D(i).name,'(','split'); %Split the name
    place = place(:,1);
    DD(i) = cellstr(place); %Save names in cells
end
C = unique(DD); %Find the unique names

%% Get the control data
index = strfind(C,'Control');
idx = find(not(cellfun('isempty', index)));
C(idx) = []; %Remove it from consideration of comparison

ContGreen = csvread('Control(green).csv'); %Load in controls
ContRed = csvread('Control(red).csv');
```

```
K1 = char(Key(:,input1)); %Find first filter
K2 = char(Key(:,input2)); %Find first filter

%% Get data and plot scatter graphs
for j = 1:size(C,2)
    %Get name of compound and find file
    e = char(C(j));
    f = sprintf('%s*.csv',e);
    F = dir(f);

    %Load in green and red data
    gr = sprintf('%s(green).csv',e);
    re = sprintf('%s(red).csv',e);
    IDgr = csvread(gr);
    IDre = csvread(re);

    %Plot red and green compound vs red and green control
    figure(j)
    scatter(IDgr(:,input1),IDgr(:,input2),'g')
    hold on
    scatter(IDre(:,input1),IDre(:,input2),'r')
    scatter(ContGreen(:,input1),ContGreen(:,input2),'x','g')
    scatter(ContRed(:,input1),ContRed(:,input2),'x','r')

    %Label plot
    CompNameG = sprintf('%s Green',e);
    CompNameR = sprintf('%s Red',e);
    legend(CompNameG,CompNameR,'Control Green','Control Red')
    lh=findall(gcf,'tag','legend');
    set(lh,'location','northeastoutside');
    title(e)
    xlabel(Key(:,input1))
    ylabel(Key(:,input2))

    %Save plot
    Name = sprintf('%s (%s Vs %s).png',e,K1,K2);
    fName = sprintf('-f%d',j);
```

```
    print(fName,Name,'-dpng')
end
ContGreenOut = ContGreen(:,[input1,input2]);
ContRedOut = ContRed(:,[input1,input2]);
IDgrOut = IDgr(:,[input1,input2]);
IDreOut = IDre(:,[input1,input2]);
end
```

Appendix Figure 7.16: MatLab® multi-parameter analysis algorithm

Raw .lsm CLSM *z*-stacks were rendered and analysed using Imaris XT. Distance Transformation analysis generated .csv data files for a variety of measureable parameters. A 'multi-parameter analysis algorithm' was created and used to extract and plot invasion, sphericity, volume and elipticity (prolate and oblate) via MatLab®. The customised algorithm was developed in collaboration with Joseph Brook, who wrote the algorithm.

8.0 References

Abbud-Antaki, R.A., Marhefka, J.N., DeLuca, A.L., and Zuromskis, M.P. (2012). The Cancer BioChip System: a functional genomic assay for anchorage-independent three-dimensional breast cancer cell growth. Horm Cancer *3*, 261-270.

Acker, H., Carlsson, J., Mueller-Klieser, W., and Sutherland, R.M. (1987). Comparative pO2 measurements in cell spheroids cultured with different techniques. Br J Cancer *56*, 325-327.

Adachi, Y., Yamamoto, H., Itoh, F., Hinoda, Y., Okada, Y., and Imai, K. (1999). Contribution of matrilysin (MMP-7) to the metastatic pathway of human colorectal cancers. Gut *45*, 252-258.

Adzhubei, A.A., Sternberg, M.J., and Makarov, A.A. (2013). Polyproline-II helix in proteins: structure and function. J Mol Biol *425*, 2100-2132.

Agrawal, N., Dasaradhi, P.V., Mohmmed, A., Malhotra, P., Bhatnagar, R.K., and Mukherjee, S.K. (2003). RNA interference: biology, mechanism, and applications. Microbiol Mol Biol Rev *67*, 657-685.

Ahmed, E.M. (2015). Hydrogel: Preparation, characterization, and applications: A review. J Adv Res *6*, 105-121.

Al-Bahlani, S.M., Al-Rashdi, R.M., Kumar, S., Al-Sinawi, S.S., Al-Bahri, M.A., and Shalaby, A.A. (2017). Calpain-1 Expression in Triple-Negative Breast Cancer: A Potential Prognostic Factor Independent of the Proliferative/Apoptotic Index. Biomed Res Int *2017*, 9290425.

Alberts, B., Johnson, A., and Lewis, J. (2002). Molecular Biology of the Cell. 4th Edition - The Extracellular Matrix of Animals, 4th edn (Garlend Science).

Albini, A., and Benelli, R. (2007). The chemoinvasion assay: a method to assess tumor and endothelial cell invasion and its modulation. Nat Protoc *2*, 504-511.

Alexander, C.M., Howard, E.W., Bissell, M.J., and Werb, Z. (1996). Rescue of mammary epithelial cell apoptosis and entactin degradation by a tissue inhibitor of metalloproteinases-1 transgene. The Journal of cell biology *135*, 1669-1677.

Alexander, S., Koehl, G.E., Hirschberg, M., Geissler, E.K., and Friedl, P. (2008). Dynamic imaging of cancer growth and invasion: a modified skin-fold chamber model. Histochem Cell Biol *130*, 1147-1154.

Allen, M.D., Thomas, G.J., Clark, S., Dawoud, M.M., Vallath, S., Payne, S.J., Gomm, J.J., Dreger, S.A., Dickinson, S., Edwards, D.R.*, et al.* (2014). Altered microenvironment promotes progression of preinvasive breast cancer: myoepithelial expression of alphavbeta6 integrin in DCIS identifies high-risk patients and predicts recurrence. Clin Cancer Res *20*, 344-357.

Allocca, G., Kusumbe, A.P., Ramasamy, S.K., and Wang, N. (2016). Confocal/two-photon microscopy in studying colonisation of cancer cells in bone using xenograft mouse models. BoneKEy Rep *5*.

Alshamsan, A., Haddadi, A., Incani, V., Samuel, J., Lavasanifar, A., and Uludag, H. (2009). Formulation and delivery of siRNA by oleic acid and stearic acid modified polyethylenimine. Mol Pharm *6*, 121-133.

Amann, A., Zwierzina, M., Gamerith, G., Bitsche, M., Huber, J.M., Vogel, G.F., Blumer, M., Koeck, S., Pechriggl, E.J., Kelm, J.M.*, et al.* (2014). Development of an innovative 3D cell culture system to study tumour--stroma interactions in non-small cell lung cancer cells. PloS one *9*, e92511.

Andersen, T., Auk-Emblem, P., and Dornish, M. (2015). 3D Cell Culture in Alginate Hydrogels. Microarrays (Basel) *4*, 133-161.

Anlar, B., and Gunel-Ozcan, A. (2012). Tenascin-R: role in the central nervous system. Int J Biochem Cell Biol *44*, 1385-1389.

Artym, V.V., Zhang, Y., Seillier-Moiseiwitsch, F., Yamada, K.M., and Mueller, S.C. (2006). Dynamic interactions of cortactin and membrane type 1 matrix metalloproteinase at invadopodia: defining the stages of invadopodia formation and function. Cancer Res *66*, 3034-3043.

Ashworth, T. (1869). A case of cancer in which cells similar to those in the tumors were seen in the blood after death. Australian Medical Journal *14*, 146-149.

Astrof, S., Crowley, D., and Hynes, R.O. (2007). Multiple cardiovascular defects caused by the absence of alternatively spliced segments of fibronectin. Dev Biol *311*, 11-24.

Aumailley, M., Bruckner-Tuderman, L., Carter, W.G., Deutzmann, R., Edgar, D., Ekblom, P., Engel, J., Engvall, E., Hohenester, E., Jones, J.C.*, et al.* (2005). A simplified laminin nomenclature. Matrix biology : journal of the International Society for Matrix Biology *24*, 326-332.

Baker, B.M., and Chen, C.S. (2012). Deconstructing the third dimension: how 3D culture microenvironments alter cellular cues. J Cell Sci *125*, 3015-3024.

Baraniak, P.R., and McDevitt, T.C. (2012). Scaffold-free culture of mesenchymal stem cell spheroids in suspension preserves multilineage potential. Cell Tissue Res *347*, 701-711.

Barbero, S., Mielgo, A., Torres, V., Teitz, T., Shields, D.J., Mikolon, D., Bogyo, M., Barila, D., Lahti, J.M., Schlaepfer, D.*, et al.* (2009). Caspase-8 association with the focal adhesion complex promotes tumor cell migration and metastasis. Cancer Res *69*, 3755-3763.

Barczyk, M., Carracedo, S., and Gullberg, D. (2010). Integrins. Cell Tissue Res *339*, 269-280.

Barsky, S.H., Rao, C.N., Grotendorst, G.R., and Liotta, L.A. (1982). Increased content of Type V Collagen in desmoplasia of human breast carcinoma. Am J Pathol *108*, 276-283.

Basset, P., Bellocq, J.P., Wolf, C., Stoll, I., Hutin, P., Limacher, J.M., Podhajcer, O.L., Chenard, M.P., Rio, M.C., and Chambon, P. (1990). A novel metalloproteinase gene specifically expressed in stromal cells of breast carcinomas. Nature *348*, 699-704.

Bauer, J.A., Ye, F., Marshall, C.B., Lehmann, B.D., Pendleton, C.S., Shyr, Y., Arteaga, C.L., and Pietenpol, J.A. (2010). RNA interference (RNAi) screening approach identifies agents that enhance paclitaxel activity in breast cancer cells. Breast Cancer Res *12*, R41.

Baum, J., and Duffy, H.S. (2011). Fibroblasts and myofibroblasts: what are we talking about? J Cardiovasc Pharmacol *57*, 376-379.

Bell, E., Ehrlich, H.P., Buttle, D.J., and Nakatsuji, T. (1981). Living tissue formed in vitro and accepted as skin-equivalent tissue of full thickness. Science *211*, 1052-1054.

Bell, E., Ivarsson, B., and Merrill, C. (1979). Production of a tissue-like structure by contraction of collagen lattices by human fibroblasts of different proliferative potential in vitro. Proc Natl Acad Sci U S A *76*, 1274-1278.

Bell, E.M., C; Solomon, D (1979). characteristics of a tissue equivalent formed by fibroblasts cast in a collagen gel. Journal of Cell Biology *83*.

Benam, K.H., Villenave, R., Lucchesi, C., Varone, A., Hubeau, C., Lee, H.H., Alves, S.E., Salmon, M., Ferrante, T.C., Weaver, J.C.*, et al.* (2016). Small airway-on-a-chip enables analysis of human lung inflammation and drug responses in vitro. Nat Methods *13*, 151-157.

Bernerd, F., and Asselineau, D. (2008). An organotypic model of skin to study photodamage and photoprotection in vitro. J Am Acad Dermatol *58*, S155-159.

Bertoli, C., Copetti, T., Lam, E.W., Demarchi, F., and Schneider, C. (2009). Calpain small-1 modulates Akt/FoxO3A signaling and apoptosis through PP2A. Oncogene *28*, 721-733.

Bhadriraju, K., and Chen, C.S. (2002). Engineering cellular microenvironments to improve cell-based drug testing. Drug Discov Today *7*, 612-620.

Bhise, N.S., Ribas, J., Manoharan, V., Zhang, Y.S., Polini, A., Massa, S., Dokmeci, M.R., and Khademhosseini, A. (2014). Organ-on-a-chip platforms for studying drug delivery systems. J Control Release *190*, 82-93.

Bialkowska, A.B., and Yang, V.W. (2012). High-throughput screening strategies for targeted identification of therapeutic compounds in colorectal cancer. Future Oncol *8*, 259-272.

Bissell, M.J., and Hines, W.C. (2011). Why don't we get more cancer? A proposed role of the microenvironment in restraining cancer progression. Nat Med *17*, 320-329.

Bissell, M.J., Rizki, A., and Mian, I.S. (2003). Tissue architecture: the ultimate regulator of breast epithelial function. Curr Opin Cell Biol *15*, 753-762.

Bledzka, K., Liu, J., Xu, Z., Perera, H.D., Yadav, S.P., Bialkowska, K., Qin, J., Ma, Y.Q., and Plow, E.F. (2012). Spatial coordination of kindlin-2 with talin head domain in interaction with integrin beta cytoplasmic tails. The Journal of biological chemistry *287*, 24585-24594.

Bohn, K.A., Adkins, C.E., Nounou, M.I., and Lockman, P.R. (2017). Inhibition of VEGF and Angiopoietin-2 to Reduce Brain Metastases of Breast Cancer Burden. Front Pharmacol *8*, 193.

Boolell, M., Allen, M.J., Ballard, S.A., Gepi-Attee, S., Muirhead, G.J., Naylor, A.M., Osterloh, I.H., and Gingell, C. (1996). Sildenafil: an orally active type 5 cyclic GMP-specific phosphodiesterase inhibitor for the treatment of penile erectile dysfunction. Int J Impot Res *8*, 47-52.

Bosse, Y., Postma, D.S., Sin, D.D., Lamontagne, M., Couture, C., Gaudreault, N., Joubert, P., Wong, V., Elliott, M., van den Berge, M.*, et al.* (2012). Molecular signature of smoking in human lung tissues. Cancer Res *72*, 3753-3763.

Boukamp, P., Tilgen, W., Dzarlieva, R.T., Breitkreutz, D., Haag, D., Riehl, R.K., Bohnert, A., and Fusenig, N.E. (1982). Phenotypic and genotypic characteristics of a cell line from a squamous cell carcinoma of human skin. J Natl Cancer Inst *68*, 415-427.

Bourdon, M.A., Wikstrand, C.J., Furthmayr, H., Matthews, T.J., and Bigner, D.D. (1983). Human glioma-mesenchymal extracellular matrix antigen defined by monoclonal antibody. Cancer Res *43*, 2796-2805.

Boyden, S. (1962). The chemotactic effect of mixtures of antibody and antigen on polymorphonuclear leucocytes. J Exp Med *115*, 453-466.

Brabletz, T., Jung, A., Reu, S., Porzner, M., Hlubek, F., Kunz-Schughart, L.A., Knuechel, R., and Kirchner, T. (2001). Variable beta-catenin expression in colorectal cancers indicates tumor progression driven by the tumor environment. Proc Natl Acad Sci U S A *98*, 10356-10361.

Brandenburger, M., Wenzel, J., Bogdan, R., Richardt, D., Nguemo, F., Reppel, M., Hescheler, J., Terlau, H., and Dendorfer, A. (2012). Organotypic slice culture from human adult ventricular myocardium. Cardiovasc Res *93*, 50-59.

Brandish, P.E., Chiu, C.S., Schneeweis, J., Brandon, N.J., Leech, C.L., Kornienko, O., Scolnick, E.M., Strulovici, B., and Zheng, W. (2006). A cell-based ultra-high-throughput screening assay for identifying inhibitors of D-amino acid oxidase. J Biomol Screen *11*, 481-487.

Bray, F., and Soerjomataram, I. (2015). The Changing Global Burden of Cancer: Transitions in Human Development and Implications for Cancer Prevention and Control. In Cancer: Disease Control Priorities, Third Edition (Volume 3), H. Gelband, P. Jha, R. Sankaranarayanan, and S. Horton, eds. (Washington (DC)).

Breslin, S., and O'Driscoll, L. (2013). Three-dimensional cell culture: the missing link in drug discovery. Drug Discov Today *18*, 240-249.

Brew, K., and Nagase, H. (2010). The tissue inhibitors of metalloproteinases (TIMPs): an ancient family with structural and functional diversity. Biochim Biophys Acta *1803*, 55-71.

Brock, A., Chang, E., Ho, C.C., LeDuc, P., Jiang, X., Whitesides, G.M., and Ingber, D.E. (2003). Geometric determinants of directional cell motility revealed using microcontact printing. Langmuir *19*, 1611-1617.

Bryant, S.J., and Anseth, K.S. (2002). Hydrogel properties influence ECM production by chondrocytes photoencapsulated in poly(ethylene glycol) hydrogels. J Biomed Mater Res *59*, 63-72.

Buchser, W., Collins, M., Garyantes, T., Guha, R., Haney, S., Lemmon, V., Li, Z., and Trask, O.J. (2004). Assay Development Guidelines for Image-Based High Content Screening, High Content Analysis and High Content Imaging. In Assay Guidance Manual, G.S. Sittampalam, N.P. Coussens, K. Brimacombe, A. Grossman, M. Arkin, D. Auld, C. Austin, J. Baell, B. Bejcek, T.D.Y. Chung*, et al.*, eds. (Bethesda (MD)).

Buffery, D. (2015). The 2015 Oncology Drug Pipeline: Innovation Drives the Race to Cure Cancer. Am Health Drug Benefits *8*, 216-222.

Burke, J.F., Yannas, I.V., Quinby, W.C., Jr., Bondoc, C.C., and Jung, W.K. (1981). Successful use of a physiologically acceptable artificial skin in the treatment of extensive burn injury. Ann Surg *194*, 413-428.

Butler, G.S., Dean, R.A., Smith, D., and Overall, C.M. (2009). Membrane protease degradomics: proteomic identification and quantification of cell surface protease substrates. Methods in molecular biology *528*, 159-176.

Caicedo-Carvajal, C.E., Liu, Q., Remache, Y., Goy, A., and Suh, K.S. (2011). Cancer Tissue Engineering: A Novel 3D Polystyrene Scaffold for In Vitro Isolation and Amplification of Lymphoma Cancer Cells from Heterogeneous Cell Mixtures. J Tissue Eng *2011*, 362326.

Cailleau, R., Olive, M., and Cruciger, Q.V. (1978). Long-term human breast carcinoma cell lines of metastatic origin: preliminary characterization. In Vitro *14*, 911-915.

Cairns, D.M., Chwalek, K., Moore, Y.E., Kelley, M.R., Abbott, R.D., Moss, S., and Kaplan, D.L. (2016). Expandable and Rapidly Differentiating Human Induced Neural Stem Cell Lines for Multiple Tissue Engineering Applications. Stem Cell Reports *7*, 557-570.

Cairns, J. (1975). Mutation selection and the natural history of cancer. Nature *255*, 197-200.

Camenisch, T.D., Schroeder, J.A., Bradley, J., Klewer, S.E., and McDonald, J.A. (2002). Heart-valve mesenchyme formation is dependent on hyaluronan-augmented activation of ErbB2-ErbB3 receptors. Nat Med *8*, 850-855.

Carapuca, E.F., Gemenetzidis, E., Feig, C., Bapiro, T.E., Williams, M.D., Wilson, A.S., Delvecchio, F.R., Arumugam, P., Grose, R.P., Lemoine, N.R.*, et al.* (2016). Anti-stromal treatment together with chemotherapy targets multiple signalling pathways in pancreatic adenocarcinoma. The Journal of pathology *239*, 286-296.

Carlson, M.W., Alt-Holland, A., Egles, C., and Garlick, J.A. (2008). Three-dimensional tissue models of normal and diseased skin. Curr Protoc Cell Biol *Chapter 19*, Unit 19 19.

Carlsson, J., and Acker, H. (1988). Relations between pH, oxygen partial pressure and growth in cultured cell spheroids. Int J Cancer *42*, 715-720.

Carpenter, P.M., Dao, A.V., Arain, Z.S., Chang, M.K., Nguyen, H.P., Arain, S., Wang-Rodriguez, J., Kwon, S.Y., and Wilczynski, S.P. (2009). Motility induction in breast carcinoma by mammary epithelial laminin 332 (laminin 5). Mol Cancer Res *7*, 462-475.

Caswell, P.T., Chan, M., Lindsay, A.J., McCaffrey, M.W., Boettiger, D., and Norman, J.C. (2008). Rab-coupling protein coordinates recycling of alpha5beta1 integrin and EGFR1 to promote cell migration in 3D microenvironments. The Journal of cell biology *183*, 143-155.

Caswell, P.T., Spence, H.J., Parsons, M., White, D.P., Clark, K., Cheng, K.W., Mills, G.B., Humphries, M.J., Messent, A.J., Anderson, K.I.*, et al.* (2007). Rab25 associates with alpha5beta1 integrin to promote invasive migration in 3D microenvironments. Dev Cell *13*, 496-510.

Cavallaro, U., and Christofori, G. (2004). Multitasking in tumor progression: signaling functions of cell adhesion molecules. Ann N Y Acad Sci *1014*, 58-66.

Chabottaux, V., Sounni, N.E., Pennington, C.J., English, W.R., van den Brule, F., Blacher, S., Gilles, C., Munaut, C., Maquoi, E., Lopez-Otin, C.*, et al.* (2006). Membrane-type 4 matrix metalloproteinase promotes breast cancer growth and metastases. Cancer Res *66*, 5165-5172.

Chambers, A.F., Groom, A.C., and MacDonald, I.C. (2002). Dissemination and growth of cancer cells in metastatic sites. Nat Rev Cancer *2*, 563-572.

Chang, H.Y., Nuyten, D.S., Sneddon, J.B., Hastie, T., Tibshirani, R., Sorlie, T., Dai, H., He, Y.D., van't Veer, L.J., Bartelink, H.*, et al.* (2005). Robustness, scalability, and integration of a wound-response gene expression signature in predicting breast cancer survival. Proc Natl Acad Sci U S A *102*, 3738-3743.

Chen, B., Kumar, G., Co, C.C., and Ho, C.C. (2013). Geometric control of cell migration. Sci Rep *3*, 2827.

Chen, C.S., Mrksich, M., Huang, S., Whitesides, G.M., and Ingber, D.E. (1997). Geometric control of cell life and death. Science *276*, 1425-1428.

Chen, Y.C., and Yoon, E. (2017). High-Throughput Cancer Cell Sphere Formation for 3D Cell Culture. Methods in molecular biology *1612*, 281-291.

Cheng, M.F., Tzao, C., Tsai, W.C., Lee, W.H., Chen, A., Chiang, H., Sheu, L.F., and Jin, J.S. (2006). Expression of EMMPRIN and matriptase in esophageal squamous cell carcinoma: correlation with clinicopathological parameters. Dis Esophagus *19*, 482-486.

Chia, N.Y., Chan, Y.S., Feng, B., Lu, X., Orlov, Y.L., Moreau, D., Kumar, P., Yang, L., Jiang, J., Lau, M.S.*, et al.* (2010). A genome-wide RNAi screen reveals determinants of human embryonic stem cell identity. Nature *468*, 316-320.

Chiquet-Ehrismann, R. (1995). Tenascins, a growing family of extracellular matrix proteins. Experientia *51*, 853-862.

Chiquet-Ehrismann, R., and Tucker, R.P. (2004). Connective tissues: signalling by tenascins. Int J Biochem Cell Biol *36*, 1085-1089.

Chitcholtan, K., Sykes, P.H., and Evans, J.J. (2012). The resistance of intracellular mediators to doxorubicin and cisplatin are distinct in 3D and 2D endometrial cancer. J Transl Med *10*, 38.

Choy, A., and McCulloch, P.G. (1993). Detection and enumeration of circulating tumour cells in colorectal cancer. Br J Surg *80*, 1490.

Chung, N., Locco, L., Huff, K.W., Bartz, S., Linsley, P.S., Ferrer, M., and Strulovici, B. (2008). An efficient and fully automated high-throughput transfection method for genome-scale siRNA screens. J Biomol Screen *13*, 142-148.

Chung, N., Marine, S., Smith, E.A., Liehr, R., Smith, S.T., Locco, L., Hudak, E., Kreamer, A., Rush, A., Roberts, B.*, et al.* (2010). A 1,536-well ultra-high-throughput siRNA screen to identify regulators of the Wnt/beta-catenin pathway. Assay Drug Dev Technol *8*, 286-294.

Clark, A.G., and Vignjevic, D.M. (2015). Modes of cancer cell invasion and the role of the microenvironment. Curr Opin Cell Biol *36*, 13-22.

Coleman, S.J., Chioni, A.M., Ghallab, M., Anderson, R.K., Lemoine, N.R., Kocher, H.M., and Grose, R.P. (2014a). Nuclear translocation of FGFR1 and FGF2 in pancreatic stellate cells facilitates pancreatic cancer cell invasion. EMBO Mol Med *6*, 467-481.

Coleman, S.J., Watt, J., Arumugam, P., Solaini, L., Carapuca, E., Ghallab, M., Grose, R.P., and Kocher, H.M. (2014b). Pancreatic cancer organotypics: High throughput, preclinical models for pharmacological agent evaluation. World J Gastroenterol *20*, 8471-8481.

Condeelis, J., and Segall, J.E. (2003). Intravital imaging of cell movement in tumours. Nat Rev Cancer *3*, 921-930.

Corning (2016). Corning Matrigel Matrix.

Correia, A.L., and Bissell, M.J. (2012). The tumor microenvironment is a dominant force in multidrug resistance. Drug Resist Updat *15*, 39-49.

Cristofanilli, M., Budd, G.T., Ellis, M.J., Stopeck, A., Matera, J., Miller, M.C., Reuben, J.M., Doyle, G.V., Allard, W.J., Terstappen, L.W.*, et al.* (2004). Circulating tumor cells, disease progression, and survival in metastatic breast cancer. N Engl J Med *351*, 781-791.

Croft, D.R., Sahai, E., Mavria, G., Li, S., Tsai, J., Lee, W.M., Marshall, C.J., and Olson, M.F. (2004). Conditional ROCK activation in vivo induces tumor cell dissemination and angiogenesis. Cancer Res *64*, 8994-9001.

Cukierman, E., Pankov, R., Stevens, D.R., and Yamada, K.M. (2001). Taking cell-matrix adhesions to the third dimension. Science *294*, 1708-1712.

Cukierman, E., Pankov, R., and Yamada, K.M. (2002). Cell interactions with three-dimensional matrices. Curr Opin Cell Biol *14*, 633-639.

Czauderna, F., Fechtner, M., Dames, S., Aygun, H., Klippel, A., Pronk, G.J., Giese, K., and Kaufmann, J. (2003). Structural variations and stabilising modifications of synthetic siRNAs in mammalian cells. Nucleic Acids Res *31*, 2705-2716.

Darby, I.A., Laverdet, B., Bonte, F., and Desmouliere, A. (2014). Fibroblasts and myofibroblasts in wound healing. Clin Cosmet Investig Dermatol *7*, 301-311.

David, L., Dulong, V., Le Cerf, D., Cazin, L., Lamacz, M., and Vannier, J.P. (2008). Hyaluronan hydrogel: an appropriate three-dimensional model for evaluation of anticancer drug sensitivity. Acta Biomater *4*, 256-263.

Davidson, L.A., and Keller, R.E. (1999). Neural tube closure in Xenopus laevis involves medial migration, directed protrusive activity, cell intercalation and convergent extension. Development *126*, 4547-4556.

Dawson, D.W., Volpert, O.V., Gillis, P., Crawford, S.E., Xu, H., Benedict, W., and Bouck, N.P. (1999). Pigment epithelium-derived factor: a potent inhibitor of angiogenesis. Science *285*, 245-248.

De Wever, O., Nguyen, Q.D., Van Hoorde, L., Bracke, M., Bruyneel, E., Gespach, C., and Mareel, M. (2004). Tenascin-C and SF/HGF produced by myofibroblasts in vitro provide convergent pro-invasive signals to human colon cancer cells through RhoA and Rac. FASEB J *18*, 1016-1018.

Dean, D.D., Martel-Pelletier, J., Pelletier, J.P., Howell, D.S., and Woessner, J.F., Jr. (1989). Evidence for metalloproteinase and metalloproteinase inhibitor imbalance in human osteoarthritic cartilage. J Clin Invest *84*, 678-685.

Degen, M., Brellier, F., Kain, R., Ruiz, C., Terracciano, L., Orend, G., and Chiquet-Ehrismann, R. (2007). Tenascin-W is a novel marker for activated tumor stroma in low-grade human breast cancer and influences cell behavior. Cancer Res *67*, 9169-9179.

Degen, M., Brellier, F., Schenk, S., Driscoll, R., Zaman, K., Stupp, R., Tornillo, L., Terracciano, L., Chiquet-Ehrismann, R., Ruegg, C*., et al.* (2008). Tenascin-W, a new marker of cancer stroma, is elevated in sera of colon and breast cancer patients. Int J Cancer *122*, 2454-2461.

Denis Semwogerere, E.R.W. (2005). Confocal Microscopy (Taylor & Francis).

DeVolder, R., and Kong, H.J. (2012). Hydrogels for in vivo-like three-dimensional cellular studies. Wiley Interdiscip Rev Syst Biol Med *4*, 351-365.

Di, Z., Klop, M.J., Rogkoti, V.M., Le Devedec, S.E., van de Water, B., Verbeek, F.J., Price, L.S., and Meerman, J.H. (2014). Ultra high content image analysis and phenotype profiling of 3D cultured micro-tissues. PloS one *9*, e109688.

Doggett, D.L., Rotenberg, M.O., Pignolo, R.J., Phillips, P.D., and Cristofalo, V.J. (1992). Differential gene expression between young and senescent, quiescent WI-38 cells. Mech Ageing Dev *65*, 239-255.

Downer, C.S., Watt, F.M., and Speight, P.M. (1993). Loss of alpha 6 and beta 4 integrin subunits coincides with loss of basement membrane components in oral squamous cell carcinomas. The Journal of pathology *171*, 183-190.

Dragu, D.L., Necula, L.G., Bleotu, C., Diaconu, C.C., and Chivu-Economescu, M. (2015). Therapies targeting cancer stem cells: Current trends and future challenges. World J Stem Cells *7*, 1185-1201.

Dreher, F., Patouillet, C., Fouchard, F., Zanini, M., Messager, A., Roguet, R., Cottin, M., Leclaire, J., and Benech-Kieffer, F. (2002). Improvement of the experimental setup to assess cutaneous bioavailability on human skin models: dynamic protocol. Skin Pharmacol Appl Skin Physiol *15 Suppl 1*, 31-39.

Dull, T., Zufferey, R., Kelly, M., Mandel, R.J., Nguyen, M., Trono, D., and Naldini, L. (1998). A third-generation lentivirus vector with a conditional packaging system. J Virol *72*, 8463-8471.

Dvorak, H.F. (1986). Tumors: wounds that do not heal. Similarities between tumor stroma generation and wound healing. N Engl J Med *315*, 1650-1659.

Dvorak, H.F. (2015). Tumors: wounds that do not heal-redux. Cancer Immunol Res *3*, 1-11.

Dvorak, H.F., Dvorak, A.M., Manseau, E.J., Wiberg, L., and Churchill, W.H. (1979). Fibrin gel investment associated with line 1 and line 10 solid tumor growth, angiogenesis, and fibroplasia in guinea pigs. Role of cellular immunity, myofibroblasts, microvascular damage, and infarction in line 1 tumor regression. J Natl Cancer Inst *62*, 1459-1472.

Edmondson, R., Broglie, J.J., Adcock, A.F., and Yang, L. (2014). Three-dimensional cell culture systems and their applications in drug discovery and cell-based biosensors. Assay Drug Dev Technol *12*, 207-218.

Egeblad, M., Littlepage, L.E., and Werb, Z. (2005). The fibroblastic coconspirator in cancer progression. Cold Spring Harb Symp Quant Biol *70*, 383-388.

Egeblad, M., and Werb, Z. (2002). New functions for the matrix metalloproteinases in cancer progression. Nat Rev Cancer *2*, 161-174.

Ehrbar, M., Sala, A., Lienemann, P., Ranga, A., Mosiewicz, K., Bittermann, A., Rizzi, S.C., Weber, F.E., and Lutolf, M.P. (2011). Elucidating the role of matrix stiffness in 3D cell migration and remodeling. Biophys J *100*, 284-293.

Ehrlich, H.P., and Hunt, T.K. (2012). Collagen Organization Critical Role in Wound Contraction. Adv Wound Care (New Rochelle) *1*, 3-9.

Elbashir, S.M., Lendeckel, W., and Tuschl, T. (2001). RNA interference is mediated by 21- and 22-nucleotide RNAs. Genes Dev *15*, 188-200.

Erickson, H.P. (1993). Tenascin-C, tenascin-R and tenascin-X: a family of talented proteins in search of functions. Curr Opin Cell Biol *5*, 869-876.

Eves, P., Layton, C., Hedley, S., Dawson, R.A., Wagner, M., Morandini, R., Ghanem, G., and Mac Neil, S. (2000). Characterization of an in vitro model of human melanoma invasion based on reconstructed human skin. Br J Dermatol *142*, 210-222.

Ewing, J. (1928). Neoplastic Diseases: A Treatise on Tumours. Third edition. Royal 8vo. Pp. 1127, with 546 illustrations. 1928. Philadelphia and London: W. B. Saunders Co. Ltd. 63s. net. British Journal of Surgery *16*, 174-175.

Falkenberg, K.J., Gould, C.M., Johnstone, R.W., and Simpson, K.J. (2014). Genome-wide functional genomic and transcriptomic analyses for genes regulating sensitivity to vorinostat. Sci Data *1*, 140017.

Fayard, B., Bianchi, F., Dey, J., Moreno, E., Djaffer, S., Hynes, N.E., and Monard, D. (2009). The serine protease inhibitor protease nexin-1 controls mammary cancer metastasis through LRP-1-mediated MMP-9 expression. Cancer Res *69*, 5690-5698.

Fendrich, V., Oh, E., Bang, S., Karikari, C., Ottenhof, N., Bisht, S., Lauth, M., Brossart, P., Katsanis, N., Maitra, A.*, et al.* (2011). Ectopic overexpression of Sonic Hedgehog (Shh) induces stromal expansion and metaplasia in the adult murine pancreas. Neoplasia *13*, 923-930.

Fidler, I.J. (2003). The pathogenesis of cancer metastasis: the 'seed and soil' hypothesis revisited. Nat Rev Cancer *3*, 453-458.

Fidler, I.J., and Kripke, M.L. (2015). The challenge of targeting metastasis. Cancer Metastasis Rev *34*, 635-641.

Fire, A., Xu, S., Montgomery, M.K., Kostas, S.A., Driver, S.E., and Mello, C.C. (1998). Potent and specific genetic interference by double-stranded RNA in Caenorhabditis elegans. Nature *391*, 806-811.

Fitzgerald, D.P., Subramanian, P., Deshpande, M., Graves, C., Gordon, I., Qian, Y., Snitkovsky, Y., Liewehr, D.J., Steinberg, S.M., Paltan-Ortiz, J.D.*, et al.* (2012). Opposing effects of pigment epithelium-derived factor on breast cancer cell versus neuronal survival: implication for brain metastasis and metastasis-induced brain damage. Cancer Res *72*, 144-153.

Fleming, A. (1929). On the antibacterial action of cultures of a penicillium, with special reference to their use in the isolation of B. influenzae. The British Journal of Experimental Pathology *10*, 226-236.

Fong, E.L., Santoro, M., Farach-Carson, M.C., Kasper, F.K., and Mikos, A.G. (2014). Tissue Engineering Perfusable Cancer Models. Curr Opin Chem Eng *3*, 112-117.

Fong, P.Y., Fesinmeyer, M.D., White, E., Farin, F.M., Srinouanprachanh, S., Afsharinejad, Z., Mandelson, M.T., Brentnall, T.A., Barnett, M.J., Goodman, G.E.*, et al.* (2010). Association of diabetes susceptibility gene calpain-10 with pancreatic cancer among smokers. J Gastrointest Cancer *41*, 203-208.

Foty, R. (2011). A simple hanging drop cell culture protocol for generation of 3D spheroids. J Vis Exp.

Foulds, L. (1954). The experimental study of tumor progression: a review. Cancer Res *14*, 327-339.

Frantz, C., Stewart, K.M., and Weaver, V.M. (2010). The extracellular matrix at a glance. J Cell Sci *123*, 4195-4200.

Frazier, K.S., and Grotendorst, G.R. (1997). Expression of connective tissue growth factor mRNA in the fibrous stroma of mammary tumors. Int J Biochem Cell Biol *29*, 153-161.

Friberg, S., and Nystrom, A. (2015). Cancer Metastases: Early Dissemination and Late Recurrences. Cancer Growth Metastasis *8*, 43-49.

Friedl, P. (2004). Prespecification and plasticity: shifting mechanisms of cell migration. Curr Opin Cell Biol *16*, 14-23.

Friedl, P., Hegerfeldt, Y., and Tusch, M. (2004). Collective cell migration in morphogenesis and cancer. Int J Dev Biol *48*, 441-449.

Friedl, P., and Wolf, K. (2003). Tumour-cell invasion and migration: diversity and escape mechanisms. Nat Rev Cancer *3*, 362-374.

Friedland, J.C., Lee, M.H., and Boettiger, D. (2009). Mechanically activated integrin switch controls alpha5beta1 function. Science *323*, 642-644.

Froeling, F.E., Feig, C., Chelala, C., Dobson, R., Mein, C.E., Tuveson, D.A., Clevers, H., Hart, I.R., and Kocher, H.M. (2011). Retinoic acid-induced pancreatic stellate cell quiescence reduces paracrine Wnt-beta-catenin signaling to slow tumor progression. Gastroenterology *141*, 1486-1497, 1497 e1481-1414.

Froeling, F.E., Marshall, J.F., and Kocher, H.M. (2010). Pancreatic cancer organotypic cultures. Journal of biotechnology *148*, 16-23.

Froeling, F.E., Mirza, T.A., Feakins, R.M., Seedhar, A., Elia, G., Hart, I.R., and Kocher, H.M. (2009). Organotypic culture model of pancreatic cancer demonstrates that stromal cells modulate E-cadherin, beta-catenin, and Ezrin expression in tumor cells. Am J Pathol *175*, 636-648.

Fusenig, N.E. (1971). Isolation and cultivation of epidermal cells from embryonic mouse skin. Naturwissenschaften *58*, 421.

Fusenig, N.E., Breitkreutz, D., Dzarlieva, R.T., Boukamp, P., Bohnert, A., and Tilgen, W. (1983). Growth and differentiation characteristics of transformed keratinocytes from mouse and human skin in vitro and in vivo. J Invest Dermatol *81*, 168s-175s.

Gabbiani, G., Ryan, G.B., and Majne, G. (1971). Presence of modified fibroblasts in granulation tissue and their possible role in wound contraction. Experientia *27*, 549-550.

Gaggioli, C., Hooper, S., Hidalgo-Carcedo, C., Grosse, R., Marshall, J.F., Harrington, K., and Sahai, E. (2007). Fibroblast-led collective invasion of carcinoma cells with differing roles for RhoGTPases in leading and following cells. Nat Cell Biol *9*, 1392-1400.

Gahwiler, B.H. (1981a). Morphological differentiation of nerve cells in thin organotypic cultures derived from rat hippocampus and cerebellum. Proc R Soc Lond B Biol Sci *211*, 287-290.

Gahwiler, B.H. (1981b). Organotypic monolayer cultures of nervous tissue. J Neurosci Methods *4*, 329-342.

Gahwiler, B.H. (1988). Organotypic cultures of neural tissue. Trends Neurosci *11*, 484-489.

Gandhi, N.S., and Mancera, R.L. (2008). The structure of glycosaminoglycans and their interactions with proteins. Chem Biol Drug Des *72*, 455-482.

Gelman, R.A., Williams, B.R., and Piez, K.A. (1979). Collagen fibril formation. Evidence for a multistep process. The Journal of biological chemistry *254*, 180-186.

Gelse, K., Poschl, E., and Aigner, T. (2003). Collagens--structure, function, and biosynthesis. Adv Drug Deliv Rev *55*, 1531-1546.

Geuijen, C.A., and Sonnenberg, A. (2002). Dynamics of the alpha6beta4 integrin in keratinocytes. Mol Biol Cell *13*, 3845-3858.

Ghajar, C.M., and Bissell, M.J. (2010). Tumor engineering: the other face of tissue engineering. Tissue Eng Part A *16*, 2153-2156.

Giampieri, S., Manning, C., Hooper, S., Jones, L., Hill, C.S., and Sahai, E. (2009). Localized and reversible TGFbeta signalling switches breast cancer cells from cohesive to single cell motility. Nat Cell Biol *11*, 1287-1296.

Gligorijevic, B., Wyckoff, J., Yamaguchi, H., Wang, Y., Roussos, E.T., and Condeelis, J. (2012). N-WASP-mediated invadopodium formation is involved in intravasation and lung metastasis of mammary tumors. J Cell Sci *125*, 724-734.

Gordon, M.K., and Hahn, R.A. (2010). Collagens. Cell Tissue Res *339*, 247-257.

Griffiths, M., Ojeh, N., Livingstone, R., Price, R., and Navsaria, H. (2004). Survival of Apligraf in acute human wounds. Tissue Eng *10*, 1180-1195.

Grozinger, K., Proudfoot, J., and Hargrave, K. (2006). Discovery and Development of Nevirapine. In Drug Discovery and Development (John Wiley & Sons, Inc.), pp. 353-363.

Gudjonsson, T., Ronnov-Jessen, L., Villadsen, R., Rank, F., Bissell, M.J., and Petersen, O.W. (2002). Normal and tumor-derived myoepithelial cells differ in their ability to interact with luminal breast epithelial cells for polarity and basement membrane deposition. J Cell Sci *115*, 39-50.

Guipponi, M., Toh, M.Y., Tan, J., Park, D., Hanson, K., Ballana, E., Kwong, D., Cannon, P.Z., Wu, Q., Gout, A.*, et al.* (2008). An integrated genetic and functional analysis of the role of type II transmembrane serine proteases (TMPRSSs) in hearing loss. Hum Mutat *29*, 130-141.

Han, W., Chen, S., Yuan, W., Fan, Q., Tian, J., Wang, X., Chen, L., Zhang, X., Wei, W., Liu, R.*, et al.* (2016). Oriented collagen fibers direct tumor cell intravasation. Proc Natl Acad Sci U S A *113*, 11208-11213.

Hanahan, D., and Coussens, L.M. (2012). Accessories to the crime: functions of cells recruited to the tumor microenvironment. Cancer Cell *21*, 309-322.

Hanley, C.J., Noble, F., Ward, M., Bullock, M., Drifka, C., Mellone, M., Manousopoulou, A., Johnston, H.E., Hayden, A., Thirdborough, S.*, et al.* (2016). A subset of myofibroblastic cancer-associated fibroblasts regulate collagen fiber elongation, which is prognostic in multiple cancers. Oncotarget *7*, 6159-6174.

Hannon, G.J., and Rossi, J.J. (2004). Unlocking the potential of the human genome with RNA interference. Nature *431*, 371-378.

Harada, K., Toyooka, S., Shivapurkar, N., Maitra, A., Reddy, J.L., Matta, H., Miyajima, K., Timmons, C.F., Tomlinson, G.E., Mastrangelo, D.*, et al.* (2002). Deregulation of caspase 8 and 10 expression in pediatric tumors and cell lines. Cancer Res *62*, 5897-5901.

Harburger, D.S., Bouaouina, M., and Calderwood, D.A. (2009). Kindlin-1 and -2 directly bind the C-terminal region of beta integrin cytoplasmic tails and exert integrin-specific activation effects. The Journal of biological chemistry *284*, 11485-11497.

Harma, V., Virtanen, J., Makela, R., Happonen, A., Mpindi, J.P., Knuuttila, M., Kohonen, P., Lotjonen, J., Kallioniemi, O., and Nees, M. (2010). A comprehensive panel of three-dimensional models for studies of prostate cancer growth, invasion and drug responses. PloS one *5*, e10431.

Hart, I.R. (1982). 'Seed and soil' revisited: mechanisms of site-specific metastasis. Cancer Metastasis Rev *1*, 5-16.

Hart, I.R., and Fidler, I.J. (1980a). Cancer invasion and metastasis. Q Rev Biol *55*, 121-142.

Hart, I.R., and Fidler, I.J. (1980b). Role of organ selectivity in the determination of metastatic patterns of B16 melanoma. Cancer Res *40*, 2281-2287.

Hartikainen, J.M., Tuhkanen, H., Kataja, V., Eskelinen, M., Uusitupa, M., Kosma, V.M., and Mannermaa, A. (2006). Refinement of the 22q12-q13 breast cancer--associated region: evidence of TMPRSS6 as a candidate gene in an eastern Finnish population. Clin Cancer Res *12*, 1454-1462.

Hashimoto, T., Kato, M., Shimomura, T., and Kitamura, N. (2010). TMPRSS13, a type II transmembrane serine protease, is inhibited by hepatocyte growth factor activator inhibitor type 1 and activates pro-hepatocyte growth factor. FEBS J *277*, 4888-4900.

Hauw, J.J., Berger, B., and Escourolle, R. (1972). [Presence of synapses in organotypic culture in vitro of human cerebellum]. C R Acad Sci Hebd Seances Acad Sci D *274*, 264-266.

Haycock, J.W. (2011). 3D cell culture: a review of current approaches and techniques. Methods in molecular biology *695*, 1-15.

Hegerfeldt, Y., Tusch, M., Brocker, E.B., and Friedl, P. (2002). Collective cell movement in primary melanoma explants: plasticity of cell-cell interaction, beta1-integrin function, and migration strategies. Cancer Res *62*, 2125-2130.

Helbling-Leclerc, A., Zhang, X., Topaloglu, H., Cruaud, C., Tesson, F., Weissenbach, J., Tome, F.M., Schwartz, K., Fardeau, M., Tryggvason, K.*, et al.* (1995). Mutations in the laminin alpha 2-chain gene (LAMA2) cause merosin-deficient congenital muscular dystrophy. Nat Genet *11*, 216-218.

Herold-Mende, C., Mueller, M.M., Bonsanto, M.M., Schmitt, H.P., Kunze, S., and Steiner, H.H. (2002). Clinical impact and functional aspects of tenascin-C expression during glioma progression. Int J Cancer *98*, 362-369.

Hess, M.W., Pfaller, K., Ebner, H.L., Beer, B., Hekl, D., and Seppi, T. (2010). 3D versus 2D cell culture implications for electron microscopy. Methods Cell Biol *96*, 649-670.

Hinz, B., Phan, S.H., Thannickal, V.J., Prunotto, M., Desmouliere, A., Varga, J., De Wever, O., Mareel, M., and Gabbiani, G. (2012). Recent developments in myofibroblast biology: paradigms for connective tissue remodeling. Am J Pathol *180*, 1340-1355.

Hiratsuka, S., Nakamura, K., Iwai, S., Murakami, M., Itoh, T., Kijima, H., Shipley, J.M., Senior, R.M., and Shibuya, M. (2002). MMP9 induction by vascular endothelial growth factor receptor-1 is involved in lung-specific metastasis. Cancer Cell *2*, 289-300.

Ho, L.H., Taylor, R., Dorstyn, L., Cakouros, D., Bouillet, P., and Kumar, S. (2009). A tumor suppressor function for caspase-2. Proc Natl Acad Sci U S A *106*, 5336-5341.

Ho, W.C., Pikor, L., Gao, Y., Elliott, B.E., and Greer, P.A. (2012). Calpain 2 regulates Akt-FoxO-p27(Kip1) protein signaling pathway in mammary carcinoma. The Journal of biological chemistry *287*, 15458-15465.

Hofmann, A., Ritz, U., Verrier, S., Eglin, D., Alini, M., Fuchs, S., Kirkpatrick, C.J., and Rommens, P.M. (2008). The effect of human osteoblasts on proliferation and neo-vessel formation of human umbilical vein endothelial cells in a long-term 3D co-culture on polyurethane scaffolds. Biomaterials *29*, 4217-4226.

Horikawa, Y., Oda, N., Cox, N.J., Li, X., Orho-Melander, M., Hara, M., Hinokio, Y., Lindner, T.H., Mashima, H., Schwarz, P.E.*, et al.* (2000). Genetic variation in the gene encoding calpain-10 is associated with type 2 diabetes mellitus. Nat Genet *26*, 163-175.

Host, L., Paye, A., Detry, B., Blacher, S., Munaut, C., Foidart, J.M., Seiki, M., Sounni, N.E., and Noel, A. (2012). The proteolytic activity of MT4-MMP is required for its pro-angiogenic and pro-metastatic promoting effects. Int J Cancer *131*, 1537-1548.

Hotary, K.B., Yana, I., Sabeh, F., Li, X.Y., Holmbeck, K., Birkedal-Hansen, H., Allen, E.D., Hiraoka, N., and Weiss, S.J. (2002). Matrix metalloproteinases (MMPs) regulate fibrin-invasive activity via MT1-MMP-dependent and -independent processes. J Exp Med *195*, 295-308.

Hou, J.M., Krebs, M.G., Lancashire, L., Sloane, R., Backen, A., Swain, R.K., Priest, L.J., Greystoke, A., Zhou, C., Morris, K.*, et al.* (2012). Clinical significance and molecular characteristics of circulating tumor cells and circulating tumor microemboli in patients with small-cell lung cancer. J Clin Oncol *30*, 525-532.

Huang, G., Gao, Q., Zhao, Y., Dong, Z., Li, T., Guan, X., and Jiang, J. (2015). A novel siRNA validation system for functional screening of effective RNAi targets in mammalian cells and development of a derivative lentivirus delivery system. Gene *558*, 278-286.

Hubbell, J.A. (1995). Biomaterials in tissue engineering. Biotechnology (N Y) *13*, 565-576.

Huber, J.M., Amann, A., Koeck, S., Lorenz, E., Kelm, J.M., Obexer, P., Zwierzina, H., and Gamerith, G. (2016). Evaluation of assays for drug efficacy in a three-dimensional model of the lung. J Cancer Res Clin Oncol *142*, 1955-1966.

Hughes, J.P., Rees, S., Kalindjian, S.B., and Philpott, K.L. (2011). Principles of early drug discovery. Br J Pharmacol *162*, 1239-1249.

Huh, D., Hamilton, G.A., and Ingber, D.E. (2011). From 3D cell culture to organs-on-chips. Trends Cell Biol *21*, 745-754.

Huh, D., Matthews, B.D., Mammoto, A., Montoya-Zavala, M., Hsin, H.Y., and Ingber, D.E. (2010). Reconstituting organ-level lung functions on a chip. Science *328*, 1662-1668.

Hulkower, K.I., and Herber, R.L. (2011). Cell migration and invasion assays as tools for drug discovery. Pharmaceutics *3*, 107-124.

Husemann, Y., Geigl, J.B., Schubert, F., Musiani, P., Meyer, M., Burghart, E., Forni, G., Eils, R., Fehm, T., Riethmuller, G.*, et al.* (2008). Systemic spread is an early step in breast cancer. Cancer Cell *13*, 58-68.

Hwang, C.M., Khademhosseini, A., Park, Y., Sun, K., and Lee, S.H. (2008). Microfluidic chip-based fabrication of PLGA microfiber scaffolds for tissue engineering. Langmuir *24*, 6845-6851.

Hynes, R.O. (1987). Integrins: a family of cell surface receptors. Cell *48*, 549-554.

Hynes, R.O. (1992). Integrins: versatility, modulation, and signaling in cell adhesion. Cell *69*, 11-25.

Hynes, R.O. (2002). Integrins: bidirectional, allosteric signaling machines. Cell *110*, 673-687.

Hynes, R.O. (2009). The extracellular matrix: not just pretty fibrils. Science *326*, 1216-1219.

Hynes, R.O., Bader, B.L., and Hodivala-Dilke, K. (1999). Integrins in vascular development. Braz J Med Biol Res *32*, 501-510.

Ibbetson, S.J., Pyne, N.T., Pollard, A.N., Olson, M.F., and Samuel, M.S. (2013). Mechanotransduction pathways promoting tumor progression are activated in invasive human squamous cell carcinoma. Am J Pathol *183*, 930-937.

Igarashi, M., Irwin, C.R., Locke, M., and Mackenzie, I.C. (2003). Construction of large area organotypical cultures of oral mucosa and skin. J Oral Pathol Med *32*, 422-430.

Imamura, T., Iguchi, H., Manabe, T., Ohshio, G., Yoshimura, T., Wang, Z.H., Suwa, H., Ishigami, S., and Imamura, M. (1995). Quantitative analysis of collagen and collagen subtypes I, III, and V in human pancreatic cancer, tumor-associated chronic pancreatitis, and alcoholic chronic pancreatitis. Pancreas *11*, 357-364.

Inglese, J., Auld, D.S., Jadhav, A., Johnson, R.L., Simeonov, A., Yasgar, A., Zheng, W., and Austin, C.P. (2006). Quantitative high-throughput screening: a titration-based approach that efficiently identifies biological activities in large chemical libraries. Proc Natl Acad Sci U S A *103*, 11473-11478.

Ishiwata, T., Takahashi, K., Shimanuki, Y., Ohashi, R., Cui, R., Takahashi, F., Shimizu, K., Miura, K., and Fukuchi, Y. (2005). Serum tenascin-C as a potential predictive marker of angiogenesis in non-small cell lung cancer. Anticancer Res *25*, 489-495.

Itano, N., Okamoto, S., Zhang, D., Lipton, S.A., and Ruoslahti, E. (2003). Cell spreading controls endoplasmic and nuclear calcium: a physical gene regulation pathway from the cell surface to the nucleus. Proc Natl Acad Sci U S A *100*, 5181-5186.

Itoh, Y., Kajita, M., Kinoh, H., Mori, H., Okada, A., and Seiki, M. (1999). Membrane type 4 matrix metalloproteinase (MT4-MMP, MMP-17) is a glycosylphosphatidylinositol-anchored proteinase. The Journal of biological chemistry *274*, 34260-34266.

Jain, M.P., Choi, A.O., Neibert, K.D., and Maysinger, D. (2009). Probing and preventing quantum dot-induced cytotoxicity with multimodal alpha-lipoic acid in multiple dimensions of the peripheral nervous system. Nanomedicine (Lond) *4*, 277-290.

Jansen, V.M., Bhola, N.E., Bauer, J.A., Formisano, L., Lee, K.M., Hutchinson, K.E., Witkiewicz, A.K., Moore, P.D., Estrada, M.V., Sanchez, V.*, et al.* (2017). Kinome-Wide RNA Interference Screen Reveals a Role for PDK1 in Acquired Resistance to CDK4/6 Inhibition in ER-Positive Breast Cancer. Cancer Res *77*, 2488-2499.

Jensen, D.H., Reibel, J., Mackenzie, I.C., and Dabelsteen, E. (2015). Single cell migration in oral squamous cell carcinoma - possible evidence of epithelial-mesenchymal transition in vivo. J Oral Pathol Med *44*, 674-679.

Jiang, W.G., Sanders, A.J., Katoh, M., Ungefroren, H., Gieseler, F., Prince, M., Thompson, S.K., Zollo, M., Spano, D., Dhawan, P.*, et al.* (2015). Tissue invasion and metastasis: Molecular, biological and clinical perspectives. Semin Cancer Biol *35 Suppl*, S244-S275.

Kadaba, R., Birke, H., Wang, J., Hooper, S., Andl, C.D., Di Maggio, F., Soylu, E., Ghallab, M., Bor, D., Froeling, F.E.*, et al.* (2013). Imbalance of desmoplastic stromal cell numbers drives aggressive cancer processes. The Journal of pathology *230*, 107-117.

Kalluri, R. (2016). The biology and function of fibroblasts in cancer. Nat Rev Cancer *16*, 582-598.

Kalluri, R., and Weinberg, R.A. (2009). The basics of epithelial-mesenchymal transition. J Clin Invest *119*, 1420-1428.

Kalluri, R., and Zeisberg, M. (2006). Fibroblasts in cancer. Nat Rev Cancer *6*, 392-401.

Karlsson, H., Fryknas, M., Larsson, R., and Nygren, P. (2012). Loss of cancer drug activity in colon cancer HCT-116 cells during spheroid formation in a new 3-D spheroid cell culture system. Exp Cell Res *318*, 1577-1585.

Kats-Ugurlu, G., Roodink, I., de Weijert, M., Tiemessen, D., Maass, C., Verrijp, K., van der Laak, J., de Waal, R., Mulders, P., Oosterwijk, E.*, et al.* (2009). Circulating tumour tissue fragments in patients with pulmonary metastasis of clear cell renal cell carcinoma. The Journal of pathology *219*, 287-293.

Kenny, H.A., Krausz, T., Yamada, S.D., and Lengyel, E. (2007). Use of a novel 3D culture model to elucidate the role of mesothelial cells, fibroblasts and extra-cellular matrices on adhesion and invasion of ovarian cancer cells to the omentum. Int J Cancer *121*, 1463-1472.

Kerr, J.F., Wyllie, A.H., and Currie, A.R. (1972). Apoptosis: a basic biological phenomenon with wide-ranging implications in tissue kinetics. Br J Cancer *26*, 239-257.

Khetan, S., Guvendiren, M., Legant, W.R., Cohen, D.M., Chen, C.S., and Burdick, J.A. (2013). Degradation-mediated cellular traction directs stem cell fate in covalently crosslinked three-dimensional hydrogels. Nat Mater *12*, 458-465.

Kiani, C., Chen, L., Wu, Y.J., Yee, A.J., and Yang, B.B. (2002). Structure and function of aggrecan. Cell Res *12*, 19-32.

Kido, H., and Okumura, Y. (2008). Mspl/Tmprss13. Front Biosci *13*, 754-758.

Kim, E.J., Sahai, V., Abel, E.V., Griffith, K.A., Greenson, J.K., Takebe, N., Khan, G.N., Blau, J.L., Craig, R., Balis, U.G.*, et al.* (2014). Pilot clinical trial of hedgehog pathway inhibitor GDC-0449 (vismodegib) in combination with gemcitabine in patients with metastatic pancreatic adenocarcinoma. Clin Cancer Res *20*, 5937-5945.

Kim, J.B., Stein, R., and O'Hare, M.J. (2004). Three-dimensional in vitro tissue culture models of breast cancer-- a review. Breast Cancer Res Treat *85*, 281-291.

Kim, W.J., Chang, C.W., Lee, M., and Kim, S.W. (2007). Efficient siRNA delivery using water soluble lipopolymer for anti-angiogenic gene therapy. J Control Release *118*, 357-363.

Kimlin, L.C., Casagrande, G., and Virador, V.M. (2013). In vitro three-dimensional (3D) models in cancer research: an update. Mol Carcinog *52*, 167-182.

Klein, C.A. (2009). Parallel progression of primary tumours and metastases. Nat Rev Cancer *9*, 302-312.

Kleinman, H.K., and Martin, G.R. (2005). Matrigel: basement membrane matrix with biological activity. Semin Cancer Biol *15*, 378-386.

Klezovitch, O., Chevillet, J., Mirosevich, J., Roberts, R.L., Matusik, R.J., and Vasioukhin, V. (2004). Hepsin promotes prostate cancer progression and metastasis. Cancer Cell *6*, 185-195.

Klumpp, M., Boettcher, A., Becker, D., Meder, G., Blank, J., Leder, L., Forstner, M., Ottl, J., and Mayr, L.M. (2006). Readout technologies for highly miniaturized kinase assays applicable to high-throughput screening in a 1536-well format. J Biomol Screen *11*, 617-633.

Kohrmann, A., Kammerer, U., Kapp, M., Dietl, J., and Anacker, J. (2009). Expression of matrix metalloproteinases (MMPs) in primary human breast cancer and breast cancer cell lines: New findings and review of the literature. BMC Cancer *9*, 188.

Kolenko, V., Uzzo, R.G., Bukowski, R., Bander, N.H., Novick, A.C., Hsi, E.D., and Finke, J.H. (1999). Dead or dying: necrosis versus apoptosis in caspase-deficient human renal cell carcinoma. Cancer Res *59*, 2838-2842.

Kou, Y.B., Zhang, S.Y., Zhao, B.L., Ding, R., Liu, H., and Li, S. (2013). Knockdown of MMP11 inhibits proliferation and invasion of gastric cancer cells. Int J Immunopathol Pharmacol *26*, 361-370.

Kramer, N., Walzl, A., Unger, C., Rosner, M., Krupitza, G., Hengstschlager, M., and Dolznig, H. (2013). In vitro cell migration and invasion assays. Mutat Res *752*, 10-24.

Kumar, C.C., Malkowski, M., Yin, Z., Tanghetti, E., Yaremko, B., Nechuta, T., Varner, J., Liu, M., Smith, E.M., Neustadt, B.*, et al.* (2001). Inhibition of angiogenesis and tumor growth by SCH221153, a dual alpha(v)beta3 and alpha(v)beta5 integrin receptor antagonist. Cancer Res *61*, 2232-2238.

Kunz-Schughart, L.A., Freyer, J.P., Hofstaedter, F., and Ebner, R. (2004). The use of 3-D cultures for high-throughput screening: the multicellular spheroid model. J Biomol Screen *9*, 273-285.

Lam, J., Truong, N.F., and Segura, T. (2014a). Design of cell-matrix interactions in hyaluronic acid hydrogel scaffolds. Acta Biomater *10*, 1571-1580.

Lam, P.Y., Fischer, R.S., Shin, W.D., Waterman, C.M., and Huttenlocher, A. (2014b). Spinning disk confocal imaging of neutrophil migration in zebrafish. Methods in molecular biology *1124*, 219-233.

Lang, N.R., Skodzek, K., Hurst, S., Mainka, A., Steinwachs, J., Schneider, J., Aifantis, K.E., and Fabry, B. (2015). Biphasic response of cell invasion to matrix stiffness in three-dimensional biopolymer networks. Acta Biomater *13*, 61-67.

Langley, R.R., and Fidler, I.J. (2011). The seed and soil hypothesis revisited--the role of tumor-stroma interactions in metastasis to different organs. Int J Cancer *128*, 2527-2535.

Languino, L.R., Gehlsen, K.R., Wayner, E., Carter, W.G., Engvall, E., and Ruoslahti, E. (1989). Endothelial cells use alpha 2 beta 1 integrin as a laminin receptor. The Journal of cell biology *109*, 2455-2462.

Larue, L., and Bellacosa, A. (2005). Epithelial-mesenchymal transition in development and cancer: role of phosphatidylinositol 3' kinase/AKT pathways. Oncogene *24*, 7443-7454.

Laurie, G.W., Leblond, C.P., and Martin, G.R. (1982). Localization of type IV collagen, laminin, heparan sulfate proteoglycan, and fibronectin to the basal lamina of basement membranes. The Journal of cell biology *95*, 340-344.

Law, R.H., Zhang, Q., McGowan, S., Buckle, A.M., Silverman, G.A., Wong, W., Rosado, C.J., Langendorf, C.G., Pike, R.N., Bird, P.I.*, et al.* (2006). An overview of the serpin superfamily. Genome Biol *7*, 216.

LeBleu, V.S., Macdonald, B., and Kalluri, R. (2007). Structure and function of basement membranes. Exp Biol Med (Maywood) *232*, 1121-1129.

Lee, G.Y., Kenny, P.A., Lee, E.H., and Bissell, M.J. (2007). Three-dimensional culture models of normal and malignant breast epithelial cells. Nat Methods *4*, 359-365.

Lee, H.K., Velazquez Sanchez, C., Chen, M., Morin, P.J., Wells, J.M., Hanlon, E.B., and Xia, W. (2016). Three Dimensional Human Neuro-Spheroid Model of Alzheimer's Disease Based on Differentiated Induced Pluripotent Stem Cells. PloS one *11*, e0163072.

Lee, J., Cuddihy, M.J., and Kotov, N.A. (2008a). Three-dimensional cell culture matrices: state of the art. Tissue Eng Part B Rev *14*, 61-86.

Lee, J., Galloway, R., Grandjean, G., Jacob, J., Humphries, J., Bartholomeusz, C., Goodstal, S., Lim, B., Bartholomeusz, G., Ueno, N.T.*, et al.* (2015). Comprehensive Two- and Three-Dimensional RNAi Screening Identifies PI3K Inhibition as a Complement to MEK Inhibitor AS703026 for Combination Treatment of Triple-Negative Breast Cancer. J Cancer *6*, 1306-1319.

Lee, S.J., Kim, B.G., Choi, Y.L., and Lee, J.W. (2008b). Increased expression of calpain 6 during the progression of uterine cervical neoplasia: immunohistochemical analysis. Oncol Rep *19*, 859-863.

Leist, M., Hasiwa, N., Rovida, C., Daneshian, M., Basketter, D., Kimber, I., Clewell, H., Gocht, T., Goldberg, A., Busquet, F.*, et al.* (2014). Consensus report on the future of animal-free systemic toxicity testing. ALTEX *31*, 341-356.

Leong, D.T., and Ng, K.W. (2014). Probing the relevance of 3D cancer models in nanomedicine research. Adv Drug Deliv Rev *79-80*, 95-106.

Levental, K.R., Yu, H., Kass, L., Lakins, J.N., Egeblad, M., Erler, J.T., Fong, S.F., Csiszar, K., Giaccia, A., Weninger, W.*, et al.* (2009). Matrix crosslinking forces tumor progression by enhancing integrin signaling. Cell *139*, 891-906.

Lewis, K.E., and Eisen, J.S. (2001). Hedgehog signaling is required for primary motoneuron induction in zebrafish. Development *128*, 3485-3495.

Li, H., Fan, X., and Houghton, J. (2007a). Tumor microenvironment: the role of the tumor stroma in cancer. J Cell Biochem *101*, 805-815.

Li, J., Chen, J., and Kirsner, R. (2007b). Pathophysiology of acute wound healing. Clin Dermatol *25*, 9-18.

Li, L., Zhou, Q., Voss, T.C., Quick, K.L., and LaBarbera, D.V. (2016). High-throughput imaging: Focusing in on drug discovery in 3D. Methods *96*, 97-102.

Liang, C.C., Park, A.Y., and Guan, J.L. (2007). In vitro scratch assay: a convenient and inexpensive method for analysis of cell migration in vitro. Nat Protoc *2*, 329-333.

Liao, D., Luo, Y., Markowitz, D., Xiang, R., and Reisfeld, R.A. (2009). Cancer associated fibroblasts promote tumor growth and metastasis by modulating the tumor immune microenvironment in a 4T1 murine breast cancer model. PloS one *4*, e7965.

Ling, C., Groop, L., Guerra, S.D., and Lupi, R. (2009). Calpain-10 expression is elevated in pancreatic islets from patients with type 2 diabetes. PloS one *4*, e6558.

Liotta, L.A. (1984). Tumor invasion and metastases: role of the basement membrane. Warner-Lambert Parke-Davis Award lecture. Am J Pathol *117*, 339-348.

Liotta, L.A., Abe, S., Robey, P.G., and Martin, G.R. (1979). Preferential digestion of basement membrane collagen by an enzyme derived from a metastatic murine tumor. Proc Natl Acad Sci U S A *76*, 2268-2272.

Liotta, L.A., Kleinerman, J., Catanzaro, P., and Rynbrandt, D. (1977). Degradation of basement membrane by murine tumor cells. J Natl Cancer Inst *58*, 1427-1431.

Liotta, L.A., and Rao, C.N. (1986). Tumor invasion and metastasis. Monogr Pathol, 183-192.

Liotta, L.A., Tryggvason, K., Garbisa, S., Hart, I., Foltz, C.M., and Shafie, S. (1980). Metastatic potential correlates with enzymatic degradation of basement membrane collagen. Nature *284*, 67-68.

Littlepage, L.E., Sternlicht, M.D., Rougier, N., Phillips, J., Gallo, E., Yu, Y., Williams, K., Brenot, A., Gordon, J.I., and Werb, Z. (2010). Matrix metalloproteinases contribute distinct roles in neuroendocrine prostate carcinogenesis, metastasis, and angiogenesis progression. Cancer Res *70*, 2224-2234.

Livak, K.J., and Schmittgen, T.D. (2001). Analysis of relative gene expression data using real-time quantitative PCR and the 2(-Delta Delta C(T)) Method. Methods *25*, 402-408.

Loessner, D., Stok, K.S., Lutolf, M.P., Hutmacher, D.W., Clements, J.A., and Rizzi, S.C. (2010). Bioengineered 3D platform to explore cell-ECM interactions and drug resistance of epithelial ovarian cancer cells. Biomaterials *31*, 8494-8506.

Lopez, J., John, S.W., Tenev, T., Rautureau, G.J., Hinds, M.G., Francalanci, F., Wilson, R., Broemer, M., Santoro, M.M., Day, C.L.*, et al.* (2011). CARD-mediated autoinhibition of cIAP1's E3 ligase activity suppresses cell proliferation and migration. Mol Cell *42*, 569-583.

Lu, P., Takai, K., Weaver, V.M., and Werb, Z. (2011). Extracellular matrix degradation and remodeling in development and disease. Cold Spring Harb Perspect Biol *3*.

Luo, W., Ren, Z., Gao, S., Jin, H., Zhang, G., Zhou, L., and Zheng, S. (2016). Clinical correlation of calpain-1 and glypican-3 expression with gallbladder carcinoma. Oncol Lett *11*, 1345-1352.

Luzzi, K.J., MacDonald, I.C., Schmidt, E.E., Kerkvliet, N., Morris, V.L., Chambers, A.F., and Groom, A.C. (1998). Multistep nature of metastatic inefficiency: dormancy of solitary cells after successful extravasation and limited survival of early micrometastases. Am J Pathol *153*, 865-873.

Maatta, M., Soini, Y., Paakko, P., Salo, S., Tryggvason, K., and Autio-Harmainen, H. (1999). Expression of the laminin gamma2 chain in different histological types of lung carcinoma. A study by immunohistochemistry and in situ hybridization. The Journal of pathology *188*, 361-368.

Macarron, R., Banks, M.N., Bojanic, D., Burns, D.J., Cirovic, D.A., Garyantes, T., Green, D.V., Hertzberg, R.P., Janzen, W.P., Paslay, J.W*., et al.* (2011). Impact of high-throughput screening in biomedical research. Nat Rev Drug Discov *10*, 188-195.

Mackenzie, I.C. (2004). Growth of malignant oral epithelial stem cells after seeding into organotypical cultures of normal mucosa. J Oral Pathol Med *33*, 71-78.

Mackenzie, I.C., and Fusenig, N.E. (1983). Regeneration of organized epithelial structure. J Invest Dermatol *81*, 189s-194s.

Macmillan, B.G. (1962). Homograft skin--a valuable adjunct to the treatment of thermal burns. J Trauma *2*, 130-141.

Makarovskiy, A.N., Ackerley, W., 3rd, Wojcik, L., Halpert, G.K., Stein, B.S., Carreiro, M.P., and Hixson, D.C. (1997). Application of immunomagnetic beads in combination with RT-PCR for the detection of circulating prostate cancer cells. J Clin Lab Anal *11*, 346-350.

Mamoune, A., Luo, J.H., Lauffenburger, D.A., and Wells, A. (2003). Calpain-2 as a target for limiting prostate cancer invasion. Cancer Res *63*, 4632-4640.

Marhefka, J.N., and Abbud-Antaki, R.A. (2012). Validation of the Cancer BioChip System as a 3D siRNA screening tool for breast cancer targets. PloS one *7*, e46086.

Marsh, D., Dickinson, S., Neill, G.W., Marshall, J.F., Hart, I.R., and Thomas, G.J. (2008). alpha vbeta 6 Integrin promotes the invasion of morphoeic basal cell carcinoma through stromal modulation. Cancer Res *68*, 3295-3303.

Marshall, J. (2011). Transwell((R)) invasion assays. Methods in molecular biology *769*, 97-110.

Martina, E., Chiquet-Ehrismann, R., and Brellier, F. (2010). Tenascin-W: an extracellular matrix protein associated with osteogenesis and cancer. Int J Biochem Cell Biol *42*, 1412-1415.

Mathes, S.H., Wohlwend, L., Uebersax, L., von Mentlen, R., Thoma, D.S., Jung, R.E., Gorlach, C., and Graf-Hausner, U. (2010). A bioreactor test system to mimic the biological and mechanical environment of oral soft tissues and to evaluate substitutes for connective tissue grafts. Biotechnol Bioeng *107*, 1029-1039.

Mayr, L.M., and Fuerst, P. (2008). The future of high-throughput screening. J Biomol Screen *13*, 443-448.

McAnulty, R.J. (2007). Fibroblasts and myofibroblasts: their source, function and role in disease. Int J Biochem Cell Biol *39*, 666-671.

McBeath, R., Pirone, D.M., Nelson, C.M., Bhadriraju, K., and Chen, C.S. (2004). Cell shape, cytoskeletal tension, and RhoA regulate stem cell lineage commitment. Dev Cell *6*, 483-495.

McDermott, U., Sharma, S.V., and Settleman, J. (2008). High-throughput lung cancer cell line screening for genotype-correlated sensitivity to an EGFR kinase inhibitor. Methods Enzymol *438*, 331-341.

McGurk, L., Morrison, H., Keegan, L.P., Sharpe, J., and O'Connell, M.A. (2007). Three-dimensional imaging of Drosophila melanogaster. PloS one *2*, e834.

McIlwain, D.R., Berger, T., and Mak, T.W. (2013). Caspase functions in cell death and disease. Cold Spring Harb Perspect Biol *5*, a008656.

McPherson, J.M., Wallace, D.G., Sawamura, S.J., Conti, A., Condell, R.A., Wade, S., and Piez, K.A. (1985). Collagen fibrillogenesis in vitro: a characterization of fibril quality as a function of assembly conditions. Coll Relat Res *5*, 119-135.

Mecham, R.P. (2008). Methods in elastic tissue biology: elastin isolation and purification. Methods *45*, 32-41.

Mehta, G., Hsiao, A.Y., Ingram, M., Luker, G.D., and Takayama, S. (2012). Opportunities and challenges for use of tumor spheroids as models to test drug delivery and efficacy. J Control Release *164*, 192-204.

Meng, W., Kallinteri, P., Walker, D.A., Parker, T.L., and Garnett, M.C. (2007). Evaluation of poly (glycerol-adipate) nanoparticle uptake in an in vitro 3-D brain tumor co-culture model. Exp Biol Med (Maywood) *232*, 1100-1108.

Miller, E.J. (1985). The structure of fibril-forming collagens. Ann N Y Acad Sci *460*, 1-13.

Miyazono, K. (2009). Transforming growth factor-beta signaling in epithelial-mesenchymal transition and progression of cancer. Proc Jpn Acad Ser B Phys Biol Sci *85*, 314-323.

Moore, K.M., Thomas, G.J., Duffy, S.W., Warwick, J., Gabe, R., Chou, P., Ellis, I.O., Green, A.R., Haider, S., Brouilette, K.*, et al.* (2014). Therapeutic targeting of integrin alphavbeta6 in breast cancer. J Natl Cancer Inst *106*.

Moreno-Luna, R., Abrante, A., Esteban, F., Gonzalez-Moles, M.A., Delgado-Rodriguez, M., Saez, M.E., Gonzalez-Perez, A., Ramirez-Lorca, R., Real, L.M., and Ruiz, A. (2011). Calpain 10 gene and laryngeal cancer: a survival analysis. Head Neck *33*, 72-76.

Moretti, D., Del Bello, B., Cosci, E., Biagioli, M., Miracco, C., and Maellaro, E. (2009). Novel variants of muscle calpain 3 identified in human melanoma cells: cisplatin-induced changes in vitro and differential expression in melanocytic lesions. Carcinogenesis *30*, 960-967.

Moutasim, K.A., Nystrom, M.L., and Thomas, G.J. (2011). Cell migration and invasion assays. Methods in molecular biology *731*, 333-343.

Mu, D., Cambier, S., Fjellbirkeland, L., Baron, J.L., Munger, J.S., Kawakatsu, H., Sheppard, D., Broaddus, V.C., and Nishimura, S.L. (2002). The integrin alpha(v)beta8 mediates epithelial homeostasis through MT1-MMP-dependent activation of TGF-beta1. The Journal of cell biology *157*, 493-507.

Mueller, D., Kramer, L., Hoffmann, E., Klein, S., and Noor, F. (2014). 3D organotypic HepaRG cultures as in vitro model for acute and repeated dose toxicity studies. Toxicol In Vitro *28*, 104-112.

Nagase, H., Visse, R., and Murphy, G. (2006). Structure and function of matrix metalloproteinases and TIMPs. Cardiovasc Res *69*, 562-573.

Nelson, C.M., and Bissell, M.J. (2006). Of extracellular matrix, scaffolds, and signaling: tissue architecture regulates development, homeostasis, and cancer. Annu Rev Cell Dev Biol *22*, 287-309.

Nicolson, G.L. (1982). Cancer metastasis. Organ colonization and the cell-surface properties of malignant cells. Biochim Biophys Acta *695*, 113-176.

Nishiyama, T., Amano, S., Tsunenaga, M., Kadoya, K., Takeda, A., Adachi, E., and Burgeson, R.E. (2000). The importance of laminin 5 in the dermal-epidermal basement membrane. J Dermatol Sci *24 Suppl 1*, S51-59.

Noel, J.C., Fernandez-Aguilar, S., Fayt, I., Buxant, F., Ansion, M.H., Simon, P., and Anaf, V. (2005). Laminin-5 gamma 2 chain expression in cervical intraepithelial neoplasia and invasive cervical carcinoma. Acta Obstet Gynecol Scand *84*, 1119-1123.

Nyga, A., Cheema, U., and Loizidou, M. (2011). 3D tumour models: novel in vitro approaches to cancer studies. J Cell Commun Signal *5*, 239-248.

Nystrom, M.L., Thomas, G.J., Stone, M., Mackenzie, I.C., Hart, I.R., and Marshall, J.F. (2005). Development of a quantitative method to analyse tumour cell invasion in organotypic culture. The Journal of pathology *205*, 468-475.

Oberst, M.D., Johnson, M.D., Dickson, R.B., Lin, C.Y., Singh, B., Stewart, M., Williams, A., al-Nafussi, A., Smyth, J.F., Gabra, H.*, et al.* (2002). Expression of the serine protease matriptase and its inhibitor HAI-1 in epithelial ovarian cancer: correlation with clinical outcome and tumor clinicopathological parameters. Clin Cancer Res *8*, 1101-1107.

Olivier, M., Langerod, A., Carrieri, P., Bergh, J., Klaar, S., Eyfjord, J., Theillet, C., Rodriguez, C., Lidereau, R., Bieche, I.*, et al.* (2006). The clinical value of somatic TP53 gene mutations in 1,794 patients with breast cancer. Clin Cancer Res *12*, 1157-1167.

Olsson, M., and Zhivotovsky, B. (2011). Caspases and cancer. Cell Death Differ *18*, 1441-1449.

Ono, Y., and Sorimachi, H. (2012). Calpains: an elaborate proteolytic system. Biochim Biophys Acta *1824*, 224-236.

Orend, G., and Chiquet-Ehrismann, R. (2006). Tenascin-C induced signaling in cancer. Cancer Lett *244*, 143-163.

Orimo, A., Gupta, P.B., Sgroi, D.C., Arenzana-Seisdedos, F., Delaunay, T., Naeem, R., Carey, V.J., Richardson, A.L., and Weinberg, R.A. (2005). Stromal fibroblasts present in invasive human breast carcinomas promote tumor growth and angiogenesis through elevated SDF-1/CXCL12 secretion. Cell *121*, 335-348.

Orkin, R.W., Gehron, P., McGoodwin, E.B., Martin, G.R., Valentine, T., and Swarm, R. (1977). A murine tumor producing a matrix of basement membrane. J Exp Med *145*, 204-220.

Orloff, J., Douglas, F., Pinheiro, J., Levinson, S., Branson, M., Chaturvedi, P., Ette, E., Gallo, P., Hirsch, G., Mehta, C.*, et al.* (2009). The future of drug development: advancing clinical trial design. Nat Rev Drug Discov *8*, 949-957.

Ott, L.M., Ramachandran, K., and Stehno-Bittel, L. (2017). An Automated Multiplexed Hepatotoxicity and CYP Induction Assay Using HepaRG Cells in 2D and 3D. SLAS Discov *22*, 614-625.

Ovcharenko, D., Jarvis, R., Hunicke-Smith, S., Kelnar, K., and Brown, D. (2005). High-throughput RNAi screening in vitro: from cell lines to primary cells. RNA *11*, 985-993.

P, O.c., Modjtahedi, H., Rhys-Evans, P., Court, W.J., Box, G.M., and Eccles, S.A. (2000). Epidermal growth factor-like ligands differentially up-regulate matrix metalloproteinase 9 in head and neck squamous carcinoma cells. Cancer Res *60*, 1121-1128.

Page-McCaw, A., Ewald, A.J., and Werb, Z. (2007). Matrix metalloproteinases and the regulation of tissue remodelling. Nat Rev Mol Cell Biol *8*, 221-233.

Paget, S. (1889). The Distribution Of Secondary Growths In Cancer Of The Breast. THE LANCET *133*, 571-573.

Paget, S. (1989). The distribution of secondary growths in cancer of the breast. 1889. Cancer Metastasis Rev *8*, 98-101.

Pampaloni, F., Reynaud, E.G., and Stelzer, E.H. (2007). The third dimension bridges the gap between cell culture and live tissue. Nat Rev Mol Cell Biol *8*, 839-845.

Pan, T., Fong, E.L., Martinez, M., Harrington, D.A., Lin, S.H., Farach-Carson, M.C., and Satcher, R.L. (2015). Three-dimensional (3D) culture of bone-derived human 786-O renal cell carcinoma retains relevant clinical characteristics of bone metastases. Cancer Lett *365*, 89-95.

Pankov, R., and Yamada, K.M. (2002). Fibronectin at a glance. J Cell Sci *115*, 3861-3863.

Pantel, K., Brakenhoff, R.H., and Brandt, B. (2008). Detection, clinical relevance and specific biological properties of disseminating tumour cells. Nat Rev Cancer *8*, 329-340.

Parenteau, N.L., Bilbo, P., Nolte, C.J., Mason, V.S., and Rosenberg, M. (1992). The organotypic culture of human skin keratinocytes and fibroblasts to achieve form and function. Cytotechnology *9*, 163-171.

Parrish, A.B., Freel, C.D., and Kornbluth, S. (2013). Cellular mechanisms controlling caspase activation and function. Cold Spring Harb Perspect Biol *5*.

Paszek, M.J., Zahir, N., Johnson, K.R., Lakins, J.N., Rozenberg, G.I., Gefen, A., Reinhart-King, C.A., Margulies, S.S., Dembo, M., Boettiger, D.*, et al.* (2005). Tensional homeostasis and the malignant phenotype. Cancer Cell *8*, 241-254.

Paulus, W., Baur, I., Beutler, A.S., and Reeves, S.A. (1996). Diffuse brain invasion of glioma cells requires beta 1 integrins. Lab Invest *75*, 819-826.

Perrimon, N., and Bernfield, M. (2001). Cellular functions of proteoglycans--an overview. Semin Cell Dev Biol *12*, 65-67.

Petersen, O.W., Ronnov-Jessen, L., Howlett, A.R., and Bissell, M.J. (1992). Interaction with basement membrane serves to rapidly distinguish growth and differentiation pattern of normal and malignant human breast epithelial cells. Proc Natl Acad Sci U S A *89*, 9064-9068.

Petrocca, F., Altschuler, G., Tan, S.M., Mendillo, M.L., Yan, H., Jerry, D.J., Kung, A.L., Hide, W., Ince, T.A., and Lieberman, J. (2013). A genome-wide siRNA screen identifies proteasome addiction as a vulnerability of basal-like triple-negative breast cancer cells. Cancer Cell *24*, 182-196.

Phelps, R.M., Johnson, B.E., Ihde, D.C., Gazdar, A.F., Carbone, D.P., McClintock, P.R., Linnoila, R.I., Matthews, M.J., Bunn, P.A., Jr., Carney, D.*, et al.* (1996). NCI-Navy Medical Oncology Branch cell line data base. J Cell Biochem Suppl *24*, 32-91.

Pickup, M.W., Mouw, J.K., and Weaver, V.M. (2014). The extracellular matrix modulates the hallmarks of cancer. EMBO Rep *15*, 1243-1253.

Pietras, K., Pahler, J., Bergers, G., and Hanahan, D. (2008). Functions of paracrine PDGF signaling in the proangiogenic tumor stroma revealed by pharmacological targeting. PLoS Med *5*, e19.

Pignolo, R.J., Cristofalo, V.J., and Rotenberg, M.O. (1993). Senescent WI-38 cells fail to express EPC-1, a gene induced in young cells upon entry into the G0 state. The Journal of biological chemistry *268*, 8949-8957.

Ponten, F., Ren, Z., Nister, M., Westermark, B., and Ponten, J. (1994). Epithelial-stromal interactions in basal cell cancer: the PDGF system. J Invest Dermatol *102*, 304-309.

Potente, M., Gerhardt, H., and Carmeliet, P. (2011). Basic and therapeutic aspects of angiogenesis. Cell *146*, 873-887.

Poujade, M., Grasland-Mongrain, E., Hertzog, A., Jouanneau, J., Chavrier, P., Ladoux, B., Buguin, A., and Silberzan, P. (2007). Collective migration of an epithelial monolayer in response to a model wound. Proc Natl Acad Sci U S A *104*, 15988-15993.

Provenzano, P.P., Eliceiri, K.W., Campbell, J.M., Inman, D.R., White, J.G., and Keely, P.J. (2006). Collagen reorganization at the tumor-stromal interface facilitates local invasion. BMC Med *4*, 38.

Provenzano, P.P., Inman, D.R., Eliceiri, K.W., Knittel, J.G., Yan, L., Rueden, C.T., White, J.G., and Keely, P.J. (2008). Collagen density promotes mammary tumor initiation and progression. BMC Med *6*, 11.

Puente, X.S., Pendas, A.M., Llano, E., Velasco, G., and Lopez-Otin, C. (1996). Molecular cloning of a novel membrane-type matrix metalloproteinase from a human breast carcinoma. Cancer Res *56*, 944-949.

Pyke, C., Salo, S., Ralfkiaer, E., Romer, J., Dano, K., and Tryggvason, K. (1995). Laminin-5 is a marker of invading cancer cells in some human carcinomas and is coexpressed with the receptor for urokinase plasminogen activator in budding cancer cells in colon adenocarcinomas. Cancer Res *55*, 4132-4139.

Qian, C.N. (2013). Hijacking the vasculature in ccRCC--co-option, remodelling and angiogenesis. Nat Rev Urol *10*, 300-304.

Quail, D.F., and Joyce, J.A. (2013). Microenvironmental regulation of tumor progression and metastasis. Nat Med *19*, 1423-1437.

Ra, H.J., and Parks, W.C. (2007). Control of matrix metalloproteinase catalytic activity. Matrix biology : journal of the International Society for Matrix Biology *26*, 587-596.

Raeber, G.P., Lutolf, M.P., and Hubbell, J.A. (2007). Mechanisms of 3-D migration and matrix remodeling of fibroblasts within artificial ECMs. Acta Biomater *3*, 615-629.

Raghunath, J., Rollo, J., Sales, K.M., Butler, P.E., and Seifalian, A.M. (2007). Biomaterials and scaffold design: key to tissue-engineering cartilage. Biotechnol Appl Biochem *46*, 73-84.

Rash, B.G., and Grove, E.A. (2007). Patterning the dorsal telencephalon: a role for sonic hedgehog? J Neurosci *27*, 11595-11603.

Ray, S.K., Patel, S.J., Welsh, C.T., Wilford, G.G., Hogan, E.L., and Banik, N.L. (2002). Molecular evidence of apoptotic death in malignant brain tumors including glioblastoma multiforme: upregulation of calpain and caspase-3. J Neurosci Res *69*, 197-206.

Regala, R.P., Justilien, V., Walsh, M.P., Weems, C., Khoor, A., Murray, N.R., and Fields, A.P. (2011). Matrix metalloproteinase-10 promotes Kras-mediated bronchio-alveolar stem cell expansion and lung cancer formation. PloS one *6*, e26439.

Rhee, S. (2009). Fibroblasts in three dimensional matrices: cell migration and matrix remodeling. Exp Mol Med *41*, 858-865.

Ricard-Blum, S. (2011). The collagen family. Cold Spring Harb Perspect Biol *3*, a004978.

Rizki, A., Weaver, V.M., Lee, S.Y., Rozenberg, G.I., Chin, K., Myers, C.A., Bascom, J.L., Mott, J.D., Semeiks, J.R., Grate, L.R.*, et al.* (2008). A human breast cell model of preinvasive to invasive transition. Cancer Res *68*, 1378-1387.

Ropponen, K., Tammi, M., Parkkinen, J., Eskelinen, M., Tammi, R., Lipponen, P., Agren, U., Alhava, E., and Kosma, V.M. (1998). Tumor cell-associated hyaluronan as an unfavorable prognostic factor in colorectal cancer. Cancer Res *58*, 342-347.

Rous, P. (1910). A Transmissible Avian Neoplasm. (Sarcoma of the Common Fowl.). J Exp Med *12*, 696-705.

Rudalska, R., Dauch, D., Longerich, T., McJunkin, K., Wuestefeld, T., Kang, T.W., Hohmeyer, A., Pesic, M., Leibold, J., von Thun, A.*, et al.* (2014). In vivo RNAi screening identifies a mechanism of sorafenib resistance in liver cancer. Nat Med *20*, 1138-1146.

Ryan, S.L., Baird, A.M., Vaz, G., Urquhart, A.J., Senge, M., Richard, D.J., O'Byrne, K.J., and Davies, A.M. (2016). Drug Discovery Approaches Utilizing Three-Dimensional Cell Culture. Assay Drug Dev Technol *14*, 19-28.

Saarialho-Kere, U.K., Kovacs, S.O., Pentland, A.P., Olerud, J.E., Welgus, H.G., and Parks, W.C. (1993). Cell-matrix interactions modulate interstitial collagenase expression by human keratinocytes actively involved in wound healing. J Clin Invest *92*, 2858-2866.

Sadikot, T., Swink, M., Eskew, J.D., Brown, D., Zhao, H., Kusuma, B.R., Rajewski, R.A., Blagg, B.S., Matts, R.L., Holzbeierlein, J.M.*, et al.* (2013). Development of a high-throughput screening cancer cell-based luciferase refolding assay for identifying Hsp90 inhibitors. Assay Drug Dev Technol *11*, 478-488.

Sahai, E., and Marshall, C.J. (2003). Differing modes of tumour cell invasion have distinct requirements for Rho/ROCK signalling and extracellular proteolysis. Nat Cell Biol *5*, 711-719.

Santiago-Walker, A., Li, L., Haass, N.K., and Herlyn, M. (2009). Melanocytes: from morphology to application. Skin Pharmacol Physiol *22*, 114-121.

Sanz-Moreno, V., Gadea, G., Ahn, J., Paterson, H., Marra, P., Pinner, S., Sahai, E., and Marshall, C.J. (2008). Rac activation and inactivation control plasticity of tumor cell movement. Cell *135*, 510-523.

Sarrazin, S., Lamanna, W.C., and Esko, J.D. (2011). Heparan sulfate proteoglycans. Cold Spring Harb Perspect Biol *3*.

Sawhney, A.S., Pathak, C.P., van Rensburg, J.J., Dunn, R.C., and Hubbell, J.A. (1994). Optimization of photopolymerized bioerodible hydrogel properties for adhesion prevention. J Biomed Mater Res *28*, 831-838.

Saxena, G., Koli, K., de la Garza, J., and Ogbureke, K.U. (2015). Matrix metalloproteinase 20-dentin sialophosphoprotein interaction in oral cancer. J Dent Res *94*, 584-593.

Schneider, R.K., Neuss, S., Stainforth, R., Laddach, N., Bovi, M., Knuechel, R., and Perez-Bouza, A. (2008). Three-dimensional epidermis-like growth of human mesenchymal stem cells on dermal equivalents: contribution to tissue organization by adaptation of myofibroblastic phenotype and function. Differentiation *76*, 156-167.

Schroeder, A., Heller, D.A., Winslow, M.M., Dahlman, J.E., Pratt, G.W., Langer, R., Jacks, T., and Anderson, D.G. (2011). Treating metastatic cancer with nanotechnology. Nat Rev Cancer *12*, 39-50.

Scott, K.A., Wood, E.J., and Karran, E.H. (1998). A matrix metalloproteinase inhibitor which prevents fibroblast-mediated collagen lattice contraction. FEBS Letters *441*, 137-140.

Senger, D.R., Perruzzi, C.A., Feder, J., and Dvorak, H.F. (1986). A highly conserved vascular permeability factor secreted by a variety of human and rodent tumor cell lines. Cancer Res *46*, 5629-5632.

Serra, M., Brito, C., Correia, C., and Alves, P.M. (2012). Process engineering of human pluripotent stem cells for clinical application. Trends Biotechnol *30*, 350-359.

Shen, Y., Tolic, N., Purvine, S.O., and Smith, R.D. (2012). Improving collision induced dissociation (CID), high energy collision dissociation (HCD), and electron transfer dissociation (ETD) fourier transform MS/MS degradome-peptidome identifications using high accuracy mass information. J Proteome Res *11*, 668-677.

Shi, J., Wang, E., Milazzo, J.P., Wang, Z., Kinney, J.B., and Vakoc, C.R. (2015). Discovery of cancer drug targets by CRISPR-Cas9 screening of protein domains. Nat Biotechnol *33*, 661-667.

Shiga, K., Hara, M., Nagasaki, T., Sato, T., Takahashi, H., and Takeyama, H. (2015). Cancer-Associated Fibroblasts: Their Characteristics and Their Roles in Tumor Growth. Cancers (Basel) *7*, 2443-2458.

Shin, S., Lee, Y., Kim, W., Ko, H., Choi, H., and Kim, K. (2005). Caspase-2 primes cancer cells for TRAIL-mediated apoptosis by processing procaspase-8. EMBO J *24*, 3532-3542.

Shivapurkar, N., Toyooka, S., Eby, M.T., Huang, C.X., Sathyanarayana, U.G., Cunningham, H.T., Reddy, J.L., Brambilla, E., Takahashi, T., Minna, J.D.*, et al.* (2002). Differential inactivation of caspase-8 in lung cancers. Cancer Biol Ther *1*, 65-69.

Shoulders, M.D., and Raines, R.T. (2009). Collagen structure and stability. Annu Rev Biochem *78*, 929-958.

Shulla, A., Heald-Sargent, T., Subramanya, G., Zhao, J., Perlman, S., and Gallagher, T. (2011). A transmembrane serine protease is linked to the severe acute respiratory syndrome coronavirus receptor and activates virus entry. J Virol *85*, 873-882.

Silverman, G.A., Bird, P.I., Carrell, R.W., Church, F.C., Coughlin, P.B., Gettins, P.G., Irving, J.A., Lomas, D.A., Luke, C.J., Moyer, R.W.*, et al.* (2001). The serpins are an expanding superfamily of structurally similar but functionally diverse proteins. Evolution, mechanism of inhibition, novel functions, and a revised nomenclature. The Journal of biological chemistry *276*, 33293-33296.

Simian, M., Hirai, Y., Navre, M., Werb, Z., Lochter, A., and Bissell, M.J. (2001). The interplay of matrix metalloproteinases, morphogens and growth factors is necessary for branching of mammary epithelial cells. Development *128*, 3117-3131.

Simon, C., Nemechek, A.J., Boyd, D., O'Malley, B.W., Jr., Goepfert, H., Flaitz, C.M., and Hicks, M.J. (1998). An orthotopic floor-of-mouth cancer model allows quantification of tumor invasion. Laryngoscope *108*, 1686-1691.

Simpson, K.J., Selfors, L.M., Bui, J., Reynolds, A., Leake, D., Khvorova, A., and Brugge, J.S. (2008). Identification of genes that regulate epithelial cell migration using an siRNA screening approach. Nat Cell Biol *10*, 1027-1038.

Singhvi, R., Kumar, A., Lopez, G.P., Stephanopoulos, G.N., Wang, D.I., Whitesides, G.M., and Ingber, D.E. (1994). Engineering cell shape and function. Science *264*, 696-698.

Smolen, G.A., Zhang, J., Zubrowski, M.J., Edelman, E.J., Luo, B., Yu, M., Ng, L.W., Scherber, C.M., Schott, B.J., Ramaswamy, S.*, et al.* (2010). A genome-wide RNAi screen identifies multiple RSK-dependent regulators of cell migration. Genes Dev *24*, 2654-2665.

Sorimachi, H., and Suzuki, K. (2001). The structure of calpain. J Biochem *129*, 653-664.

Sreenath, T., Matrisian, L.M., Stetler-Stevenson, W., Gattoni-Celli, S., and Pozzatti, R.O. (1992). Expression of matrix metalloproteinase genes in transformed rat cell lines of high and low metastatic potential. Cancer Res *52*, 4942-4947.

Stark, H.J., Baur, M., Breitkreutz, D., Mirancea, N., and Fusenig, N.E. (1999). Organotypic keratinocyte cocultures in defined medium with regular epidermal morphogenesis and differentiation. J Invest Dermatol *112*, 681-691.

Stechmiller, J., Cowan, L., and Schultz, G. (2010). The role of doxycycline as a matrix metalloproteinase inhibitor for the treatment of chronic wounds. Biol Res Nurs *11*, 336-344.

Steele, F.R., Chader, G.J., Johnson, L.V., and Tombran-Tink, J. (1993). Pigment epithelium-derived factor: neurotrophic activity and identification as a member of the serine protease inhibitor gene family. Proc Natl Acad Sci U S A *90*, 1526-1530.

Storr, S.J., Carragher, N.O., Frame, M.C., Parr, T., and Martin, S.G. (2011). The calpain system and cancer. Nat Rev Cancer *11*, 364-374.

Strovel, J., Sittampalam, S., Coussens, N.P., Hughes, M., Inglese, J., Kurtz, A., Andalibi, A., Patton, L., Austin, C., Baltezor, M.*, et al.* (2004). Early Drug Discovery and Development Guidelines: For Academic Researchers, Collaborators, and Start-up Companies. In Assay Guidance Manual, G.S. Sittampalam, N.P. Coussens, K. Brimacombe, A. Grossman, M. Arkin, D. Auld, C. Austin, J. Baell, B. Bejcek, T.D.Y. Chung*, et al.*, eds. (Bethesda (MD)).

Suh, H., and Lee, J.E. (2002). Behavior of fibroblasts on a porous hyaluronic acid incorporated collagen matrix. Yonsei Med J *43*, 193-202.

Sung, K.E., Su, G., Pehlke, C., Trier, S.M., Eliceiri, K.W., Keely, P.J., Friedl, A., and Beebe, D.J. (2009). Control of 3-dimensional collagen matrix polymerization for reproducible human mammary fibroblast cell culture in microfluidic devices. Biomaterials *30*, 4833-4841.

Sutherland, R.M., and Durand, R.E. (1984). Growth and cellular characteristics of multicell spheroids. Recent Results Cancer Res *95*, 24-49.

Sutherland, R.M., Inch, W.R., McCredie, J.A., and Kruuv, J. (1970). A multi-component radiation survival curve using an in vitro tumour model. Int J Radiat Biol Relat Stud Phys Chem Med *18*, 491-495.

Sutherland, R.M., McCredie, J.A., and Inch, W.R. (1971). Growth of multicell spheroids in tissue culture as a model of nodular carcinomas. J Natl Cancer Inst *46*, 113-120.

Takita, J., Yang, H.W., Bessho, F., Hanada, R., Yamamoto, K., Kidd, V., Teitz, T., Wei, T., and Hayashi, Y. (2000). Absent or reduced expression of the caspase 8 gene occurs frequently in neuroblastoma, but not commonly in Ewing sarcoma or rhabdomyosarcoma. Med Pediatr Oncol *35*, 541-543.

Tanaka, K., Hiraiwa, N., Hashimoto, H., Yamazaki, Y., and Kusakabe, M. (2004). Tenascin-C regulates angiogenesis in tumor through the regulation of vascular endothelial growth factor expression. Int J Cancer *108*, 31-40.

Teitz, T., Wei, T., Valentine, M.B., Vanin, E.F., Grenet, J., Valentine, V.A., Behm, F.G., Look, A.T., Lahti, J.M., and Kidd, V.J. (2000). Caspase 8 is deleted or silenced preferentially in childhood neuroblastomas with amplification of MYCN. Nat Med *6*, 529-535.

Teitze, H. (1965). Famous Problems of Mathematics: Solved and Unsolved Mathematical Problems from Antiquity to Modern Times (New York: Graylock Press).

Thayer, S.P., di Magliano, M.P., Heiser, P.W., Nielsen, C.M., Roberts, D.J., Lauwers, G.Y., Qi, Y.P., Gysin, S., Fernandez-del Castillo, C., Yajnik, V.*, et al.* (2003). Hedgehog is an early and late mediator of pancreatic cancer tumorigenesis. Nature *425*, 851-856.

Thiery, J.P. (2002). Epithelial-mesenchymal transitions in tumour progression. Nat Rev Cancer *2*, 442-454.

Thiery, J.P., Acloque, H., Huang, R.Y., and Nieto, M.A. (2009). Epithelial-mesenchymal transitions in development and disease. Cell *139*, 871-890.

Thoma, C.R., Stroebel, S., Rosch, N., Calpe, B., Krek, W., and Kelm, J.M. (2013). A high-throughput-compatible 3D microtissue co-culture system for phenotypic RNAi screening applications. J Biomol Screen *18*, 1330-1337.

Thomas, G.J., Lewis, M.P., Hart, I.R., Marshall, J.F., and Speight, P.M. (2001a). AlphaVbeta6 integrin promotes invasion of squamous carcinoma cells through up-regulation of matrix metalloproteinase-9. Int J Cancer *92*, 641-650.

Thomas, G.J., Lewis, M.P., Whawell, S.A., Russell, A., Sheppard, D., Hart, I.R., Speight, P.M., and Marshall, J.F. (2001b). Expression of the alphavbeta6 integrin promotes migration and invasion in squamous carcinoma cells. J Invest Dermatol *117*, 67-73.

Thomas, G.J., Nystrom, M.L., and Marshall, J.F. (2006). Alphavbeta6 integrin in wound healing and cancer of the oral cavity. J Oral Pathol Med *35*, 1-10.

Thomas, G.J., Poomsawat, S., Lewis, M.P., Hart, I.R., Speight, P.M., and Marshall, J.F. (2001c). alpha v beta 6 Integrin upregulates matrix metalloproteinase 9 and promotes migration of normal oral keratinocytes. J Invest Dermatol *116*, 898-904.

Timpl, R., Rohde, H., Robey, P.G., Rennard, S.I., Foidart, J.M., and Martin, G.R. (1979). Laminin--a glycoprotein from basement membranes. The Journal of biological chemistry *254*, 9933-9937.

Tolboom, T.C., and Huizinga, T.W. (2007). In vitro matrigel fibroblast invasion assay. Methods Mol Med *135*, 413-421.

Tombran-Tink, J., Chader, G.G., and Johnson, L.V. (1991). PEDF: a pigment epithelium-derived factor with potent neuronal differentiative activity. Exp Eye Res *53*, 411-414.

Tompkins, R.G., and Burke, J.F. (1990). Progress in burn treatment and the use of artificial skin. World J Surg *14*, 819-824.

Torisawa, Y.S., Mosadegh, B., Cavnar, S.P., Ho, M., and Takayama, S. (2011). Transwells with microstamped membranes produce micropatterned two-dimensional and three-dimensional co-cultures. Tissue Eng Part C Methods *17*, 61-67.

Torre, L.A., Bray, F., Siegel, R.L., Ferlay, J., Lortet-Tieulent, J., and Jemal, A. (2015). Global cancer statistics, 2012. CA Cancer J Clin *65*, 87-108.

Tuhkanen, H., Hartikainen, J.M., Soini, Y., Velasco, G., Sironen, R., Nykopp, T.K., Kataja, V., Eskelinen, M., Kosma, V.M., and Mannermaa, A. (2013). Matriptase-2 gene (TMPRSS6) variants associate with breast cancer survival, and reduced expression is related to triple-negative breast cancer. Int J Cancer *133*, 2334-2340.

Tzu, J., and Marinkovich, M.P. (2008). Bridging structure with function: structural, regulatory, and developmental role of laminins. Int J Biochem Cell Biol *40*, 199-214.

Usui, T., Sakurai, M., Kawasaki, H., Ohama, T., Yamawaki, H., and Sato, K. (2017). Establishment of a novel three-dimensional primary culture model for hippocampal neurogenesis. Physiol Rep *5*.

Valastyan, S., Reinhardt, F., Benaich, N., Calogrias, D., Szasz, A.M., Wang, Z.C., Brock, J.E., Richardson, A.L., and Weinberg, R.A. (2009). A pleiotropically acting microRNA, miR-31, inhibits breast cancer metastasis. Cell *137*, 1032-1046.

Valastyan, S., and Weinberg, R.A. (2011). Tumor metastasis: molecular insights and evolving paradigms. Cell *147*, 275-292.

Valcourt, U., Alcaraz, L.B., Exposito, J.Y., Lethias, C., and Bartholin, L. (2015). Tenascin-X: beyond the architectural function. Cell Adh Migr *9*, 154-165.

van der Flier, A., and Sonnenberg, A. (2001). Function and interactions of integrins. Cell Tissue Res *305*, 285-298.

van Roy, F., and Berx, G. (2008). The cell-cell adhesion molecule E-cadherin. Cell Mol Life Sci *65*, 3756-3788.

van Zijl, F., Krupitza, G., and Mikulits, W. (2011). Initial steps of metastasis: cell invasion and endothelial transmigration. Mutat Res *728*, 23-34.

Velling, T., Risteli, J., Wennerberg, K., Mosher, D.F., and Johansson, S. (2002). Polymerization of type I and III collagens is dependent on fibronectin and enhanced by integrins alpha 11beta 1 and alpha 2beta 1. The Journal of biological chemistry *277*, 37377-37381.

Vial, E., Sahai, E., and Marshall, C.J. (2003). ERK-MAPK signaling coordinately regulates activity of Rac1 and RhoA for tumor cell motility. Cancer Cell *4*, 67-79.

Vinci, M., Gowan, S., Boxall, F., Patterson, L., Zimmermann, M., Court, W., Lomas, C., Mendiola, M., Hardisson, D., and Eccles, S.A. (2012). Advances in establishment and analysis of three-dimensional tumor spheroid-based functional assays for target validation and drug evaluation. BMC Biol *10*, 29.

von der Mark, K., Gauss, V., von der Mark, H., and Muller, P. (1977). Relationship between cell shape and type of collagen synthesised as chondrocytes lose their cartilage phenotype in culture. Nature *267*, 531-532.

Vorsmann, H., Groeber, F., Walles, H., Busch, S., Beissert, S., Walczak, H., and Kulms, D. (2013). Development of a human three-dimensional organotypic skin-melanoma spheroid model for in vitro drug testing. Cell Death Dis *4*, e719.

Vracko, R. (1974). Basal lamina scaffold-anatomy and significance for maintenance of orderly tissue structure. Am J Pathol *77*, 314-346.

Wadell, H. (1932). Volume, Shape, and Roundness of Rock Particles. The Journal of Geology *40*, 443-451.

Wagenseil, J.E., and Mecham, R.P. (2007). New insights into elastic fiber assembly. Birth Defects Res C Embryo Today *81*, 229-240.

Wakeling, A.E., Guy, S.P., Woodburn, J.R., Ashton, S.E., Curry, B.J., Barker, A.J., and Gibson, K.H. (2002). ZD1839 (Iressa): an orally active inhibitor of epidermal growth factor signaling with potential for cancer therapy. Cancer Res *62*, 5749-5754.

Wang, C., Tang, Z., Zhao, Y., Yao, R., Li, L., and Sun, W. (2014). Three-dimensional in vitro cancer models: a short review. Biofabrication *6*, 022001.

Ware, M.J., Colbert, K., Keshishian, V., Ho, J., Corr, S.J., Curley, S.A., and Godin, B. (2016). Generation of Homogenous Three-Dimensional Pancreatic Cancer Cell Spheroids Using an Improved Hanging Drop Technique. Tissue Eng Part C Methods *22*, 312-321.

Waymack, P., Duff, R.G., and Sabolinski, M. (2000). The effect of a tissue engineered bilayered living skin analog, over meshed split-thickness autografts on the healing of excised burn wounds. The Apligraf Burn Study Group. Burns *26*, 609-619.

Weaver, V.M., Petersen, O.W., Wang, F., Larabell, C.A., Briand, P., Damsky, C., and Bissell, M.J. (1997). Reversion of the malignant phenotype of human breast cells in three-dimensional culture and in vivo by integrin blocking antibodies. The Journal of cell biology *137*, 231-245.

Weber, P., Montag, D., Schachner, M., and Bernhardt, R.R. (1998). Zebrafish tenascin-W, a new member of the tenascin family. J Neurobiol *35*, 1-16.

Weiss, L. (1990). Metastatic inefficiency. Adv Cancer Res *54*, 159-211.

Wells, A., Grahovac, J., Wheeler, S., Ma, B., and Lauffenburger, D. (2013). Targeting tumor cell motility as a strategy against invasion and metastasis. Trends Pharmacol Sci *34*, 283-289.

Wernert, N. (1997). The multiple roles of tumour stroma. Virchows Arch *430*, 433-443.

West, D.C., Shaw, D.M., Lorenz, P., Adzick, N.S., and Longaker, M.T. (1997). Fibrotic healing of adult and late gestation fetal wounds correlates with increased hyaluronidase activity and removal of hyaluronan. Int J Biochem Cell Biol *29*, 201-210.

Wilhelmsen, K., Litjens, S.H., and Sonnenberg, A. (2006). Multiple functions of the integrin alpha6beta4 in epidermal homeostasis and tumorigenesis. Mol Cell Biol *26*, 2877-2886.

Williams, B.R., Gelman, R.A., Poppke, D.C., and Piez, K.A. (1978). Collagen fibril formation. Optimal in vitro conditions and preliminary kinetic results. The Journal of biological chemistry *253*, 6578-6585.

Wise, S.G., and Weiss, A.S. (2009). Tropoelastin. Int J Biochem Cell Biol *41*, 494-497.

Wolf, K., Mazo, I., Leung, H., Engelke, K., von Andrian, U.H., Deryugina, E.I., Strongin, A.Y., Brocker, E.B., and Friedl, P. (2003). Compensation mechanism in tumor cell migration: mesenchymal-amoeboid transition after blocking of pericellular proteolysis. The Journal of cell biology *160*, 267-277.

Wolf, K., Wu, Y.I., Liu, Y., Geiger, J., Tam, E., Overall, C., Stack, M.S., and Friedl, P. (2007). Multi-step pericellular proteolysis controls the transition from individual to collective cancer cell invasion. Nat Cell Biol *9*, 893-904.

Wolf, M.K. (1970). Anatomy of cultured mouse cerebellum. II. Organotypic migration of granule cells demonstrated by silver impregnantion of normal and mutant cultures. J Comp Neurol *140*, 281-298.

Wood, G.C. (1960). The formation of fibrils from collagen solutions. 2. A mechanism of collagen-fibril formation. Biochem J *75*, 598-605.

Worst, P.K., Mackenzie, I.C., and Fusenig, N.E. (1982). Reformation of organized epidermal structure by transplantation of suspensions and cultures of epidermal and dermal cells. Cell Tissue Res *225*, 65-77.

Worst, P.K., Valentine, E.A., and Fusenig, N.E. (1974). Formation of epidermis after reimplantation of pure primary epidermal cell cultures from perinatal mouse skin. J Natl Cancer Inst *53*, 1061-1064.

Wu, Q., and Parry, G. (2007). Hepsin and prostate cancer. Front Biosci *12*, 5052-5059.

Wu, T., Li, Y., Lu, J., Qiao, Q., Bao, G., Wang, N., He, X., and Du, X. (2013). Increased MMP-21 expression is associated with poor overall survival of patients with gastric cancer. Med Oncol *30*, 323.

Yamada, K.M., and Cukierman, E. (2007). Modeling tissue morphogenesis and cancer in 3D. Cell *130*, 601-610.

Yamaguchi, H., Lorenz, M., Kempiak, S., Sarmiento, C., Coniglio, S., Symons, M., Segall, J., Eddy, R., Miki, H., Takenawa, T.*, et al.* (2005). Molecular mechanisms of invadopodium formation: the role of the N-WASP-Arp2/3 complex pathway and cofilin. The Journal of cell biology *168*, 441-452.

Yamaguchi, H., Yoshida, N., Takanashi, M., Ito, Y., Fukami, K., Yanagihara, K., Yashiro, M., and Sakai, R. (2014). Stromal fibroblasts mediate extracellular matrix remodeling and invasion of scirrhous gastric carcinoma cells. PloS one *9*, e85485.

Yanagishita, M. (1993). Function of proteoglycans in the extracellular matrix. Acta Pathol Jpn *43*, 283-293.

Yang, H., Cheng, R., Liu, G., Zhong, Q., Li, C., Cai, W., Yang, Z., Ma, J., Yang, X., and Gao, G. (2009). PEDF inhibits growth of retinoblastoma by anti-angiogenic activity. Cancer Sci *100*, 2419-2425.

Yee, D., Rosen, N., Favoni, R.E., and Cullen, K.J. (1991). The insulin-like growth factors, their receptors, and their binding proteins in human breast cancer. Cancer Treat Res *53*, 93-106.

Zaman, M.H., Trapani, L.M., Sieminski, A.L., Mackellar, D., Gong, H., Kamm, R.D., Wells, A., Lauffenburger, D.A., and Matsudaira, P. (2006). Migration of tumor cells in 3D matrices is governed by matrix stiffness along with cell-matrix adhesion and proteolysis. Proc Natl Acad Sci U S A *103*, 10889-10894.

Zanoni, M., Piccinini, F., Arienti, C., Zamagni, A., Santi, S., Polico, R., Bevilacqua, A., and Tesei, A. (2016). 3D tumor spheroid models for in vitro therapeutic screening: a systematic approach to enhance the biological relevance of data obtained. Sci Rep *6*, 19103.

Zelenka, P.S., and Arpitha, P. (2008). Coordinating cell proliferation and migration in the lens and cornea. Semin Cell Dev Biol *19*, 113-124.

Zhang, G., Miyake, M., Lawton, A., Goodison, S., and Rosser, C.J. (2014). Matrix metalloproteinase-10 promotes tumor progression through regulation of angiogenic and apoptotic pathways in cervical tumors. BMC Cancer *14*, 310.

Zhang, K., and Kramer, R.H. (1996). Laminin 5 deposition promotes keratinocyte motility. Exp Cell Res *227*, 309-322.

Zhang, S., Gelain, F., and Zhao, X. (2005). Designer self-assembling peptide nanofiber scaffolds for 3D tissue cell cultures. Semin Cancer Biol *15*, 413-420.

Zhang, T., Guan, M., Xu, C., Chen, Y., and Lu, Y. (2007). Pigment epithelium-derived factor inhibits glioma cell growth in vitro and in vivo. Life Sci *81*, 1256-1263.

Zhivotovsky, B. (2003). Caspases: the enzymes of death. Essays Biochem *39*, 25-40.

Zhou, Z., Wang, J., Cao, R., Morita, H., Soininen, R., Chan, K.M., Liu, B., Cao, Y., and Tryggvason, K. (2004). Impaired angiogenesis, delayed wound healing and retarded tumor growth in perlecan heparan sulfate-deficient mice. Cancer Res *64*, 4699-4702.

Zhu, W., Murtha, P.E., and Young, C.Y. (1995). Calpain inhibitor-induced apoptosis in human prostate adenocarcinoma cells. Biochem Biophys Res Commun *214*, 1130-1137.

Zimmermann, W.H., Melnychenko, I., Wasmeier, G., Didie, M., Naito, H., Nixdorff, U., Hess, A., Budinsky, L., Brune, K., Michaelis, B.*, et al.* (2006). Engineered heart tissue grafts improve systolic and diastolic function in infarcted rat hearts. Nat Med *12*, 452-458.